Freie Universität Berlin
Fachbereich Geowissenschaften

# The Pitted Impact Deposits on Asteroid 4 Vesta: An In-Depth Analysis

Dissertation zur Erlangung des akademischen Grades eines

**Doktors der Naturwissenschaften (Dr. rer. nat.)**

eingereicht am Fachbereich Geowissenschaften,
Institut für Geologie der Freien Universität Berlin

vorgelegt von **Tanja Michalik**

Berlin, 2021

| | |
|---|---|
| Erstgutachter: | Prof. Dr. Ralf Jaumann<br>Freie Universität Berlin<br>Institut für Geologische Wissenschaften<br>Fachrichtung Planetologie und Fernerkundung |
| Zweitgutachter: | Prof. Dr. Kai Wünnemann<br>Museum für Naturkunde<br>Leibniz-Institut für Evolutions- und Biodiversitätsforschung<br>sowie<br>Freie Universität Berlin<br>Institut für Geologische Wissenschaften<br>Fachrichtung Planetologie und Fernerkundung |
| Tag der Disputation: | 3. März 2022 |

# Eidesstattliche Erklärung zur Urheberschaft

Ich versichere, dass ich die vorliegende Arbeit selbstständig verfasst habe und dass ich keine anderen als die angegebenen Quellen und Hilfsmittel verwendet habe. Die aus anderen Quellen wörtlich oder inhaltlich übernommenen Stellen sind unter Angabe der entsprechenden Literatur gekennzeichnet. Diese Arbeit hat in gleicher oder ähnlicher Form keiner anderen Hochschule zur Prüfung vorgelegen.

"The more I learn, the more I realize how much I don't know."

*Albert Einstein*

*dedicated to my daughters*

*May you be encouraged to pursue your dreams no matter what others tell you.*

# Acknowledgements

First of all, I would like to gratefully acknowledge the opportunity to work and study at DLR, which I foremost owe to Prof. Dr. Ralf Jaumann. What might have been a small decision for him, was my entrance into the field of plantery science, the place I longed for since I was a child.

I furthermore owe the opportunity to conduct my PhD studies at DLR to Dr. Katharina A. Otto, who built the DLR Junior Research Group and hired me to conduct my PhD studies. She always provided every possible support, both technical and administratively. You were happy for my pregnancy and supported me even if it meant difficulties for you and the group. Thank you!

A special thanks also goes to Klaus-Dieter Matz, who patiently listened to my many questions regarding Linux or IDL and tried his best to provide answers and a code if needed. I do not know how this PhD would have ended without your help!

I want to thank Dr. Alessandro Maturilli under the department lead of Dr. Jörn Helbert for access to the Planetary Spectroscopy Laboratory and the continued help he offered in order to conduct and complete the experiments and measurements. This also goes to Ines Büttner who helped preparing the samples and providing laboratory equipment.

I want to thank the many DLR colleagues that accompanied me during my studies and who helped me with many beneficial discussions about scientific and non-scientific topics, including Elke Kersten, Dr. Katrin Krohn, Dr. Katrin Stephan, Dr. Stefan Schröder, Dr. Jean-Baptiste Vincent, Dr. Daniela Tirsch, Dr. Nilda Oklay, Rutu Ashwin Parekh, Frank Preusker and more. Additionally, I was allowed to attend several conferences as well as Dawn Team Meetings and I am grateful for the financial support provided by DLR as well as the insights and useful conversations I obtained there. I moreover want to thank Dr. Ralf Milke, Prof. Dr. Lutz Hecht and Dr. Felix Kaufmann for the opportunity to analyze my samples via EPMA. Your straightforward support meant a lot to me and I will not forget it.

I also owe a considerable amount of my advances to international colleagues who have likewise helped me during my studies, although partly not even knowing me, including Dr. Edward Cloutis, Dr. Livio L. Tornabene and Prof. Dr. Paul G. Lucey.

At this point, I also want to thank the DAAD (German Academic Exchange Service) for providing the financial opportunity to study abroad. I received two scholarships to conduct an internship in Brisbane, Australia and two semesters of my Masters' studies at UH Mānoa in Hawai'i for which I will eternally be grateful. These times were unforgettable and strengthened my confidence widely. I learned many additional things, not only about geology and planetary science but about humans, societies and cultures. A special thanks here goes to Dr. Myriam Lemelin for helping me to get settled in Hawai'i both at the university and in the Hawai'ian life and for being a wonderful friend. I will never forget the Aloha spirit and the fruitful and cooperative environment I was allowed to experience.

My husband receives the highest degree of gratitude as he patiently endured the many times of lost confidence or troubles regarding this PhD. He dealt with a higher load of childcare especially in the last months and helped me coping with and going through the many months of the SARS-CoV-2 pandemic which undoubtedly severely effected my research work. What kept me going was his unconditional support and my inner urge, passion and curiosity to find out 'what's going on out there'.

# Kurzfassung

Diese Arbeit analysiert geomorphologische Entgasungserscheinungen auf dem atmosphärenlosen Asteroiden Vesta, insbesondere jene, die mit dem Krater Marcia assoziiert sind. Diese machen über 96% der Gesamtanzahl aus und sind die einzigen, die in der Ejekta eines Kraters auftreten. Diese *Pitted Impact Deposits* (*PIDs*, zu deutsch: Einschlagsablagerungen, die eng gruppierte Senken/Mulden aufweisen) wurden zuvor bereits auf Vesta, sowie schon auf dem Mars und auf dem Zwergplaneten Ceres beobachtet. Die eng gruppierten Senken treten als Ansammlung von mehreren Kilometern Länge auf, können überlappen und teilen sich häufig ihre Ränder. Lokal sind sie stark begrenzt zu ihrem direkten Umfeld, welches ebenfalls aus Einschlagsablagerungen besteht. Sie zeigen zudem keine erhöhten Ränder, was für Einschlagskrater typisch wäre. Diese Senken sind polygonal bis rund geformt und zeigen zudem spektrale Besonderheiten, wie höhere Reflektanz bei 750 nm und intensivere Pyroxen-Absorptionsbanden bei ~0.9 und 1.9 µm, auf. Während eindeutig ist, dass diese Erscheinungsformen durch Entgasung bzw. Devolatilisierung der Ejekta entstehen, blieb die genaue Entstehungsursache auf Vesta bisher jedoch ungeklärt.

Viele Studien haben zusätzlich zum bereits bekannten und vorherrschenden, pyroxenreichen HED-ähnlichen Material (von den pyroxenreichen HED-Meteoriten: Howardite, Eukrite, Diogenite) OH-haltiges Material und 'dunkles Material', wahrscheinlich von kohligen Chondriten stammend, im Regolith von Vesta nachgewiesen bzw. eindeutige Hinweise darauf gefunden. Dieses OH liegt in den Kristallstrukturen von Phyllosilikaten vor und kann unter Temperatureinwirkung aus der Kristallstruktur gelöst werden und entgasen bzw. devolatilisieren. Alle hier dargestellten Beobachtungen des Asteroiden Vesta stützen sich auf Daten, die von der NASA-Raumsonde Dawn aufgenommen wurden.

Die hier vorgestellten Analysen zeigen, dass die Entgasung mit Senkenbildung vornehmlich durch das Verhältnis von Volumen zur Oberfläche bzw. Tiefe der Ablagerung kontrolliert wird, da viele PIDs in bereits vor dem Impakt existierenden Kratern und an steilen topografischen Erhöhungen auftreten. Das Vorkommen an solch topographisch eindeutigen Morphologien ermöglicht die Abschätzung der Topographie vor dem Marcia-bildenden Impakt sowie die Abschätzung der Ausprägung und Form der Einschlagsablagerungen nach Impakt. Die Akkumulation von Ejekta an diesen topographisch markanten Stellen führt zu einer verlangsamten Abkühlung des Ejektamaterials, einem größeren erhitzten Volumen welches nicht an der Oberfläche der Weltraumumgebung ausgesetzt wird und dabei zu einer verlängerten Möglichkeit, Volatile aus Mineralstrukturen zu lösen. Die Tiefe der Ablagerung bedingt die Ausprägung der entstehenden Entgasungsschlote und damit der Senken. Der Anteil an Volatilen in der Gesamtejekta wird mit 2% geschätzt und der Anteil bei Ausgasung der PIDs mit 1%. Dies zeigt, dass besonders hohe Volatilanteile nicht benötigt werden, um diese Erscheingsformen hervorzurufen.

PIDs sind immer Teil einer größer ausgeprägten Einschlagsablagerung, was ein identisches Ausgangsmaterial suggeriert. Die spektralen Veränderungen von PIDs im Vergleich zu ihrer direkten Umgebung sind nicht konsistent mit Veränderungen von Korngrößen, Rauigkeit oder dem Vorhandensein von Glaskomponenten im Material. Eine Möglichkeit, die gezeigten spektralen Eigenschaften zu erzeugen, ist das Entfernen von 'dunklem Material'. Bei erhöhten Temperaturen können organische Strukturen (die meist dunkel sind) sowie andere Komponenten von kohligen Chondriten zerfallen. Tochilinit zum Beispiel, ein Hauptbestandteil der Matrix im kohligen Chondrit Murchison, zerfällt bereits bei 400 °C. Jedoch kann die bloße Entfernung von 'dunklem Material' nicht alle Aspekte der spektralen Eigenschaften der PIDs erklären, wie z.B. das höhere Verhältnis der Stärke der Pyroxenabsorption im Vergleich zur Reflektanz bei 750 nm im Vergleich zu anderen typischen Regionen auf Vesta.

Diese Arbeit präsentiert darüber hinaus Laborexperimente, die die spektralen Eigenschaften der PIDs erklären sollten. Diese wurden mit terrestrischem und meteoritischem Material, welches sich

zur Simulation des Regoliths auf Vesta sehr gut eignet, durchgeführt. Die Temperaturexperimente zeigen die Entstehung von Hämatit durch Oxidation und damit einhergehend eine sehr starke Steigung der Reflektanz im visuellen Wellenlängenbereich. Dies wird nicht auf Vesta beobachtet, was jedoch auch andere Gründe haben kann. Zum einen ist das Material auf Vesta sehr inhomogen gemischt, was zu verlangsamten Reaktionen führen kann. Außerdem liegt die geschätzte Ausgasungszeit der PIDs auf Vesta bei Stunden oder wenigen Tagen, was unter Umständen dazu führt, dass die Bildung von Hämatit noch nicht begonnen hat oder nur in einem so geringen Maß, welches nicht per Spektroskopie erkannt werden kann. Des Weiteren ist wenig über die Verwitterung von Hämatit, welches der Weltraumumgebung über geologische Zeiträume ausgesetzt wurde, bekannt, was ebenso eine Rolle spielen könnte.

Vor allem jedoch zeigen die Laborexperimente, in Verbindung mit bereits existierender Literatur zu dem Thema, dass eine oxidierende Umgebung in Verbindung mit erhöhten Temperaturen ($\geq$400 °C, weit unter dem Schmelzpunkt der Minerale) genau jene Erscheinung der PIDs – erhöhte Reflektanzen und intensivere Pyroxen-Absorptionsbanden – hervorrufen kann. Dabei könnten $Fe^{2+}$-Kationen aus ihrer Kristallposition mobilisiert werden und zu den Partikelrändern migrieren. In vielen Studien, auch mit extraterrestrischem Material, wurde dies bereits beobachtet; mit dem Resultat, dass $Fe^{2+}$ zu $Fe^{3+}$ oxidiert und nach Verlassen der Pyroxenstruktur in Verbindung mit den verfügbaren Volatilen Hämatit ($Fe_2O_3$) oder andere Eisen(hydr-)oxide bildet. Eine mögliche Anreicherung von $Fe^{2+}$-Kationen während dieses Prozesses an den Partikelrändern führt dazu, dass eletromagnetische Energie (Licht) zunächst auf mehr Eisen-Kationen im Kristallgitter trifft, was eine Intensivierung der Absorptionsbanden nach sich zieht. Alternativ kann es sein, dass sich im ursprünglich ungeordneten Kristall durch die Erhöhung der Temperatur die Kationen neu ordnen können und $Fe^{2+}$ in seine bevorzugte kristallographische M2-Position migriert. Auch dies würde eine Intensivierung der Pyroxen-Absorptionsbanden hervorrufen. Diese Arbeit zeigt, dass Oxidationsprozesse auch auf Körpern geschehen können, die eigentlich als "trocken" gelten. Die oberflächliche Kontamination mit kohligen Chondriten ermöglicht dabei diesen Prozess, was für zukünftige Missionen und die Suche nach organischem Material eine Rolle spielen könnte.

# Abstract

This work analyzes geomorphological devolatilization features on the atmosphereless asteroid Vesta. In particular, it predominantly analyzes the features associated with the crater Marcia, as those add up to more than 96% on the whole body and are the only ones occurring within the ejecta of a crater. These features are called *Pitted Impact Deposits*, or short *PIDs*, and they have been previously identified on Mars, Vesta and the dwarf planet Ceres. PIDs are characterized by closely spaced pits that occur as locally confined clusters of several kilometers length. The individual pits can overlap and often share boundaries. They lack raised rims as would be typical of an impact crater and are polygonal to circular in shape. Furthermore, they show distinct spectral characteristics like higher reflectance at 750 nm and more intense pyroxene absorptions near 0.9 and 1.9 µm. It is evident through previous studies that PIDs formed via degassing or devolatilization of parts of the ejecta, yet the detailed mechanism behind remained debated.

Additionally to the previously known dominance of pyroxene-rich HED-like material on Vesta (HED: howardite, eucrite, diogenite meteorites), many studies have reported on the existence of OH-bearing material and the so-called 'dark material' which has been proposed to originate from influx of carbonaceous chondrite material. The identified OH is likely bound within the crystal structure of phyllosilicates (that are commonly found in carbonaceous chondrites) and is able to leave the crystal structure when heated. All remote observations shown here were obtained by NASA's Dawn mission.

The presented analysis show that the formation of PIDs is controlled by the proportion of an ejecta deposit's volume to surface area, or depth. Many PIDs are located in small craters or at steep topographic slopes that existed prior to the Marcia impact or to the time of PID formation. This enables the estimation of the pre-existing topography and therefore of the shape and extent of the post-impact ejecta deposit. The accumulation of ejecta at these sites leads to a slower cooling of the ejecta deposit, a larger volume not exposed to the space environment and an extended possibility for volatiles to escape from its host mineral. The depth of the ejecta deposit appears to control the shape and extent of the developing devolatilization vents and therefore, of the individual pits themselves. The proportion of volatiles within the whole ejecta is estimated here to be less than 2 wt% and the proportion of lost volatiles at the PIDs' sites to ~1 wt%. This shows that particularly elevated volatile contents are not needed to form PIDs.

PIDs are always part of a larger impact deposit not featuring a pitted surface. This suggest that the original material of both deposit parts were identical or very similar. The spectral changes of the PIDs with respect to their immediate surroundings are not consistent with variations in grain size, roughness or glass content. One possibility of creating similar spectral characteristics is the removal of darkening agents. At high temperatures, organic material (which are commonly dark) can decompose, as do other components of carbonaceous chondrites. Tochilinite for example is a major constituent in the carbonaceous chondrite Murchison and decomposes already at 400 °C. However, the mere removal of dark components cannot explain all aspects of spectral characteristics shown for PIDs, i.e. the ratio of pyroxene band strength to reflectance at 750 nm with respect to other more typical regions on Vesta.

This thesis furthermore presents laboratory experiments in order to explain the PIDs' spectral characteristics. Both terrestrial and meteoritic materials were used. These were assembled to adequately represent the Vestan regolith. The experiments involving the heating of these analog materials show that hematite formed due to oxidation and therefore, a strong reddening of the visible spectral slope of the samples was observed. This is not observed on Vesta, yet might be explained. First, the ejecta deposit on Vesta is likely very heterogeneous, as has been shown by previous studies. This can lead to a smaller and slower extent of these oxidation processes. Second, the estimated devolatilization duration is in the range of hours to days, possibly inhibiting the onset of hematite formation or the incapability of remote spectrometers to record the small amounts that might have already formed. Third, the processes of space weathering of hematite over geological timescales are not well-known, which could additionally play a role.

In combination with existing literature, the laboratory experiments presented here show that an oxidizing environment together with higher temperatures ($\geq$400 °C, well below the minerals' melting point) can result in similar spectral characteristics, i.e. higher reflectance and pyroxene band strength, as shown for PIDs. The underlying process could involve the migration of $Fe^{2+}$ to the grain surfaces, where it increases the relative iron abundance that electromagnetic energy (i.e., light) encounters first which in turn intensifies the pyroxene absorption. Many studies have observed similar processes where $Fe^{2+}$ is converted to $Fe^{3+}$ and forms hematite ($Fe_2O_3$) or other iron (hydr-)oxides. An alternative explanation also includes the migration of $Fe^{2+}$, yet to its preferred crystallographic M2 site, where it likewise would intensify the pyroxene absorption. Original pyroxene crystals might have been disordered regarding their cation distribution, whereas the temperature increase would enable the cations to migrate to their preferred position. This work shows that oxidation processes can occur on planetary bodies thought to be dry. The surficial contamination with carbonaceous chondrite material enables this process, which might be relevant to future space missions and could influence the search for organic matter.

# Contents

# List of Figures

# List of Tables

# Glossary

| | |
|---|---|
| AOA | Amoeboid Olivine Aggregates |
| AU | Astronomical unit(s) |
| BSE | Backscattered electrons |
| CAIs | Ca-Al-rich inclusions |
| CC | Carbonaceous chondrite |
| CCD | Charged coupled device |
| CM | Mighei group of carbonaceous chondrites |
| DLR | Deutsches Zentrum für Luft- und Raumfahrt e.V. (German Aerospace Center) |
| DTM | Digital Terrain Model |
| EDS | Energy-Dispersive Spectrometry |
| EM | Electromagnetic energy |
| EPMA | Electron Probe Microanalysis |
| FC | Framing Camera |
| GRaND | Gammy Ray and Neutron Detector Instrument |
| HAMO | High altitude mapping orbit |
| HED | Howardite, Eucrite, Diogenite meteorites |
| HST | Hubble Space Telescope |
| I/F | Radiance/solar irradiance, commonly used as reflectance |
| IR | Infrared |
| INAF | Instituto Nationale di Astrofisica, Rome, Italy |
| JaH | Jiddat al Harasis |
| LAMO | Low altitude mapping orbit |
| MPS | Max Planck Institute for Solar System Studies |
| NASA | National Aeronautics and Space Administration |
| NWA | North West Africa |
| NIR | Near infrared wavelength range (0.8-2.5 µm) |
| PID | Pitted impact deposit |
| PSL | Planetary Spectroscopy Laboratory |
| RELAB | Reflectance Experiment Laboratory |
| RGB | Red, Green, Blue; used as channels in an image |
| UV | Ultra violet wavelength range (0.1-0.4 µm) |
| VIS | Visible wavelength range (0.4-0.8 µm) |
| VIR | Visible and Infra-Red Imaging Spectrometer |
| WDS | Wavelength-Dispersive Spectrometry |

# 1 Introduction

## 1.1 Motivation and Outline of this Work

The work undertaken for this dissertation is part of the Junior Research Group "The Physics of Volatile-Related Morphologies on Asteroids and Comets" led by Katharina A. Otto at the German Aerospace Center (DLR e.V.). Asteroids and comets are fascinating objects to study: they are not only remnants of the early solar system that still represent records of the earliest processes and events, but can also serve as carriers of material throughout the system, like for example water. One of the most famous long standing question that has puzzled mankind for decades is whether Earth received its water from extraterrestrial materials. It is therefore crucial to study and understand the past and present volatiles on these bodies in order to understand the evolution of life on Earth and possibly on other objects in our solar system. Volatile-related morphologies can help constrain volatile abundance as well as distribution in and on the body and thus are important features to understand the various processes shaping the surface and/or interior of these solar system objects.

The volatile-related morphologies I studied in this work are the *Pitted Impact Deposits* (PIDs) on Vesta, formerly called 'pitted terrains' or 'pitted materials'. These features were also observed on Mars and Ceres and represent rapid volatile loss from material that was heated by impacts. They are characterized by dense clusters of irregular shaped depressions, mostly lacking a raised rim.

The presence of these features on Vesta was surprising, as Vesta was thought to be dry and differentiated. Presently, the origin of the volatile species forming the pitted impact deposits is still under debate and it is one major objective of this work to test and place further constraints on the existing hypotheses explaining the origin and emplacement of pitted impact deposits. Furthermore, the spectral characteristics of these features have not been analyzed in detail yet although spectrophotometry (or spectroscopy as it is commonly called) is an important tool to characterize the mineralogy of a material.

In this work, I present new geomorphological and spectral observations of the pitted impact deposits on Vesta. This includes mappings, profiles, statistics on pitted impact deposit distribution, size and area as well as a catalogue containing spectral information of these features and spectral comparisons with data obtained from meteorites. Spectral information were obtained by two Dawn instruments and both will be included in this work. In order to understand the spectral changes the material of the pitted impact deposits underwent, I will moreover present laboratory experiments that I undertook in the Planetary Spectroscopy Laboratory at DLR in Berlin and discuss the results of all observations.

This dissertation was partly published in Icarus. The majority of this publication is included in this dissertation and Table 1.1 lists the sections according to the projects and includes the proportion of my work. I will also mention published parts throughout the dissertation. I compiled this dissertation in a way that the reader can follow a red thread which separates some parts of the published version. The publication includes the geomorphological observations and the spectral observations with NASA's Dawn Framing Camera and partly VIR data (2.8 µm band): "The unique spectral and geomorphological characteristics of pitted impact deposits associated with Marcia crater on Vesta" (2021) Icarus 369, by T. Michalik, K.-D. Matz, S.E. Schröder, R. Jaumann, K. Stephan, K. Krohn, F.Preusker, C.A. Raymond. C.T. Russell, K.A. Otto. DOI: 10.1016/j.icarus.2021.114633

Table 1.1: Overview of Thesis projects, (published) sections and T. Michalik's proportion of work.

| # | Topic | sections covered | T. Michalik's work proportion |
|---|---|---|---|
| 1 | PIDs' Geomorphological and Spectral Characteristics as seen by Dawn FC | published sections: 3.4.2, 4.4, 4.5, 4.6, 4.7, 4.8, 6 except 6.5<br>unpublished sections: 4.1, 4.2, 4.3, 4.10 | Concept: 85% (other parts by K. A. Otto)<br>Implementation: 100%<br>Data acquisition: NASA/JPL-Caltech/DLR/MPS/IDA (FC Dawn-Team)<br>Data visualization: 100%<br>Writing: 95% (other parts with help by reviewers and co-authors) |
| 2 | PIDs Spectral Characteristics as seen by VIR | unpublished sections: 4.9, 6.5 | Concept: 100%<br>Implementation: 100%<br>Data acquisition: by VIR-Team (INAF) and K.-D. Matz (DLR)<br>Data visualization: 100%<br>Writing: 100% |
| 3 | Laboratory Experiments & Measurements: Unraveling the Spectral Characteristics of the Vestan PIDs | unpublished sections: 5 and all subsections, 7 | Concept: 80% (other parts by K. A. Otto and E. Cloutis)<br>Implementation: 60% (other parts by A. Maturilli (PSL), R. Milke (FUB) and F. Kaufmann (MfN))<br>Data acquisition: 95% (other parts by A. Maturilli (PSL), R. Milke (FUB) and F. Kaufmann (MfN))<br>Data visualization: 100%<br>Writing: 100% |

## 1.2 Evolution of the Solar System and the Asteroid Belt

Vesta orbits the sun at a distance of ~2.36 AU within the so-called asteroid belt, a conglomeration of millions of individuals objects circling the sun at similar distances and similar orbits but with varying properties and compositions (see Figure 1.1). At current, more than one million asteroids have been discovered with millions more estimated (daily updating source: Minor Planet Center (MPC), operating under the auspices of Division F of the International Astronomical Union (IAU) and funded by NASA). The asteroid belt is believed to represent leftover parts of planetesimals that could not evolve to planets due to collisional disruption and/or gravitational forces (e.g., Bottke et al., 2015; Marchi et al., 2015; Morbidelli et al., 2015; Johansen et al., 2015; and references therein). Figure 1.1 shows the location of Vesta and other bigger objects in the asteroid belt, the mass distribution within the belt and the distribution of spectral types, which will be addressed in the next section.

Studying the objects of the asteroid belt is fascinating and crucial in order to understand what kind of processes took place in the early solar system and afterwards. At present, we understand the formation of the early solar system as a molecular cloud collapsing to form the solar nebula, leaving a young still forming stellar object and a gas and dust disk, agglomerating to larger objects (e.g., White, 2013; Marov, 2018; Johansen et al., 2015; and references therein). The first condensates from the solar nebula are metals, oxides and silicates organized in so-called Amoeboid Olivine Aggregates (AOA) as well as Ca-Al-rich inclusions (CAI) (e.g., Krot et al., 2004; White, 2013; Scott and Krot,

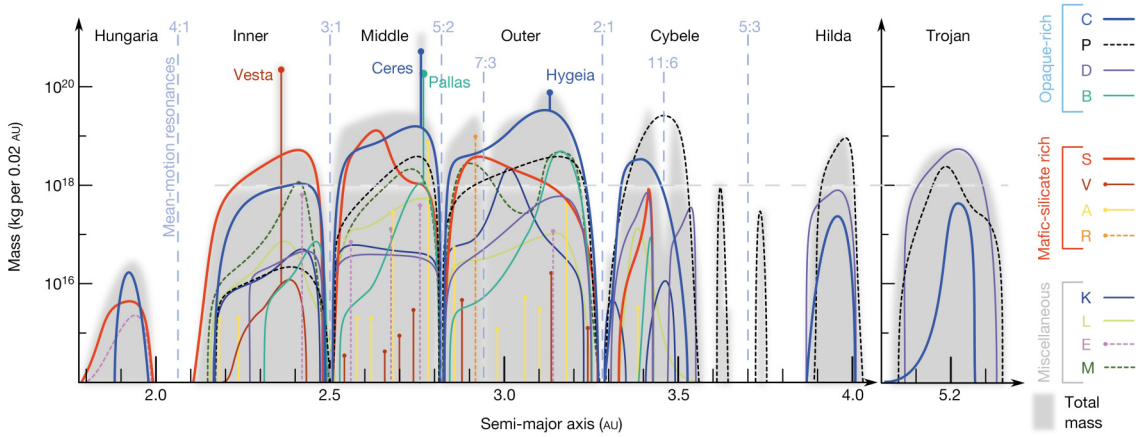


Figure 1.1: The asteroid belt seen by semi major axis vs. mass (taken from DeMeo and Carry (2014))

2014; and references therein) which are still existent in the most primitive carbonaceous chondrites. New findings are challenging the current understanding of agglomeration of the earliest condensates and present hypotheses in which large planetesimals can form very rapidly within just a few Ma after CAI formation (e.g., Johansen et al., 2015 and references therein). Due to the presence of several short-lived radionuclides, most importantly $^{26}$Al, these objects were able to melt and differentiate rapidly, forming a core and other planetary layers like mantles and crusts (e.g., Davis and McKeegan, 2014 and references therein).

Vesta, the second largest object of the asteroid belt, is thought to represent one such remaining planetesimal from these earliest times. It is now believed that gravitational interactions with Jupiter and Saturn prevented this object (and others in the belt) from forming a planet (e.g., Kirkwood, 1867 as well as Morbidelli et al., 2007; Morbidelli et al., 2010; Walsh et al., 2012; Morbidelli et al., 2015; and references therein describing the so-called *Nice Model* & *The Grand Tack Model*). After formation and placement in the asteroid belt, the main processes Vesta experienced are collisions, impact cratering and mass wasting (e.g., Jaumann et al., 2012; Bottke et al., 2015; O'Brien et al., 2014; Krohn et al., 2014b; Otto et al., 2013). Luckily, the (partly massive) collisions that Vesta experienced throughout its history (see section 1.3 and 3.1) were not strong enough to disrupt the object, leaving humankind the opportunity to study it.

## 1.3 Vesta before Dawn

Vesta was initially discovered by Wilhelm Olbers on March 29$^{\text{th}}$, 1807, while specifically searching the sky for asteroids (Olbers et al., 1894). It was the fourth object in the main belt to be discovered after (1) Ceres, (2) Pallas and (3) Juno. Its official name contains the number '4' (4 Vesta) as is common for naming asteroids yet I will omit this number throughout this document. As seen in Figure 1.1, Vesta resides in the inner asteroid belt between the 4:1 and 3:1 resonance gaps of Jupiter ("*Kirkwood gaps*", Kirkwood, 1867). Main-belt asteroids are furthermore divided into families with similar orbital inclinations and eccentricities (e.g., Hirayama, 1922; Brouwer, 1951; Nesvorný et al., 2015) as well as into groups of similar surface mineralogy characterized by visible and infrared reflectance spectra (e.g., Gaffey and McCord, 1978; DeMeo et al., 2015; Masiero et al., 2015). Vesta belongs to the *Vesta family* which resides from ~2.26 to ~2.47 AU with proper eccentricity and sine of inclination values ranging from ~0.08 to ~0.12 and ~0.10 to ~0.14 (~5.6-7.1° orbital inclination), respectively (Burbine et al., 2001). Vesta furthermore belongs to the *V-type* asteroids which are characterized by distinct pyroxene-dominated reflectance spectra (e.g., McCord et al., 1970; Gaffey and McCord, 1978; Masiero et al., 2015). McCord et al. (1970) were the first to make the connection to the HED meteorites due to their similar reflectance spectra (Figure 1.2). The HEDs are a suite of achondritic meteorites called howardites, eucrites and diogenites and will be

addressed in detail in section 3.2.

The *Vestoids* are asteroids that are believed to directly originate from Vesta due to their Vesta-like reflectance spectrum (e.g., Binzel and Xu, 1993; Burbine et al., 2001). Vesta is, with its approximate diameter of 500 km (e.g., Thomas et al., 1997), by far the largest object (being the only object >50 km) among all asteroids that exhibit this distinct pyroxene spectrum (Burbine et al., 2001); therefore it is believed that a massive collision generated these asteroid chunks. This was proved to be well possible when Thomas et al. (1997) discovered a possible impact structure near the south pole with Hubble Space Telescope (HST) data, which was confirmed by the Dawn mission's observations and is now called the Rheasilvia Basin (Jaumann et al., 2012).

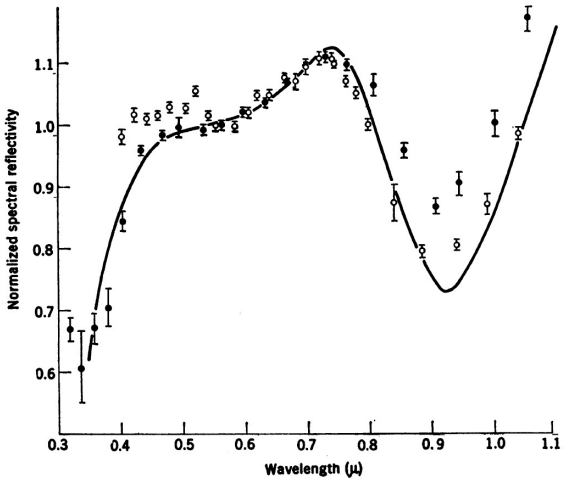


Figure 1.2: Wavelength vs. normalized spectral reflectivity of Vesta (circles with error bars) and Nuevo Laredo (eucrite) (solid line) taken from McCord et al. (1970) showing the distinct first pyroxene absorption band which centers around 0.9 µm.

Binzel et al. (1997) furthermore observed a hemispherical dichotomy of Vesta, with one hemisphere showing basaltic, eucrite-like characteristics as well as lower relative albedo and the other one showing more plutonic, possibly olivine-bearing and diogenitic characteristics as well as higher relative albedo. NASA's Dawn mission proved that these observations were mostly accurate, which will be shown in section 3.1.

## 1.4 The Dawn Mission - Objectives and Operations

The Dawn mission, which was operating in orbit of Vesta and Ceres from 2011 to 2018, was part of the NASA discovery program and started its journey from Earth in 2007 (Russell et al., 2007). The mission aimed at targeting the two largest objects in the main belt: Vesta and Ceres. Prior to the Dawn mission, these two objects were already known to be likely of different origin due to Earth-based (e.g., McCord et al., 1970; Cochran et al., 2004, Morrison, 1976; Lebofsky, 1978) and HST (e.g., Parker et al., 2002; Zellner et al., 1997; Thomas et al., 1997; Binzel et al., 1997) observations revealing some of their spectral, morphological and physical characteristics and thus, implications on their composition and density. Vesta and Ceres represent two contrasting remnants of the early solar system as Vesta is thought to have differentiated early while Ceres likely formed later, without forming an iron core and still bearing water/ice (e.g., Russell et al., 2004). Both bodies have remained intact since their formation, recording processes and events since the time of accretion and planet formation. The main goals of the Dawn mission were to characterize these largest objects mineralogically, geologically, geophysically and chemically as well as elucidate processes and events that have taken place in the 'early hours' of our solar system as well as afterwards (e.g., Russell et al., 2004). Dawn also intended to better understand the differences and their origin of the rocky inner planetary bodies and the outer ice-rich bodies.

The three different science orbits of Dawn at Vesta are displayed in Fig. 1.3. In this work I use data derived from the high altitude and low altitude mapping orbits (HAMO and LAMO,

respectively). The payload comprised four instruments: 1) The Gamma Ray and Neutron Detector (*GRaND*, Prettyman et al., 2011), 2) the Framing Camera (*FC*, Sierks et al., 2011), 3) the Visible and InfraRed Spectrometer (*VIR*, De Sanctis et al., 2011) and 4) Gravity Science (radio tracking) (Konopliv et al., 2011). The spacecraft used an Ion Propulsion system (IPS) fueled by xenon as well as a hydrazine-based reaction control system (RCS). It also required additional operating power which was generated by two large solar arrays (Rayman et al., 2006).

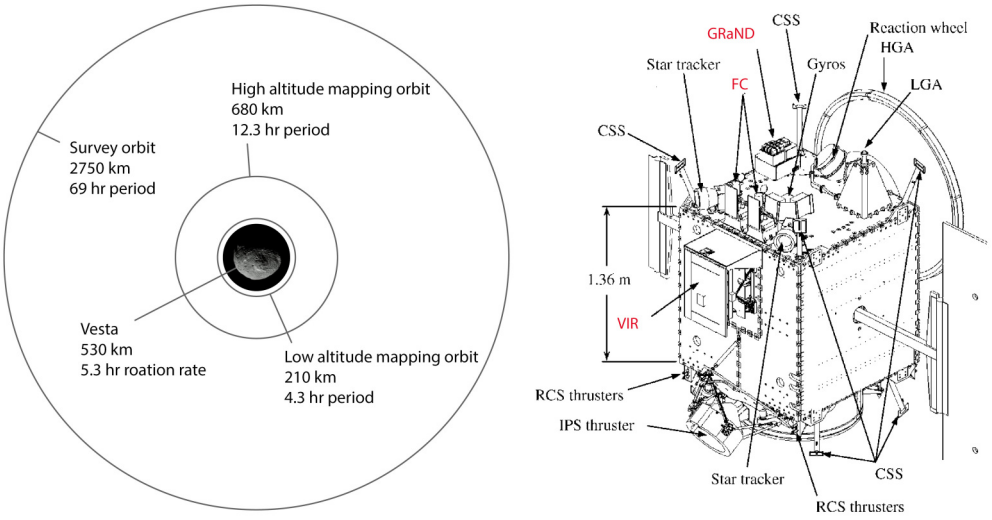


Figure 1.3: Left: The different science orbits of Dawn at Vesta, modified after Rayman and Mase (2014), Right: The Dawn spacecraft with highlighted main science instruments (red) (CSS – Coarse Sun Sensors, HGA – High Gain Antenna, LGA – Low Gain Antenna, RCS – Reaction Control System), taken from (Rayman et al., 2006).

Dawn was originally planned to complete its primary mission in June 2016 yet was extended due to availability of hydrazine until October 2018. The spacecraft went into an elliptical orbit around Ceres to receive higher resolution images and data of, among others, the highly interesting crater Occator and its central salt-rich surface deposits called *faculae* which were likely formed by cryovolcanic activity (e.g., Raymond et al., 2018; Quick et al., 2019; Ruesch et al., 2019; Scully et al., 2019).

# 2 Data and Methods

## 2.1 The Dawn Framing Camera

### 2.1.1 General

This study's main observations are derived from data collected by NASA's Dawn Framing Camera (FC). The FC is the German contribution to the Dawn mission and was built by a collaboration of the Max-Planck-Institute for Solar System Research, the Institute of Planetary Research at the German Aerospace Center and the Institute of Computer and Network Engineering at the University of Braunschweig. Sierks et al. (2011) give a comprehensive description of the FC.

The FC has one panchromatic clear filter and seven band-pass filters in the visible (VIS) and near infrared (NIR) (~0.43-0.97 µm, Sierks et al., 2011). The filters of the FC focus on this wavelength region as Vesta's surface mineralogy is dominated by pyroxenes, showing a distinct iron absorption at ~0.9 µm (McCord et al., 1970). The filters are installed within a filter-wheel which rotates above the CCD (Fig. 2.1). Thus, images acquired through different filters cannot be taken at the same time and have to undergo a correction process in order to combine them. The minimum time delay between two images of different filters is approximately seven seconds (Sierks et al., 2011). The responsivity functions of each filter are given in Figure 2.2.

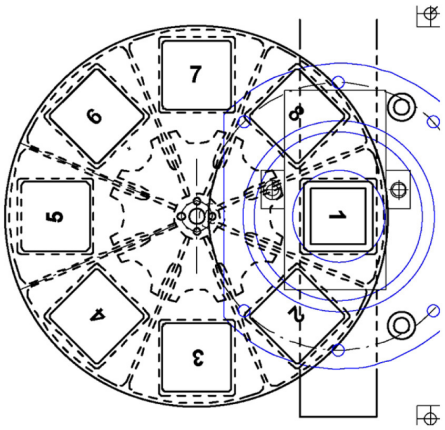


Figure 2.1: Filter-wheel geometry as seen from the CCD, taken from Sierks et al. (2011).

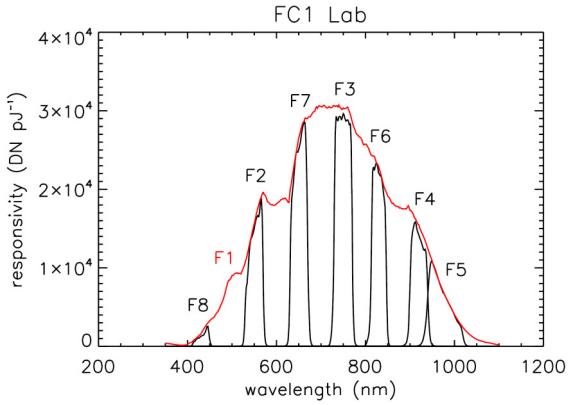


Figure 2.2: Responsivity of the eight FC filters, taken from Sierks et al. (2011).

All maps shown here (also the VIR data) are based on the Claudia coordinate system (Russell et al., 2012; Supplementary Text) and presented in equidistant projection orientated with north toward the top. The FC mosaics are calibrated and photometrically corrected to I/F at $i$ = 30°, $e$ = 0°, and $p$ = 30° (incidence, emission and phase angle, respectively), using the Akimov function as described in Schröder et al. (2013, 2014). Schröder et al. (2013) used standard stars, star fields and other solar system objects on Dawn's way to Vesta for point source calibration. The filter-specific flat field and stray light correction by Schröder et al. (2014) is used to create radiometrically accurate and near-seamless mosaics of the Vestan surface and is accurate to a few percent. I will use the term 'reflectance' for the photometrically corrected I/F throughout this work. Clear filter images for geomorphological observations are depicted at LAMO resolution (Low Altitude Mapping Orbit up to 16 m/px, Roatsch et al., 2013), while the shown RGB composite depicting multispectral information were produced with HAMO resolution (High Altitude Mapping Orbit ~60 m/px, Roatsch et al., 2012), which is the highest resolution with complete filter coverage.

FC data is also the basis of the Digital Terrain Model (DTM) by Preusker et al. (2014, 2016). This DTM was modified for this work by including LAMO images and implementing a triaxial ellipsoid (286 x 279 x 223 [km]) in order to reach the most realistic approximation to the actual geophysical altitudes and their relations in the Marcia area. With a lateral resolution of ~70 m/px

and a vertical accuracy of ~6 m, the DTM helps to examine the topographic context of the PIDs. No vertical exaggeration was applied. I note at this point that this DTM was built for the Marcia area only and values differ from the global DTM shown in Figure 3.1, left.

Geological analysis on the basis of FC data in this work is undertaken through visual mapping and identification of (potential) PIDs, the extent of the Marcia ejecta blanket and by using topographic profiles in order to reveal possible underlying structures as well as to derive impact deposit thickness and extent. Additionally, the distances from the Marcia rim to external PIDs were measured. These analysis were executed in the software ArcGIS.

### 2.1.2 Useful Framing Camera Ratios for Vesta and the Pitted Impact Deposits

In the past, studies using Dawn FC data commonly employed the Clementine-type RGB composite to show spectral variation on the Vestan surface. This RGB composite was introduced by Pieters et al. (1994) for the lunar data set obtained during the Clementine mission. The Clementine-type RGB composite include the following ratios for the respective channels: R=750/415 [nm], G=750/950 [nm], B=415/750 [nm], and were used for Vesta in e.g. Reddy et al. (2012b), Denevi et al. (2012), Le Corre et al. (2013) and Williams et al. (2014a). This composite can give valuable information about the surface composition and/or degree of space weathering (especially on the Moon). The red and blue band ratio in the Clementine-type RGB composite is sensitive to soil maturity (spectral 'reddening' positively correlates with maturity) as well as composition (Pieters et al., 1994), whereas the green band is sensitive to strength and character of the common mafic absorption near 1 µm which is caused by the presence of iron.

In this work, I use another RGB composite to illustrate compositional and/or physical differences. It is tightly connected to my observations of the PIDs and Vesta in general. As low-Ca orthopyroxenes predominate the Vestan spectra, pyroxene absorption band positions of the Vestan surface vary between ~920 and 935 nm (Ammannito et al., 2013a; De Sanctis et al., 2013), mostly depending on their Fe/Mg contents. Diogenites generally have pyroxene absorption band positions at shorter wavelengths than eucrites due to higher Mg contents of their orthopyroxenes (see Fig. 2.5 left panel and e.g., Gaffey, 1976; Mittlefehldt, 2015). Therefore, their spectra exhibit higher 965/917 [nm] values than eucrites, while howardites are in between. I therefore use the 965/917 [nm] ratio for the red channel as it is the most significant parameter in order to distinguish between the main Vestan rock types diogenites and eucrites, which was previously described in Le Corre et al. (2011), Reddy et al. (2012b) and Thangjam et al. (2013).

The reflectance of HEDs and Vestan spectra is generally at its highest around 750 nm, before it drops due to the absorption of electromagnetic energy by the iron-bearing pyroxene (see Fig. 2.5, left panel). As pyroxene absorption band positions on Vesta are closest to the 917 nm filter of the FC, the ratio 750/917 [nm] is best suited to characterize the material's pyroxene absorption strength. The PIDs differ from their immediate surrounding in their reflectance at 750 nm and especially the pyroxene absorption band strength. Consequently, I chose the green and blue band of the new RGB composite accordingly (750 nm and 750/917 [nm], respectively). The global RGB composite is shown in Figure 2.4 in section 2.3.

In summary, greenish and cyan colors in the presented RGB composite denote higher reflectance and pyroxene absorption band strength. I emphasize that all images of this RGB composite use the same stretch while the standard deviation stretch type with n=1.3 showed the best results with respect to the perception of the viewer. I also note that artefacts occur in the HAMO RGB composite as a result of the mosaicking process (along single image boundaries) and due to missing or incomplete data, e.g. in shadowed areas.

## 2.2 The Dawn VIR Spectrometer

The VIR experiment is the Italian contribution to the Dawn mission and was built by the Instituto Nationale di Astrofisica (INAF) and SELEX Galileo. It is a hyperspectral mapping spectrometer that covers wavelength ranges from the UV (ultraviolett) at 0.25 µm to the IR (infrared) at 5 µm. The instrument is composed of two channels (VIS and IR) with >400 bands, one covering the range from the UV to 1.05 µm and the other one from 1.0 to 5.0 µm. Obviously, it has a much higher spectral resolution than the FC and a wider wavelength range. Therefore, it can identify minerals and molecules that are outside the range of FC filters and that have more subtle spectral features. Yet the spatial resolution is relatively low with respect to the FC. The maximum resolution of images used here is around 165 m/px.

I use VIR data in this work to investigate whether the effect seen in FC data also applies to VIR data and the second pyroxene absorption band around 2 µm. Here, the recently recalibrated VIR data was used with a method established by Rousseau et al. (2019). This data was photometrically corrected at DLR based on photometric properties reported in Li et al. (2013). VIR data used in this work were analyzed and further processed by using the software ENVI and IDL (Version 5.6 and 8.8, respectively).

The recent recalibration of VIR data was firstly done for Ceres VIS data (Rousseau et al., 2019) but was applied to Vesta data as well (e.g., Rousseau et al., 2020a), with a special treatment of VIS data due to temperature effects affecting the CCD. Raponi et al. (2021) introduced new IR data for Ceres applying the procedure presented in Rousseau et al. (2020b). Vesta IR data was recalibrated according to these presented methods. The recalibration includes the usage of a multiplicative correction factor for every single VIR spectrum which was derived by generating a ratio between a smoothed ground-based spectrum and an averaged VIR-IR spectrum after artifact correction. Artifact correction is presented in Carrozzo et al. (2016)) and comprise the 'odd-even band effect' where spectra show a saw-tooth pattern associated with even or odd band number, 'spectral spikes' which are random anomalies caused by random events on detector pixels (e.g., cosmic rays) and 'vertical stripes' in images caused by different relative responses of the sample detectors. Moreover, the non-homogeneous instrumental response of the detector can furthermore cause artifacts at a smaller spectral scale (Carrozzo et al., 2016).

Figure 2.3 shows a reflectance spectrum of Vesta, obtained by VIR during the approach phase of Dawn. Both VIS and IR channels were combined in this Figure, which is taken from De Sanctis et al. (2012a).

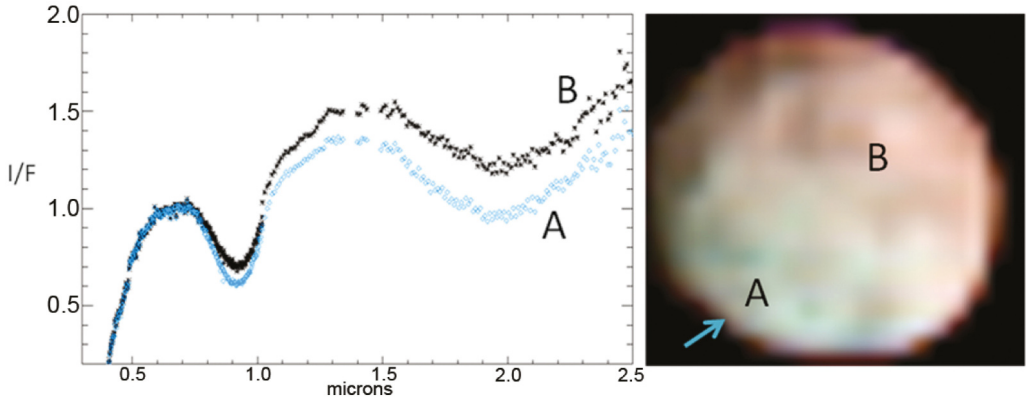


Figure 2.3: Left: Spectra (normalized at 0.7 µm) of regions A and B indicated in the VIR image. Right: VIR color composite (red = 0.92 µm, green = 0.62 µm, blue = 0.44 µm). Spatial resolution is approximately 25 km. Arrow indicates the south pole. This caption is taken from De Sanctis et al. (2012a). It is now known that the depicted region A corresponds to the more diogenitic southern hemisphere and B to the more eucritic northern hemisphere.

The used VIR cubes were recalibrated at INAF and have slightly offset Latitude and Longitude values than the DLR FC LAMO mosaic (section 4.9). The difference is due to varying spice kernels

that were updated at a later stage of the Dawn mission but not implemented in the older FC mosaics. Therefore, I manually georeferenced the VIR images in order to show them with spatial context over FC LAMO mosaics. Small Lat/Lon offsets are therefore likely.

## 2.3 A Global Overview

Here I present four global Vesta maps relevant to this work. A) of Figure 2.4 is the clear filter LAMO global mosaic displaying the identified PIDs in pink (exaggerated for global-scale identification). I personally doubt that there is an identifiable PID within Numisia (A4 in Figure 2.4) yet it was reported in Denevi et al. (2012) as a possible occurrence so it is included here as well. Licinia (A1) is the only occurrence within surface material dominated by diogenitic characteristics. Diogenitic characteristics appear in B) as light purple colors. B) shows the RGB composite described in section 2.1.2. C) displays a global DTM with 40% transparency over A). Last but not least, D) shows the 2.8 µm absorption band depth derived by Combe et al. (2015a). They calculated the absorption band depth by subtracting the reflectance at the band center from the continuum applied on the shoulders of the absorption.

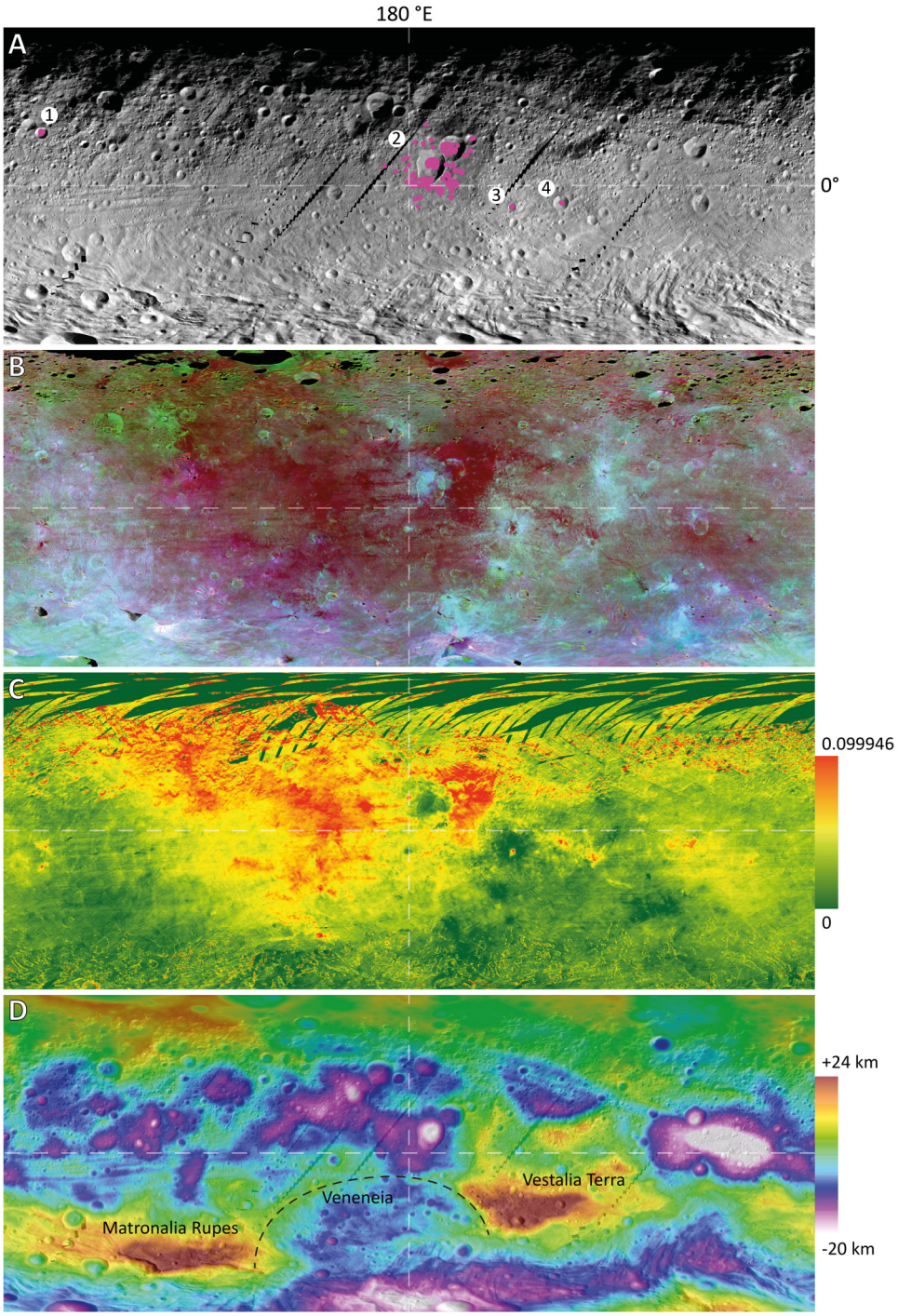


Figure 2.4: Global mosaics in equidistant projection. Due to scarce availability of space, I only display relevant data from 70° S to 70° N. A: Clear filter mosaic in LAMO resolution with all mapped PID occurrences (pink, 1 - Licinia, 2 - Marcia area, 3 - Cornelia, 4 - Numisia.) B: RGB composite presented in section 2.1.2 in HAMO resolution (R= 965/917 [nm], G=750 nm and B=750/917 [nm]). C: Band depth distribution of the 2.8 µm absorption, generated by Combe et al. (2015a). D: DTM with highlighted important features: The two highest elevations Vestalia Terra and Matronalia Rupes and some of the basin rim of Veneneia.

## 2.4 Spectral Data of Meteorites

In this work I use HED as well as carbonaceous chondrite and olivine spectral data for comparative observations. These data were obtained from the RELAB database at the Brown University, which is publicly available under: http://www.planetary.brown.edu/relabdocs/relab_disclaimer.htm.

Additional meteorite data were also provided by Edward Cloutis from the University of Winnipeg. In order to compare the meteorite spectra with Framing Camera data, the meteorite spectra were resampled to fit the format of the responsivity functions of the respective filter (Sierks et al., 2011). The resampling of the RELAB meteorite spectra occurred as follows:

$$R_{mfc}(\lambda) = \frac{\int R_m r_i(\lambda) d\lambda}{\int r_i(\lambda) d\lambda} \quad (1)$$

where $R_{mfc}$ is the reflectance value of the resampled meteorite spectrum for the respective filter, $R_m$ is the original reflectance of the meteorite spectrum obtained in the laboratory, $r_i$ is the responsivity function for each filter and $\lambda$ is the respective FC filter wavelength.

In total, data from 239 RELAB spectra are used in this study, with 142 being from HED meteorites and 82, 33 and 27 spectra from eucrites, diogenites and howardites, respectively. Many meteorites were measured multiple times, e.g. because different grain sizes were measured or powders vs. slabs. I incorporate everything in order to display the greatest possible diversity. In total, the following quantities of actual meteorites were measured: 44 eucrites, 16 howardites and 14 diogenites. I did not consider any pairing of meteorites, as it is mostly irrelevant for this work. Yet I acknowledge that it might further decrease the number of actually measured meteorites.

Other spectra used here include the mineral olivine (19 spectra) as well as carbonaceous chondrites (69 spectra from 44 individual carbonaceous chondrites). As mentioned in section 3.2, CM2 clasts predominate HEDs as the main carbonaceous chondrite clasts. Therefore, I mainly use spectra derived from CM-type chondrites, which are distinguished in Figure 2.5. I also include spectral data of impact melts (9 spectra) originating from howardites, eucrites, ordinary chondrites and an unclassified object. Spectra IDs and corresponding meteorite names are given in the supplementary material (Table S1, 11).

Figure 2.5 displays the resampled meteorite data for the two most significant parameters (750/917 [nm] vs. 965/917 [nm], right panel) to distinguish different lithologies on Vesta (i.e., howardites, eucrites, diogenites and olivine-rich regions as well as areas contaminated by 'dark material'). These ratios are especially sensitive to the pyroxene absorption band position and the band strength, which are the main FC-covered spectral variations observed on Vesta (Fig. 2.5 and e.g., Le Corre et al., 2011; Reddy et al., 2012b; Thangjam et al., 2013). The left panel of Figure 2.5 illustrates four representative spectra of a diogenite (red), eucrite (yellow), olivine (green) and carbonaceous chondrite (dark blue) and the relevant filter positions (grey dashes). This Figure best illustrates the differences of eucrites and diogenites in terms of pyroxene band position and its effect on the ratio 965/917 [nm] as previously described. In section 4.7, the right panel of Figure 2.5 will serve for comparisons with Vestan FC data, which are extracted for different locations from global HAMO mosaics. As there is no uncertainty available for the RELAB measurements, I do not apply any error bars to the data points and as the data are displayed as ratios, possible systematic uncertainties regarding the measurements or the responsivity functions are cancelled out. The instrument error of the RELAB spectrometer is given as 0.25% which is smaller than the data points' symbols in Figure 2.5. All meteorite spectra were processed by using the software IDL.

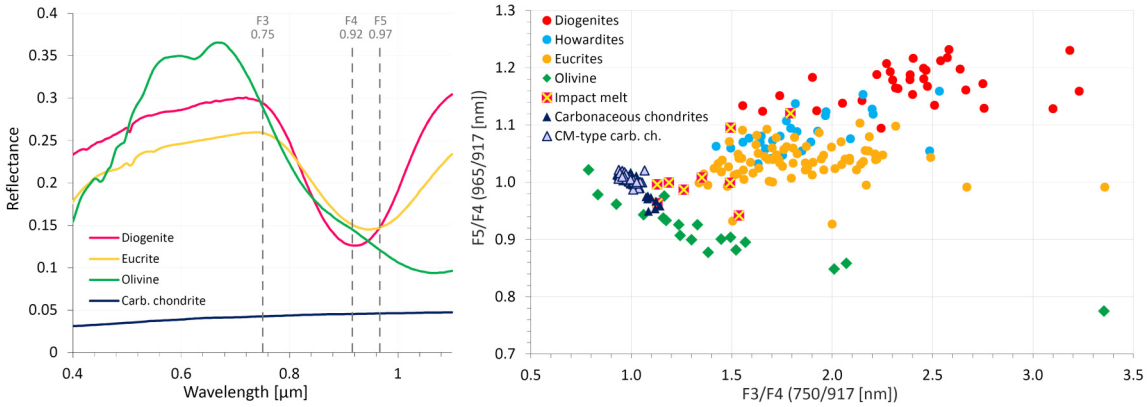


Figure 2.5: Left panel: Wavelengths vs. Reflectance of four different rock types. Dashed vertical lines indicate filter positions of the FC filters used in this study. Diogenite = Ellemeet (ID bkr1mp113), eucrite = ALHA81011 (ID bkr1mp122), olivine from Chassigny (ID bkr1dd001) and Carbonaceous chondrite = Mighei (ID bkr1ma062). Right panel: 750/917 [nm] vs. 965/917 [nm] for resampled RELAB meteorite and olivine data.

## 2.5 The Planetary Spectroscopy Laboratory

### 2.5.1 Facility and Experimental Design

The pitted impact deposits are characterized by higher reflectance as well as pyroxene band strength and form as a result of an impact. In this work I therefore conduct heating experiments and related measurements in order to understand why they display these spectral characteristics. These experiments and reflectance measurements were undertaken in the Planetary Spectroscopy Laboratory (PSL) which is located at the Institute of Planetary Research at DLR in Berlin, Germany.

The facility includes three Bruker Vertex 80V Fourier Transform InfraRed (FT-IR) spectrometers that can obtain bidirectional spectra from the near UV (0.2 µm) to the far IR (up to 200 µm) (Maturilli et al., 2019). The employment of an interferometer enables FT-IR spectrometers to measure multiple frequencies simultaneously and very rapidly (e.g., King et al., 2004). An interferogram is generated by using a beamsplitter to split the EM source beam into two beams which are then reflected by two mirrors. One mirror is located at a fixed position and one is moving in order to create phase differences of the light waves. These two beams are then recombined again by the beamsplitter and sent to the sample and subsequently to the detector, creating an interferogram in which each data point contains information about one of the desired frequencies. The interferometer (electrical detector signal vs. phase difference) is then converted to a spectrum (here, wavelength vs. reflectance) by a Fourier Transform (e.g., King et al., 2004).

The PSL facility also contains an 'emissivity chamber' connected to one of the spectrometers in which the emissivity of samples can be measured in near-vacuum while heating them by means of an induction plate. I use this chamber for the heating experiments presented here. Vacuum reached for the presented heating experiments is around 0.1 mbar. The facility also includes sample preparation possibilities as well as further analysis to characterize samples like XRD (X-ray diffraction) and microscopes. A more detailed overview of the facility is given in Maturilli and Helbert (2016) and Maturilli et al. (2019, 2017) and Helbert and Maturilli (2008).

Every run of a heating experiment includes the following working procedure: **1)** prepare sample and store in dry cabinet for 60 min, **2)** seal (to minimize air affecting sample) and cool down to approximately -80°C, **3)** transport to chamber, adjust temperature sensor, apply vacuum, **4)** once vacuum is established, start heating via induction (starting current at about 2.0 A, except for low-temperature experiments), **5)** once temperature was applied for the desired amount of time, let cool down in vacuum, **6)** extract sample and leave in dry cabinet until reflectance measurement. The heating procedure occurred at rates ranging from 3 °C/min (for low temperatures) to about 12 °C/min (for higher temperatures).

All samples were measured at an incidence angle of 30° and emission angle at 0° (phase angle = 30°) by means of a biconical Bruker A513 accessory. These are the same angles used to calibrate Framing Camera data. Thus, the resulting reflectance spectra will represent the most realistic comparison. All samples were measured at a spectral resolution of 4 $cm^{-1}$ by 200 scans, yielding a high signal-to-noise ratio. The aperture for all measurements was 2 mm. I acquired every measurement twice or more times while turning the sample for approximately 30°-120° in order to account for natural material differences. These differences were mostly very small with standard deviations of <0.003 for 70% of all samples, <0.005 for 90% of samples and <0.009 for 100% of the samples for the resampled value at 750 nm (which ranges from ~0.03-0.4). These multiple spectra were averaged to one representative spectra of the respective sample.

As the analyses presented in this work focus on the first pyroxene absorption band at 0.9 µm, a VIS detector (Si-Diode) with a range from 0.4 to 1.1 µm was used. All measurements in this wavelength range were obtained using a tungsten lamp as light source and a $CaF_2$ beam splitter. For these measurements, a white Spectralon® standard was taken as reference. For a few samples, NIR spectra were acquired (1.0 - 16 µm) in order to characterize the second pyroxene absorption band around 2 µm. These measurements were obtained using a Globar lamp as light source, a KBr beam splitter, a MCT detector (MCT = Mercury Cadmium Telluride) and an Infragold® standard as reference.

For most of the samples, it was not possible to measure the reflectance spectrum in vacuum as

the samples contain phyllosilicates which are presumably responsible for 'degassing events' while measuring. Phyllosilicates contain water in their mineral structure and are prone to lose their volatiles when exposed to such a sudden vacuum. This resulted in the spread of the sample within the measurement chamber, partly clouding the mirrors. This in turn resulted in incorrect spectra which is why I chose to acquire the spectra at ambient pressure as air does not influence the pyroxene absorptions I am analyzing.

Throughout the experimental work, the setup of experiments slightly changed. I started conducting experiments in large sample containers with several grams of material. Those sample containers were too large to directly measure the spectra and thus, the sample had to be transported to a smaller sample container. The original surface therefore became destroyed. At a later stage, I used meteorite analogs and due to the scarcity of the material I used smaller sample containers that directly can be transferred to the reflectance measurement unit. In this way, the original surface after heating remained intact. I later discovered that the surface of the heated samples show different spectral characteristics than the interior particles, which will be discussed in detail later on. In conclusion, I first present results from mere temperature increase with respect to an unheated sample and later continue with results showing spectra of the sample surface and interior. This is one of the most important aspects of this work which is why I emphasize this already at this point.

Considerations towards the spectral characteristics of the pitted impact deposits include temperature exposure in general as well as temperature exposure to different durations to see whether the exposure duration could be relevant. I also consider effects of grain size, dark material abundance and compositional variations. Spectra are processed with the software IDL, an example code is given in the Appendix (12.1). A laser spike produced by the spectrometer for internal calibration was removed and the spectra were corrected with a factor of 0.98 for the VIS and NIR measurements and 0.8 for longer wavelength NIR measurements as required by the standard references.

I will both show whole reflectance spectra of the samples and resampled values for spectral parameters like the reflectance at 750 nm, band strength (750/917 [nm]), band position (965/917 [nm]) and the visible spectral slope (750/430 [nm]). The resampled values match the data processing of Dawn FC data in order to better compare the results with the PIDs on Vesta. For the NIR measurements, the reflectance at 1.44602 are displayed (which is closest to the selected band from the VIR instrument) as well as the values of the according band strength ratio 1.44602/1.90992 [µm]. Ratios are often used as systematic errors or effects of illumination conditions and topography are cancelled out. Band strengths would generally better be comparable when the continuum of the spectra would be removed. A continuum is generally a tangent line that represents the overall slope of the spectra but is often used to compare absorption bands. When comparing absorption bands, this tangent is applied to the two shoulders of the respective absorption band. However, as the second shoulder of the first pyroxene band (around 1.4 µm) is not observed by Dawn FC or the detector used in the data acquisition of the experimental data presented here, I cannot show it here. Likewise, I will refrain from applying a continuum removal to the VIR data shown in section 4.9. Due to the artificial water absorption band in laboratory acquired NIR data, it is furthermore not reasonable to apply a continuum removal to this data.

### 2.5.2 Analog Materials

Analog materials for the presented experiments were designed to resemble the Vestan surface regolith considering findings presented by Reddy et al. (2012a) and Michalik et al. (2021) (which is presented in this work). Therefore, the samples used here comprise an 'endogenic', pyroxene-rich portion and an 'exogenic', dark, CC-like portion. Both terrestrial and meteorite materials were used to prepare different analogs.

The terrestrial analogs comprise a *Phobos Simulant* as the exogenic, 'dark' component which was developed as a carbonaceous chondrite (CC) analog for the MMX (Martian Moons eXploration) mission led by JAXA (Japan Aerospace Exploration Agency, Miyamoto et al., 2018; Miyamoto et al., 2021). This CC analog was assembled based on Tagish Lake, a C2 ungrouped carbonaceous chondrite, and is officially called UTPS-TB (University of Tokyo Phobos Simulant Tagish Lake-based (Miyamoto et al., 2018; Miyamoto et al., 2021). It contains 60.5 wt% of phyllosilicate, 10.3

wt% of carbonate, 9.2 wt% of sulfide, 7.7 wt% of magnetite, 7.3% of olivine, and roughly 5 wt% of carbon (including polymer organic materials) (Miyamoto et al., 2021, in press). I used two different 'endogenic' analogs, one of which is, highly simplified, solely hypersthene (Ca-poor pyroxene like the pyroxene in HEDs/on Vesta, see section 3.2 and 2.1.2). Moreover, hypersthene was readily available in the quantities needed. The second analog is a more complex eucritic analog comprising pigeonite (55 wt%) (pyroxene commonly found in eucrites, Mittlefehldt, 2015) combined with anorthite and labradorite (43 wt%) (both are members of the plagioclase series) as main constituents and a minor amount of ilmenite (2 wt%).

Additionally, small amounts of meteorite samples were used in this work. These include the CM2 meteorite Murchison and several HEDs (NWA5230, NWA5749, NWA3359 and JaH626) which were provided by Dr. A. Morlok and Prof. Dr. H. Hiesinger from the University of Münster. The prefixes NWA and JaH denote the location they were found, here: North West Africa and Jiddat al Harasis, respectively. Meteorites are normally written with a space between this prefix and the number, yet I omit the space for reasons of simplicity in this work. In the following, I summarize characteristics of these meteorites, mainly taken from the Meteoritical Bulletins #48, #90, #96, #100 and #102, Ruesch et al. (2015), Bland et al. (2004) and Fendrich and Ebel (2021).

JaH626 is a shocked eucrite comprising impact melt and polymict clasts of basaltic and cumulate eucrites. It contains pyroxene with augite exsolution lamellae and partly fine-grained recrystallization textures. Plagioclase partly occurs as fine anisotropic blades as a result from shock and quenching from melt. NWA3359 is a polymict recrystallized eucrite showing clasts of basaltic eucrites and impact melt within a fine-grained clastic matrix. Diogenite fragments occur. NWA5230 is a heavily-shocked polymict eucrite comprising basalt clasts and brecciated diogenite clasts within a fine-grained matrix. Impact melt clasts and droplets occur and plagioclase was transformed to maskelynite due to shock. Pyroxene grains show augite exsolution lamellae. NWA5748 is a howardite and contains eucrite and diogenite clasts and mineral fragments within a fine-grained matrix. Impact melt clasts and glassy spherules occur. Murchison is a CM2 carbonaceous chondrite consisting of 72% matrix and 28% inclusions. Total mineral composition is as follows: cronstedtite/tochilinite (matrix, 58.5%), serpentine (22.8%), olivine (11.6%), pyrrhotite (2.9%), enstatite (2.2%), calcite (1.1%), pentlandite (0.5%) and magnetite (0.4%). Chondrules are rare.

Due to the considerations about the abundance of CM2 material in the Vestan regolith presented in Reddy et al. (2012a) and Michalik et al. (2021), I choose the exogenic, dark component of the analogs to constitute 15 wt% for most of the (heated) samples. Yet for selective samples this value can range from 1 to 30 wt%. Table 2.1 summarizes the analogs presented in this work.

The Phobos Simulant was used with grain sizes from <25 to 63 µm to account for the widely small grain sizes of CM2 chondrites, whereas the Murchsison sample also contains small amounts of larger grain sizes up to 250 µm in order to have a wider range of possible grain size distributions.

All HEDs and HED analogs contain various grain sizes from <25-500 µm, which are described in the following. For Hypersthene: 40 wt% of 25-63 µm, 25 wt% of 63-125 µm, 15 wt% of 125-250 µm and 5 wt% of 250-500 µm. The Eucrite Analog is a more complex analog comprising pigeonite (55 wt%) as HED pyroxene analog, labradorite/anorthite (43 wt%) as HED plagioclase analog as well as small amounts of ilmenite (2 wt%), which is a minor constituents as described for example in Mittlefehldt (2015) and references therein.

The HED samples from the University of Münster have different defined grain size fractions. They were mixed with the following average proportions: 31.5 wt% of <45 µm, 36.5 wt% of 45-90 µm, 21.0 wt% of 90-250 µm and 11.0 wt% of 250-500 µm.

Table 2.1: Overview of sample mixtures.

| Sample name | HED/HED analog | wt% | Murchison/CC analog | wt% |
|---|---|---|---|---|
| Hypersthene | Hypersthene | 100 | - | 0 |
| Phobos Simulant | - | 0 | Phobos Simulant | 100 |
| Murchison | - | 0 | Murchison | 100 |
| NWA5748M | NWA5748 | 80 | Murchison | 20 |
| NWA5748 | NWA5748 | 100 | - | 0 |
| NWA5230M | NWA5230 | 85 | Murchison | 15 |
| JaH626M | JAH626 | 85 | Murchison | 15 |
| NWA3359 | NWA3359 | 100 | - | 0 |
| H98P02 | Hypersthene | 98 | Phobos Simulant | 2 |
| H95P05 | Hypersthene | 95 | Phobos Simulant | 5 |
| H92P08 | Hypersthene | 92 | Phobos Simulant | 8 |
| H90P10 | Hypersthene | 90 | Phobos Simulant | 10 |
| H80P20 | Hypersthene | 80 | Phobos Simulant | 20 |
| H70P30 | Hypersthene | 70 | Phobos Simulant | 30 |
| EA90P10 | Eucrite Analog | 90 | Phobos Simulant | 10 |
| HypMoCa | Hypersthene | 71 | Montmorillonite and carbon black | 29 |
| HypMur | Hypersthene | 99 | Murchison | 1 |

### 2.5.3 Experiment Description

In the following, I describe the different intents of the selected experiments undertaken and presented in this work.

A) Grain size segregation might occur during degassing events. In order to investigate this possibility as the cause for the spectral distinctness of the PIDs, analogs were placed above an ice water layer and then heated/sublimated. The resulting grains within the sample holder, outside the sample holder and grains collected from a lid partly covering the sample holder were measured separately. Additionally, I compared spectral characteristics of different grain size fractions of various HEDs which were measured in the RELAB facility and at the University of Winnipeg. Those results have already been presented in Michalik et al. (2021) and are shown separately in section 6.

B) As some dark component of the regolith might decompose due to impact heating (e.g., Cloutis et al., 2012), the combined effect of grain size segregation and abundance of the dark component was investigated. In this investigation, different grain size fractions of hypersthene were mixed with different contents of the Phobos simulant and the results compared. This part does not include heating of the samples.

C) The main focus lies on the temperature experiments. I heated several of the described analogs to different temperatures as well as for different durations. Table 2.2 gives an overview of the analogs and the selected temperatures that were applied as well as the duration.

D) While heating the samples to various temperatures, I observed a remarkable effect: For several samples, the surface of the heated samples had developed different spectral characteristics than the interior of the samples. This effect resembles the observations on Vesta and will be shown separately from the mere temperature increase investigations (C).

Table 2.2: Temperatures (T) and durations (t) of heating experiments presented in this work.

| Sample name | T [°C] | t [h] |
|---|---|---|
| Hypersthene | 400 | 72 |
| Phobos Simulant | 400 | 72 |
| Murchison | 400 | 72 |
| NWA5748M | 200, 400, 600 | 2, 72 |
| NWA5748 | 400 | 72 |
| NWA5230M | 300, 400, 600 | 2, 72, 168 |
| JaH626M | 200, 400, 600 | 2, 72, 168 |
| NWA3359 | 400 | 72 |
| H90P10 | 200, 400, 600 | 2, 72, 168 |
| H80P20 | 400 | 2, 72 |
| H70P30 | 400 | 72 |
| EA90P10 | 400 | 72 |

## 2.6 Electron Probe Microanalysis

In order to understand the spectral changes observed during the experiments in the PSL, I also analyzed the samples Murchison and NWA5748M via Electron Probe Microanalysis (EPMA). The supervisors for this analysis were Dr. Ralf Milke at the Free University Berlin, Institute of Geological Sciences as well as Prof. Dr. Lutz Hecht and Dr. Felix Kaufmann at the Museum für Naturkunde Berlin.

EPMA is a powerful tool to evaluate the composition of a material. It works by shooting an electron beam at the sample which results in the emission of X-rays, whose wavelengths are characteristic of the emitting species. Elemental composition can then be displayed by a WDS (Wavelength-Dispersive Spectroscopy) system which uses an analytical crystal to select X-rays that satisfy Bragg's law and transfer these X-rays to a detector. Bragg's law is defined as follows

$$n\lambda = 2d\,sin(\theta) \tag{2}$$

with $n$ being the diffraction order, $\lambda$ the wavelength, $d$ the grating constant of the crystal and $\theta$ the angle between the planes of incidence rays and reflecting rays on the crystal surface. Additionally, an EDS (Energy-Dispersive Spectrometer) was used, which yielded quick results to identify main elements and the host mineral species.

The samples were prepared as polished grains embedded in epoxy. Due to the reddish character of the heated samples (see sections 5.2.1 and 5.2.2), I specifically searched for oxides, as hematite ($Fe_2O_3$)) is a likely candidate resulting from oxidation and is known for its reddening character. Therefore, WDS analysis are based on oxides only. Analyzed species were $SiO_2$ (Standard Cr-Augite, NMNH 1649C, TAP crystal), $TiO_2$ (Standard Ilmenite, USNM 96189, PETJ crystal), $Cr_2O_3$ (Standard Chromite, USNM 11707, LIFH crystal), FeO (Standard Magnetite, USNM 11488, LIFH crystal), MnO (Standard Ilmenite, USNM 96189, PETJ crystal). The applied voltage was 15 kV with a current of 15 nA and a focused beam. The ratio of the molecular weights of hematite and the measured FeO is 1.1113, so this factor will be applied to the FeO results in section 5.5. Images are displayed in BSE (BackScattered Electrons) mode, which is sensitive to the atomic number of the elements. Hematite will therefore show a higher signal (i.e., bright) than for example olivine or pyroxene.

# 3 Scientific Background

## 3.1 The Dawn mission - Main outcomes relevant to this work

Vesta's dimensions were found to resemble an ellipsoid of (~285 x 229 km). Its surface is dominated by numerous impact craters in a variety of sizes (~40 m at the resolution limit up to 500 km) and a relatively steep topography of height differences up to ~40 km (e.g., Jaumann et al., 2012; Preusker et al., 2014; Preusker et al., 2016). Due to the large topographic differences, mass wasting also plays an important role in shaping the surface topography (e.g., Krohn et al., 2014b; Otto et al., 2013).

Furthermore, Dawn confirmed the connection to the HED meteorites (howardite, eucrite, diogenite) through numerous studies (e.g., Reddy et al., 2012b; De Sanctis et al., 2012a and De Sanctis et al., 2013; Ammannito et al., 2013a; Prettyman et al., 2012; Thangjam et al., 2013). This suite of meteorites comprises achondritic igneous rocks that display the upper range of a differentiated body: ultramafic rocks composed of Magnesium-rich orthopyroxenes (diogenites), crustal cumulates and basalts (eucrites) as well as surface regolith (howardites; e.g., Mittlefehldt, 2015 and references therein). More details are given in section 3.2.

As mentioned earlier, it was already suspected that Vesta shows signs of a large collision near its south pole. The Dawn mission quickly revealed that the asteroid had not only undergone one massive collision but two. The older Veneneia Basin (~400 km) partly overlaps with the younger Rheasilvia basin as seen in Fig. 3.1 (Jaumann et al., 2012). The Rheasilvia basin spans the south pole area with a giant diameter of approximately 500 km (almost the diameter of Vesta itself). Together with the youngest large crater Marcia, which is the focus of this work, these three major impacts mark the chronology of Vesta, reported in Williams et al. (2014b) and seen in Fig. 3.2, left. It is believed that the Rheasilvia impact is the origin of the hemispherical mineralogical dichotomy and possibly the origin of the olivine occurrences yet the latter is debated and the olivine might (partly) have come from exogenic sources or revealed by older impacts (Ruesch et al., 2014; Nathues et al., 2015).

Le Corre et al. (2013) studied the so-called orange material on Vesta. It was called orange material as this type of material appears orange in the false-color Clementine-type ratio RGB (see Fig: 3.2, right), which is discussed in section 2.1.2. The orange material is foremost characterized by a larger visible slope than other, more typical material on Vesta. Le Corre et al. (2013) discussed whether the orange material would represent olivine or impact melt and concluded that the most likely explanation is impact melt.

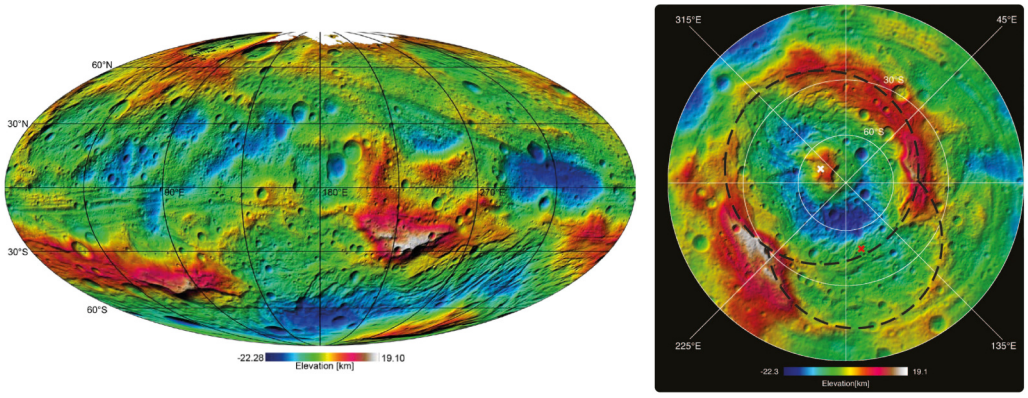


Figure 3.1: Left: Topography of Vesta obtained from HAMO Framing Camera images Preusker et al. (2014), Right: The two large impact basins Rheasilvia and Veneneia taken from (Jaumann et al., 2012).

Rheasilvia unearthed diogenitic lithologies (i.e., ultramafic Ca-poor and Mg-rich orthopyroxene and partly olivine) and displays a large scarp on its rim where the most prominent occurrence of diogenitic spectral signatures occur (e.g., Ammannito et al., 2013a). Veneneia is believed to have delivered at least some of the dark material now found in numerous locations and broadly mixed into

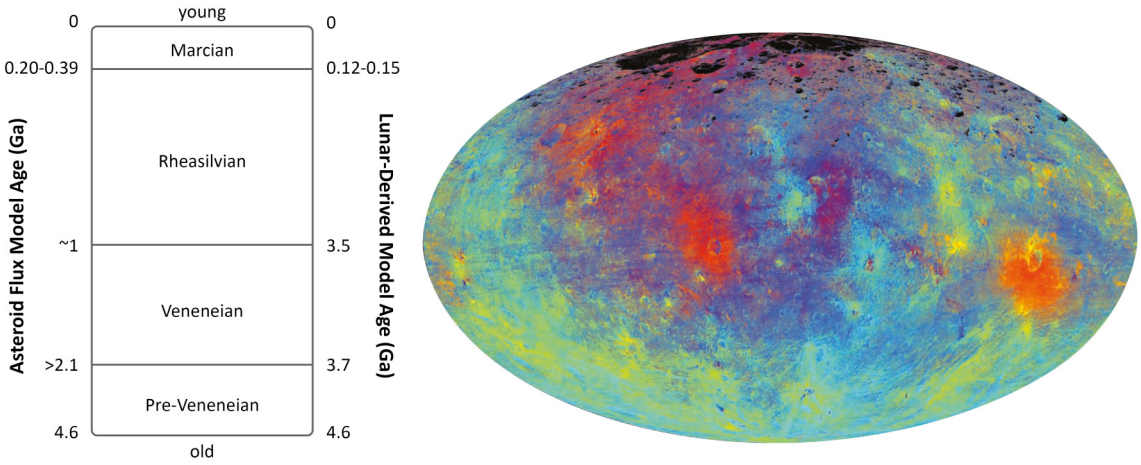


Figure 3.2: Left: Chronology of Vesta modified after Williams et al. (2014b), Right: Clementine-type false color RGB from Framing Camera ratios in Mollweide projection highlighting the mineralogical differences of the surface regolith, taken from Russell et al. (2015).

the surface regolith (e.g., Jaumann et al., 2014; McCord et al., 2012; Stephan et al., 2014, Reddy et al., 2012a). Occurrences of this dark material are strongly linked to OH-bearing material seen by the VIR instrument (e.g., De Sanctis et al., 2012b) and are thought to originate from carbonaceous chondrites, impacting on Vesta over geological timescales (possibly not only Veneneia) and thus obscuring the reflectance spectra on this object.

One such broad occurrence of dark material and an enrichment in OH extends from an equatorial region to the north pole (roughly 200,000 km$^2$, between 70 °E to 220 °E and 30 °N to 30 °S; e.g., De Sanctis et al., 2012b; Combe et al., 2015a). This region can be seen as bluish/purple colors in Figure 3.2, right, and as brighter areas in Figure 3.3. The false color RGB image in 3.2, right, will be explained in more detail in section 2.1.2. The reflectance spectra in this region generally show a decrease of reflectance at visible wavelengths and diminishment of absorption features in contrast to 'brighter' areas on Vesta (e.g., Zambon et al., 2014). Several studies (e.g., McCord et al., 2012; Reddy et al., 2012a; Cloutis et al., 2013a; Nathues et al., 2014; Jaumann et al., 2014) suggest that this darkening agent most likely originates from the infall of carbonaceous chondrites (possibly CM-type) over geological time scales. This exogenic contamination is important when considering the delivery of water through the solar system. As we have learned from Dawn, even differentiated objects can hold considerable amounts of 'water' within their regolith which influences the asteroids' surface geology.

Prettyman et al. (2012) furthermore reported on relatively high amounts of exogenic hydrogen on Vesta's surface. The highest concentrations are found in equatorial regions, west of the crater Marcia. It is approximately the same area where the largest band depths at 2.8 µm (indicating OH-abundance) occur. Another enriched area is present just east of Marcia, likewise with larger band depths at 2.8 µm. Marcia crater itself is characterized by very low OH- and H-abundances, indicating that the impact led to the disappearance of these elements/molecules.

Pieters et al. (2012) reported on the space weathering mechanisms on Vesta and found that nanophase iron, as observed on the moon, does not occur on Vesta. Instead, space weathering on Vesta is dominated by mechanical mixing and brecciation of surface components due to small impacts and relatively high regolith mobility due to large topography contrasts observed on Vesta. The high topography contrast also leads to asymmetrical crater shapes where upslope ejecta becomes deposited on the downslope crater rim as seen in Krohn et al. (2014a).

After Dawn acquired the first high resolution images, so-called *pitted terrains* were observed and reported on in the study by Denevi et al. (2012). These features are characterized by dense clusters of rimless, irregular-shaped depressions which were found so far on Mars ('pitted materials'), Vesta and Ceres ('pitted terrains'). On all three bodies, they exclusively occur in primary impact deposits. Following the suggestion of Dr. Livio L. Tornabene and in accordance with my co-workers,

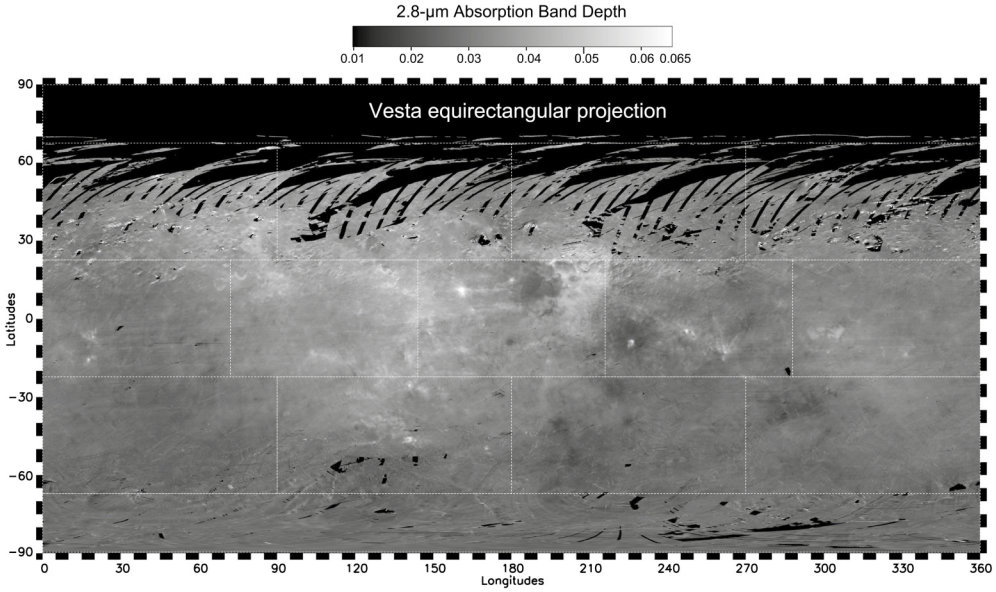


Figure 3.3: Caption adopted from Combe et al. (2015a): Vesta's surface global map of absorption band depth of hydroxyl at 2.8 $\mu$m. The dashed-line rectangles correspond to the conventional division into fifteen quadrangles.

I renamed these terrains to **Pitted Impact Deposits** (**PIDs**) to account for this origin. These terrains are closely linked to a rapid loss of volatiles as was shown before for the Martian counterparts by Tornabene et al. (2007), Tornabene et al. (2012) and Boyce et al. (2012). Therefore, volatiles appear to play an important role in forming the PIDs. I will describe these early observations in more detail in section 3.5.1 and 3.5.2.

Furthermore, Scully et al. (2015) found evidence for transient water flow on Vesta and discovered curvilinear gullies on the crater walls of Marcia. They suggested that subsurface ice deposits could survive in the regolith over geological timescales and furthermore could have provided the necessary volatiles to form the pitted impact deposits. Denevi et al. (2012) did not suggest this possibility and found the volatiles most likely to derive from the carbonaceous chondrite material identified in the Vestan regolith. A detailed analysis has been missing in order to answer this question which is provided in this work.

Last but not least, the surface of the interior Marcia crater and its surroundings have been found to contain a higher percentage of eucritic material (Ammannito et al., 2013a; Prettyman et al., 2013), indicating that the impact excavated eucritic crustal material. This was also confirmed by De Sanctis et al. (2015b) using VIR data. The eucritic enrichment is best illustrated in Russell et al. (2015) which is shown here in Figure 3.4.

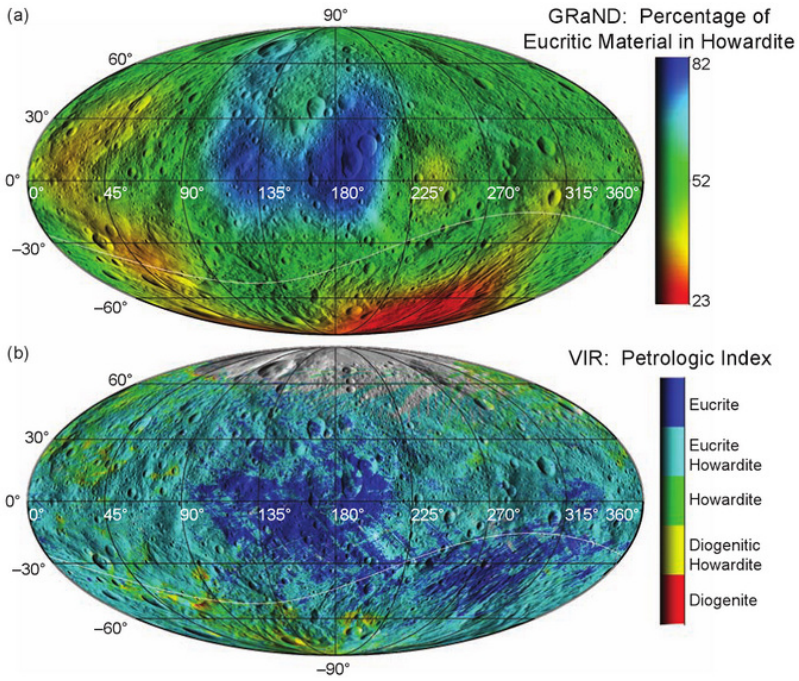


Figure 3.4: Text modified from Russell et al. (2015): Lithologic maps of Vesta remapped in Mollweide projection. (a) Map of the percentage of eucritic material from GRaND data (Prettyman et al. (2013)). (b) Map of HED distribution mapped by VIR (Ammannito et al. (2013a)). Eucritic regions appear as blue, whereas regions that are more diogenitic appear as red.

## 3.2 HED meteorites (howardites, eucrites, diogenites)

The HEDs are a suite of three different types of meteorites and are thought to originate from Vesta. HED stands for: **H**owardites, **E**ucrites and **D**iogenites. Howardites are polymict breccias of diogenites and eucrites while eucrites generally represent upper crustal rocks and diogenites lower crustal/upper mantle rocks (e.g., Mittlefehldt, 2015 and references therein).

Vesta as their origin is a somewhat fragile assumption as there are many HEDs deviating from the 'standard'. HEDs commonly have a uniform oxygen isotopic composition which points to global-scale melting (≥50%, Greenwood et al., 2005), yet some specimen show deviations from this standard (e.g., Scott et al., 2009; Mittlefehldt et al., 2016). This is shown in Figure 3.5, left, and suggests multiple parent bodies for the HEDs. Moreover, Wasson (2013) even questioned any actual connection of Vesta and the HEDs at all due to the large number (>30) of existing iron meteorite groups (which equals a large number of asteroids that experienced fractional crystallization and were destroyed) and a geochemical connection to the IIIAB irons, which would indicate that the HED parent body has already been destroyed long ago. Nevertheless, I assume in this work that the majority of HEDs are direct representatives of the Vestan lithologies, which was confirmed by the Dawn mission as mentioned earlier (e.g., McSween et al., 2013b). Assuming this connection, Vesta would be the only known asteroid parent body for meteorites found on earth while it is assumed that >100 asteroid parent bodies should exist (e.g., Meibom and Clark, 1999; Burbine et al., 2002).

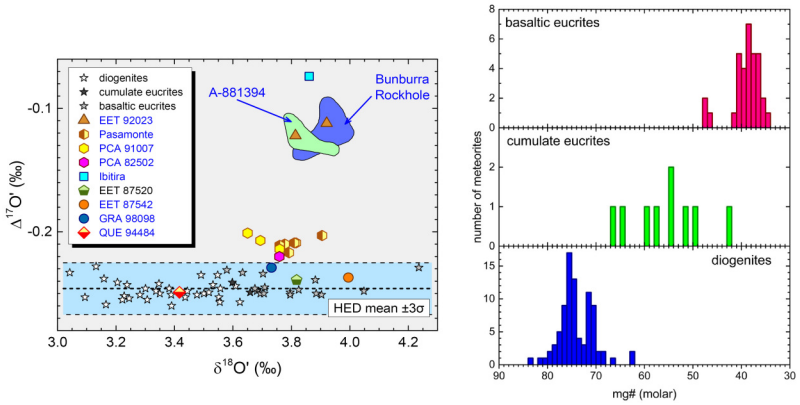


Figure 3.5: Left: Caption adopted from Mittlefehldt et al. (2016): O-isotope compositions of mafic achondrites, diogenites and eucrites. Right: Caption adopted from Mittlefehldt (2015): Histograms of low-Ca pyroxene mg#s in diogenites, cumulate eucrites and basaltic eucrites.

Both eucrites and diogenites largely consist of pyroxenes and yet the molar mg-number differs in these rock types. Diogenite pyroxenes incorporate considerably more Mg than eucrite pyroxenes which also affects their spectral characteristics as will be later demonstrated. These differences are shown in Figure 3.5, right. The pyroxenes in both petrologic types contain various degrees of high-Ca exsolution lamellae. Most HEDs are brecciated yet unbrecciated specimen also occur. Mittlefehldt (2015) wrote a comprehensive review about these meteorites and for the following subsections, I will use many information from his review and the references therein. Figure 3.6 shows information about the modal mineralogy and classification of HEDs from Mittlefehldt (2015) which will be referred to in the following subsections.

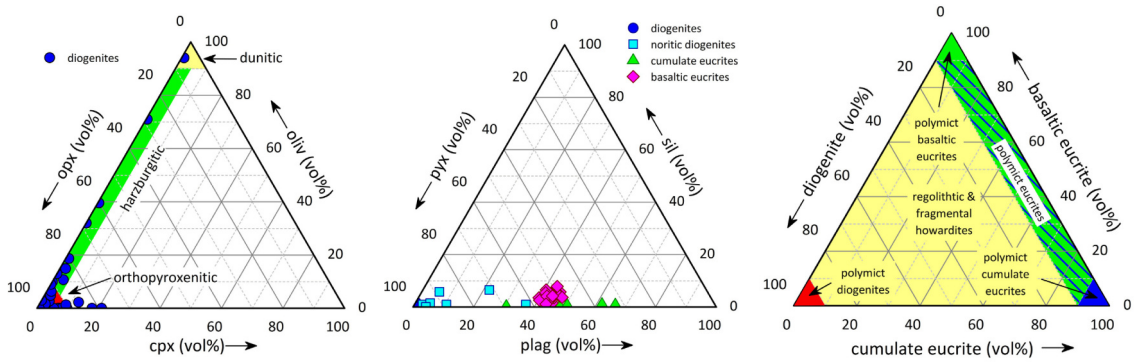


(a) (b) (c)

Figure 3.6: Modal mineralogy and classification scheme for diogenites (a), eucrites (b) and HED breccias (c) (incl. howardites).

### 3.2.1 Diogenites

As previously mentioned, diogenites represent ultramafic Mg-rich and Ca-poor rocks which mainly consist of orthopyroxene (Figure 3.6, a). Most are classified as orthopyroxenitic yet there are specimen containing various amounts of olivine and are therefore harzburgitic and dunitic.

Noritic diogenites contain more ferroan orthopyroxene as well as pigeonite (clinopyroxene) and plagioclase and represent transitional rocks to cumulate eucrites. The majority of diogenites are breccias and there also exist polymict breccias (additionally containing fragments of eucrites). Diogenites are usually coarse-grained with grains up to 5 cm.

This dissertation focuses on an area near the equator, which is rich in eucritic lithologies. Thus, diogenitic lithologies are not in the focus of this work. Nevertheless, understanding the spectral characteristics of the whole Vestan surface is important to understand the surface and geology of Vesta as well as the regional differences and their effects on the spectral characteristics. This is shown in sections 2.1.2 and 3.3.2.

Minor phases in diogenites are high-Ca pyroxene, chromite, plagioclase, silica, troilite and metal.

### 3.2.2 Eucrites

Eucrites contain more clinopyroxenes (pigeonite) as well as plagioclase and their pyroxenes contain more iron with respect to diogenites. Both diogenites and eucrites contain low abundances of silica (Fig. 3.6, b).

Eucrites are dominated by clinopyroxene (pigeonite) as well as plagioclase and can generally be divided in basaltic and cumulate eucrites. Cumulate eucrites are coarser-grained gabbros while basaltic eucrites are more fine-grained and thought to represent shallow dikes and sills. Cumulate eucrites mainly contain low-Ca pyroxenes with intermediate molar mg-numbers between diogenites and basaltic eucrites (see Figure 3.5, right). Basaltic eucrites have a relatively uniform content of plagioclase and contain low levels of silica while the plagioclase content of cumulate eucrites differ to larger degrees and silica has even lower abundances (Fig. 3.6, b). Of all three HED endmember types (diogenites, basaltic eucrites, cumulate eucrites), basaltic eucrites show the most limited range in major and minor element composition.

Minor phases in eucrites are chromite, ilmenite, olivine, metal, troilite, whitlockite, appatite, zircon and baddeleyite.

### 3.2.3 HED breccias/Howardites

Howardites are polymict breccias mostly composed of fragmented diogenites and eucrites and hence likely represent the lithified upper debris layer of Vesta. Mittlefehldt (2015) points out

that howardites are not the only rocks representing surface debris.

Polymict breccias that contain less than 10% of diogenites are called polymict eucrites and those containing less than 10% of eucrites are called polymict diogenites. View Figure 3.6, c, for the whole classification of polymict breccias.

Howardites commonly contain glassy spheres and irregular shaped particles which is a likely result of the generation of melt by impacts and impact gardening on the surface of Vesta. Furthermore, the polymict HED breccias commonly contain chondritic clasts and even other meteorite classes were identified. The most common carbonaceous chondrite clast-type are CM2 chondritic clasts, making up ~81% of all clasts identified in the analyzed HED samples by Zolensky et al. (1996). CR2 chondrites were the next common clast-type but much less abundant.

## 3.3 Reflectance Spectroscopy

### 3.3.1 Background

Reflectance spectroscopy is a powerful tool to obtain compositional and mineralogical information about a material. It is a non-destructive passive analyzing technique and can be used in-situ, e.g., during a field trip or with a laboratory spectrometer, but also from far distances on spacecrafts and satellites. Many minerals have characteristic *reflectance spectra* due to their crystallographic properties and elemental compositions. In this section, I will summarize the basics of this technique.

Reflectance spectroscopy is based on the ability of electromagnetic (EM) energy (i.e. here, light) to be reflected, transmitted and/or absorbed by a material. EM energy can also be emitted, but I do not cover this topic in this thesis. These processes are dependent on wavelength, material properties and optical pathways. For example, the Spectralon® standard described in section 2.5 reflects light to almost 100% in all wavelengths of the VIS and NIR wavelength region (~0.4 - 1.1 µm) whereas many rock-forming minerals absorb EM energy at specific wavelengths yet at the same time can also partly transmit and reflect EM energy of other wavelengths. This results in characteristic, sometimes very complex reflectance spectra, especially for particulate media of different minerals (e.g., surface regolith of planetary bodies). This principle of EM energy interaction with surfaces is responsible for any sort of colors we can see with our own eyes. Our eyes are in this case a detector recording EM energy in the 'visible' wavelength region (~0.4 - 0.7 µm) whereas today's scientific instruments can capture a much wider range of wavelengths from the high-frequency gamma rays at the beginning of the EM spectrum ($10^{-16}$ m) up to radio waves at $10^{8}$ m wavelength. These instruments also have a much higher spectral resolution so that we are able to systematically derive information about a material. This technique has been invaluable for planetary (and Earth) science and has advanced our understanding of our solar system in multiple disciplines.

On an average planetary body, the sun is by far the major EM energy source. Irradiation of the sun's EM energy on a planetary surface behaves in all described manners: it can be transmitted through transparent minerals, reflected on crystal faces and absorbed (Fig. 3.7). The EM energy collected by a spacecraft instrument is the remaining reflected energy that was not absorbed or transmitted:

$$E_i = E_r + E_a + E_t \tag{3}$$

with $E_i$ being the incident energy (for Vesta, this is the sun), $E_r$ the reflected energy, $E_a$ the absorbed energy and $E_t$ the transmitted energy (Gupta, 2003). The space craft sensors collect the reflected light at a specific angle. This angle is called the phase angle $p$, which is the angle between the irradiating light onto the surface and the emitted light from the surface, also dependent on the azimuthal angle $\theta$, which is the angle between the plane of incidence and plane of emergence, respectively (Fig. 3.7). Other important angles are the incidence and emission angle ($i$ and $e$, respectively) of the irradiating EM energy and the reflected energy, respectively. Different incidence, emission and phase angles yield different energies which is why this has to be accounted for when calibrating/correcting data.

Remotely acquired reflectance spectra are commonly expressed as $I/F$, which is the bidirectional reflectance of the surface relative to that of a Lambertian surface (reflects equally in all directions), or also called the *radiance factor* (e.g., Hapke, 2012; Schröder et al., 2013). Hapke (2012) defines the radiance factor $RADF$ as:

$$RADF(i, e, p) = \pi\, r(i, e, p) \tag{4}$$

with $r(i, e, p)$ being the bidirectional reflectance. The radiance factor for the calibration of Dawn FC data at Vesta was described by Schröder et al. (2013) as $r_F$:

$$r_F(\lambda) = \frac{\pi\, d^2\, L(\lambda)}{F_{sol}(\lambda)} \tag{5}$$

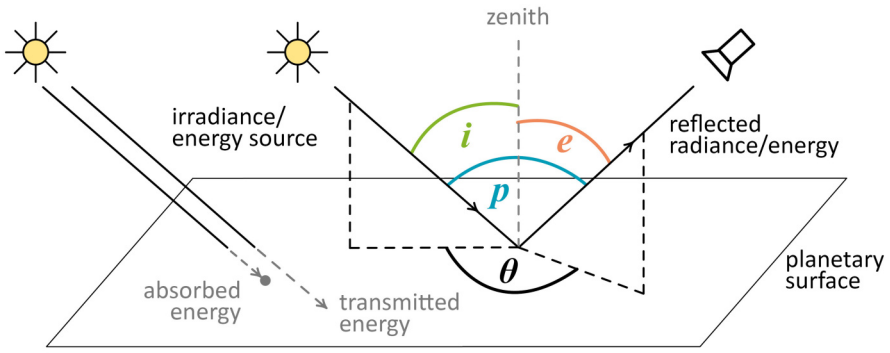


Figure 3.7: Schematic illustration of the geometry and interaction of light with a planetary surface, modified after Hapke (2012) and Gupta (2003).

where $d$ is the distance of Vesta to the sun, $L(\lambda)$ is the wavelength-dependent reflected radiance, and $F_{sol}(\lambda)$ is the wavelength-dependent solar irradiance. Both irradiance and reflected radiance are dependent on incidence, emission and phase angle. Schröder et al. (2014) develop another expression for the radiance factor for the purpose of seamless mosaicking the surface of Vesta, which includes a phase function (as equigonal albedo is decreasing with increasing phase angle, Schröder et al., 2014) and a disk function developed by Shkuratov et al. (2011):

$$r_F(\lambda) = A_{eq}(p)\, D(\mu_0, \mu, p) \tag{6}$$

with $A_{eq}$ being the equigonal albedo (incidence angle equals emission angle and equals half the phase angle) and $D(\mu_0, \mu, p)$ the disk function with $\mu_0 = cos(i)$ and $\mu = cos(e)$. The disk function describes the brightness variation across the planetary disk and Schröder et al., 2014 adopted the Akimov disk model, as it was found to work well for Vesta (Schröder et al., 2013, 2014). The Akimov model only depends on the incidence, emergence and phase angle.

The reflectance acquired by the PSL FT-IR spectrometer is described as the *reflectance factor*, which is defined as the ratio of the reflectance of the surface to that of a perfectly diffuse surface under the same conditions of illumination and measurement (Hapke, 2012, here, the Spectralon® standard). As the reflectance factor of a perfect Lambertian surface is $r_L = \mu_0/\pi$, with $\mu_0 = cos(i)$ (Hapke, 2012), the reflectance factor $REFF$ is:

$$REFF(i, e, p) = \frac{\pi\, r(i, e, p)}{\mu_0} \tag{7}$$

The mentioned characteristic reflectance spectra of minerals are mainly characterized by so-called *absorption bands*. These are characterized by a decrease of reflectance at a specific wavelength (range). Absorptions occur due to energetic transformations within the crystal lattice, which are classified into 'vibrational' (/rotational) and 'electronic processes'.

The most common electronic process can be explained by the so-called *crystal field theory*. Burns (1993) gives a comprehensive overview on this topic. The crystal field theory is based on the ability of energy levels to split when transition elements with unfilled $d$ (and $f$) orbitals such as Ni, Cr, Co, Fe, Mn etc., are situated within a crystal field. The ligands surrounding a transitional metal act as negative charges and have, depending on the orbital geometry, different degrees of repulsive effects on the electrons of the unfilled $d$ orbitals, resulting in destabilized orbitals and different orbital energy states. This enables electrons to be energetically excited when EM energy enters the crystal field. EM energy can only be transformed in this way if it matches the energy difference between the split energy states ('*splitting energy*'). The excited state of an electron will be given up in favor of a lower energy state, resulting in the emission of EM energy, which is usually not the same wavelength it was absorbed. The crystal field effect is causing the dominant absorptions of pyroxene, which is presented in the following section.

Another prominent electronic process causing absorptions is the charge transfer effect (e.g.,

Burns, 1993; Clark, 1999; Hapke, 1981; Gupta, 2003; and references therein) where electrons move from one ion to another ion or ligand (e.g., $Fe^{2+}$-$Fe^{3+}$ or Fe-O). The strength of these absorptions is significantly higher than of the previously described crystal field effects yet predominantly occur in the UV region and nearby (short VIS). This results for example in the characteristic red color of iron (hydr-)oxides. Other electronic processes comprise moving electrons throughout the whole crystal lattice ('conduction bands') and electrons that prefer to be bound by means of EM energy where defects occur ('color centers').

Vibrational (or rotational) processes are based on the ability of a molecule or crystal lattice to vibrate (/rotate) through its bonds. These motions - which occur at various frequencies - can be influenced by EM energy when it is absorbed. For example, water and hydroxyl bound in minerals have very prominent absorptions due to these vibrational processes. Carbonates (e.g., important for Ceres-like bodies) likewise have characteristic absorptions due to this process.

Absorption bands are influenced by multiple factors. As previously discussed, elemental composition, crystal geometry and also viewing geometry are major factors, yet for a chemically identical material, differences in grain size and roughness for example can also alter a spectrum.

Mathematically, an absorption can be expressed by *Beer's law* (e.g., Clark, 1999), where $I$ is the observed intensity:

$$I = I_0 \, e^{-kx} \tag{8}$$

$I$ is dependent on $I_0$, the original light intensity, and the parameters *absorption coefficient* $k$ and *distance travelled through the medium*, $x$. The absorption coefficient depends on the wavelength $\lambda$ and the *extinction coefficient* $K$, which is in turn the imaginary part of the complex index of refraction $m$, with $n$ being the real part of the index of refraction and $j = (-1)^{0.5}$.

$$k = \frac{4\pi \, K}{\lambda} \tag{9}$$

$$m = n - jK \tag{10}$$

In-situ spectroscopy of a planetary body always requires to take into account space weathering effects. Space weathering denotes a process by which a planetary surface changes due to solar irradiation, micrometeorite bombardment and sputtering, where single atoms are disconnected from the solid material. The effects of space weathering are well-studied for the moon and less well-studied for other objects in the solar system. On the moon, space weathering leads to the formation of nanophase iron on single grains, which yields in a *redder* spectrum of a material (e.g., Pieters et al., 2000). A red-sloped spectrum shows increased reflectance towards longer wavelengths. Accordingly, there are *blue* slopes which for example occurr at well-preserved craters on Ceres (Stephan et al., 2017). Space weathering on the moon also yields diminished absorption bands (e.g., Adams and McCord, 1973; Pieters et al., 2000). On Vesta, Pieters et al. (2012) describe the space weathering processes as the result of breakdown of surface components due to constant (micro-)meteorite and/or asteroid bombardment over geological timescales, slowly building a uniform 'spectral background'. An overall reddening of spectra similar to the moon is not observed on Vesta. Instead, freshly exposed bright materials exhibit relatively redder spectra in the visible part of the EM spectrum while fresh dark materials even exhibit 'bluer' spectra than the background soil (Pieters et al., 2012).

### 3.3.2 HED and Vesta specifics

As discussed before, the Vestan and HED reflectance spectra and the HEDs mineralogy are dominated by the mineral pyroxene. Pyroxene is one of the most common rock-forming minerals on planetary bodies and well-studied. The $SiO_4$-tetraeders in pyroxene are configurated in chains along the c-axis with cations being bound within the chains and between chains, occupying two crystallographic sites. These positions are commonly called *M1* and *M2*. The M1 and M2 cations in Ca-poor pyroxenes are similar-sized and in *octahedral* configuration with six ligands around them.

(Burns, 1993). As HEDs and Vesta show a Ca-poor pyroxene-dominated lithology and reflectance spectrum, I will discuss the specifics of this mineral group and its spectra here.

The chemical formula of Ca-poor pyroxenes is $M1^{[6]}M2^{[6]}[X^{[4]}O_6]$. Numbers in superscript square brackets denote the ligand configuration of the corresponding cations M1, M2 and X. In calcic pyroxenes, the M2 cite can also be surrounded by eight oxygen ligands, yet in Ca-poor pyroxenes, both sites are more or less octahedrally configurated, with the M2 site showing larger distortions and more variable distances from oxygen ligands than the M1 site (Fig. 3.8 and e.g., Burns, 1993 and references therein). Therefore, M2 can be occupied by larger cations. X is predominantly occupied by Si and Al. The larger M2 site can generally be occupied by: $Na^{+}$, $Ca^{2+}$, $Fe^{2+}$, $Mg^{2+}$ and $Mn^{2+}$, whereas the M1 site can be occupied by: $Fe^{2+}$, $Mg^{2+}$, $Mn^{2+}$, $Zn^{2+}$, $Fe^{3+}$, $Al^{3+}$, $Cr^{3+}$, $V^{3+}$ and $Ti^{3+}$ (Okrusch and Matthes, 2010). Iron is one of the most stable elements and therefore the most common transition metal occupying one of these sites. $Fe^{2+}$ prefers to occupy the M2 site and is then responsible for the characteristic bands near 1 and 2 µm. In contrast, weaker absorption bands at around 1.0 and 1.2 µm, which occur in clinopyroxenes, are attributed to $Fe^{2+}$ occupying the M1 site (e.g., Burns, 1993; Cloutis and Gaffey, 1991).

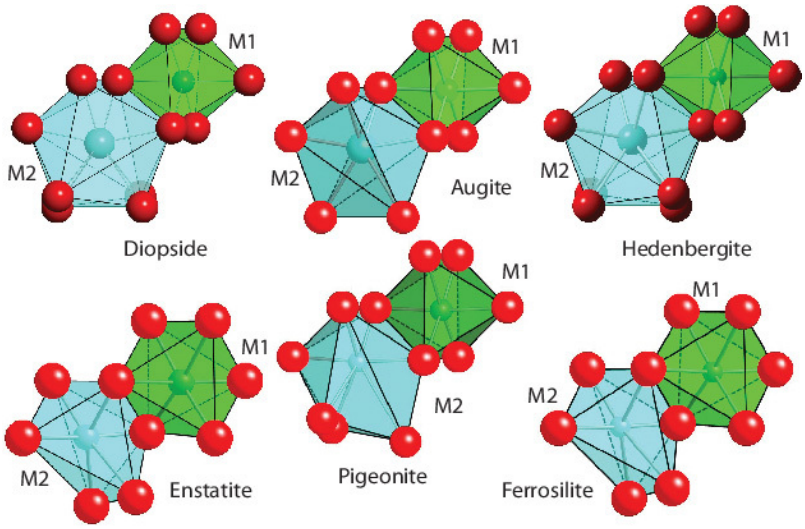


Figure 3.8: Caption adopted from Dyar et al. (2013): "View down the a axis of different pyroxenes distributed across the Ca-Mg-Fe quadrilateral, illustrating variations in average geometry of the M1 and M2 sites in pyroxene as a function of space group and composition."

Figure 3.9 is taken from Clark (1999) and shows reflectance spectra of two different pyroxenes. This best illustrates that spectra can be very characteristic depending on mineralogy. Diopside is a calcic pyroxene crystallizing in the monoclinic system and Bronzite a Ca-poor pyroxene crystallizing in the orthorhombic system. Both band positions and band shapes can easily be distinguished from one another. On Vesta, low-Ca pyroxenes predominate and thus spectra of HEDs and Vesta look more similar to the Bronzite spectra shown. This Figure also displays the longer wavelengths of the calcic pyroxene absorptions.

Figure 2.5 in section 2.4 shows spectra of, among others, a diogenite and eucrite. As diogenites contain very high abundances of pyroxenes, their absorption bands are generally stronger (i.e., larger band depth). Furthermore, due to their higher Mg content, their absorptions' band positions are at slightly shorter wavelength, as discussed in 2.1.2. Figure 2.5 also includes the positions of the three used FC filters onboard Dawn, which shows that these filters can be used to characterize the first pyroxene absorption band of these lithologies. The main band position of another common rock-forming mineral of planetary bodies, olivine, is at significantly longer wavelength, which enables the clear distinction of pyroxene and olivine signatures on Vesta which several studies have shown (Ammannito et al., 2013b; Le Corre et al., 2013; Thangjam et al., 2014; Nathues et al., 2015).

Another feature taken into consideration in this work is the known absorption band at ~2.8 µm. This absorption is caused by hydroxyl groups (OH). While HEDs generally show little content

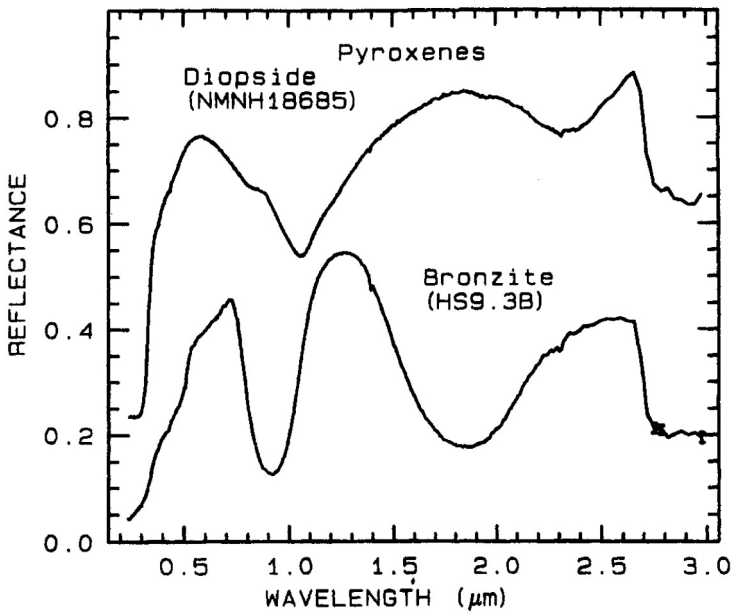


Figure 3.9: Image caption taken from Clark (1999): Reflectance spectra of two pyroxenes, showing the change in $Fe^{2+}$ absorption band position and shape with composition (from Clark et al., 1993b). Diopside, sample NMNH18685, is $CaMgSi_2O_6$, but some $Fe^{2+}$ substitutes for Mg. Brinzite, sample HS9.3B, is (Mg,Fe)$SiO_3$ with mostly Mg. The 1 $\mu$m versus the 2 $\mu$m band position of a pyroxene describes the pyroxene composition [...]. The diopside spectrum is offset 0.2 unit upward.

of CC clasts (maximum of few vol%, e.g., Zolensky et al., 1996), the surface of Vesta shows broad distributions of detectable absorptions at 2.8 µm within the regolith (De Sanctis et al., 2012b). A possible explanation for this ambiguous observation is that the impact that formed Rheasilvia is thought to have released the material that might represent today's Vestoids and HED meteorites. Thus, the surface regolith of Vesta might not be sampled by our meteorite collection.

## 3.4 Carbonaceous chondrites and their relationship to Vesta

### 3.4.1 Carbonaceous chondrites

Carbonaceous chondrites (CC) are of particular interest in this study as 1) CC clasts were found in HED meteorites (Zolensky et al., 1996 and references therein) and 2) Dawn found dark material on the surface of Vesta as well as OH-bearing phases (e.g., De Sanctis et al., 2012b) and increased hydrogen values (e.g., Prettyman et al., 2012). Multiple studies consequently suggested carbonaceous chondrites as the origin of these observations (e.g., Reddy et al., 2012a, McCord et al., 2012, Jaumann et al., 2014). Thus, CC material is widely distributed in the Vestan regolith and appears to be involved in the formation of PIDs which is shown in this work.

The term *chondrite* refers to meteorites that commonly have not differentiated and contain so-called *chondrules*, little melt-droplets thought to originate from the solar nebula or possibly from early collisions (e.g., Scott and Krot, 2014 and references therein). Chondrites are divided into several classes, one of which are the CCs. These contain carbon-rich phases and contain the oldest known solar-system materials: CAIs and AOAs, as previously mentioned. Through dating of these earliest phases, we estimate the solar system to be roughly 4.567 Ga old (Amelin et al., 2010; Connelly et al., 2012).

As already presented in section 3.2.3, Zolensky et al. (1996) presented that the majority of CC clasts in HEDs belong to the CM2 group. Therefore, I used Murchison, which is a CM2 chondrite, for some of the experiments presented in section 5. As presented in section 2.5.2, Murchison contains more than three quarters of matrix which contains high amounts of phyllosilicates (serpentine and cronstedtite) as well as tochinilite, a hydrated sulfide. Thus, relatively high volumes of volatiles can be released upon heating.

### 3.4.2 The surface of Vesta and the Marcia area

The surface of Vesta, and especially the region around Marcia, where the vast majority of PIDs occur, is characterized by multiple occurrences of dark material and enrichment in OH and H (e.g., De Sanctis et al., 2012b; Prettyman et al., 2012; Jaumann et al., 2014; Combe et al., 2015a). Dark material is characterized by low albedo and diminished spectral features (i.e., absorption bands). Dark material occurs as discrete locations, for example in crater rays or at crater rims, as well as broadly mixed into the surface regolith, lowering albedo levels over larger spatial extents.

In order to examine the PIDs and identify the process driving the formation of these features, it is necessary to take their surrounding into consideration, especially the spectral and geomorphologic features of Marcia and Calpurnia craters and their ejecta. Figure 3.10 displays the broad Marcia region as seen through clear filter LAMO images (a), the new HAMO RGB composite (b), DTM data (c) and the 2.8 µm absorption depth (Combe et al., 2015a) (d). In Figure 3.10b, green and cyan colors indicate material with higher reflectance and pyroxene band strength, while red colors indicate regions with lower reflectance and pyroxene band strength values (R= 965/917 [nm], G=750 nm and B=750/917 [nm]). In Figure 3.10d, dark green colors indicate lower OH content whereas red colors indicate higher OH content.

Figure 3.10 illustrates distinct regional differences in spectral and geomorphological properties. In general, regions with higher OH absorptions correlate well with regions of lower reflectance and pyroxene band strength. The NW and center of Marcia crater are strongly depleted in OH with respect to other regions nearby. A few km off the rim in the E and NE, a well-defined boundary between brighter/OH-depleted material and darker/OH-enriched material is visible (Fig. 3.10b and d). I use this boundary to define two different units of Marcia (and/or Calpurnia) ejecta (Fig. 3.11): Ejecta unit 1 (E1) is generally higher in reflectance, higher in pyroxene band strength (green/cyan in Fig. 3.10b) and lower in OH abundance (green in Fig. 3.10d), while ejecta unit 2 (E2) is lower in reflectance, lower in band strength (reddish in Fig. 3.10b) and higher in OH abundance (orange/red in Fig. 3.10d). In E2, pre-existing craters and topography are largely overprinted by Marcia ejecta and hardly recognizable whereas numerous pre-existing craters can be observed in E1, indicating that E1 is thinner than E2.

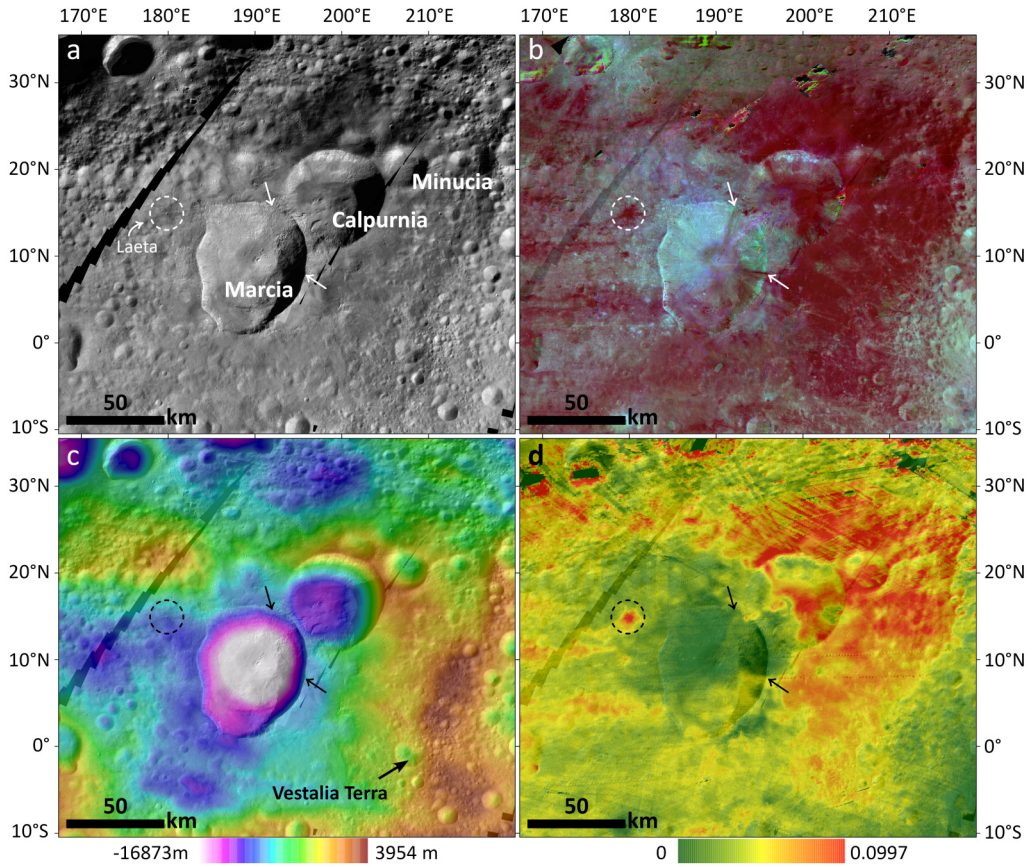


Figure 3.10: Spatial and spectral context of Marcia crater and its broad surrounding. a) LAMO clear filter data. This is also the base layer for the other panels, b) HAMO RGB composite (R= 965/917 [nm], G=750 nm and B=750/917 [nm], 20% transparency), c) DTM (50% transparency), d) VIR 2.8 µm band depth map from Combe et al. (2015a) (30% transparency). The arrows just east and northeast of Marcia indicate input of material from the rim into the crater which will be explained later on. Dashed circle NW of Marcia indicates Laeta crater.

I further subdivided E2 into E2a and E2b, where E2a is strongly influenced by the presence of Vestalia Terra, a mountain range to the east of Marcia (Fig. 3.10c), and characterized by lobate slope deposits, lobate uphill features as well as lower reflectance/pyroxene band strength and slightly higher OH absorption values than E2b. Figure 3.12 illustrates lobate uphill features as well as lobate slope deposits in E2a. E2b does not feature these specifics but is still lower in reflectance and pyroxene band strength than E1 and also shows larger 2.8 µm absorptions band depths than E1. Moreover, the OH-rich spectral signature of E2a ends quite abruptly near the top of Vestalia Terra and overlaps well with lobate uphill features (Fig. 3.12d). The high OH abundance is therefore strongly tied to ejecta.

As material of E2a is correlated with thick ejecta, subsequent space weathering processes (Pieters et al., 2012) probably foremost reworked the ejecta and not pre-existing regolith. Therefore, spectral characteristics of this ejecta unit might still be very similar to the characteristics of the original ejecta. Table 1 summarizes the spectral properties of the presented three ejecta units and displays that, in comparison with the whole Vesta, Marcia (and Calpurnia) ejecta are generally darker and richer in OH than the average of Vesta (as observed before by De Sanctis et al., 2012b and Combe et al., 2015a). Data for E1 in Table 1 do not include areas obviously contaminated by dark material (e.g. Laeta crater within E1, dashed circle in Fig. 3.10; Jaumann et al., 2014).

Figure 3.11 displays E1, E2a and E2b mapped over clear filter LAMO images and faint overlain HAMO RGB composite. Laeta crater NW of Marcia excavated dark material with the same spectral characteristics as E2a, suggesting that E1 superposes E2a. The spectral signatures of E1 and E2b

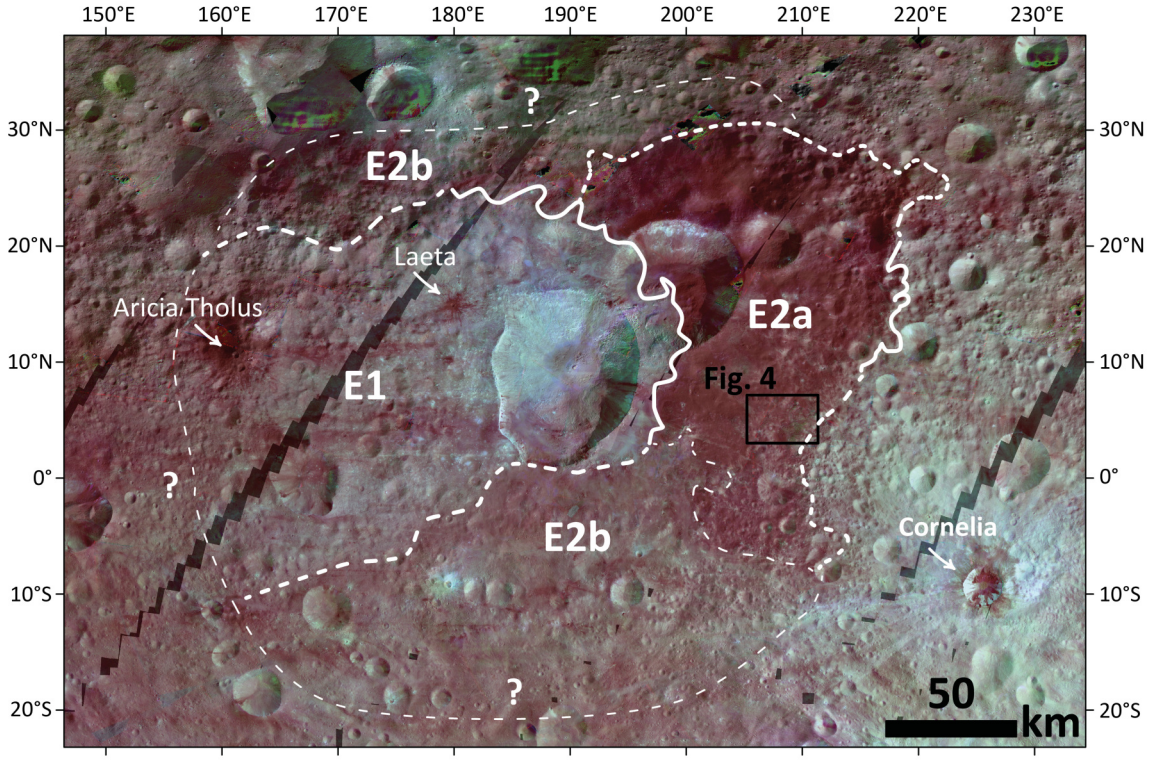


Figure 3.11: Map of the ejecta units E1, E2a and E2b. Clear filter LAMO data overlain by the new RGB composite (R=965/917 [nm], G=750 nm and B=750/917 [nm], 50% transparency). Solid line indicates apparent boundary, dashed lines indicate approximate boundaries and faint dashed lines indicate uncertain boundaries. Cornelia crater is displayed in this map on the lower right.

Table 3.1: 750 nm reflectance, 750/917 [nm] and 2.8 µm band depth values (from Combe et al., 2015a) of E1, E2a and E2b. Values are given with one standard deviation.

| Unit | Mean 750 nm reflectance | Mean 750/917 [nm] | Mean 2.8 µm band depth | n (pixel number) |
|---|---|---|---|---|
| E1 | 0.185 ± 0.010 | 1.443 ± 0.042 | 0.031 ± 0.003 | 755,550 |
| E2a | 0.142 ± 0.012 | 1.291 ± 0.114 | 0.048 ± 0.006 | 1,675,878 |
| E2b | 0.161 ± 0.014 | 1.346 ± 0.041 | 0.038 ± 0.006 | 1,918,785 |
| whole Vesta | 0.194 ± 0.034 | 1.445 ± 0.133 | 0.030 ± 0.009 | 3.56*10$^8$ |

gradually attenuate to the west, south and north. The boundary I mapped in these regions is approximate and based on lobate features that I observed and interpret as ejecta flow fronts (similar to the example in Fig. 3.12a, white arrows). The extent of Marcia and Calpurnia ejecta is larger than what was mapped by Williams et al. (2014a) on the basis of geomorphologic observations at a resolution of 260 m/px (Survey orbit).

It is still under debate whether the OH-rich ejecta unit (E2a) results from the Calpurnia or Marcia impact. The spectrally very different ejecta units E1 and E2a clearly suggest different origins. However, the relationships of E1 and E2a are not easily unraveled. For example, E1 clearly appears to superpose E2a (e.g., as seen at Laeta crater and within Calpurnia), yet just east of Marcia, material from E2a seems to merge into E1 and overprint it. The extent of E2a favors an origin in the older crater Calpurnia, yet the shape of the Vestalia Terra highlands coincide with the shape of the OH-rich and dark margin of E2a, possibly leading to the current shape by coincidence and thus questioning Calpurnia as the origin of E2a. Moreover, there are no PIDs occurring north

of Calpurnia. Furthermore, E2b spectrally appears as a mixture between E1 and E2a und its extent is not readily explained by two craters forming at different times. In summary, I am fairly confident that the majority of E1 materials originate from the Marcia-forming impact event, yet I am less confident that all of E2 can be assigned to Marcia and may actually originate from Calpurnia. This would also suggest a possible oblique impact angle for the Marcia projectile, as E1 is distributed asymmetrically around the crater.

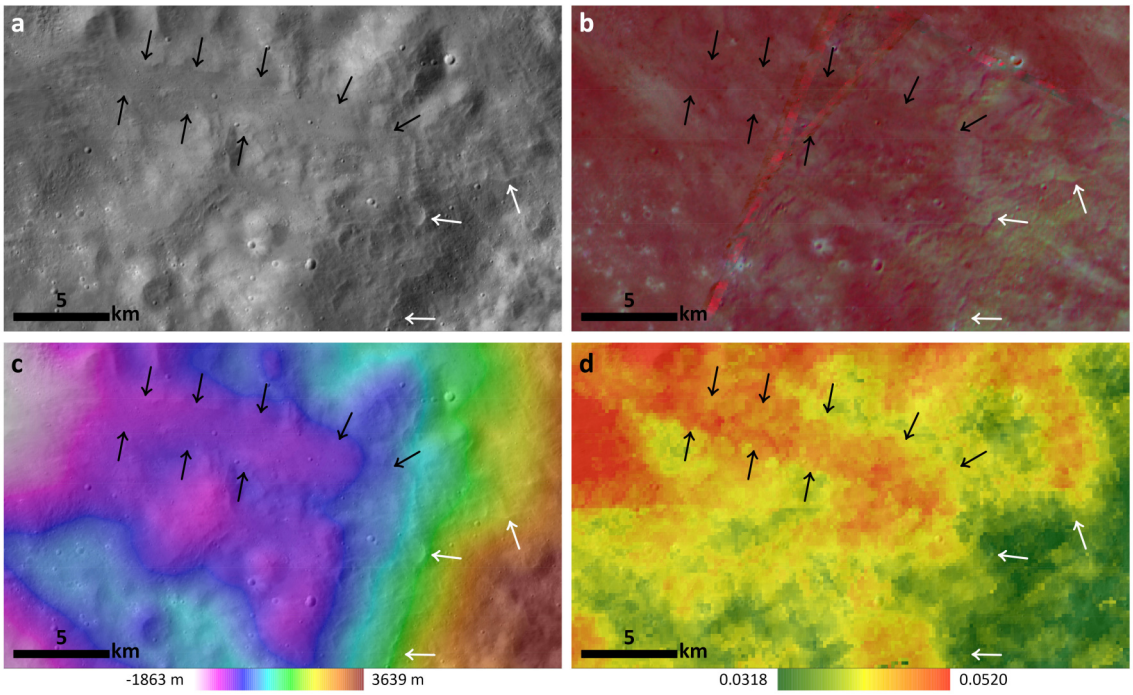


Figure 3.12: Lobate uphill features (white arrows) and lobate slope deposit (black arrows) in E2a, for spatial context see Figure 3. a) LAMO clear filter data, b) HAMO RGB composite (R= 965/917 [nm], G=750 nm and B=750/917 [nm]), c) DTM (50% transparency) over LAMO clear filter data, d) VIR 2.8 µm band depth map from Combe et al. (2015). Straight red lines in b) indicate artefacts from the mosaicking process.

While it is likely that at least E2a originates from Calpurnia, I will refer to all PIDs in this area as one large occurrence. As all of the ejecta units appear well-preserved, a large age difference between different PIDs and therefore different preservation states can be excluded. Modeled ages from crater-counting methods could not show definite age differences between these different ejecta units (Williams et al., 2014b, Appendix A), though model age determination shows an increased uncertainty for 'young' ejecta blankets (e.g., Williams et al., 2018). It might also be plausible that the Calpurnia and Marcia impactors once built a binary object with different compositions, impacting on Vesta nearly simultaneously with the Calpurnia impactor hitting just before the Marcia impactor. This could also explain the mobility of E2a, slumping into Marcia crater after its final formation as well as the 'intermediate' ejecta unit E2b. While the distinction of ejecta units is important for the observations presented here, the determination of the parent crater of PIDs in the broad Marcia region is not a key element in this work and independent from my findings. This is why I will only address this marginally.

## 3.5 Pitted impact deposits

Prior to this work, pitted impact deposits were already described on Mars, Vesta and Ceres as pitted materials or pitted terrains. In this section, I will summarize the scientific knowledge prior to this work, which is partly taken from Michalik et al. (2021).

### 3.5.1 Mars

Pitted materials have firstly been described on Mars. Figure 3.13 shows pitted materials on the floor of Zumba crater (A) and individual pits on the floor of Mojave crater (B). The pits making up the pitted materials are often polygonal shaped and share their boundaries within a cluster of pits similar to a soap froth pattern (Boyce et al., 2012). The parent craters of pitted materials on Mars show a range of ejecta types and are among the most well- and best-preserved craters on Mars, indicating that pitted materials can be obscured over geological time scales (Tornabene et al., 2012). On Mars, pits are relatively shallow and show none or subtly raised rims. They do not show ejecta materials but often a cover of dust and other wind-blown materials. At some locations, outcropping meter- to decameter-sized rock fragments (Fig. 3.13B) can be observed in pit walls.

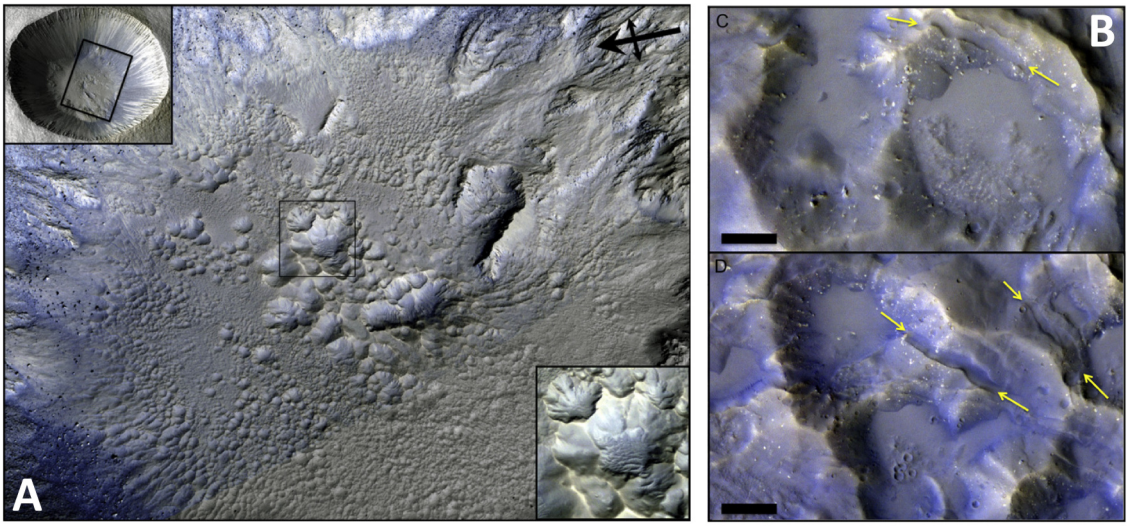


Figure 3.13: A: Fig. 1 from Tornabene et al. (2012). Pitted materials on the floor of Zumba crater in Daedalia Planum. The pitted crater-fill deposit is about 1.1 km in diameter and aeolian bedforms are present on the floor of pits. B: Fig. 4, C and D from Tornabene et al. (2012). Individual pits within a larger cluster on the floor of Mojave crater. The black scale bar is approximately 60 m in the upper image and 70 m in the lower image. Fine-grained materials partly cover the pit floors and light-toned fragments or blocks crop out of pit walls.

The Martian pitted materials have been recognized as primary impact deposits earlier by Tornabene et al. (2007), yet it was the extensive survey of more than 200 craters by Tornabene et al. (2012) that confirmed the primary impact-related nature of these geomorphologic features with the pits representing volatiles escaping from a non-ambient and possibly melt-rich deposit. This and the study by Boyce et al. (2012) revealed more insights in the formation mechanism, the relationship to the host deposit and parent crater, age, as well as global distribution and abundance.

They found that these pitted materials occur preferentially in mid-latitudes suggesting a dependence on the water/ice-silicate ratio as volatile content increases with latitude on Mars. Furthermore, pit size as well as cluster extent positively correlate with parent crater size as do preservation states of pitted materials and their parent craters. Additionally, similarities to the impact melt-bearing breccia suevite at the Ries impact structure in Germany were concluded as both target materials are/were volatile-rich (e.g., Boyce et al., 2012; Newsom et al., 1986; Tornabene et al., 2007, 2012). Tornabene et al. (2012) inferred that the pitted materials on Mars and their host deposits most likely resemble impact melt-bearing breccias. Within the suevite outside of the Ries

crater, 'chimney-like degassing pipes' were identified (e.g., Engelhardt, 1972; Newsom et al., 1986) which suggests devolatilization after suevite deposition. The pitted materials on Mars could thus result from the formation of similar vents through the host deposit.

Boyce et al. (2012) find that degassing of Martian pitted materials occurred in a more explosive manner than on Earth, mostly due to the different gravity regimes and atmospheric pressure. These differences lead to higher escape velocities of the steam coming from those deposits. To that effect, an increased flow speed of the steam and entrained clasts lead to a quicker abrasive erosion of the degassing pipes and the widening of these pipes towards the surface, which then forms the pits we see today (Boyce et al., 2012). For Mars, Boyce et al. (2012) estimate a terminated supply of volatiles/gas within ~ 2 weeks to 3 months, depending on the materials' volatile content. They also expect a mantle of fine-grained material to form on top of and near the pitted materials, which is confirmed by Tornabene et al. (2012) who show examples of dunes on the floor of individual pits. The considerations about the PID formation on Vesta of both Denevi et al. (2012) and Michalik et al. (2021) (this work) are based on the work analyzing Martian PIDs presented by Tornabene et al. (2012) and Boyce et al. (2012).

### 3.5.2 Vesta

Denevi et al. (2012) were the first and only to study the pitted impact deposits (or 'pitted terrains' in Denevi et al., 2012) on Vesta which at that time have not yet been observed on other airless bodies. They described the locations, spatial distribution and, to some extent, the geomorphologic setting of PIDs. They reported the Vestan PIDs to lack raised rims and range in size from the resolution limit (~30 m) to roughly 1 km. Pits often coalesce and overlap, leading to polygonal boundaries between pits. The observed PIDs occur where ejecta fills topographic lows, on smooth deposits within crater-fill deposits, atop the southern terrace of Marcia and in the continuous ejecta blanket of Marcia. On the ejecta blanket and on the southern terrace of Marcia, individual pits are on average smaller than in the crater-fill deposit, which will be shown in more detail in this work, as well. Pits can be buried by slumped material but can also occur in slumped material as seen within Marcia and Cornelia craters.

Where the crater-fill deposits of Marcia are probably thickest, pits increase in size (Denevi et al., 2012) and evidence for subsidence of some parts of the deposits were also found. Denevi et al. (2012) partially also report on the spectral characteristics of the crater-fill PIDs in Marcia as well as Cornelia and report them to be 6 to 13% lower in reflectance at 750 nm than average values for Vesta. For Marcia, this was also stated by De Sanctis et al. (2015c). Pyroxene absorption bands appear to be 4 to 9% shallower than the average Vestan values in Denevi et al. (2012)'s analysis.

As there is no observable spatial alignment and due to the distinct morphology, Denevi et al. (2012) infer that the PIDs could not form from drainage into the subsurface but, similar to the Martian features, from rapid degassing of volatiles. Moreover, due to the volatile-poor nature of Vesta according to analysis of the HED meteorites and subsequent formation models (e.g., Wilson and Keil, 1996), the volatiles appear to have an exogenic origin. Denevi et al. (2012) suggest carbonaceous chondrites as likely candidates as they can possess up to 9 wt% mineralogically bound water. Thus, carbonaceous chondrites could be present in the regolith of Vesta to significant portions and devolatilize upon impact. Denevi et al. (2012) also suggest that pit size is more correlated with deposit thickness than specific volatile content.

Scully et al. (2015) investigated geomorphological features that might indicate a transient flow of water on Vesta, seen through curvilinear gullies, mostly found on crater walls. For PIDs, they suggest that subsurface ice was stable in the subsurface and lead to the formation of PIDs through devolatilization upon impact.

In this work I present further geomorphologic evidence that support the theory by Denevi et al. (2012) and present detailed analysis of the PIDs' spectral characteristics that might reveal novel processes occurring within Vestan ejecta.

### 3.5.3 Ceres

Sizemore et al. (2017) likewise presented a detailed survey of PIDs on the dwarf planet Ceres' surface. They found that Cerean PIDs (Fig. 3.14) strongly resemble those on Vesta and Mars and accordingly inferred a rapid post-impact formation model. The PIDs' formation models for Ceres is likewise based on the extensive analysis from Tornabene et al. (2012) and Boyce et al. (2012) for Mars. However, for the intriguing crater Occator on Ceres (largest well-preserved crater showing 'bright' spots), Schenk et al. (2020) found that volatile-related pits are in general less common and distinct from the densely clustered pits observed on Mars. Similar to the lack of pitted materials in high latitudes on Mars (Tornabene et al., 2012), this might result from (too) high volatile contents in the crust (up to ~60 % ice and clathrates, Ermakov et al., 2017; Fu et al., 2017). Sizemore et al. (2017) linked Cerean pit formation to available volatiles in the regolith whose source could both be minerals and ice (see also e.g., Combe et al., 2016; De Sanctis et al., 2015a). As previously mentioned, this is still under debate for Vesta (Denevi et al., 2012; Scully et al., 2015) and will be addressed in this work.

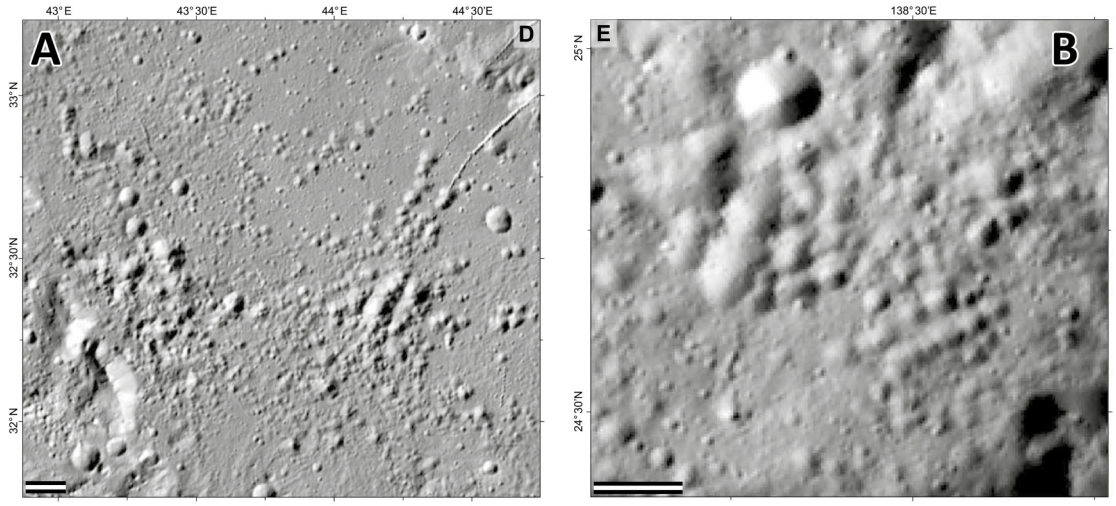


Figure 3.14: A (small D in Sizemore et al., 2017): 'Pitted terrain' in Ikapati crater. B (small E in Sizemore et al., 2017): 'Pitted terrain' in Dantu crater. Images taken from Sizemore et al. (2017), Fig. 3. Scale bar is 1 km in both images.

# 4 The Pitted Impact Deposits on Vesta

On Vesta, currently only four parent craters are identified to show PIDs (Marcia, Cornelia, Numisia, Licinia; Denevi et al., 2012), of which only two are undoubted occurrences (Marcia and Cornelia). Calpurnia crater adjacent to Marcia could also be the parent crater for some of the PIDs (i.e., PIDs originating from Calpurnia impact deposits), yet in this work I/we consider the PIDs in this area as belonging to Marcia, which will be addressed in more detail later on. If Calpurnia likewise is the parent crater for some PIDs, five craters on Vesta could be PID parent craters.

In the following, I will report on the occurrences of PIDs on Vesta with a strong emphasis on Marcia-associated PIDs, which were presented in Michalik et al. (2021). Details on Cornelia, Licinia and Numisia craters are not presented there but in the following subsections.

A PID on Vesta is generally defined as a cluster of irregularly shaped, rimless depressions, at times also overlapping with other pits (Denevi et al., 2012). Denevi et al. (2012) concluded that the PIDs formed, similarly as on Mars, through explosive volatile outgassing. They suggest that volatile-bearing deposits like those from carbonaceous chondrites have been emplaced in the subsurface by pre-Marcia exogenic impactors und subsequently led to the formation of PIDs upon impact of the Marcia impactor. Scully et al. (2015) suggest that icy subsurface deposits could also be responsible for the formation of PIDs. It is the main objective of this work to put further constraints on the volatiles involved in the formation of PIDs and to elucidate why they formed in the first place, as Vesta was thought to be dry due to the differentiation process. A crucial tool to investigate this is the analysis of the geological setting. While Denevi et al. (2012) report that PIDs often occur in topographic lows, a detailed analysis of the local geological setting of the PIDs on Vesta has not yet been undertaken.

PIDs occurring in Marcia's ejecta blanket exhibit higher reflectance and pyroxene band strength than their immediate surrounding. This will be shown in detail in section 4.6. However, not all PIDs show these spectral properties, especially those within crater-fill material of parent craters. In the following, I will first present details on the PIDs present in the smaller parent craters Cornelia, Licinia and Numisia followed by the main body of work which covers the Marcia-associated PIDs which is taken from Michalik et al. (2021) and only slightly modified. The published version of Michalik et al. (2021) can be found under the DOI: 10.1016/j.icarus.2021.114633.

## 4.1 Cornelia

Cornelia crater is situated east of Marcia on the Vestalia Terra highlands (see Figure 2.4). It is one of the best-preserved craters on Vesta and features numerous boulders in its crater walls and surrounding as well as very well-preserved outcrops and lobate deposits at its crater walls. Cornelia clearly exhibits dark, OH-rich material at different heights of its crater walls and a prominent PID covering most of its floor (Fig 4.1). The Cornelia crater-fill PID shows different spectral properties than the majority of PIDs associated with Marcia. It does not display elevated reflectance or pyroxene band strength with respect to its surrounding. However, it is characterized by a slightly larger ('redder') visible slope. There are no PIDs in Cornelia's ejecta. Figure 4.1 shows high resolution LAMO images of Cornelia as well as the previously presented RGB composite, 2.8 µm absorption depth distribution map and DTM data. The crater-fill PID is low in reflectance and pyroxene band strength and with respect to the crater walls, exhibits intermediate OH contents. As the direct surrounding of the crater-fill PID has very high OH contents which appear to be deposited on the floor by mass wasting (northern, southern and eastern crater wall), the intermediate 2.8 µm absorption depth values of the PID strongly indicate that OH was lost at this site.

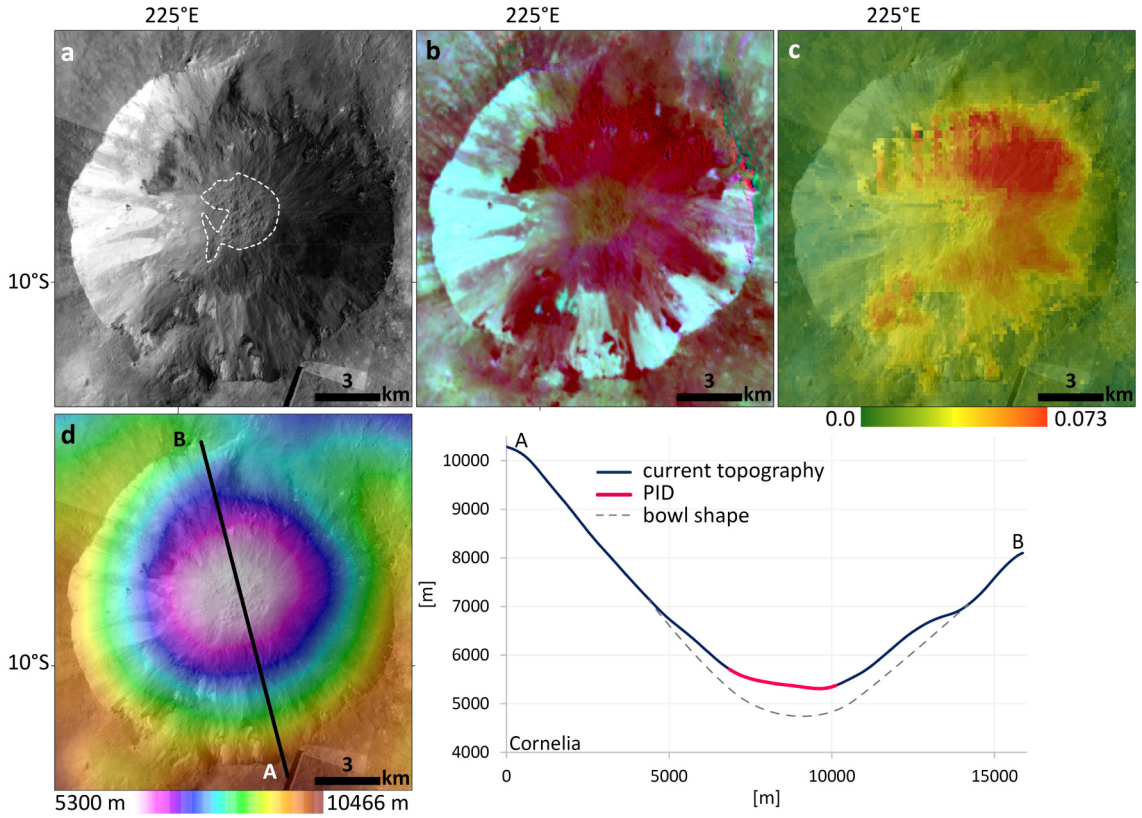


Figure 4.1: Cornelia crater as seen via FC LAMO clear filer (a), RGB color composite (b), 2.8 µm absorption depth distribution map (data from Combe et al., 2015a) and DTM data (d). The profile of Cornelia crater shows that impact deposits cover the crater floor, letting its shape deviate from a typical bowl shape.

## 4.2 Licinia

While Cornelia, Numisia and Marcia are located in a somewhat vicinity, Licinia is located farther away, belonging to a region generally larger in pyroxene band strength and more diogenite-rich (e.g., Reddy et al., 2012b). Nevertheless, relatively high 2.8 µm absorption depth values can be observed at its southeastern crater wall. In contrast to the other smaller parent craters Cornelia and Numisia, Licinia displays smooth crater-fill deposits and multiple PIDs within (Fig. 4.2) as well as a central peak structure. A profile running through two of these deposits and the crater floor indicates voluminous impact deposits.

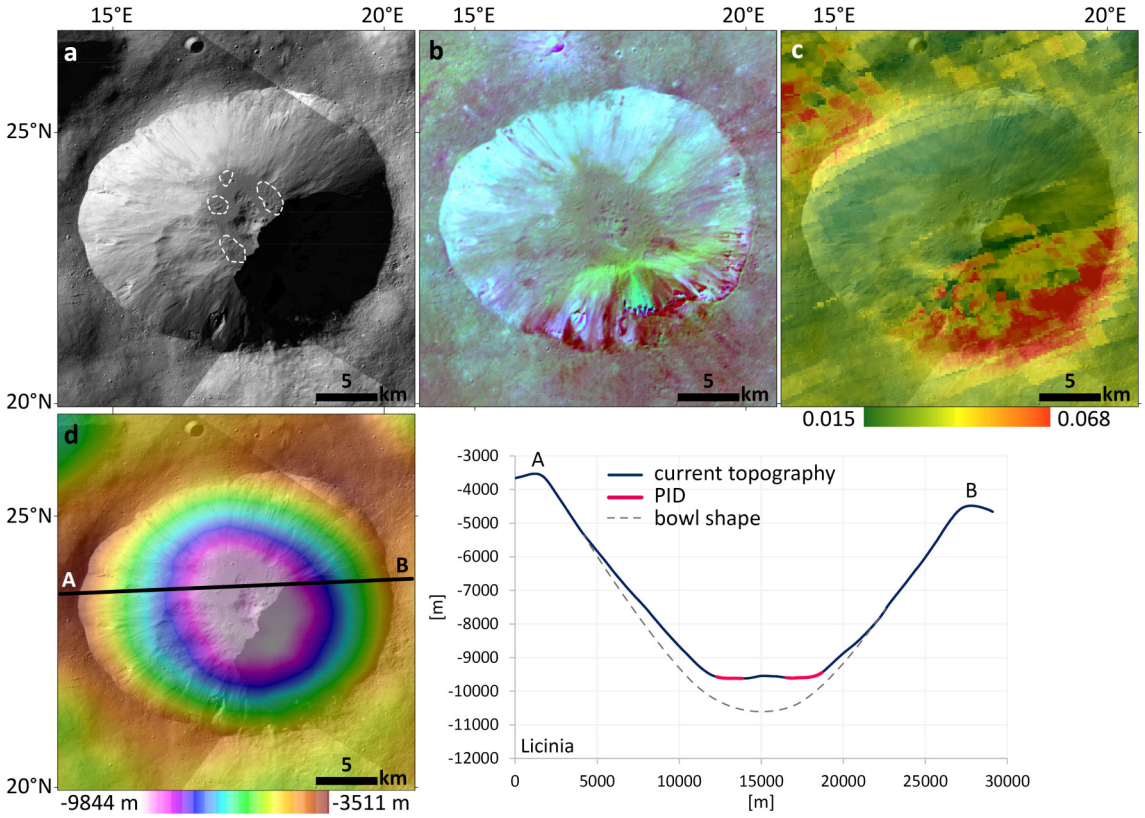


Figure 4.2: Licinia crater as seen via FC LAMO clear filer (a), RGB color composite (b), 2.8 µm absorption depth distribution map (data from Combe et al., 2015a) and DTM data (d). The profile of Licinia crater shows that large impact deposits cover the crater floor, letting its shape deviate from a typical bowl shape. The bright green area in the southeastern area of b) is an artifact due to shadowing, which probably also affects the VIR data (c).

## 4.3 Numisia

Numisia crater is located just east of Cornelia (see Fig. 2.4) and displays dark and OH-rich material mostly in its northern crater walls. At its southern rim, a tiny crater appears to have released dark material into its ejecta. The PID within Numisia can only tentatively made out (see also Denevi et al., 2012) and I doubt its occurrence is associated with the other occurrences. This potential PID is the smallest of all observed within the crater-fill deposits of parent craters and individual pits can hardly be made out. Nevertheless, a profile going through Numisia likewise shows a deviation from a typical bowl shape, indicating possibly volatile-bearing impact deposits. The location of the possibly PID within the deposit (red part of profile) is typical for PIDs ( relatively flat, near the center of the deposit, see section 4.5) and indicates that it might be real.

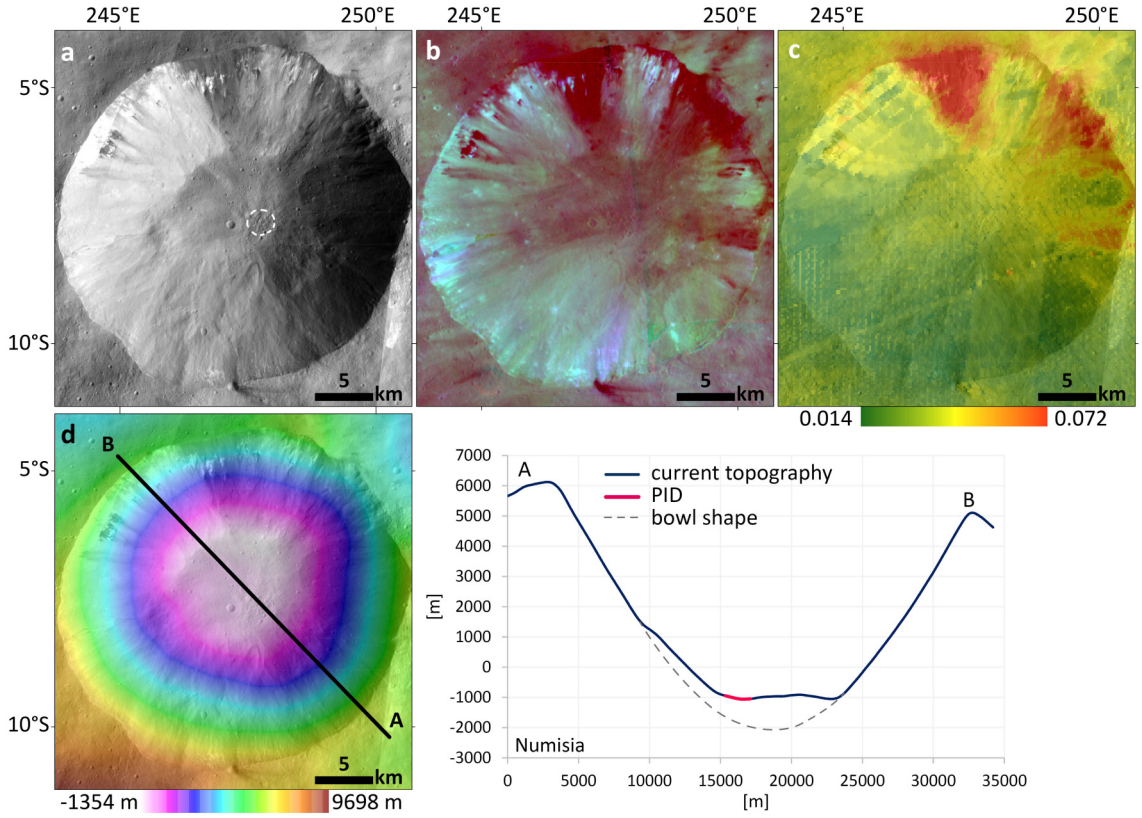


Figure 4.3: Numisia crater as seen via FC LAMO clear filer (a), RGB color composite (b), 2.8 µm absorption depth distribution map (data from Combe et al., 2015a) and DTM data (d). The profile of Numisia crater shows that impact deposits possibly cover the crater floor, letting its shape deviate from a typical bowl shape.

## 4.4 Marcia and its surrounding

Marcia is ~58 km wide and 68 km long and possesses a relatively large wall-slump or terrace off the southern rim (Fig. 4.4) . Calpurnia and Minucia are two adjacent craters to the NE (Fig. 3.10a). Marcia and its surroundings exhibit numerous PIDs (we count >100). The occurrences associated with Marcia crater (Fig. 4.4) account for ~96% of all PIDs on the asteroid (this study). The crater is situated within the already mentioned spectrally darker extended area (De Sanctis et al., 2013, 2012b, 2015c, Combe et al., 2015a) at around 190° E and 10° N (Claudia Coordinate system) and is the best-preserved large crater on Vesta. While the Rheasilvia Basin covering the South Pole is thought to be around 1 or 3.5 Ga old (modelling ages by Marchi et al., 2012 and Schmedemann et al., 2014, respectively), Marcia is the next largest well-preserved crater and considerably younger with modeled ages of ~40 to 390 Ma (Williams et al., 2014b). Marcia has been of high interest to many studies (e.g., Williams et al., 2014a,c; De Sanctis et al., 2015b,c; Denevi et al., 2012; Scully et al., 2015; Keihm et al., 2015) due to its unusual and asymmetric shape, reflectance spectra, thermal properties and geomorphologic features including PIDs as well as gully-like features. Marcia is also the focus of this work due to the remarkable preponderance of PIDs situated in and around this crater. The following sections mostly analyze the Marcia-associated PIDs.

Figure 4.4 displays the mapped PIDs of this work and indicates craters that existed prior to Marcia and now host PIDs in blue circles. In total, we mapped 120 individual PIDs. Some PIDs might be part of a bigger cluster or could be subdivided into smaller units as identification of boundaries is limited due to the given image resolution. 43 of the 120 PIDs mapped are located in E1, 21 in E2a and 39 in E2b. The remaining PIDs are situated within the crater.

We identified 13 pre-existing craters that host one or more PIDs (excluding the large craters

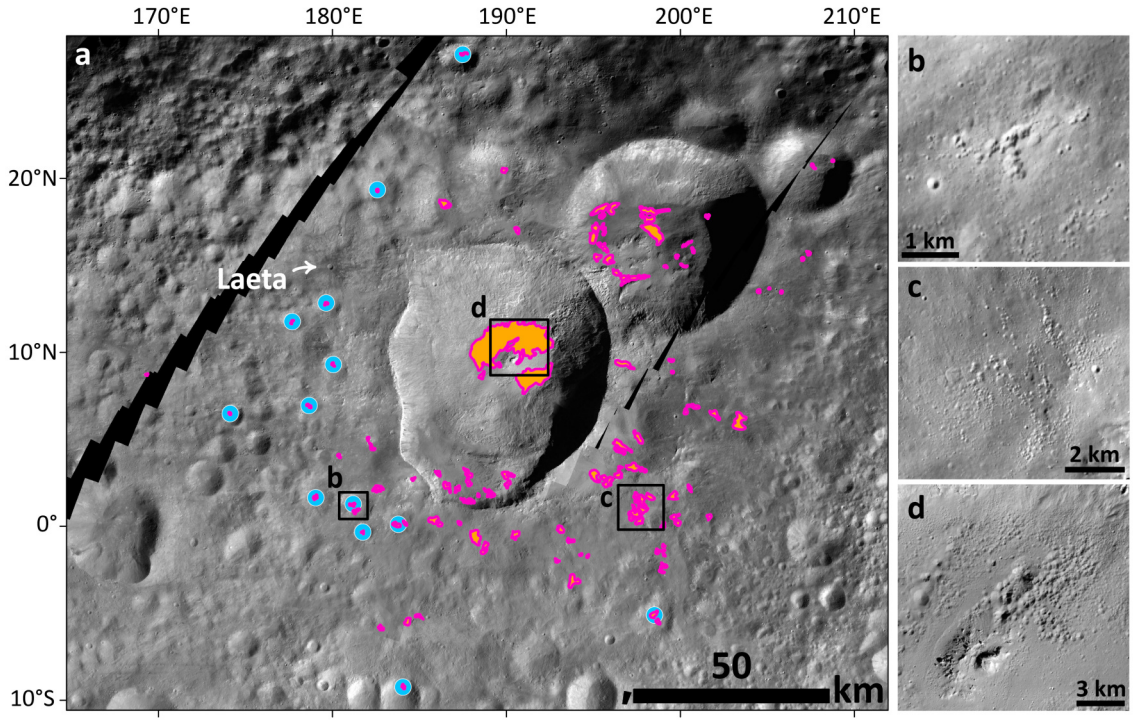


Figure 4.4: A) Distribution map of PIDs (in total 119 individual terrains) associated with Marcia ejecta (LAMO clear filter). Blue dots denote small craters housing PIDs which will be described in section 4.5. b), c) and d) examples of PIDs. b) is situated within E1, c) is situated within E2b and d) is part of the crater-fill PIDs.

Calpurnia and Minucia). Nine of those craters are situated in E1 and four of these craters in E2b. More details will be discussed and shown in section 4.5. Figure 4.4b, c and d display high-resolution examples of PIDs whereas 4.4b is situated in E1, 4.4c in E2b and 4.4d is part of the crater-fill PIDs. We refer the term 'crater-fill' only to the PIDs around Marcia's central peak and not to PIDs on the mentioned southern terrace of Marcia (see Fig. 4.4 for spatial context) as this material most likely represents material thrown out of the transient cavity during crater formation before the crater wall collapsed. Figure 4.5 serves as spatial orientation for close-up images presented in the following sections.

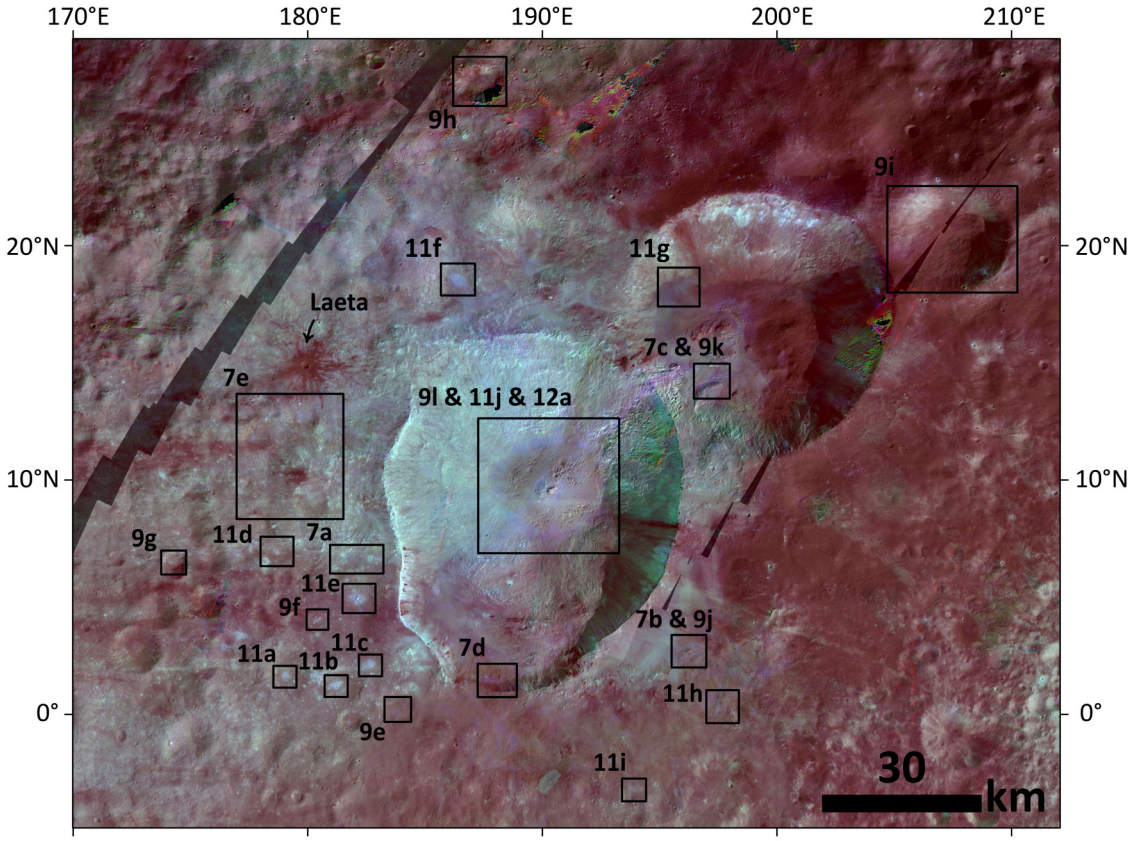


Figure 4.5: Spatial context of locations presented throughout this study. Clear filter LAMO data overlain by the new HAMO RGB composite (R= 965/917 [nm], G=750 nm and B=750/917 [nm], 50% transparency). This Figure was adopted from Michalik et al. (2021). The corresponding Figure numbers are shown in Table 4.1.

Table 4.1: Corresponding Figures to the ones depicted in Figure 4.5 of Michalik et al. (2021).

| Fig. number in Fig. 4.5 | Corresp. Fig. number in this dissertation |
|---|---|
| 7 | 4.6 |
| 9 | 4.8 |
| 11 | 4.10 |
| 12 | 4.11 |

## 4.5 Geomorphology

Identifying a PID on the basis of its visual appearance is not trivial as a range of possible morphologies indicating volatile loss can be observed within the ejecta blanket of Marcia. PIDs have been defined as clusters of individual, irregular shaped, rimless pits (Tornabene et al., 2012; Denevi et al., 2012). However, already the identification of a cluster of pits is challenging on Vesta. Figure 4.6 displays an example of 'possible' PIDs. The pits are not densely clustered but rather individually located in each other's vicinity and could therefore also represent secondary cratering or later impacts. Limited image resolution prevents an analysis of single pit and potential ejecta morphology. A secondary impact origin (i.e., post-Marcia) can therefore not be excluded for these pits although they appear to only occur in smooth deposits as do the PIDs.

Moreover, their spectral characteristics are also consistent with PIDs (i.e., cyan colors in the

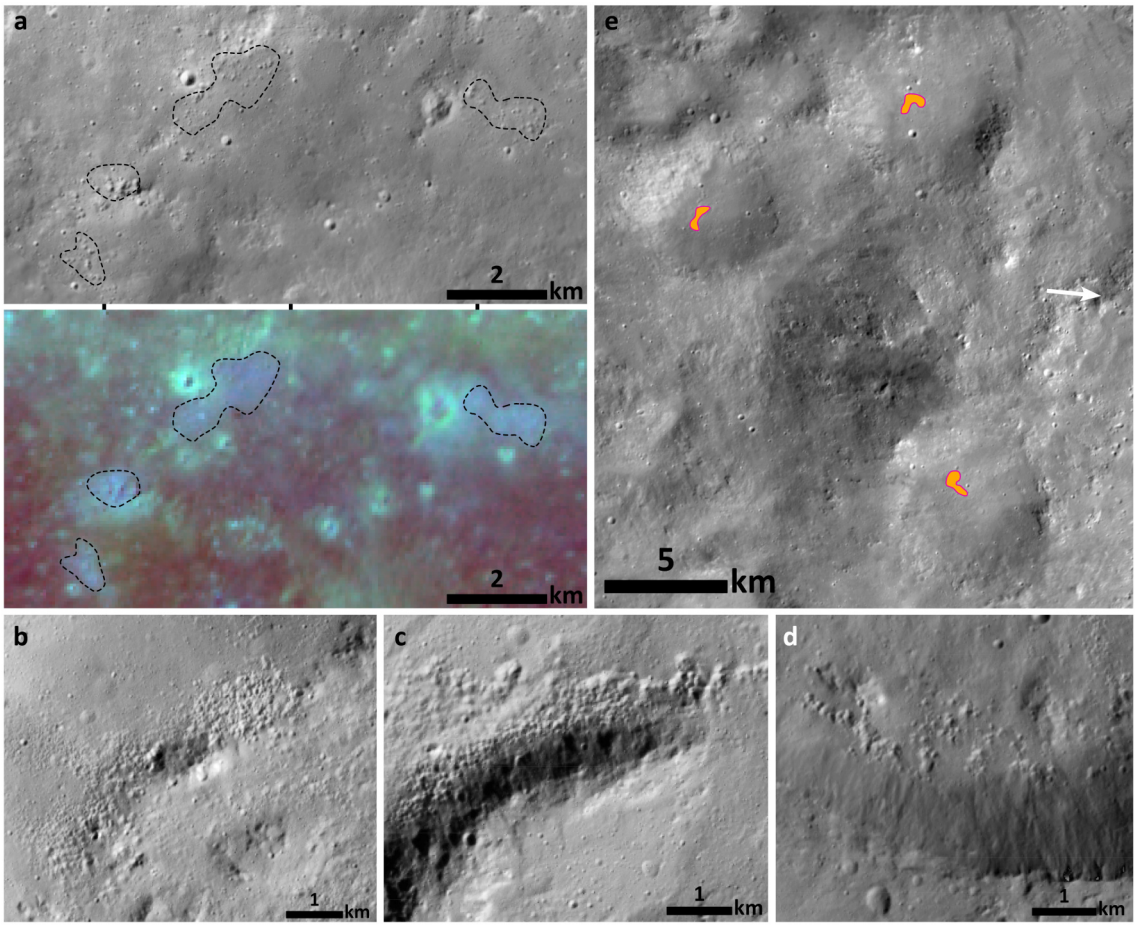


Figure 4.6: a) 'Possible' PIDs (dashed lines) with a lack of obvious clustering and distinct pit morphology but showing the characteristic spectral properties of PIDs (upper panel: clear filter LAMO image, lower panel: HAMO RGB composite). b), c) & d): Examples of PIDs that exist adjacent to a topographic high. e) Example of three PIDs west of Marcia which are situated in craters (yet do not exhibit a detectable positive topography); colored polygons indicate PID (as in Fig. 4.4). For spatial context of a)-e) see Fig. 4.5.

presented RGB composite, Fig. 4.6, lower panel; more details on the spectral characteristics in the following section 4.6). Those 'possible' PIDs can be observed especially within E1 and their presence indicates a more widespread and pervasive devolatilization process than previously suspected. We did not include the particular feature from Figure 4.6 into my counts but several others not mapped in Denevi et al., 2012. The identification of a cluster of pits is biased and strongly depends on the individual mapping the feature. Several 'possible' PIDs were not included due to identification uncertainty.

Excluding the crater-fill PIDs around Marcia's central peak, PIDs have an average areal extent of a few square km (1.9 $km^2$) and roughly range from less than 10 to more than 80 individual pits per cluster. As individual pits often reach the resolution limit, We point out that counting of individual pits and measuring pit diameters occurred for representative clusters only. The diameter of individual pits ranges from less than 50 m (resolution limit) to more than 500 m with the largest ones occurring within Marcia's crater-fill deposits. The average pit size within ejecta PIDs is 120 m while it is 290 m for PIDs within the crater-fill deposit. This is consistent with what has been observed for Martian PIDs (i.e., pits are largest in crater-fill deposits; Tornabene et al., 2012). An increase in pit size of PIDs on Marcia's southern terrace with respect to those within the ejecta was not observed. Numerous PIDs show many 'possible' smaller pits (i.e., dark individual pixels as possible pit wall shadows), which cannot be identified with confidence due to the limited image

resolution. A dependence of PID size vs. parent crater diameter seen on Mars (Tornabene et al., 2012) is hardly derivable for Vesta as the number of parent craters is very low, yet we report crater diameter vs. the largest pit within the crater-fill deposit for the four parent craters reported in Denevi et al. (2012) in Table 4.2. We note that the value given for the largest pit and PID area in Numisia is fragile because it is hard to make out any individual pits. It is furtermore notable that among the three smaller craters Numisia, Licinia and Cornelia, the area covered by PIDs is increasing with decreasing crater size.

Table 4.2: Crater diameter and largest devolatilization pit diameter for the four described parent craters.

| Crater | Crater diameter [km] | Largest pit diameter [m] | Area of PID(s) [km$^2$] |
|---|---|---|---|
| Marcia | 63 | 1300 | ~180 |
| Numisia | 30 | 590 | 3.57 |
| Licinia | 22 | 400 | 6.40 |
| Cornelia | 15 | 280 | 7.98 |

The depth of the individual pits can also not be resolved by the existing data, yet an assumption of depth by considering shadows and incidence angles gives a rough average depth of 25-50% of the pit diameter, though smaller and higher values are observable as well (e.g., Fig. 4.10h shows relatively shallow pits). PIDs appear to be flatter in E2a and E2b. These values are higher than what Tornabene et al. (2012) found for Martian PIDs (pit depth ~0.1 pit diameters). Boyce et al. (2012) present a rapid formation model for the PIDs where steam release is expended in days to weeks after deposition, strongly depending on the volatile content and energetics of the degassing process. Lower volatile contents within the hot ejecta deposits of the Marcia impact would be exhausted earlier. This could produce steeper pits as the vents on the top progressively widen with time (Boyce et al., 2012). A lower gravitational acceleration can also increase the steam escape rates (Boyce et al., 2012) which could favor the formation of steeper pits. However, Sizemore et al. (2017) applied the Boyce et al. (2012) model for Cerean pits and found that they are broadly comparable on Ceres and Mars.

The shape of individual pits within a PID appears more cone-like and less bowl-shaped as for nearby small craters which is helping the identification (as can be observed in e.g., Fig. 4.4a & b, Fig. 4.11). Assuming a conical shape for the pits and a depth of the respective pit radius (upper limit), we calculated volumes (Table 4.3) of the now lost volatiles of the PIDs shown in Figure 4.10, divided into the crater-fill PIDs around the central peak and all other PIDs (incl. PIDs on the southern terrace of Marcia). The calculations assume that the voids within the pits equal the volume of volatiles released which is a rough simplification. The given volumes are therefore upper limits as other materials might also have been extracted during this process (Boyce et al., 2012) and are part of the volume now lost. We measured only the largest pits within a cluster as smaller pits are close to the resolution limit and do not contribute significant amounts to the total volume. We interpolated the values of the representative PIDs shown in Figure 4.10a-i to infer the total amount of volatiles lost for all PIDs (except the crater-fill PIDs).

Table 4.3 summarizes the calculated volumes and shows that a higher volume of volatiles has been released from the crater-fill material than from the ejecta material. The volume per km2-value for the crater-fill PIDs is more than twice the value of the other PIDs which likely results from the difference in pit size and volume of the initial crater-fill impact deposit. If Calpurnia is the source of E2a PIDs, the difference between the volatile volumes of Marcia crater-fill PIDs and external PIDs is even larger. The individual pits measured within the crater-fill material are on average significantly larger than elsewhere (290 m vs. 120 m) and moreover the largest connected crater-fill PID is 145 km2 while the largest PID elsewhere is around 13 km2. This illustrates a significant difference between crater-fill PIDs and elsewhere around (or on the southern terrace of) Marcia crater. In summary, the total volumes of lost volatiles are similar for the PIDs around the central peak and all other PIDs altogether, yet the number of volatiles per km2 and the connected area of

!ht

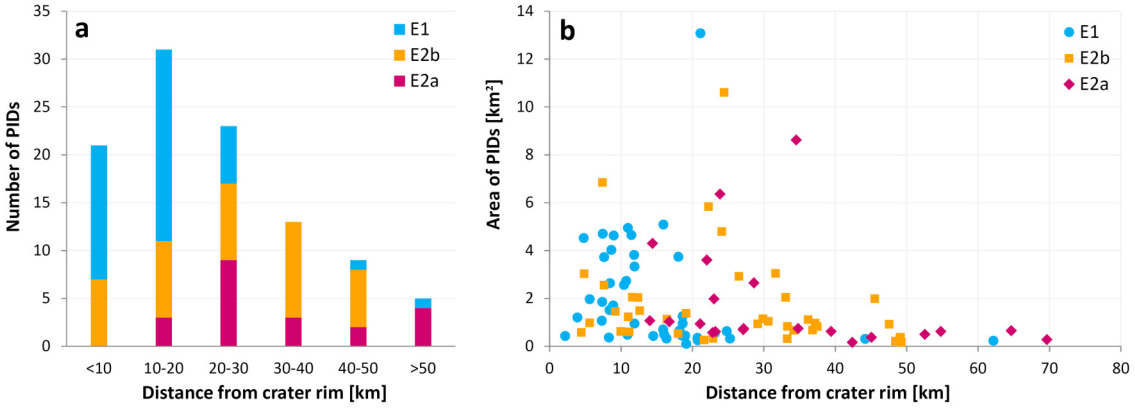


Figure 4.7: a) Distance of PIDs from Marcia crater rim (closest distance) vs. the number of PIDs occurring within the given ranges. b) Distance of PIDs from Marcia crater rim (closest distance) vs. the area spanned by the individual clusters separated into the three different ejecta classes within which they occur (see section 3.4.2).

pitted terrain is larger for the crater-fill PIDs.

Table 4.3: Estimates of lost volatile volumes due to explosive devolatilization.

| | Area [km$^2$] reflectance | Volume [m$^3$] | Volume/km$^2$ band depth |
|---|---|---|---|
| PIDs in Fig. 4.10 | ~29 | ~7*10$^7$ | ~2.3*10$^6$ |
| All PIDs (excl. crater-fill) | ~212 | ~5*10$^8$ | ~2.3*10$^6$ |
| Crater-fill PIDs | ~180 | ~9*10$^8$ | ~5.0*10$^6$ |

The PIDs are not distributed uniformly around the crater. Most clusters are found from the SW to the SE and inside Calpurnia (see Fig. 4.4), but a few also occur in other areas. All of the external PIDs are in proximal distance to the crater rim (i.e., about one crater diameter). Figure 4.7 illustrates the dependency of distance vs. number of PIDs as well as distance vs. area of the PIDs for all PIDs external to Marcia. The farthest PID is located 69 km off the crater rim (within Minucia crater) while about 50% of the PIDs are located within 20 km off the crater rim and 73% are located within 30 km (i.e., one crater radius). On average, PIDs within E1 (blue circles in Fig. 4.7b) are slightly larger than PIDs elsewhere (2.2 km$^2$ vs. 1.8 km$^2$) and are located closer to Marcia than PIDs within E2a (red diamonds) and E2b (orange squares). This might reflect the thinning of the ejecta with distance from Marcia and therefore the decrease in pit size and abundance. This relationship has been observed for Mars as well (Tornabene et al., 2012).

PIDs are less abundant within 10 km off the rim than at 10-20 km (Fig. 4.7a). This could have several reasons. The most likely explanation is that post-impact modification processes (slumping, collapsing) prevail in the closest regions to the rim (e.g., Melosh, 1989) and might have overprinted existing PIDs. Furthermore, the considered area increases with distance, i.e. so that the number of PIDs/km$^2$ is nearly identical for the first two columns (assuming an elliptical shape for Marcia with a = 27 km, b = 34 km) before this value drops significantly for distances >20 km. Lastly, E2a PIDs possibly originate from Calpurnia and therefore do not naturally occur near the rim of Marcia, possibly adding to this slight variation in PID distribution.

Higher numbers of individual pits within a cluster imply a higher local volatile content, assuming that PIDs are related to volatile outgassing (Boyce et al., 2012; Denevi et al., 2012; Tornabene et al., 2012). Individual pits in the clusters do not always overlap and the arrangements of individual pits within the clusters often do not seem to follow any systematics. The clusters exhibit diverse shapes

(circular, circular with a lack of pits in the center, oval, polygonal or as directional 'pit chains', see Fig. 4.10), which illustrates a heterogeneous distribution of the degassing conduits within the host material. The 'soap froth' pattern of PIDs described in Tornabene et al. (2012) and Boyce et al. (2012) is present at multiple PID locations (best-developed within the crater fill-deposits), yet many PIDs do not feature shared rims and this extensive close packing which can be seen in Figure 4.4 and 4.10. This is likely due to the lower availability of volatiles on Vesta with respect to Mars and the concomitant decreased duration of volatile loss. Intervening smooth regions between pits also occur frequently (best illustrated in Fig. 4.10 in section 4.6) which has also been reported for Martian PIDs (Tornabene et al., 2012).

PIDs always occur within 'smooth material' (Denevi et al., 2012; Williams et al., 2014a), which could be impact melt or an impact melt-bearing breccia linked to Marcia ejecta. A connection of pitted material with fluid flow features and smooth melt-bearing impact deposits was also observed for Mars and Ceres (Sizemore et al., 2017; Tornabene et al., 2012). This smooth material is characterized by very few and small impact craters and an even surface appearance within the resolution limits. PIDs are mostly located on slight slopes (~2°-15° with respect to the triaxial ellipsoid, see section 2.1) and with minor exceptions (e.g. in Calpurnia and Minucia craters), these slopes are facing the direction from where Marcia ejecta were excavated (e.g., Figure 4.6e, white arrow indicates the direction towards the Marcia center). These slopes are consistent with the slope range in which Martian PIDs are present (>15°, Tornabene et al., 2012), indicating that the critical slope below which pits can form is independent of the body's gravitation. Within Calpurnia and Minucia, PIDs occur near the margins of the crater-fill deposits, at the lowest elevations and at topographic highs (i.e. crater wall, large blocks).

Furthermore, we found 17 PIDs located within 13 relatively small craters (2-9 km, see Fig. 4.4) that existed prior to the Marcia impact (as seen by smooth rims and ejecta-filled crater interiors, e.g. Figs. 4.6e and 4.10d). In this consideration, we exclude the large craters Calpurnia and Minucia due to possibly misleading statistics and interpretations. These small pre-existing craters occur foremost in E1 (compare Figs. 3.11 and 4.4) and there are no small pre-existing craters hosting PIDs within E2a. Some ambiguous 'craters' hosting a PID were found but not included here. Moreover, we identified several locations where the DTM shows a positive local topography (bulge) linked to the PIDs.

Another important observation is that some PIDs occur near or directly at topographic highs, i.e., the pits are aligned and densest where the deposit is in contact with crater walls and ridges/large blocks. This can be observed, for example, a few kilometers SE of Marcia (Fig. 4.6b), within Calpurnia (Fig. 4.6c) and at the Marcia southern crater wall (Fig. 4.6d). PIDs are clearly aligned along these features, indicating a structural control on the formation of PIDs.

Figure 4.8 illustrates twelve profiles of PIDs where a PID is connected to positive local topography, is identified within a pre-existing small crater or is aligned along a topographic high (9k). The red part of the current topography indicates a pitted surface and the dashed grey line indicates an approximate putative surface profile without overlying ejecta assuming the steepest parts of the slopes/crater walls still display the pre-Marcia-impact topography (simple bowl shape for craters). The 'halo' (yellow part of the current topography) within Marcia is a spectrally distinct part of the crater-fill PIDs and will be described in detail in section 4.6. The halo for all other PIDs represents smooth material exhibiting the distinct spectral characteristics of the adjacent PID, which will also be shown in detail in section 4.6. A PID host deposit thus differs greatly in both spectral (i.e., 'dark' and 'bright') and geomorphological (pitted and smooth) characteristics. View Figure 4.5 for the spatial context of the profiles and the supplementary material (S3, 11) for the exact location and course of the profiles. S3 also includes an indication of the excavation direction from Marcia; e.g., for profiles a, b, c, e and i Marcia ejecta arrived from the right of the profile and for profiles e, h and j, from the left of the profile.

The occurrence of a PID therefore appears to be linked to accumulation of volatile-bearing ejecta controlled by pre-impact topography. According to the estimated pre-Marcia topography presented here (dashed line), PIDs mainly reside where the host deposit is thickest, yet they can also occur near the margins of the host deposit (e.g., within Minucia, 9i and along topographic highs). We did not observe a correlation of the 13 presented host crater diameters and area or thickness of the

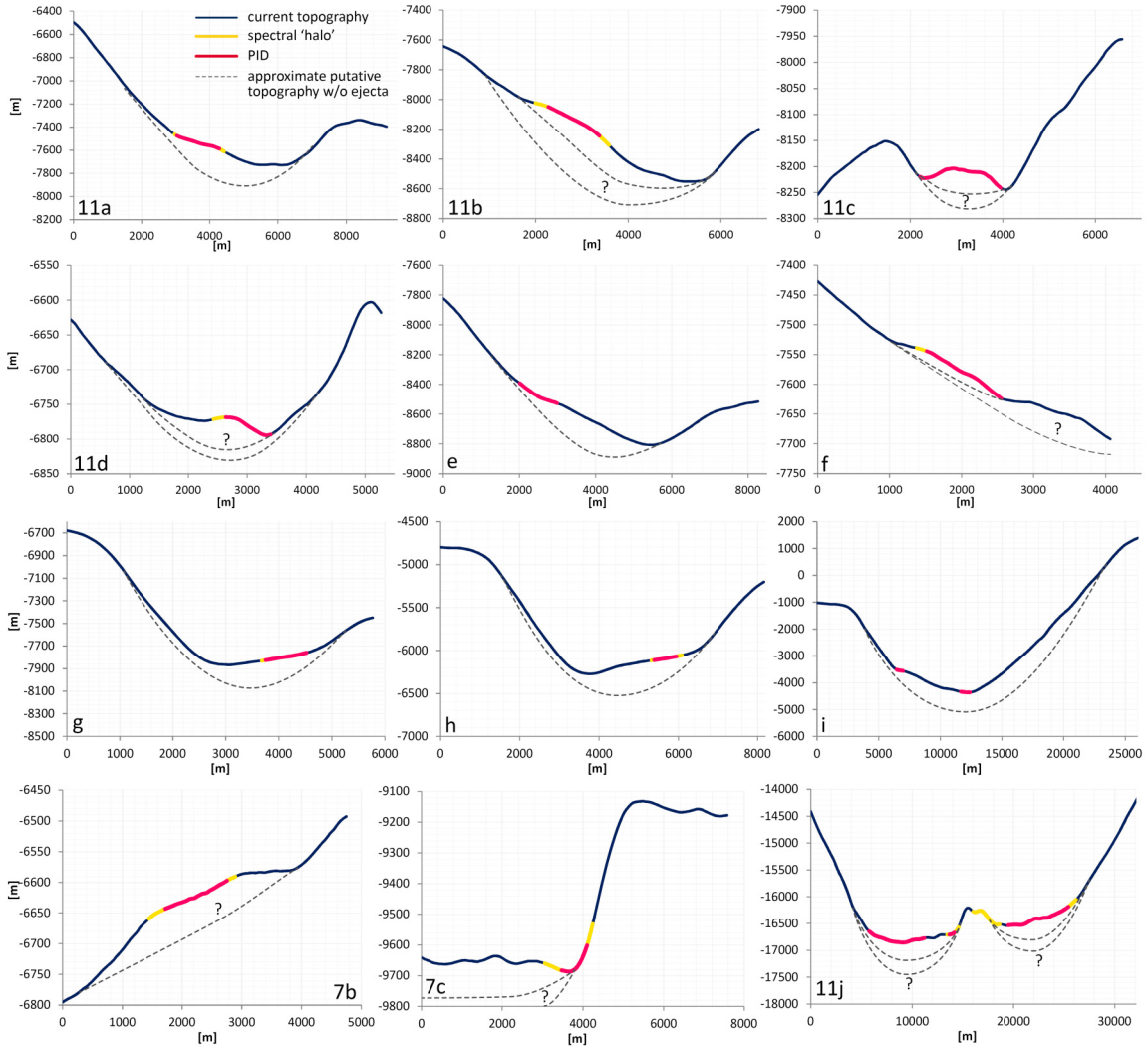


Figure 4.8: DTM-derived profiles: Dark blue line displays the current topography. Dashed line represents the putative topography prior to the emplacement of Marcia ejecta. Red colored part denotes a PID, yellow color denotes the halo around the respective PID and for the Marcia profile (l), also the halo near the central peak not associated with a pitted surface. Spatial context is given in Fig. 4.5 while exact profile locations are displayed in the supplements (S3, 11). No vertical exaggeration applied.

PID deposit. Thus, PID size does not appear to be related to the deposit thickness, possibly as a result of heterogeneous compositions within the ejecta.

For the examples in Figure 4.8, the thickness of the PIDs' material ranges from 20 m to roughly 300 m. In the larger craters Marcia (9l) and Minucia (9i), the thickness of the host deposits might be in the order of ~500 m and are therefore significantly larger than the deposits elsewhere. Furthermore, the profiles clearly illustrate that the PIDs are part of larger impact deposits, whose surfaces are otherwise smooth. This is best illustrated where host deposits of PIDs reside in pre-Marcia-existing craters (9a, b, d, e, g, h, i).

## 4.6 Spectral properties from FC data

Williams et al. (2014a) report a "distinctive color signature" of pitted terrain in FC false color ratio images, which they describe as "gray-brown" in the Clementine-type ratios (Pieters et al., 1994; R= 750/438 [nm], G= 750/917 nm, B= 438/750 [nm]). This statement applies to the large PIDs on Marcia's floor, which were described by Denevi et al. (2012) and De Sanctis et al. (2015c) to exhibit a spectrum darker than the average of Vesta. However, some PIDs outside of Marcia exhibit a significantly higher reflectance and pyroxene band strength than the average of Vesta or Marcia's crater-fill PIDs. Figure 4.9 displays FC spectra of nine sample locations and Vesta's average spectrum. Included is also the spectrum of the crater-fill PID within Cornelia crater, which is slightly darker with a higher visible slope than the crater-fill PIDs of Marcia. Cornelia is a very well-preserved, bright crater SE of Marcia (Fig. 3.11) located on top of the Vestalia Terra highlands that also contains very dark material in its walls and a single PID on its floor (Fig. 4.6, upper right panel). The contrast between the PID on the floor and bright material within Cornelia crater is higher than the contrast between Marcia's crater-fill PIDs and bright material from its rim, possibly due to age differences between the craters. Figure 4.9 illustrates that PIDs exhibit stronger absorptions with respect to locations with similar reflectance levels in the visible region. Most notably is the spectrum of the crater (light orange) right next to the PID SW of Marcia (orange) in comparison with the PID itself and also to the halo of the crater-fill deposit. The spectrum of this crater shows a discernably smaller absorption band than the halo and the nearby PID while showing very similar patterns from 400 to 750 nm. We do not show normalized spectra in order to emphasize the different absolute reflectance values of the sample locations.

All PIDs mapped during this study exhibit higher reflectance and pyroxene band strengths (i.e., cyan in the new RGB composite) than their immediate surrounding except the crater-fill PIDs, which generally exhibit lower reflectance and weaker pyroxene absorptions with respect to their immediate surrounding. The surroundings of PIDs comprise smooth materials from the same ejecta host deposit (e.g., Fig. 4.4b, c & d, Fig. 4.8) which do not exhibit the same spectral characteristics (Fig. 4.10). The majority of PIDs only exhibit minor differences with respect to their surroundings, but they are still distinguishable (e.g., Fig. 4.10g-i). In general, the PIDs exhibit an increase in reflectance of up to ~7% at 750 nm (Figure 4.9). The Marcia crater-fill PIDs are the only ones showing a decrease of reflectance and pyroxene band strength with respect to their immediate surrounding, which will be discussed later on.

External to the crater, there are numerous examples of spectrally distinct PIDs located in different topographic settings distributed in all directions (see Fig. 4.4a). Figure 4.10 displays several examples of the most characteristic PIDs (high 750/917 [nm] and 750 nm values and/or distinct geomorphologic appearance) in clear filter LAMO images (1st panel), topographic setting (2nd panel) and FC false color ratio RGB (3rd panel, R= 965/917 [nm], G=750 nm and B=750/917 [nm]). Reflectance and pyroxene band strength of the PIDs are positively correlated (see also Fig. 4.9 and Table 4.4). The 4th panel in each row of Figure 4.10 displays the absorption band depth at 2.8 µm (i.e., the abundance of OH-bearing minerals) created with VIR data by Combe et al. (2015a) who derived the absorption depth from the reflectance between a calculated continuum above the 2.8 µm absorption and the band center. These maps show a definite local depletion of OH-bearing minerals for six of the external PIDs with respect to their immediate surrounding, indicating the loss of hydroxyl groups upon PID formation. We note that many PIDs show ambiguous OH depletions, likely due to the limited resolution of the VIR instrument (~200 m/px).

The lowest OH abundances of the Marcia area are observed within the Marcia crater and even for the PIDs within the crater-fill material, which generally exhibit a lower average reflectance and pyroxene band strength values as seen in Figs. 3.10, 4.9, 4.10j and Table 4.4. The lower than average reflectance was previously described in Denevi et al. (2012) and De Sanctis et al. (2015c). This is a contrary observation to all other PIDs, where lower 2.8 µm band depth values are linked to higher reflectance and stronger pyroxene absorptions (i.e., bright = OH-depleted). External PIDs with similar reflectance and pyroxene band strength values as the crater-fill PIDs (e.g., Fig. 4.10h) show higher 2.8 µm band depth values as well as darker and more featureless immediate surroundings than the PIDs within the crater-fill material. We therefore emphasize here that the crater-fill PIDs are different to all other PIDs.

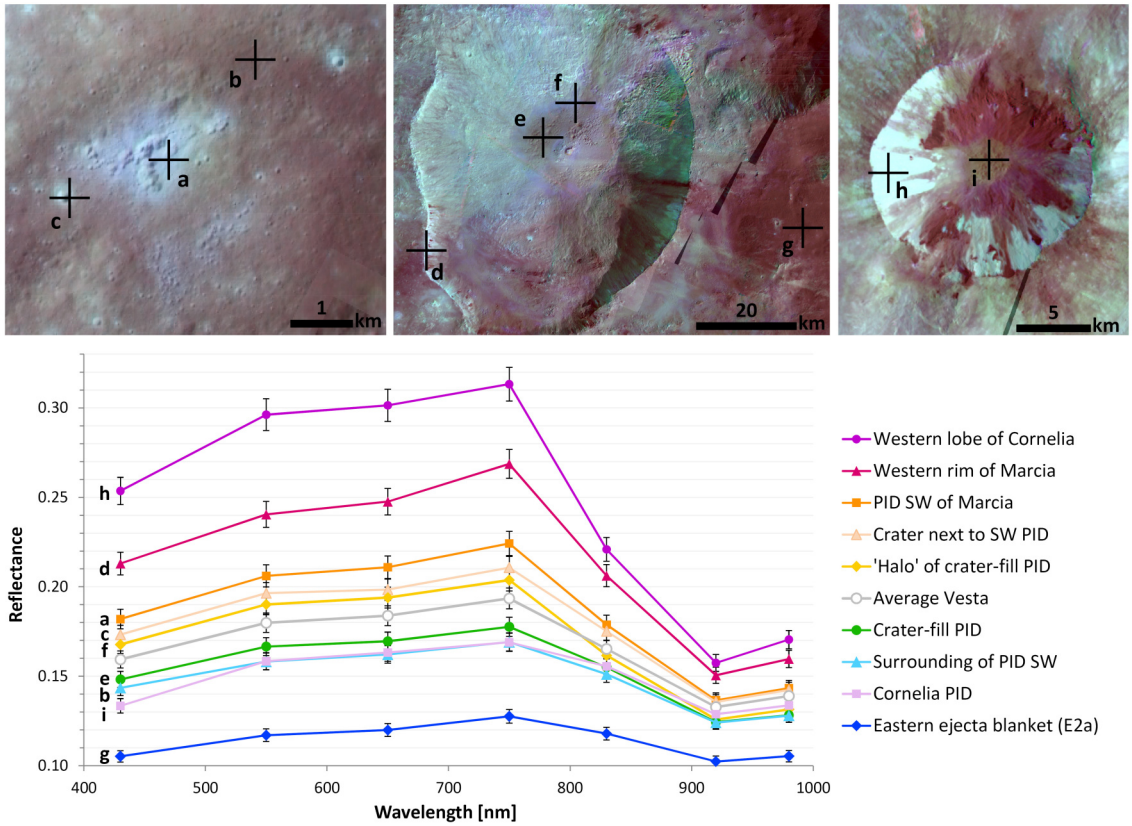


Figure 4.9: Upper panel: Spatial context for spectra displayed in lower panel. Lower panel: FC spectra of different regions of interest on Vesta (mostly Marcia-related but for comparison, the Cornelia PID and a bright slope deposit inside Cornelia are shown). Note that reflectance and pyroxene band strength are positively correlated. The vertical error displays 1σfor the Vestan FC data according to the approximate calibration uncertainty after Schröder et al. (2014). Here, an uncertainty of 3% was assumed. The uncertainty is mostly caused by the stray light removal, which varies from image to image and from filter to filter (e.g. Schröder et al., 2014). For spatial context of the upper left two panels, see Fig. 4.4a and b and for Cornelia crater Fig. 3.11.

However, the PIDs within the crater-fill material are not exclusively 'darker' and appear to have a spectral 'halo' where they meet and embay the crater wall (Fig. 4.11a, dashed outline and arrows). Especially at the northern and western margins of the crater-fill material areas with higher reflectance and pyroxene band strength are visible (Fig. 4.11b and Table 4.4), consistent with those of external PIDs. These areas comprise significantly smaller pits than the rest of the PID (Fig. 4.11b), and appear smooth where the halo does not show a pitted surface. The northern halo material generally resides on larger slopes (~5° to 15°) than the rest of the crater-fill PIDs towards the central peak (~1° to 6°). The southwestern halo (Fig. 4.11a, arrows) is located at lower elevations and generally smaller slopes than the northern halo (Fig. 4.11a, dashed line) and appears smooth with minor pitting. Small pits down to the resolution limit can be observed in the close-up image in Figure 4.11b. The crater-fill PIDs are therefore not homogenous in terms of their spectral characteristics which makes them unique among the 118 mapped PIDs in and around Marcia. An important observation is moreover that in some parts the described halo is superposed by material input from the crater wall which is best illustrated on the right side of Figure 4.11b. This is also valid for the spectral characteristics as the superposing slumps show lower reflectance and pyroxene band strength (compare with Fig. 4.11a).

Moreover, an area with the same spectral characteristics as the 'halo' is found around the central peak (Fig. 4.11c). The higher reflectance and pyroxene band strength is strongly correlated with a confined area of pitted and smooth terrain showing signs of subsidence along a small topographical

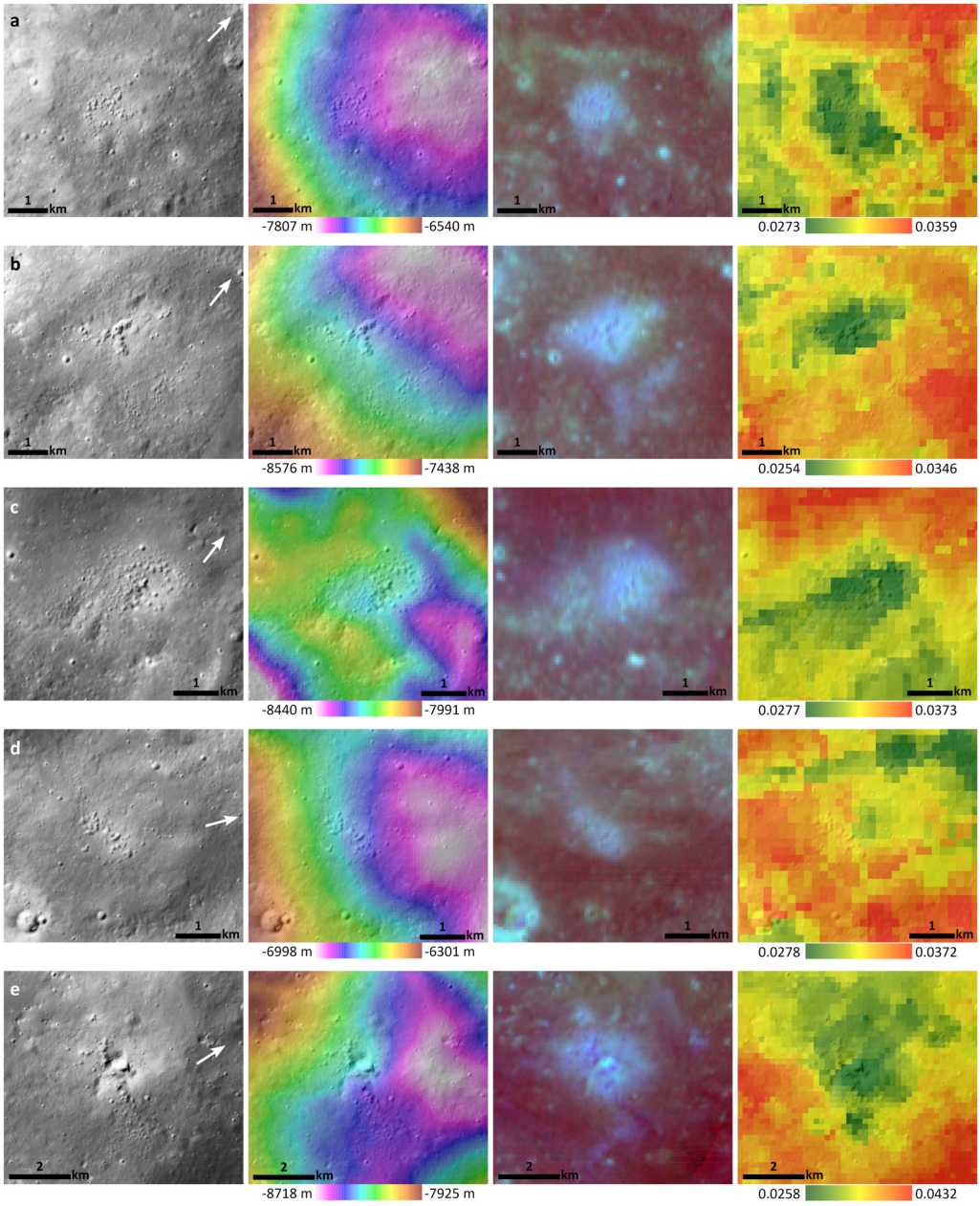


Figure 4.10: Ten examples of PIDs in and around Marcia showing eucrite-like spectral features and in six cases definite local depletions of hydroxyl groups (i.e., decrease of absorption at 2.8 µm). The first panel in each row shows clear filter LAMO data and white arrows indicate the direction to the primary cavity of Marcia. 2nd panel: DTM data (50% transparency over LAMO clear filter data). 3rd panel: HAMO RGB composite (R= 965/917 [nm], G=750 nm and B=750/917 [nm], same stretch in every row), greenish/cyan colors represent higher reflectance and pyroxene band strength. 4th panel: 2.8 µm band depth distribution map from Combe et al. (2015a). Row j shows the central PIDs of the Marcia crater floor. Spatial context is displayed in Fig. 4.5.

scarp (arrows in Fig. 4.11c). Signs of subsidence were already reported for other regions within the crater-fill deposit (Denevi et al., 2012), but these do not show this distinct spectral signature. In the northwestern part, it cannot be determined if the topographic feature is a scarp or a ridge and the DTM does not resolve this topographical difference. The highest reflectance and pyroxene band strength values in this central peak halo are observed for a smooth appearing area WNW of the central peak and for a pitted area ESE of the central peak.

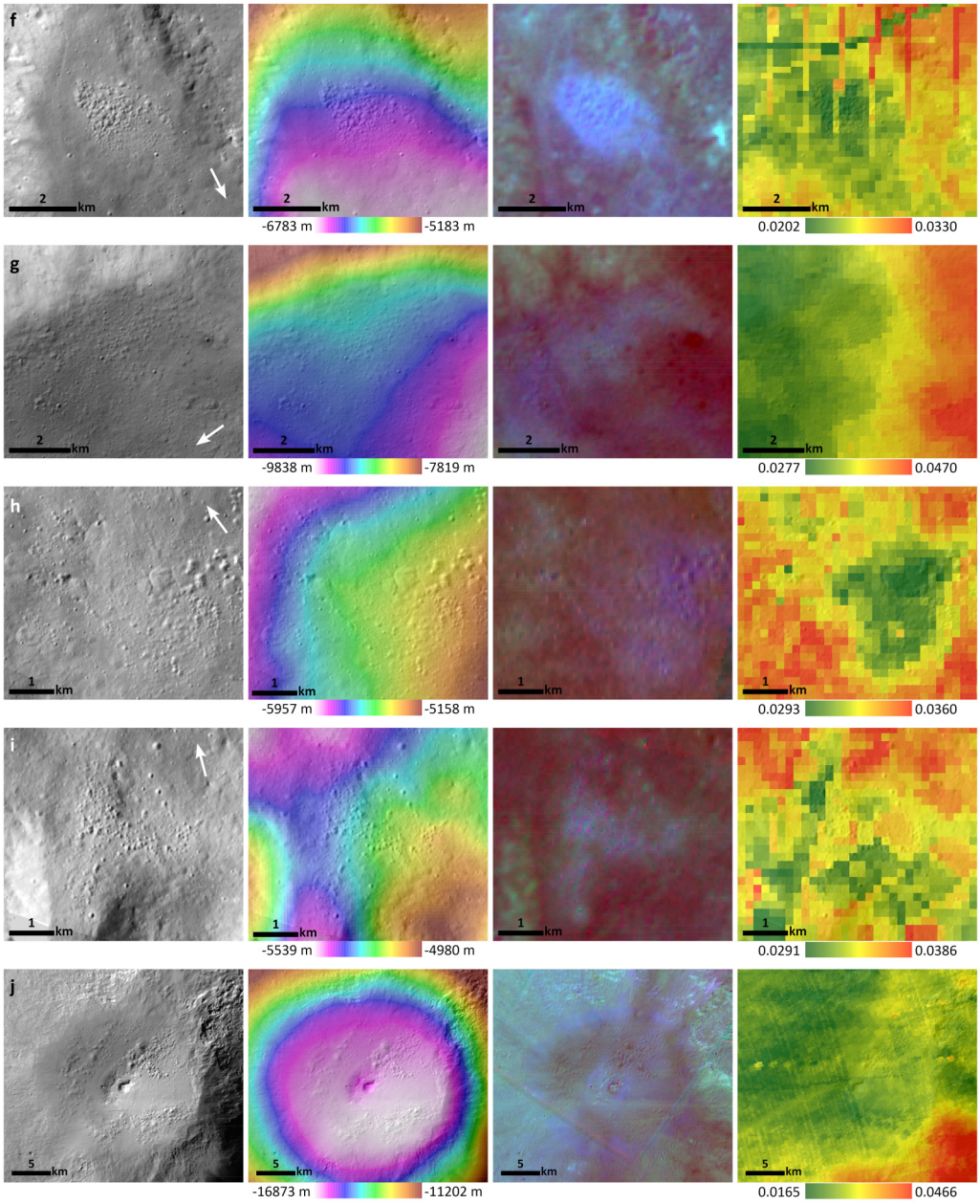


Figure 4.10: continued

Table 4.4 displays the mean reflectance at 750 nm, 750/917 [nm] and 2.8 µm band depth values of Marcia-related regions of interest relevant for this study. Values for 'PIDs' (1st row) include the nine PIDs in Figure 4.10a-i and values of their 'surroundings' (2nd row) include only the surroundings of these nine PIDs. The 3rd row denotes the PIDs surrounding the central peak of Marcia crater, excluding the ones on the southern terrace. 'Halo floor' denotes the outlined area in Fig. 4.11a.

Table 4.4 and Figure 4.10 demonstrate that the PIDs significantly differ from their immediate surroundings, especially considering the 750/917 [nm] values. We note that the values for the whole Vesta reported in Michalik et al. (2021) are only correct in Table 3.1, not in Table 4.4. This is corrected here. In comparison with the PIDs on the crater floor and the whole Vesta, PIDs have a similar mean in reflectance at 750 nm but a higher mean in the 750/917 [nm] values, as does the halo. A more intuitive Figure (4.13) is displayed in section 4.8. PIDs have similar mean reflectance values like the average Vesta as they comprise both brighter and darker PIDs which will also be shown in section 4.8. Additionally, 2.8 µm band depth values show that the PIDs and their

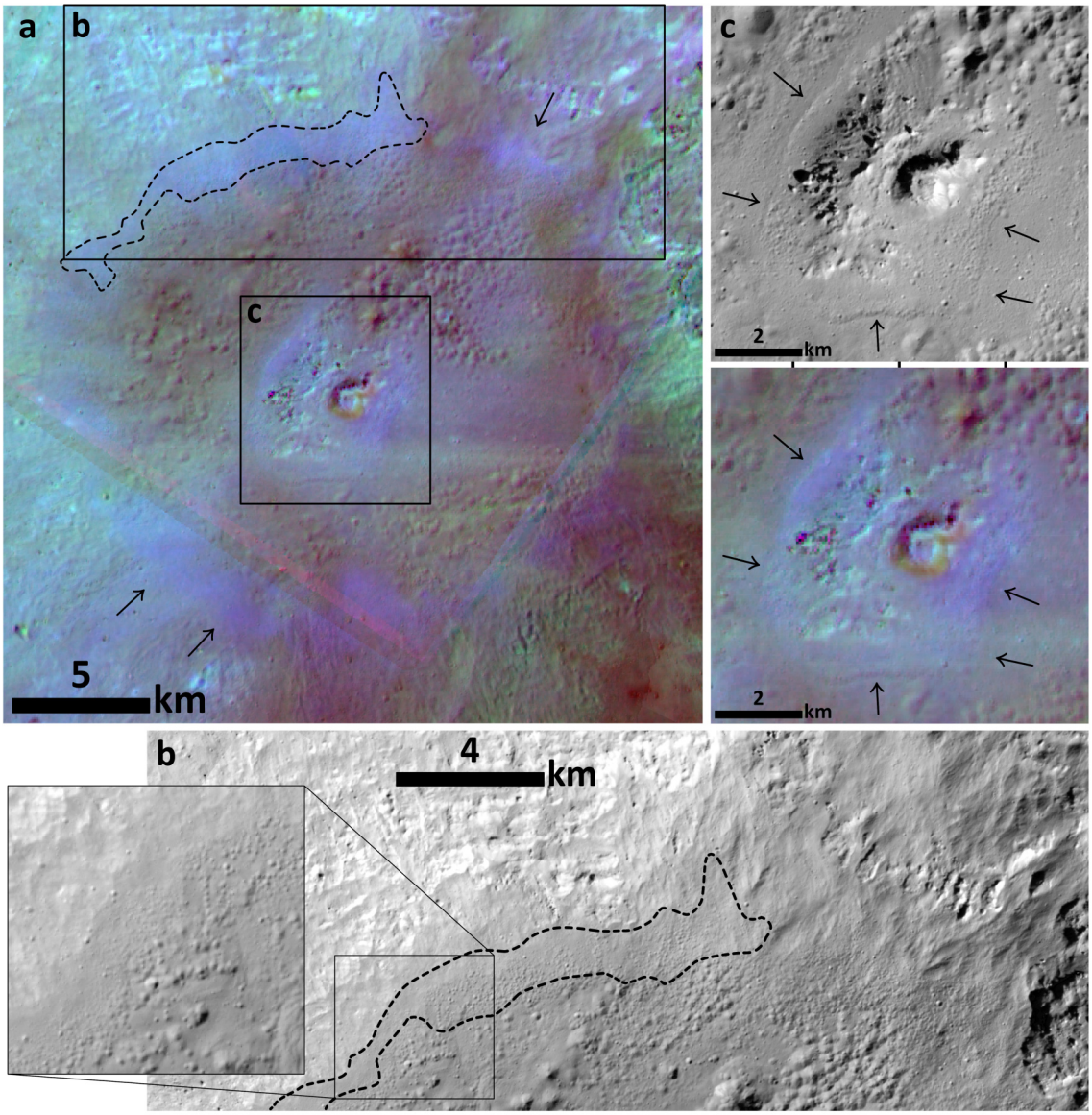


Figure 4.11: a) HAMO RGB composite of the Marcia crater-fill PIDs. The spectral halo of the crater-fill PIDs at the margin towards the crater wall appears cyan/bluish. One part of the halo is indicated by dashed lines, others are indicated by arrows. b) LAMO clear filter image, area of the spectral halo appears to contain both pitted and smooth material while the pits are close to the resolution limit. c) displays the area around the central peak showing signs of subsidence as well as distinct PIDs comprising very small pits (upper panel) and higher reflectance and pyroxene band strength (cyan/bluish in lower panel). Spatial context is given in Fig. 4.5.

surroundings (i.e., ejecta material) are both enriched in OH with respect to materials within the crater (PIDs, halo and NW crater wall).

The distinct spectral characteristics of the PIDs are not exclusively confined to the pits themselves. Instead, the spectral signatures reach several tens of meters outward building another sort of halo around the PIDs (see especially Fig. 4.10b, e & f). Thus, some parts of the smooth surface of the host deposit show the same spectral characteristics as the pitted parts. However, due to the resolution limit, it cannot be excluded that there are smaller pits inside these halos (>50 m). We note that for other (potential) PIDs identified on Vesta by Denevi et al. (2012) we did not observe such apparent spectral variations (i.e., in craters Cornelia, Licinia and Numisia).

Table 4.4: 750 nm reflectance, 750/917 [nm] and 2.8 µm band depth values (from Combe et al., 2015a) of locations of interest. Values are given with one standard deviation.

| Unit | Mean 750 nm reflectance | Mean 750/917 [nm] | Mean 2.8 µm band depth | n (pixel number) |
|---|---|---|---|---|
| PIDs (Fig. 4.10a-i) | 0.190 ± 0.017 | 1.529 ± 0.100 | 0.031 ± 0.004 | 3,707 |
| Surroundings | 0.167 ± 0.012 | 1.379 ± 0.048 | 0.034 ± 0.004 | 22,982 |
| PIDs floor (Fig. 4.10j) | 0.183 ± 0.007 | 1.443 ± 0.029 | 0.023 ± 0.002 | 26,089 |
| Halo floor | 0.201 ± 0.004 | 1.579 ± 0.026 | 0.020 ± 0.002 | 4,509 |
| NW craer wall | 0.217 ± 0.008 | 1.576 ± 0.031 | 0.021 ± 0.001 | 64,21 |
| whole Vesta | 0.194 ± 0.034 | 1.445 ± 0.133 | 0.030 ± 0.009 | $3.56*10^8$ |

## 4.7 Spectral comparison with HED meteorites

Figure 4.12 displays FC data ratios of the most prominent PIDs (i.e., 4.10a, b, c and f which exhibit the highest 750/917 [nm] values, magenta colored data cloud) in comparison with other locations of interest on Vesta and the meteorite spectra from RELAB (Figure 2.5, now black & grey symbols), showing that the data points of these PIDs overlap with the main data cloud of eucrites (light grey circles). The NW crater wall of Marcia shows very similar values like the PIDs, but with slightly lower 750/917 [nm] values. The surroundings of the PIDs (light turquoise), as well as the PIDs on the Marcia crater floor (purple) have relatively equal values and also overlap with eucrite data points but with lower 750/917 [nm] values with respect to the selected PIDs. E2a (light blue) and Aricia Tholus (dark blue) have even lower 750/917 [nm] values. All of these regions of interest together plot on a mixing line between eucrite and carbonaceous chondrite data (indicated by shortly-dashed line). They show a slight difference in 965/917 [nm] values. This observation is consistent with previous studies suggesting carbonaceous chondrites as the source for the observed dark material on Vesta.

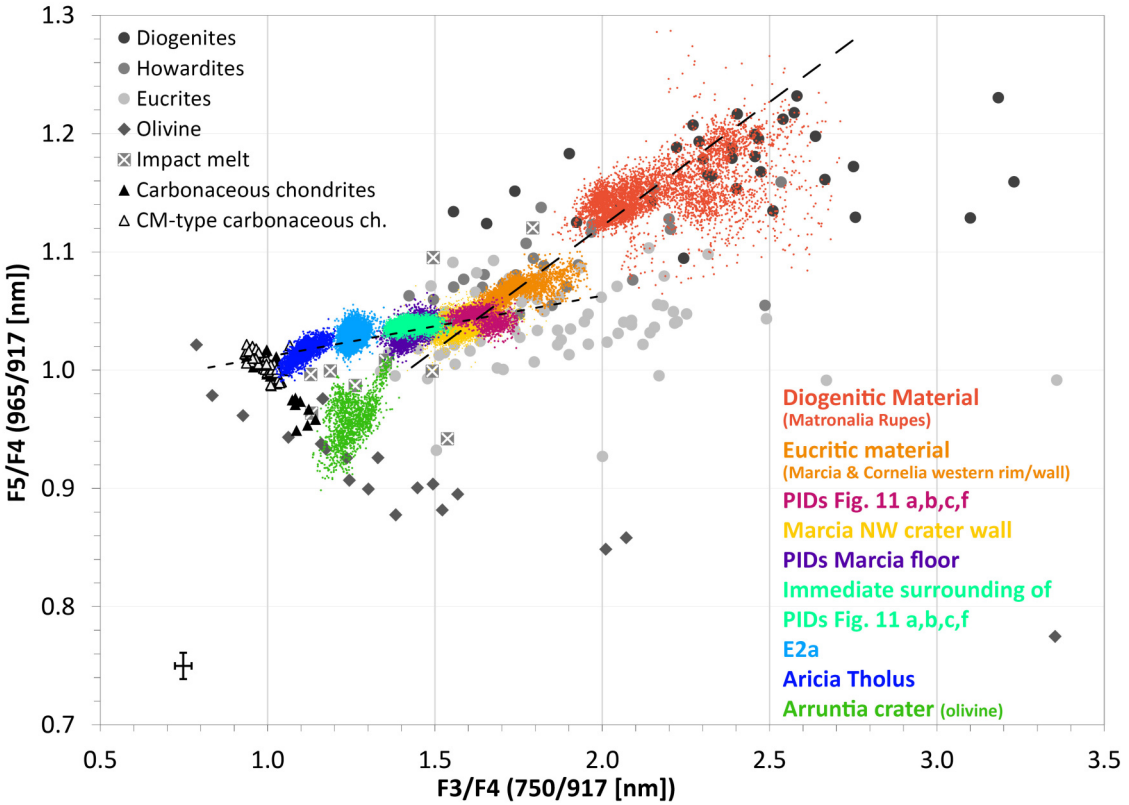


Figure 4.12: 750/917 [nm] vs. 965/917 [nm] of various locations of interest (colored data) with RELAB meteorite data from Fig. 2.5 in black, white, and grey colors. The FC ratio values of selected external PIDs overlap with data points of eucrites as well as partly with data for the most eucritic regions on Vesta (orange data points, taken from Marcia western rim and Cornelia western wall). These PIDs can therefore be spectrally separated from their immediate surroundings (light turquoise) and from the PIDs on the Marcia floor (purple). Dashed lines represent spectral trends of contaminated material (flatter line between carbonaceous chondrites and eucrites) and uncontaminated material (long dashes, purely HED). The error indicator on the lower left displays an approximate calibration uncertainty of 3% after Schröder et al. (2014). Note that the diogenitic material (dark orange) overlaps well with the diogenite data points (black circles), indicating an accurate calibration and the feasibility of this comparison.

On this 'contamination mixing line', PIDs appear to represent the eucrite-rich endmember. Eucritic regions of interest with even 'purer' (i.e., less contaminated) eucritic compositions (orange)

likely representing exposed eucritic bedrock, such as at the rim of Marcia crater (Fig. 4.9, upper middle panel) and the bright slope deposit on Cornelia's western wall (Fig. 4.9, upper right panel), show even higher 750/917 [nm] and significantly higher 965/917 [nm] values.

Matronalia Rupes – a scarp at the Rheasilvia Basin rim – was previously reported to be composed of diogenitic rock (e.g., Ammannito et al., 2013a; McSween et al., 2013a; Stephan et al., 2015), which is consistent with the comparison in Figure 4.12 (dark orange). Carbonaceous chondrites have values around 1.0 for 965/917 [nm] and 750/917 [nm], while Vestan data generally have higher values for both ratios (Fig. S4). This suggests that larger values for 965/917 [nm] and 750/917 [nm] indicate less contamination with carbonaceous chondrite material (or other reflectance-lowering components). Moreover, seemingly "pure" regions (eucritic and diogenitic characteristics) are characterized by another dependency than contaminated areas and plot on a different trend line (dashed lines in Fig. 4.12).

The cause for these two distinct trend lines is 1) the contamination by dark (carbonaceous chondrite) material and 2) that the Marcia region is characterized by a high eucritic abundances with no diogenitic occurrences (Ammannito et al., 2013a; Prettyman et al., 2013). Therefore, the slope of the "contaminated trend line" in Figure 4.12 is significantly lower than the HED trendline including diogenites. For the Marcia region, only only observe a very subtle change in the pyroxene band position (indicated by the 965/917 [nm] ratio), which can be attributed to the described contamination.

The mineral olivine, which commonly occurs in planetary materials, does not contribute to the spectral characteristics of the PIDs either. Firstly, it has not been detected in the Marcia area (Ammannito et al., 2013b; Palomba et al., 2015; Thangjam et al., 2014), and secondly, olivine exhibits lower values in both considered ratios (see Fig. 2.5 and 4.12), which is contrary to my observations of the PIDs. However, detection of olivine by the Dawn instruments is challenging and might not be possible below 30 vol% (Beck et al., 2013; Le Corre et al., 2013), adding uncertainties in these interpretations.

HED data plot on a trend line when the pyroxene band I center is plotted against the pyroxene band II center (e.g., De Sanctis et al., 2012a, 2015c). Most of the Vestan surface is slightly deviating from this trend, which can again be explained by the contamination of impacting carbonaceous chondritic material. The same is observed when plotting FC color ratios against each other (Thangjam et al., 2013 and this study, long dashes in Figs. 4.12 & S4), which only cover the first pyroxene absorption band. The vast majority of Vestan FC data plot near eucrites/howardites but with a small bulge toward carbonaceous chondrites. This is displayed in the supplementary Figure S4 (11). The highest density of the Vestan surface plots around 1.44, 1.05 (ratio values), whereas some of the PIDs plot around 1.65 (and more) and 1.04, which furthermore suggests that the main parameter to distinguish the different terrains is the indicator for pyroxene band strength, 750/917 [nm].

In summary, the major parameter for the distinction between the PIDs and their surrounding is the FC ratio 750/917 [nm] (F3/F4). The data points of selected PIDs outside of Marcia overlap with data points of eucrites, consistent with previous findings that the Marcia region is enriched in eucritic rock types (e.g., De Sanctis et al., 2015b; Prettyman et al., 2012). The spectral comparison with HED meteorites shows that PID-related regions of interest (PIDs, PID surroundings and E2a) are consistent with contamination by carbonaceous chondrites. Changes in pyroxene mineralogy towards diogenitic lithologies is not observed.

## 4.8 Combined FC observations

Linking all these previous observations, we can separate the PIDs external to Marcia (102 PIDs) into two different types according to the ejecta units defined in section 3.4.2. PIDs of type 1 comprise PIDs located in E1, where the ejecta blanket generally exhibits higher reflectance and stronger pyroxene absorptions (as does the NW part of Marcia, see Fig. 3.10b). These PIDs exhibit higher mean reflectance at 750 nm (Table 4.5), a higher mean value for the 750/917 [nm] ratio and slightly lower 2.8 µm absorption depths compared with average Vestan values. Furthermore, they have larger spatial extents (mean of 2.2 km2) than type 2 PIDs (mean of 1.8 $km^2$). In total, 42 out of 103 external PIDs are of type 1 and ten of them occur within craters that existed prior to the Marcia impact (i.e., ~24% of PIDs in E1 are located in small pre-existing craters).

Type 2 PIDs exhibit lower than average mean reflectance at 750 nm (Table 4.5) and their 750/917 [nm] ratios resemble the value of the average Vesta. Their 2.8 µm absorption depths are above the average of Vesta. Seven of the 17 identified PIDs in pre-existing craters are of type 2 (i.e., ~12% from type 2 PIDs are located in small pre-existing craters), yet all of these seven occurrences are located within E2b, which corresponds to v18% of this ejecta unit's PIDs (39 PIDs within E2b and 21 within E2a). Type 2 PIDs are more abundant and are located within E2a and E2b. Considering PIDs/km2, PIDs are more abundant in E1. This indicates that E1 contained more volatiles than E2a and E2b (all have roughly the same spatial extent), which is contrary to the general higher reflectance and pyroxene band strength nature of E1. However, if E2a (and possibly E2b) were to originate from Calpurnia, the Marcia impactor would have hit a relatively young ejecta blanket (i.e., Calpurnia ejecta shows a similar age as Marcia ejecta, Williams et al., 2014b; Appendix A) and overprinted possibly already existing PIDs sourced from Calpurnia. The impact event forming Marcia could have incorporated volatiles from the well-preserved Calpurnia ejecta. Furthermore, as ejecta deposits are more abundant close to the parent crater, E1 might comprise more PIDs/km2 as it represents the closest ejecta deposits to Marcia.

Table 4.5: 750 nm reflectance, 750/917 [nm] and 2.8 µm band depth values (from Combe et al., 2015a) of the two PID types. Values are given with one standard deviation.

| Unit | Mean 750 nm reflectance | Mean 750/917 [nm] | Mean 2.8 µm band depth | n (pixel number) |
|---|---|---|---|---|
| PIDs type 1 (Fig. 4.10a-f) | 0.206 ± 0.008 | 1.621 ± 0.060 | 0.028 ± 0.003 | 1,667 |
| Surroundings type 1 | 0.172 ± 0.010 | 1.402 ± 0.042 | 0.033 ± 0.004 | 14,784 |
| PIDs type 2 (Fig. 4.10g-i) | 0.174 ± 0.005 | 1.431 ± 0.020 | 0.033 ± 0.002 | 2,040 |
| Surroundings type 2 | 0.158 ± 0.009 | 1.336 ± 0.020 | 0.037 ± 0.004 | 8,198 |

Figure 4.13 is a key figure in this study and summarizes the values given in Tables 4.4 and 4.5, showing that PIDs show a deviating trend regarding both reflectance at 750 nm and OH content (i.e., 2.8 µm band depth) with respect to 750/917 [nm] values. The surroundings of PIDs, the NW crater wall, the crater next to the SW PID (shown in Fig. 4.9) and the average Vesta roughly plot on a common trend line (dashed) in both displayed diagrams, indicating a 'typical' dependence of reflectance (and OH content) and pyroxene band strength for Marcia-related regions of interest and the average Vestan values. PIDs clearly deviate from this trend (dotted line). PIDs generally have higher 750/917 [nm] values with respect to 750 nm reflectance and 2.8 µm band depth values of other more typical Marcia-related materials. This furthermore illustrates that the PIDs' materials have undergone a process changing the original spectral nature of Vestan material.

We note that while the crater-fill PIDs show similar reflectance and pyroxene band strength values as for example the average Vesta, their OH contents are significantly lower, putting them in their own category (purple circle in Figure 4.13, right panel). As described before, the crater-fill PIDs are not nearly as spectrally homogeneous like all other PIDs (see section 4.6 and Figs. 4.10 and 4.11). Instead, these PIDs show spectral and geomorphological variations (see 'halo' and 'crater-fill' PIDs in Figs. 4.13 and 4.11) and furthermore are the only PIDs that exhibit lower reflectance

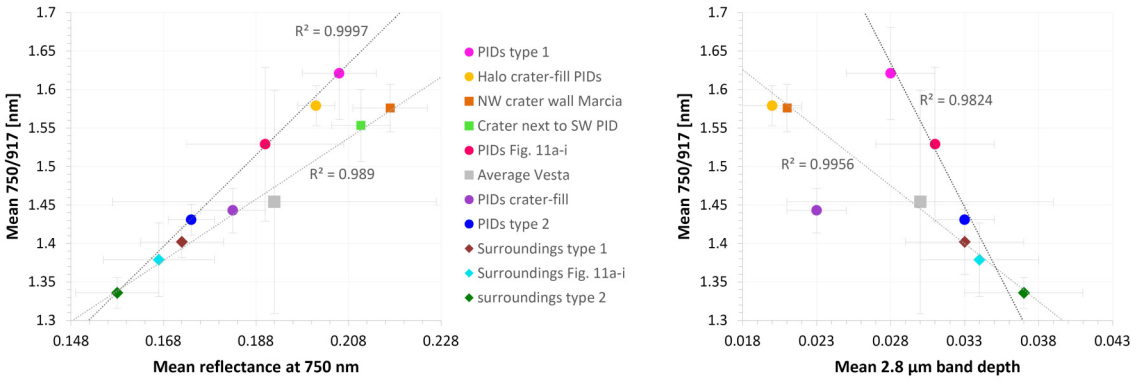


Figure 4.13: Left panel: Mean reflectance at 750 nm vs. Mean 750/917 [nm] of regions of interest reported in Tables 4.4 & 4.5 and a small crater next to a PID (Figure 4.9, left panel). Right panel: Mean 2.8 µm band depth vs. mean 750/917 [nm] reported in Tables 4.4 & 4.5. Error bars indicate the given standard deviations, for the 'crater next to SW PID', an error of 3% is displayed, as described for Fig. 4.9. There is no 2.8 µm band depth available for this crater due to the limited resolution of the VIR instrument. Regression line for PIDs contains the three PID data points. Regression line for the Marcia-related regions of interest contains the NW crater wall, the crater next to the SW PID (only for the left panel, Figure 4.9), the average Vesta and the three surroundings of PIDs.

and pyroxene band strength values than their immediate surroundings (Figs. 4.10j and 4.11) while also showing the lowest OH abundance of all PIDs. The crater-fill PIDs and their individual pits moreover are significantly larger than all other PIDs (see section 4.5 and Fig. 4.4). The crater-fill halo (orange circle in Fig. 4.13) likewise represents its own category linked to the crater-fill PIDs, yet comprise very small individual pits down to the resolution limit (Fig. 4.11b) and also smooth material. In the left panel of Figure 4.13, the halo plots roughly on the same trend line as the external PIDs (dotted). If we would plot a regression line for the data points of the halo and the crater-fill PID, it would show an even steeper slope in the left panel and a line roughly parallel to the PID regression line in the right panel, indicating similar characteristics.

The presence of two types of PIDs is closely linked to the ejecta units described in section 3.4.2. Therefore, we again acknowledge that PIDs of type 2 might originate from the impact that formed Calpurnia crater. It remains challenging to explain the occurrence, extent and spectral characteristics of E2b if Calpurnia is the source. Again, the determination of the PID parent crater is not crucial for this study. The most important observations and interpretations are not tied to this separation. Moreover, if the ejecta units did not form from a single event, it shows that the unique spectral changes the material underwent upon PID formation is not a singularity, but instead can form during other impact events too. Yet we note that Calpurnia and Marcia are adjacent to each other and likely sampled the same target material. Unfortunately, there are no other large and well-preserved craters on Vesta's surface in order to see whether impact events in other areas of Vesta could likewise have generated spectrally distinct PIDs.

Lastly, we emphasize the unique spectral trend for PIDs by presenting the left panel of Figure 4.13 with additional data from known diogenitic sites (i.e., Matronalia Rupes scarp and craters Aelia, Lollia and Antonia) which is displayed in Figure S5. These diogenitic sites plot parallel to the 'Marcia-related' regression line, strengthening the unique trend for PIDs.

## 4.9 Spectral properties as seen by VIR

As the pyroxene absorption band I (at ~0.9 µm) is covered by the Framing Camera, I focus here on the characteristics of the second pyroxene absorption band at around 2 µm and therefore, the IR channel of the VIR instrument. What was observed for the first pyroxene absorption band appears to be valid for the second pyroxene absorption band as well. The reflectance at around 1.4 µm is elevated with respect to the immediate surrounding of PIDs and the band ratio characterizing the band strength, here 1.446/1.910 [µm], stands out with respect to other locations in the vicinity. The Marcia area is covered by several VIR cubes, yet only three enable the identification of some of the most prominent PIDs due to the limited spatial resolution. I will show the results of those three cubes for external PIDs around Marcia. Furthermore, I will show one cube that covers some parts of the interior of Marcia and two other additional cubes that cover parts of the craters Cornelia and Licinia. The spatial context is illustrated with the help of higher resolution FC data.

Figure 4.14 shows an area west of Marcia with several of the most prominent PIDs (mostly in the lower part of the image, see Figure 4.15). This cube and its PIDs is situated within ejecta unit E1 (see section 3.4.2). While the PIDs can (for most occurrences) already be distinguished from their surroundings by a higher reflectance at 1.446 and 1.910 µm, they clearly differ distinctly from the surroundings by their higher 1.446/1.910 [µm] ratio values. This can be observed in detail in Figure 4.15 where spatial context and exact PID location are given. Some locations unrelated to PIDs also show higher reflectance and pyroxene band strength, yet expose either bedrock or are impacts into impact deposits, which could reveal similar material as seen at the PIDs. This clearly shows that both pyroxene band I and pyroxene band II are similarly affected by a mechanism altering the spectra of impact deposits. Table 4.6 reports spectral parameters of all PIDs observed here by VIR and their surroundings as well as four presumable bedrock exposures, followed by a Figure illustrating these values.

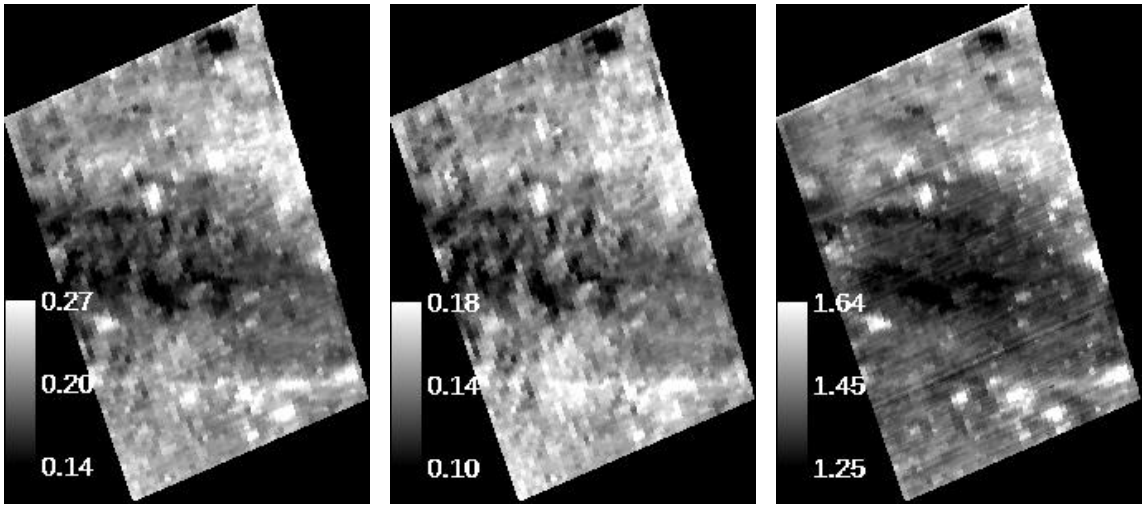


(a) (b) (c)

Figure 4.14: VIR cube 394858895. a) Reflectance at 1.446 µm, b) reflectance at 1.910 µm, c) reflectance ratio 1.446/1.910 [µm].

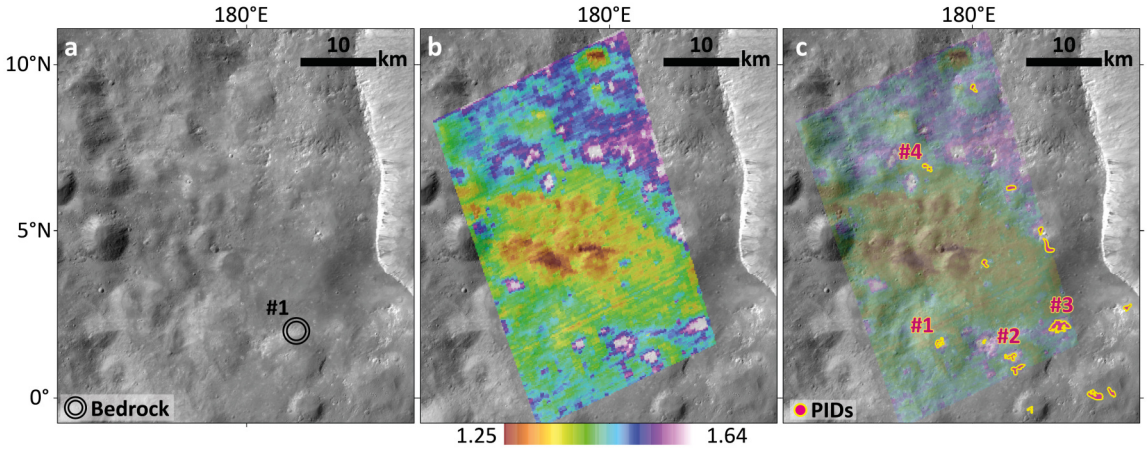


Figure 4.15: VIR cube 394858895 on Dawn FC mosaic with locations of PIDs and presumably exposed bedrock. A) spatial context image, Marcia western rim can be seen in the right, numbered bedrock location in double circle, b) reflectance ratio 1.446/1.910 [µm] (50% transparency on FC mosaic), c) superposed PID map (on 85% transparent 1.446/1.910 [µm] ratio and FC mosaic) with different color code than in Figure 4.4 for an easier perception, numbering according to Table 4.6.

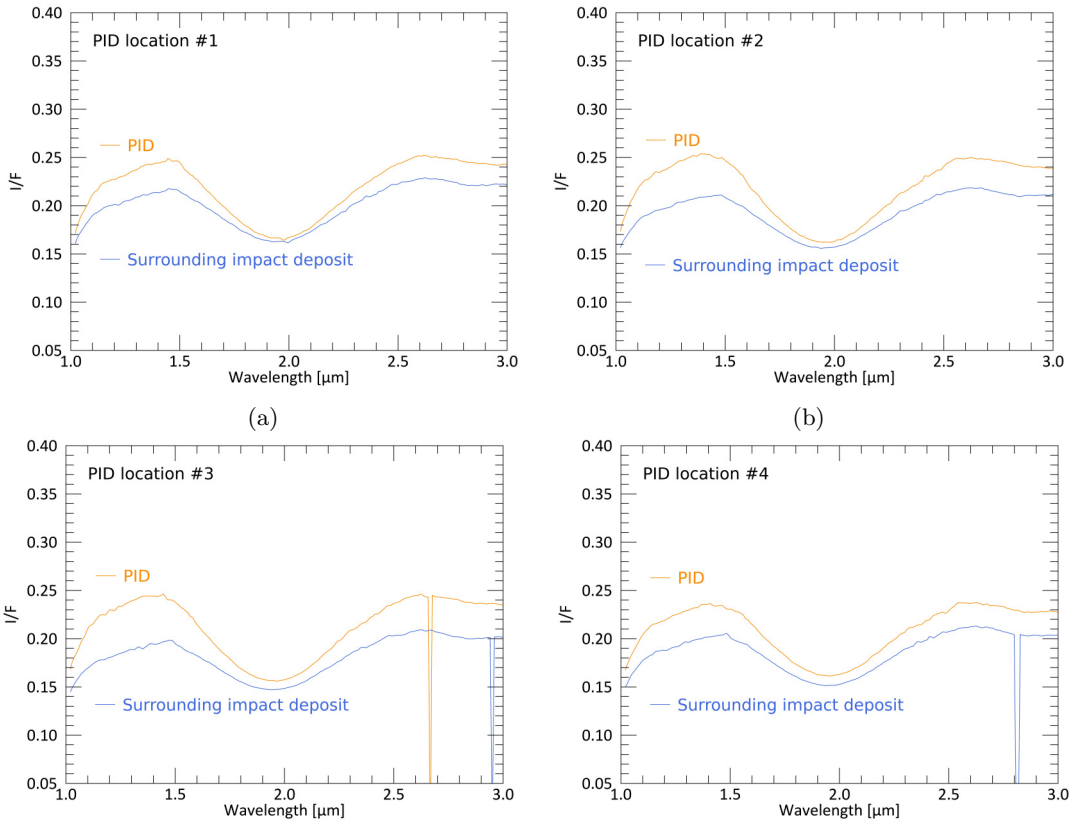


Figure 4.16: Spectra of PIDs and their impact deposit surrounding taken from VIR cube 394858895. Spatial context is given in Figure 4.23. For all four PIDs, the surrounding impact deposit shows lower overall reflectance and pyroxene absorption strength.

Figure 4.17 shows data of the VIR cube 395166968, which is located just north of Marcia and covers areas of ejecta units E1 and E2b. In this cube, it is remarkable to observe how strongly the ratio 1.446/1.910 [µm] is deviating from the perception gained by reflectance only. The most

prominent PID in this image (lower left part) is PID #5 (see Figure 4.23 for exact location) which does not show a particularly elevated reflectance at 1.446 and 1.910 µm with respect to other materials in its vicinity and can hardly be made out. However, as seen in Figure 4.17c, the pyroxene band strength ratio (1.446/1.910 [µm]) clearly points out the location of this PID (black arrow). Figure 4.18 presents spatial context and location of PIDs. The spectra of two PIDs (#5 and #6) will be shown in Figure 4.19.

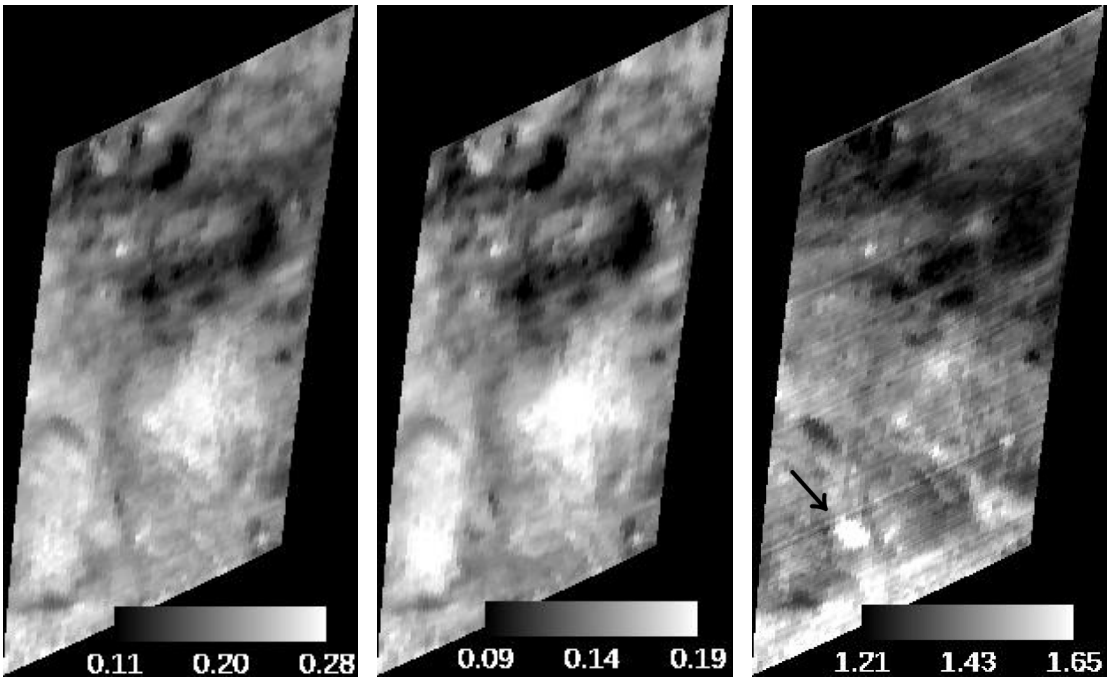


(a) (b) (c)

Figure 4.17: VIR cube 395166968. A) reflectance at 1.446 µm, b) reflectance at 1.910 µm, c) reflectance ratio 1.446/1.910 [µm] with black arrow pointing out PID #5.

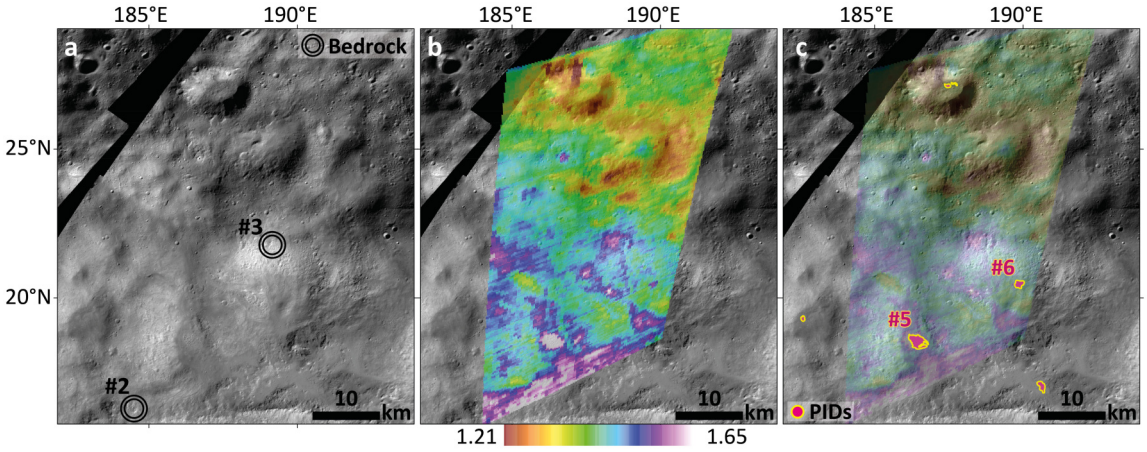


Figure 4.18: VIR cube 395166968 on Dawn FC mosaic with locations of PIDs and presumably exposed bedrock. A) spatial context image, Marcia western rim can be seen in the right, numbered bedrock locations in double circles, b) reflectance ratio 1.446/1.910 [µm] (50% transparency on FC mosaic), c) superposed PID map (on 85% transparent 1.446/1.910 [µm] ratio and FC mosaic) with different color code than in Figure 4.4 for an easier perception, numbering according to Table 4.6.

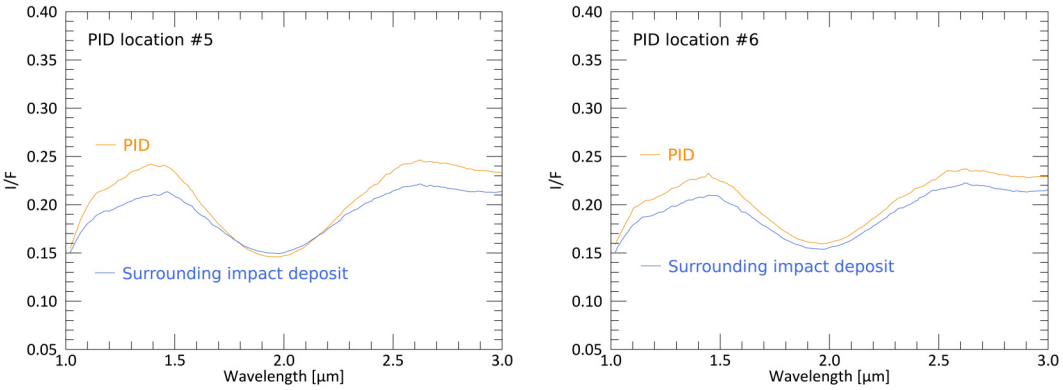


(a) (b)

Figure 4.19: Spectra of PIDs and their impact deposit surrounding taken from VIR cube 395166968. Spatial context is given in Figure 4.23. For the displayed two PIDs, the surrounding impact deposit shows lower overall reflectance and pyroxene absorption strength.

Figure 4.20 shows VIR cube 394992761, covering an area just south of Marcia. This area is situated within ejecta unit E2b, where pyroxene band strengths generally exhibit lower values than in E1 (Fig. 3.11). This can similarly be observed in VIR data. However, reflectance values resemble each other for all three cubes. Figure 4.21 additionally displays lobate flow lines (dashed black) which appear to represent the boundary of Marcia's continuous ejecta blanket. Beyond this boundary, no PIDs occur. Due to the two prominent craters exposing bright material in the lower part of the VIR image, PIDs do not prominently stand out like in the other presented VIR cubes. The spectra of three PIDs are presented in Figure 4.22 and their location in Figure 4.23.

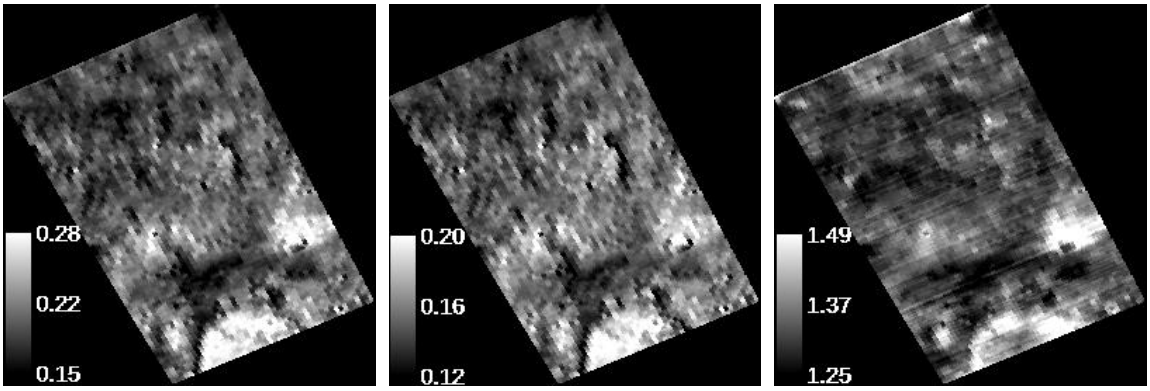


(a) (b) (c)

Figure 4.20: VIR cube 394992761. a) Reflectance at 1.446 µm, b) reflectance at 1.910 µm, c) reflectance ratio 1.446/1.910 [µm].

Table 4.6 summarizes the absolute values of PIDs and their surroundings as well as other locations of interest. As described before, these values confirm that the second pyroxene band likewise shows increased reflectance and band strength for the PIDs with respect to their immediate surrounding. Bedrock values have generally smaller OH contents, yet with respect to PIDs also show lower overall band strength values. The average absolute difference between PIDs and their surroundings is 0.027 (±0.014) for reflectance at 1.446 µm and 0.144 (±0.057) for 1.446/1.910 [µm].

Figure 4.24 illustrates the values presented in Table 4.6. It shows that for similar reflectance and/or 2.8 µm absorption depths, PIDs have generally higher 1.446/1.910 [µm] values than their surroundings and bedrock. Although $R^2$ values are very low, a clear difference between these regions of interest can be identified, similar to what was presented in Figure 4.13 from Michalik et al. (2021) and what will be shown in the next section in Figure 4.34. However, I note at this point that these are point-source data and interpretational care should be applied especially to

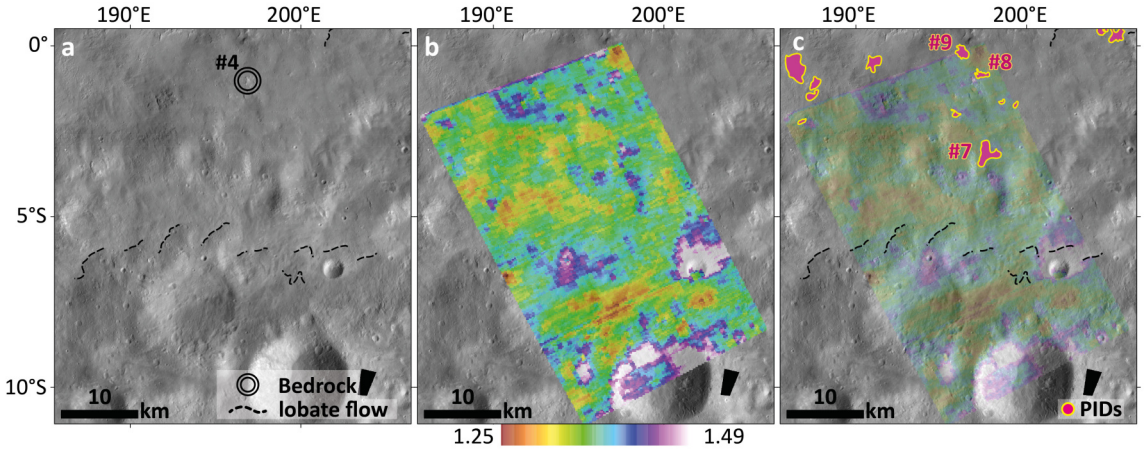


Figure 4.21: VIR cube 394992761 on Dawn FC mosaic with locations of PIDs and presumably exposed bedrock. A) spatial context image, Marcia western rim can be seen in the right, numbered bedrock location in double circle, b) reflectance ratio 1.446/1.910 [µm] (50% transparency on FC mosaic), c) superposed PID map (on 85% transparent 1.446/1.910 [µm] ratio and FC mosaic) with different color code than in Figure 4.4 for an easier perception, numbering according to Table 4.6.

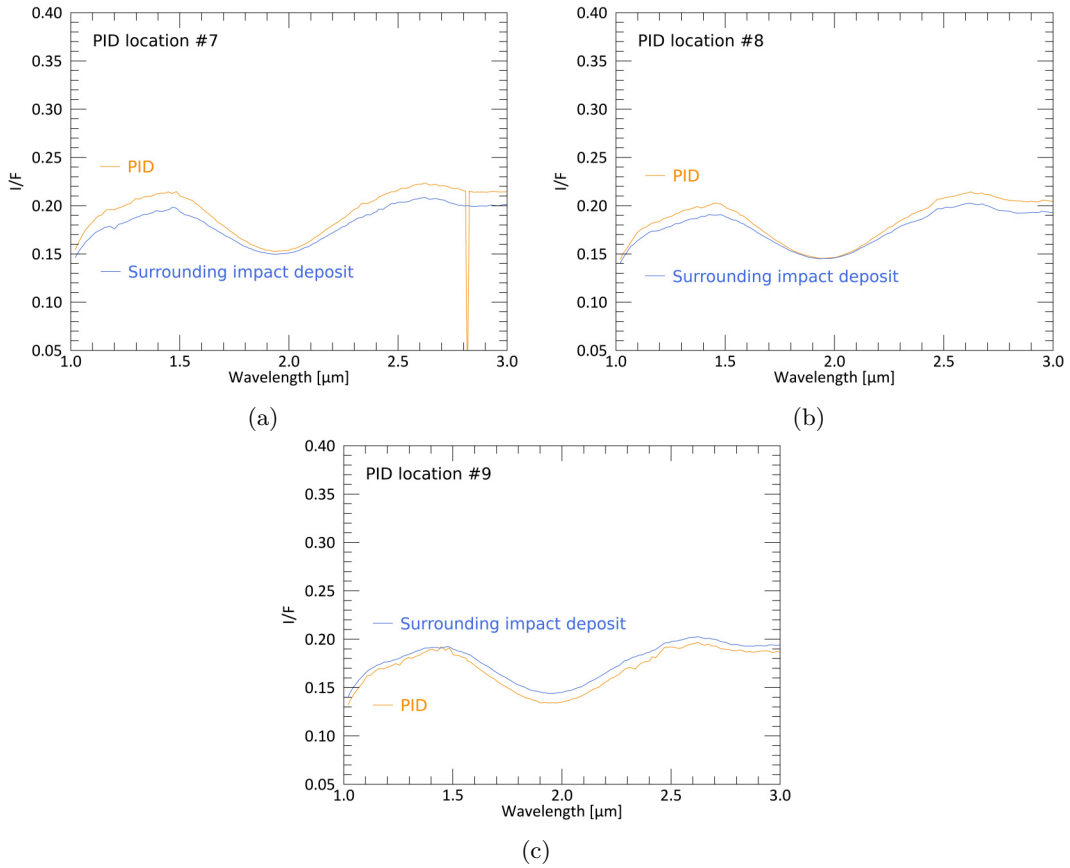


Figure 4.22: Spectra of PIDs and their impact deposit surrounding taken from VIR cube 394992761. Spatial context is given in Figure 4.23. For PIDs #7 and #8, the surrounding impact deposit shows lower overall reflectance and pyroxene absorption strength. Surrounding #9 shows higher overall reflectance but lower pyroxene absorption band strengths than PID #9.

the 2.8 µm absorption depths as this data have the lowest spatial resolution and might not resolve variations at small regions of interest.

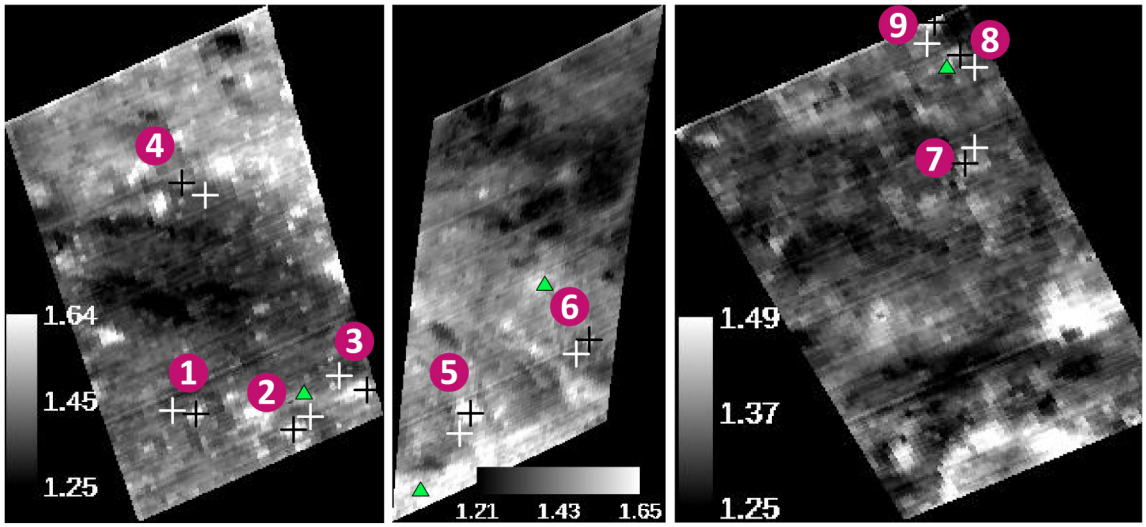


Figure 4.23: Locations in VIR cubes of the nine PIDs and their surroundings that were selected for spectrum display. Black crosses denote the locations of PID spectra and white crosses the respective surroundings. Green triangles denote locations of presumably exposed bedrock. The exact locations (sample and line number of cube) are given in the Appendix (12.2). As data base, the ratio 1.446/1.910 [µm] of each cube is displayed for an easier identification of the PIDs.

Table 4.6: Spectral parameters of locations depicted in Figure 4.23: Reflectance at 1.446 µm, band strength ratio 1.446/1.910 [µm] and the 2.8 µm absorption depth derived from data produced by Combe et al. (2015a).

| Location | refl. at 1.446 µm | 1.446/1.910 [µm] | 2.8 µm abs. depth |
|---|---|---|---|
| PID #1 | 0.249 | 1.490 | 0.0294 |
| Surrounding #1 | 0.218 | 1.330 | 0.0301 |
| PID #2 | 0.251 | 1.526 | 0.0281 |
| Surrounding #2 | 0.210 | 1.339 | 0.0324 |
| PID #3 | 0.246 | 1.563 | 0.0308 |
| Surrounding #3 | 0.197 | 1.332 | 0.0359 |
| PID #4 | 0.234 | 1.443 | 0.0332 |
| Surrounding #4 | 0.203 | 1.336 | 0.0333 |
| PID #5 | 0.241 | 1.638 | 0.0250 |
| Surrounding #5 | 0.212 | 1.406 | 0.0283 |
| PID #6 | 0.235 | 1.455 | 0.0263 |
| Surrounding #6 | 0.210 | 1.356 | 0.0301 |
| PID #7 | 0.214 | 1.394 | 0.0350 |
| Surrounding #7 | 0.195 | 1.304 | 0.0369 |
| PID #8 | 0.202 | 1.382 | 0.0344 |
| Surrounding #8 | 0.190 | 1.307 | 0.0347 |
| PID #9 | 0.192 | 1.432 | 0.0381 |
| Surrounding #9 | 0.193 | 1.327 | 0.0354 |
| Bedrock #1 | 0.245 | 1.413 | 0.0306 |
| Bedrock #2 | 0.248 | 1.410 | 0.0290 |
| Bedrock #3 | 0.253 | 1.470 | 0.0258 |
| Bedrock #4 | 0.214 | 1.389 | 0.0314 |

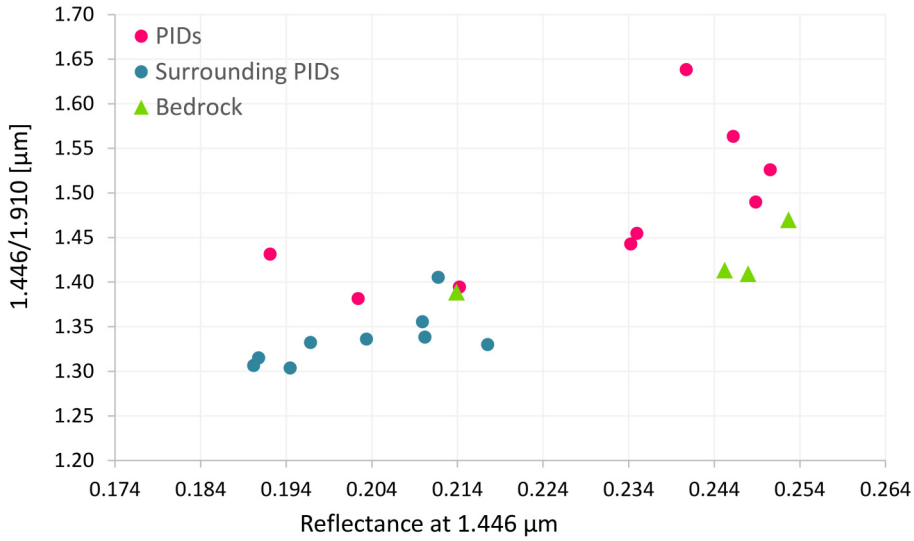


(a)

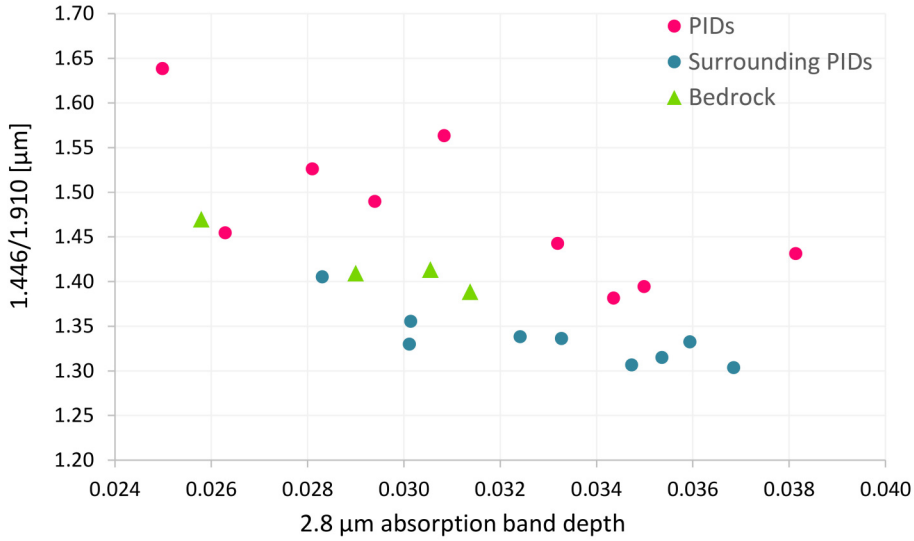


(b)

Figure 4.24: a) Reflectance at 1.446 µm vs. 1.446/1.910 [µm] for PIDs (red), their surroundings (dark turquoise) and the four presumably exposed bedrock locations (green). Rounded $R^2$ values for PIDs are 0.48, for their surroundings 0.42 and for bedrock 0.53. b) 2.8 µm absorption depth vs. 1.446/1.910 [µm] for PIDs (red), their surroundings (dark turquoise) and the four presumably exposed bedrock locations (green). Rounded $R^2$ values for PIDs are 0.52, for their surroundings 0.67 and for bedrock 0.91. Data taken from Table 4.6.

Following the analysis of the Marcia-surrounding PIDs, I present VIR-IR data of the Marcia crater-fill material and report on the characteristics of Cornelia and Licinia PIDs. FC data of the crater-fill deposits within Marcia show a 'halo' around the central PID. While the central PID shows lower reflectance and band strength with respect to its crater-wall surrounding, the halo - which also features small PIDs - exhibits higher reflectance and pyroxene band strength just like other PIDs in the ejecta of Marcia (see Figure 4.11 and accompanying text). The same can be observed in VIR-IR data which is shown in the following. Figure 4.25 shows again both the reflectance at 1.446 µm and at 1.910 µm as well as the ratio 1.446/1.910 [µm], where the halo is clearly identifiable. Figure 4.26 gives the spatial context over a FC mosaic and Figure 4.27 displays spectra of the halo, the darker central crater-fill PID and a nearby crater wall. Table 4.7 illustrates the spectral values. I refrain from analyzing 2.8 µm absorption depth for the crater-fill area as it is uniformly depleted in OH as seen in Figures 3.10 and 4.10.

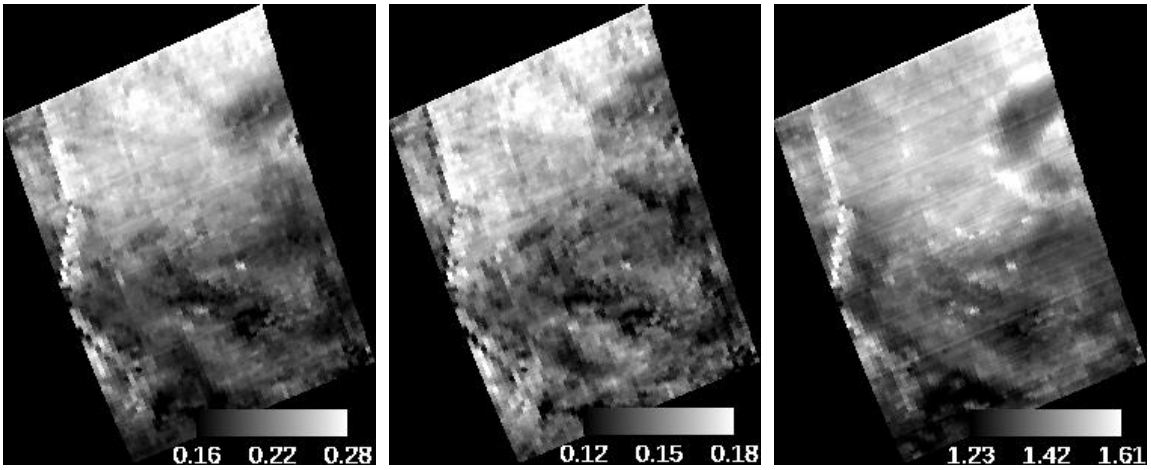


(a) (b) (c)

Figure 4.25: VIR cube 395301549. a) Reflectance at 1.446 µm, b) reflectance at 1.910 µm, c) reflectance ratio 1.446/1.910 [µm].

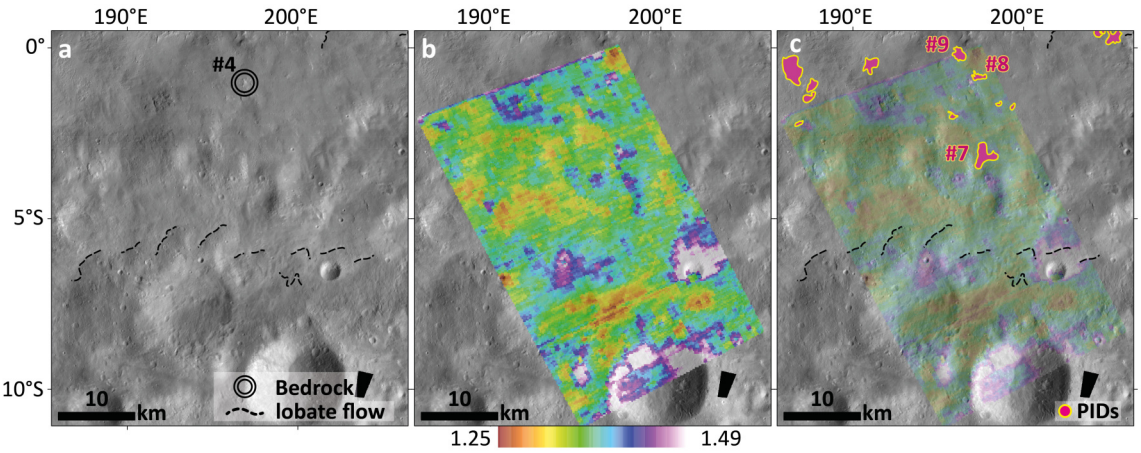


Figure 4.26: VIR cube 395301549 on Dawn FC mosaic with locations of the crater-fill PIDs. A) spatial context image, b) reflectance ratio 1.446/1.910 [µm] (50% transparency on FC mosaic), c) superposed PID map (on 85% transparent 1.446/1.910 [µm] ratio and FC mosaic) with different color code than in Figure 4.4 for an easier perception.

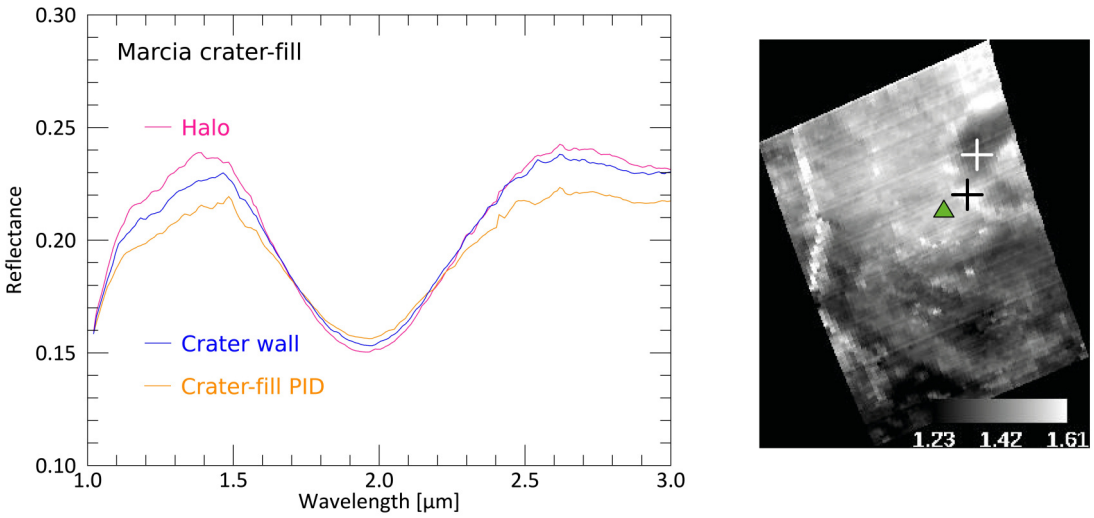


(a) (b)

Figure 4.27: A) Spectra of the crater-fill PID, the halo and their crater wall surrounding taken from VIR cube 395301549. B) Locations of spectra shown in a), white cross denotes location of crater-fill PID spectrum, black cross of halo spectrum and green triangle denotes the location of the crater wall spectrum.

Table 4.7: Spectral parameters of the spectra/locations depicted in Figure 4.27: Reflectance at 1.446 µm and pyroxene band strength ratio 1.446/1.910 [µm].

| Location | refl. at 1.446 µm | 1.446/1.910 [µm] |
|---|---|---|
| Halo | 0.237 | 1.563 |
| Crater wall | 0.228 | 1.474 |
| crater-fill PID | 0.217 | 1.376 |

Figure 4.28 displays the reflectance at 1.446 µm, at 1.910 µm and the ratio 1.446/1.910 [µm] for parts of Cornelia crater. For the Cornelia crater-fill PID, no elevated reflectance or pyroxene band strength similar to the Marcia-surrounding PIDs or crater-fill halo can be observed (see also Figure 4.29 for more spatial context), which conforms with FC observations. Likewise, no elevated reflectance or pyroxene band strength can be made out for Licinia, which is shown in Figures 4.30 and 4.31. The manual georeferencing for the Licinia cube was challenging and produced multiple distortions. However, the low reflectance and pyroxene band strength nature of the Licinia crater floor (and PIDs) can still be identified.

Finally, I present spectra of interest normalized at 1.446 µm in order to better visualize the pyroxene absorption strengths. This is done exemplary for PID #2 (Fig. 4.32a) and the halo/crater-fill PID/wall spectra from Figure 4.27 (Fig. 4.32b).

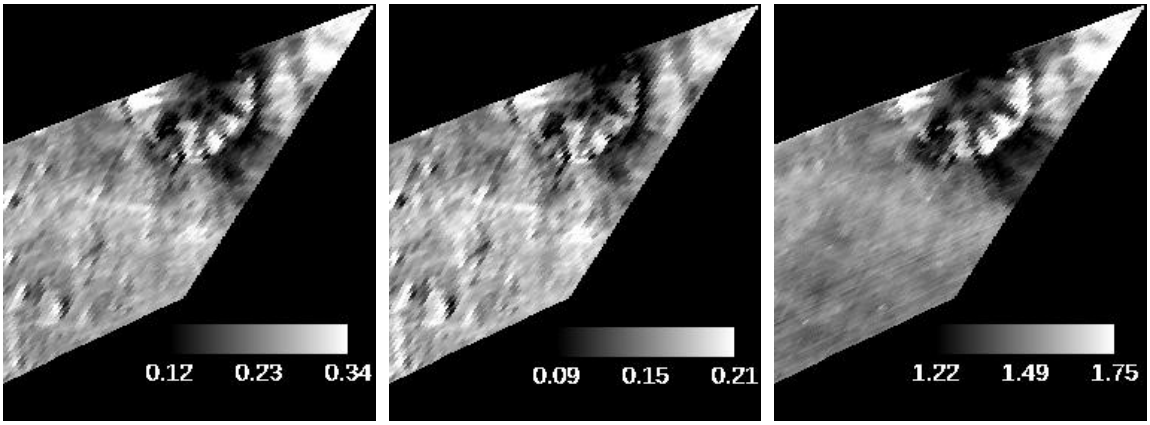


(a) (b) (c)

Figure 4.28: VIR cube 373313780 showing Cornelia crater in the upper right corner. The left part of the cube was left out for an easier display. a) Reflectance at 1.446 µm, b) reflectance at 1.910 µm, c) reflectance ratio 1.446/1.910 [µm].

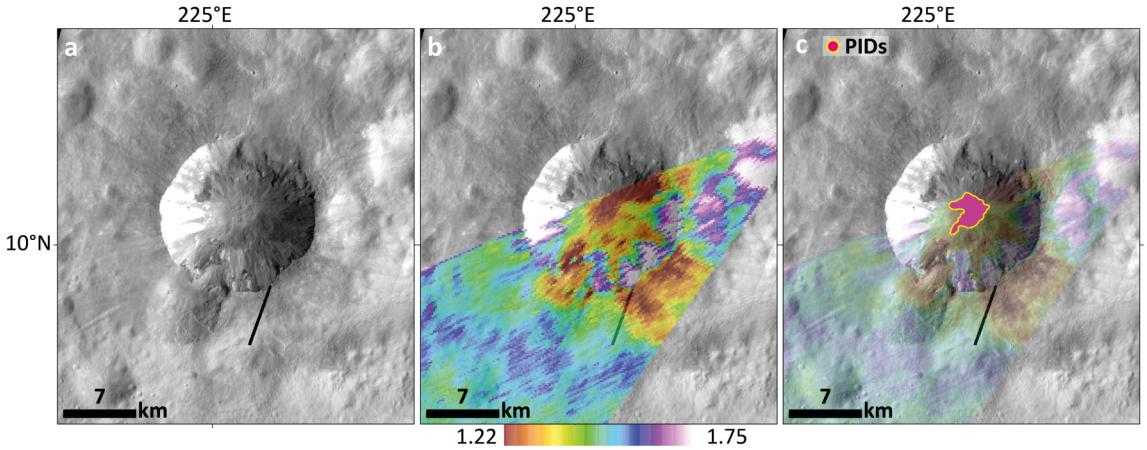


Figure 4.29: VIR cube 373313780 on Dawn FC mosaic with location of the crater-fill PID. a) Spatial context image, b) reflectance ratio 1.446/1.910 [µm] (50% transparency on FC mosaic), c) superposed PID map (on 85% transparent 1.446/1.910 [µm] ratio and FC mosaic) with different color code than in Figure 4.4 for an easier perception.

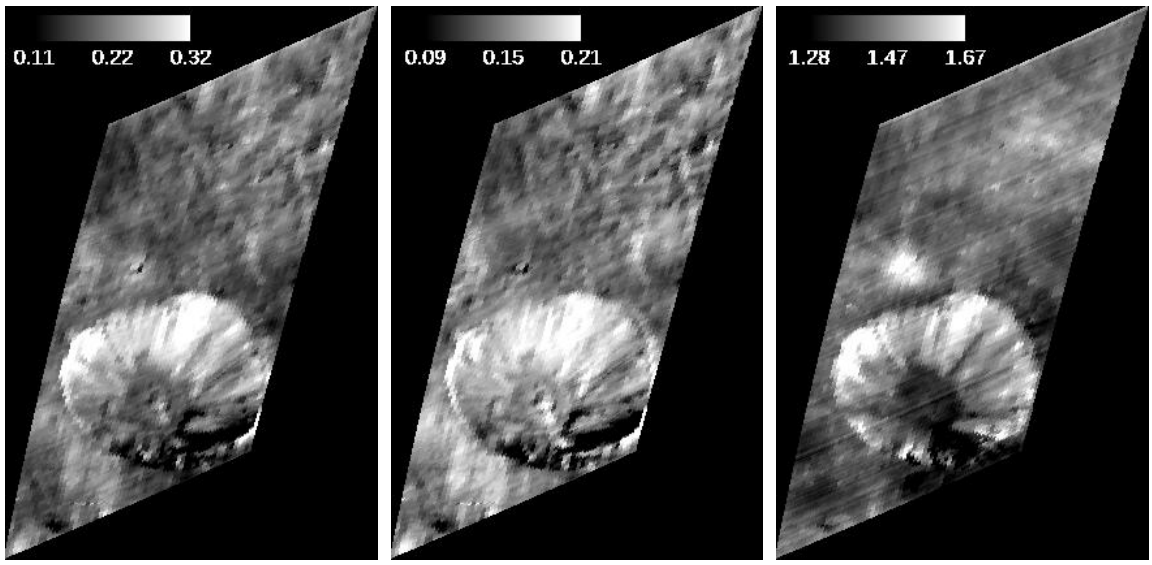


(a) (b) (c)

Figure 4.30: VIR cube 395387692 showing Licinia crater in the lower image part. A) Reflectance at 1.446 µm, b) reflectance at 1.910 µm, c) reflectance ratio 1.446/1.910 [µm].

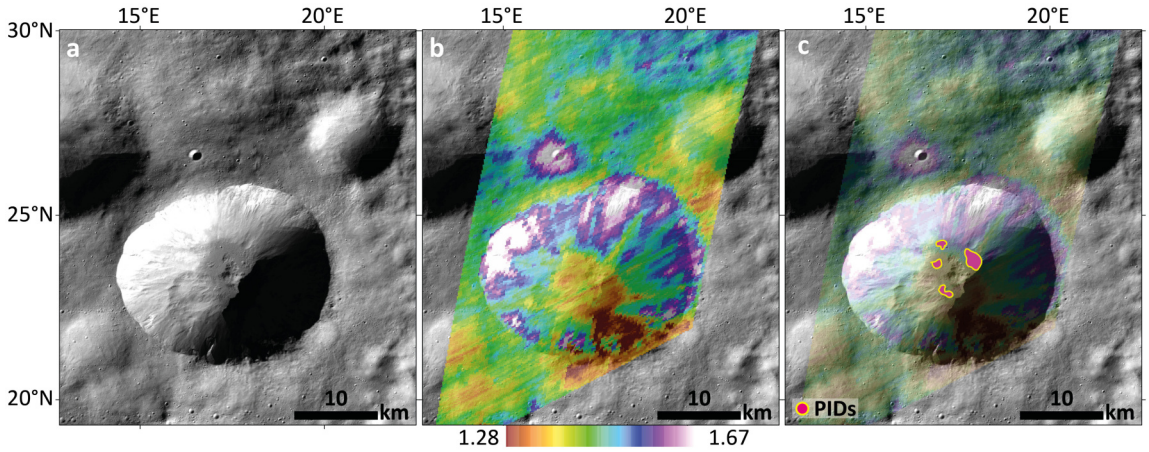


Figure 4.31: VIR cube 395387692 on Dawn FC mosaic depicting Licinia crater. a) Spatial context image, b) reflectance ratio 1.446/1.910 [µm] (50% transparency on FC mosaic), c) superposed PID map (on 85% transparent 1.446/1.910 [µm] ratio and FC mosaic) with different color code than in Figure 4.4 for an easier perception.

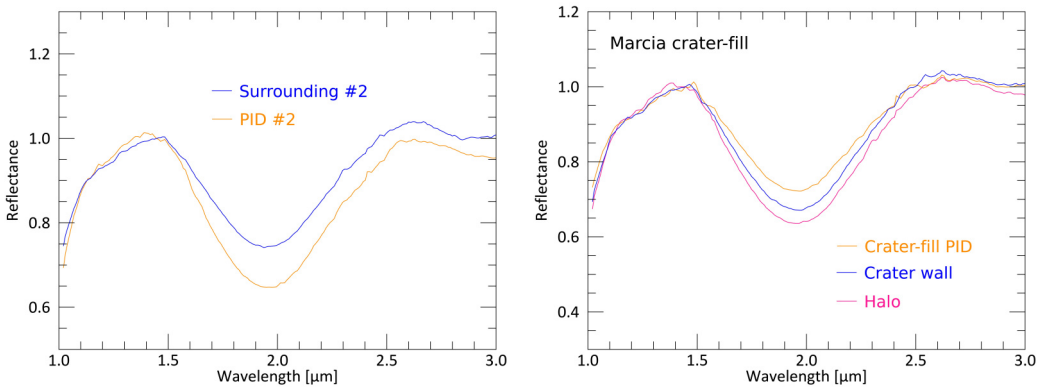


(a) (b)

Figure 4.32: Normalized spectra of (a) PID #2 and its surrounding from Fig. 4.16 and (b) the crater-fill PID, halo and crater wall spectra from Fig. 4.27.

## 4.10 Detailed spectral data for individual PIDs and their surroundings

This section presents data that have not been published in Michalik et al. (2021). In Michalik et al. (2021), PIDs' spectral data were averaged for all PIDs and for type 1 and type 2 PIDs, separately. Here I will present individual PIDs' spectral data and give more detail on the spectral trend arising from this. The nine chosen PIDs presented in the following are the same PIDs identified in VIR data, introduced in the previous section 4.9.

Figure 4.33 presents FC reflectance spectra and location of the nine PIDs. All of them show higher reflectance at 750 nm as well as higher pyroxene band strengths than their surroundings. Absolute values of the reflectance at 750 nm and pyroxene band strength (750/917 [nm]) as well as pyroxene band position (965/917 [nm]) and visible spectral slope (750/430 [nm]) are depicted in Table 4.8, including additional values from PIDs shown in Figure 4.10e, g and h, adding up to twelve PIDs in total. Spectra of PID #3 and its surrounding are shown in Figure 4.9. All PID and surrounding spectra show a small kink at 650 nm.

The average absolute difference between PIDs and their surroundings is 0.024 (±0.014) for reflectance at 750 nm and 0.149 (±0.057) for 750/917 [nm]. 965/917 [nm] values tend to increase for PIDs with respect to their surrounding, yet is only present for 9 out of 12 PIDs. This is not necessarily observable in Figure 4.12 and a new result. Visible spectral slopes tend to increase for PIDs with respect to their surroundings, which is valid for all presented PIDs except PID #12, which is situated in Calpurnia crater and is not representative of the PIDs in the ejecta, where the spectral changes are more systematic.

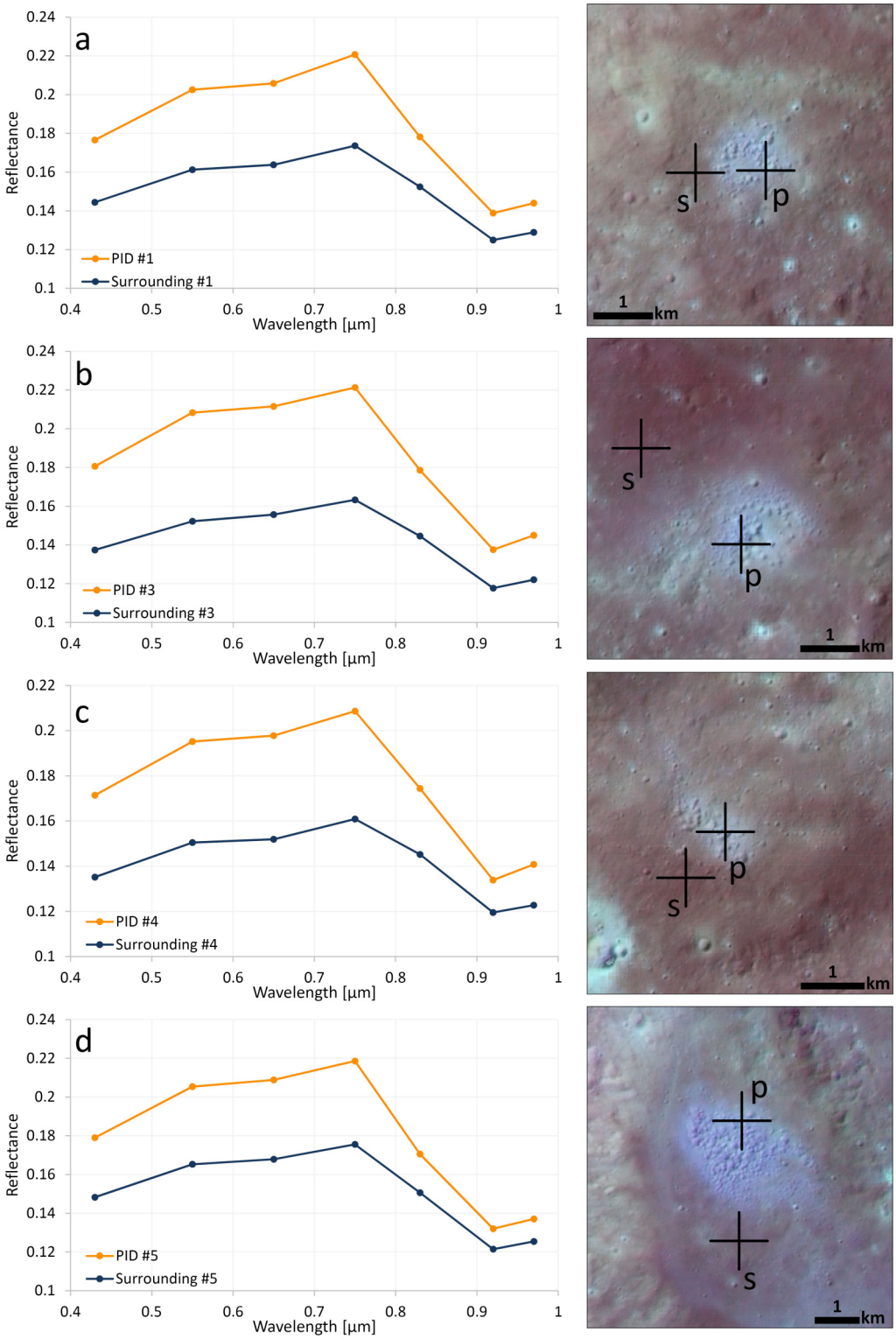


Figure 4.33: Spectra and locations of the nine PIDs and their surroundings presented in section 4.9. Crosses denote the location from where the spectra were taken, with p for PID and s for surrounding.

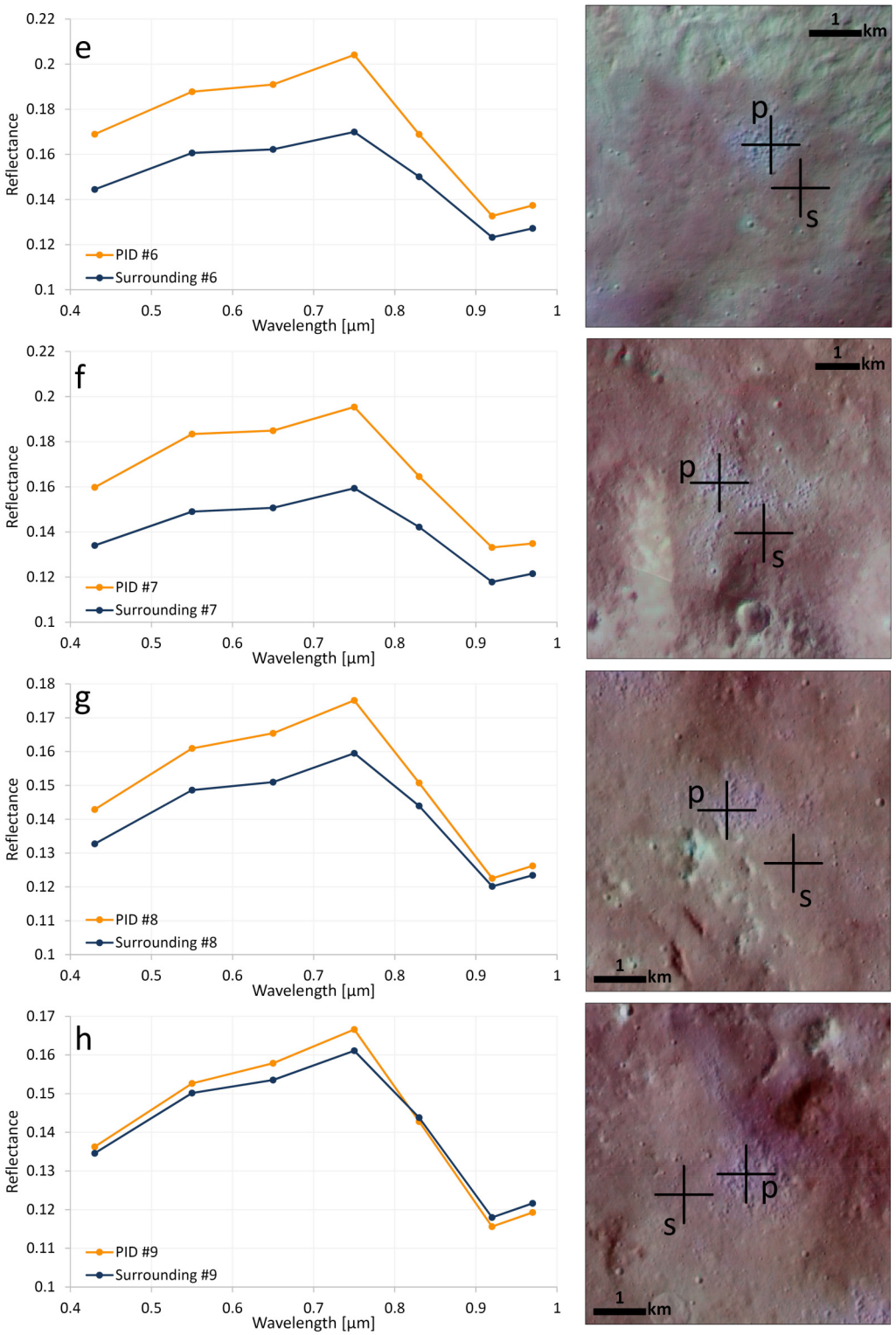


Figure 4.33: continued

Table 4.8: Spectral parameters of PIDs depicted in Figure 4.33: Reflectance at 750 nm, pyroxene band strength ratio 750/917 [nm], band position ratio 965/917 [nm] and visible spectral slope expressed by the ratio 750/430 [nm].

| Location | refl. at 750 nm | 750/917 [nm] | 965/917 [nm] | 750/430 [nm] |
|---|---|---|---|---|
| PID #1 | 0.209 | 1.586 | 1.037 | 1.250 |
| Surrounding #1 | 0.176 | 1.404 | 1.032 | 1.202 |
| PID #2 | 0.216 | 1.618 | 1.050 | 1.232 |
| Surrounding #2 | 0.173 | 1.388 | 1.032 | 1.179 |
| PID #3 | 0.211 | 1.608 | 1.054 | 1.225 |
| Surrounding #3 | 0.168 | 1.387 | 1.037 | 1.188 |
| PID #4 | 0.198 | 1.513 | 1.051 | 1.217 |
| Surrounding #4 | 0.167 | 1.367 | 1.027 | 1.190 |
| PID #5 | 0.202 | 1.685 | 1.038 | 1.221 |
| Surrounding #5 | 0.186 | 1.471 | 1.033 | 1.184 |
| PID #6 | 0.196 | 1.528 | 1.035 | 1.208 |
| Surrounding #6 | 0.176 | 1.413 | 1.032 | 1.176 |
| PID #7 | 0.183 | 1.450 | 1.013 | 1.223 |
| Surrounding #7 | 0.162 | 1.352 | 1.031 | 1.189 |
| PID #8 | 0.170 | 1.429 | 1.030 | 1.226 |
| Surrounding #8 | 0.163 | 1.343 | 1.027 | 1.202 |
| PID #9 | 0.165 | 1.435 | 1.032 | 1.223 |
| Surrounding #9 | 0.164 | 1.356 | 1.031 | 1.197 |
| PID #10 | 0.200 | 1.582 | 1.037 | 1.272 |
| Surrounding #10 | 0.161 | 1.366 | 1.032 | 1.194 |
| PID #11 | 0.171 | 1.436 | 1.037 | 1.198 |
| Surrounding #11 | 0.165 | 1.342 | 1.043 | 1.191 |
| PID #12 | 0.175 | 1.428 | 1.036 | 1.205 |
| Surrounding #12 | 0.148 | 1.318 | 1.037 | 1.229 |

Figure 4.34 is an advancement of Figure 4.13 which includes data of the PIDs presented in Figure 4.10 and section 4.9 as well as other locations of interest. In total, 12 PIDs and their surroundings are presented. A complete list of these PIDs and all other regions of interest and their values is included in the Appendix (12.3). Among the "eucritic" regions of interests are: northwestern crater wall of Marcia, another Marcia crater wall part directly above the halo, Cornelia crater wall, Cornelia ejecta, Fabia crater wall as well as regolith near the craters Fabia, Teia and Oppia. Among the "diogenitic" regions of interest are: Aelia ejecta, Lollia ejecta, Matronalia Rupes, Antonia crater wall, Fonteia crater wall, ejecta of a small crater just below Serena crater as well as regolith of the more diogenitic-rich part of Vesta, north of Matronalia Rupes. All regions of interest are additionally depicted for spatial context in the Appendix (12.4).

The most obvious difference of these two Figures is that the PIDs in Figure 4.34 do not show such a strongly deviating slope from the diogenitic and/or eucritic trend. Instead, their trend line runs almost parallel to that of diogenites and/or eucrites. It has to be kept in mind that additional PIDs were used here with respect to Fig. 4.13, so this difference might be caused by natural variations. The slopes are: 4.04 for eucritic regions, 4.49 for PIDs and 5.06 for diogenitic regions. Furthermore, 2.8 µm absorption depth values have to be handled with care as the resolution of this map is significantly lower than FC data (see Fig. 4.10). Thus, some areas like small PIDs or craters cannot be resolved by the 2.8 µm absorption depth data. This is also the reason why I excluded Aelia ejecta and the ejecta of the small unnamed crater below Serena crater from the data set for the 2.8 µm absorption depth (Fig. 4.34b), as nearby ejecta is high in 2.8 µm absorption depth values. Moreover, I excluded the diogenite-rich regolith from Figure 4.34a since it makes the plot less intuitive, as diogenite-rich materials can scatter anywhere below the illustrated trend line. The depicted line only illustrates the most diogenitic exposures (as mentioned in e.g., Combe et al., 2015b; Palomba et al., 2014; Stephan et al., 2015; Zambon et al., 2014, 2015). Data for

halo and crater-fill PID are off trends in both depicted plots. In Figure 4.34b, this is due to the OH-depleted nature of the crater center and 4.34a, the halo plots on the PID trendline whereas the crater-fill PID plots on the trendline of the surroundings, which is reasonable for the assumed process creating the spectral characteristics of these two regions of interest (see 6).

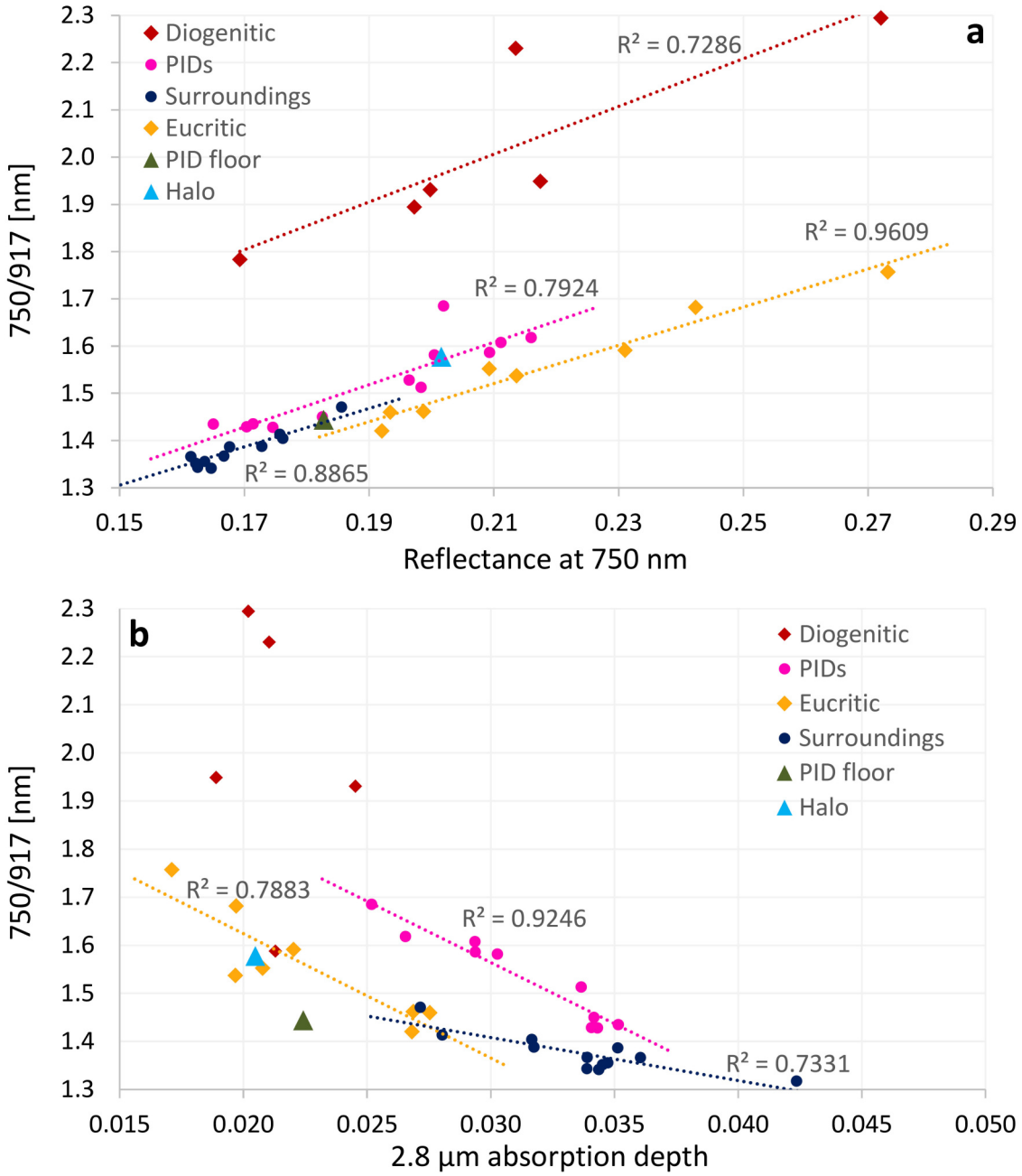


Figure 4.34: Reflectance at 750 nm vs. pyroxene band strength (750/917 [nm]) (**a**) and 2.8 µm absorption depth (generated by Combe et al. (2015a)) vs. pyroxene band strength (750/917 [nm]) (**b**) for PIDs, their surroundings, eucritic regions of interest, diogenitic regions of interest as well as the crater-fill PID ("PID floor") and the halo (see 4.11.

Despite this uncertainty, PIDs still stand out due to their higher pyroxene band depth ratio with respect to their reflectance at 750 nm. With respect to eucritic regions, these values tend to be generally larger. Similar values to those of PIDs do occur on Vesta. For example, for the range of 0.2-0.22 for reflectance at 750 nm and for 1.55-1.7 for 750/917 [nm] (largest values for PIDs),

various crater walls and also partly ejecta of well-preserved craters show these values (e.g., Marcia, Cornelia, Fabia, Lollia, and many other diogenite-rich craters), yet for Marcia ejecta, they appear distinct for PIDs (red in Fig. 4.35). In combination with the 2.8 µm absorption depth values, PIDs appear unique on Vesta.

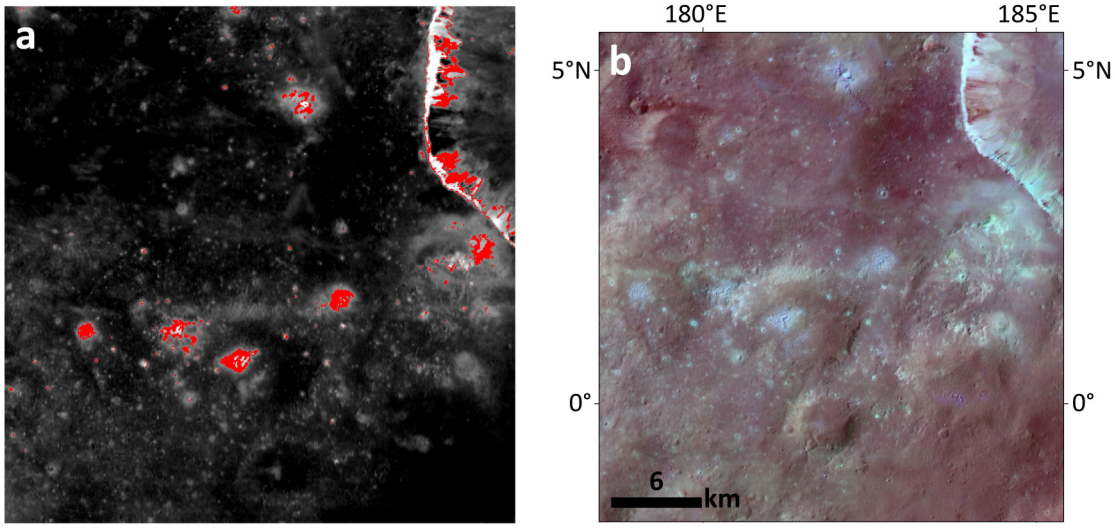


Figure 4.35: A: Region of interest (red) highlighting pixels that satisfy both a range of 0.2-0.22 for reflectance at 750 nm AND (intersected) for 1.55-1.7 for 750/917 [nm] over a HAMO 750/917 [nm] map. B: Spatial context showing several distinct PIDs, HAMO RGB composite (R= 965/917 [nm], G=750 nm and B=750/917 [nm]) over LAMO clear filter mosaic.

Finally, and to emphasize the spectral differences with respect to band strength, in Figure 4.36 I present two exemplary diagrams with normalized spectra of PID #2 and its surrounding as well as the halo, the crater-fill PID and the wall above the halo, according to what is shwon in Figure 4.32 for the second pyroxene absorption band. An interesting observation here is that the spectra of the wall above the halo does not feature the slight kink at 650 nm.

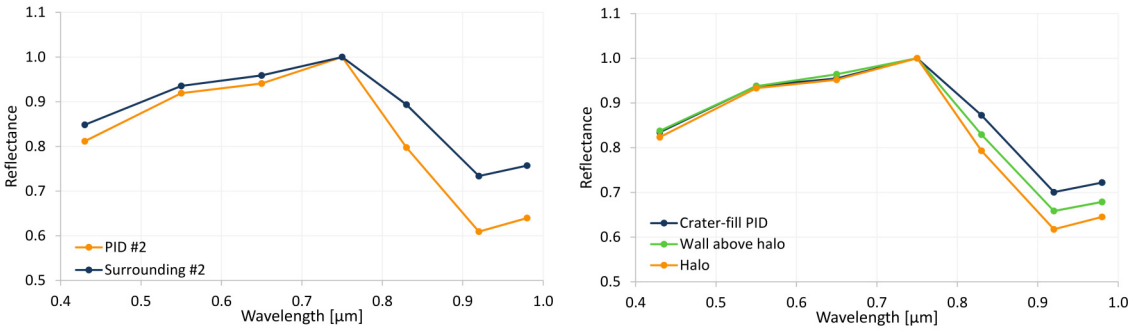


(a) (b)

Figure 4.36: Normalized spectra of (a) PID #2 and its surrounding and (b) the crater-fill PID, halo and crater wall spectra according to Figure 4.32.

# 5 Laboratory experiments at the Planetary Spectroscopy Laboratory

## 5.1 Grain Size and Compositional Variations

In the first set of experiments, devolatilization events were simulated. Grains that were transported during 'explosive events' were collected after the experiment with the best-possible efforts and their reflectance measured. The setup includes a cylindrical sample container of about 5 cm in diameter which contained various materials: **1)** "HypMoCa": A mixture of hypersthene (~71 wt%, <63-250 µm), montmorillonite (~28 wt%, <50 µm) and carbon black (~1 wt%, <50 µm) and **2)** "HypMur": A mixture of hypersthene (~99 wt%, <63-250 µm) and Murchison (~1 wt%, <50 µm). The montmorillonite serves as an analog for phyllosilicates in the Vestan regolith and the carbon black as a darkening agent as observed on Vesta (e.g., De Sanctis et al., 2012b; McCord et al., 2012). Murchison also serves as a darkening agent, although to a much lesser extent.

Both mixtures HypMoCa and HypMur were placed atop a distilled water ice layer and heated to 200 °C in order to enhance sublimation and degassing processes (termed "layered 200°C" in Figs. 5.1 and 5.2). HypMoCa was additionally placed atop a distilled water ice layer and left to sublimate at room temperature (termed "layered"). Another aliquot of HypMoCa was mixed with liquid water before cooling down (termed "muddy") and also left to sublimate at room temperature. After sample preparation and the procedure described in section 2.5, samples were put into vacuum and left to sublimate, partly while heating them to 200 °C (as described before).

The muddy HypMoCa sample did not show any signs of grain movement, instead, its surface appeared as a 'frozen mud', experiencing small cracks (max. 1 mm). For HypMoCa atop the water ice layer sublimating at room temperature, no grain transport or degassing events were observed. The measured reminder after sublimation is termed "layered" in Figures 5.1 and 5.2. Figure 5.1 illustrates the spectral parameters of the laboratory experiments as shown for Vesta and HED data in Figs. 2.5, 4.12, again calculated with the same method used to resample the meteorite spectra (to match the Dawn FC format) as shown in section 2.4, equation (1). In Figure 5.1, multiple measurements were not averaged and all measurements are shown as single data points. Figure 5.2 illustrates the results of HypMoCa and HypMur as whole absolute reflectance spectra, for which multiple measurements were averaged.

For experiments that involved heating (termed "layered 200 °C"), the layered samples on top of water ice produced grain transport outside the chamber and a lid was placed on top of the sample holder, leaving an opening for particles to escape of a few mm. On this lid, grains became attached and were collected for measurement (termed "dust"). For both mixtures, only fine-grained material was observed sticking to the lid and this dust also contained dark grains. The remainder within the sample container of HypMoCa (termed "layered 200°C") still contained various grain sizes and fine-grained light and dark grains were observed to stick on the larger hypersthene grains. For HypMur, this remainder mostly contained large hypersthene grains. Retrieved dust particles generally exhibit high overall reflectance but lower pyroxene band strength values for both mixtures (Fig. 5.2). Important to note, intermediate particles were also observed to emerge from the sample container through the lid opening yet did not became attached to the lid. For HypMur, these emerged grains were retrieved from the experiment chamber and measured (termed "emerged material" in Fig. 5.1). Interestingly, this emerged material exhibits larger pyroxene band strength, but also higher 965/917 [nm] values. The HypMoCa remainder, formerly atop water ice, after sublimating at room temperature, has a very similar spectra with respect to the dry mixture. Both mixtures that were heated to 200 °C and remained within the sample holder show lower absolute reflectance but similar 750/917 [nm] and 965/917 [nm] values with respect to the dry sample. In general, spectral changes that occurred in this set of experiments affect both the 750/917 [nm] and 965/917 [nm] values (Fig. 5.1). None of the treated samples resulted in spectral characteristics similar to that of the PIDs with respect to their surrounding. Limitations of the presented grain size considerations are discussed in section 7.

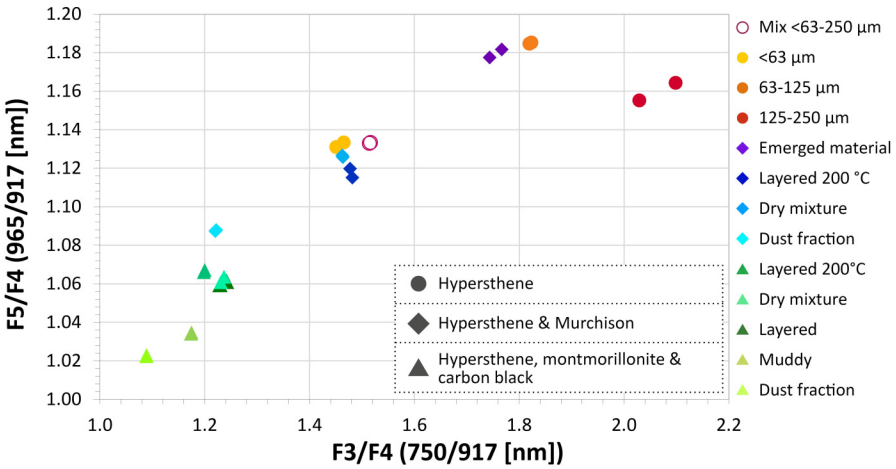


Figure 5.1: 750/917 [nm] vs. 965/917 [nm] for laboratory sublimation experiments including the mixtures HypMoCa and HypMur. For comparison, several grain size fractions of pure hypersthene are displayed. None of the treated mixtures increase their pyroxene band strength (750/917 [nm]). Given Filter numbers illustrate that values were calculated according to the Dawn FC filter format. See Fig. 4.12 for PID and surrounding values.

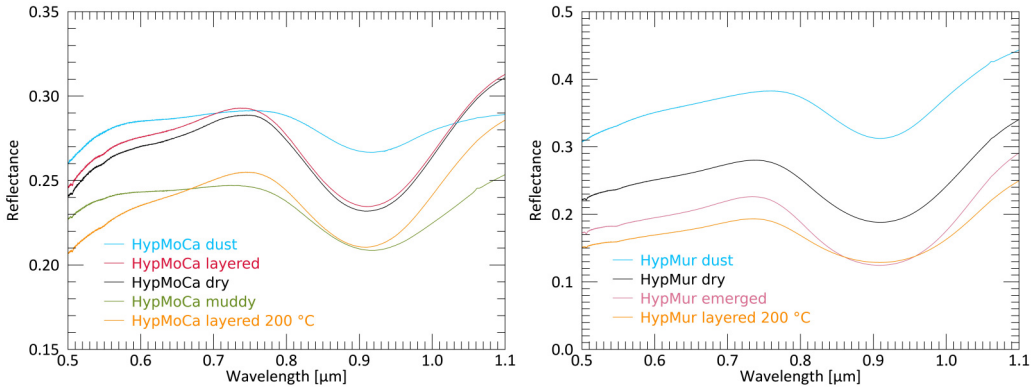


(a) (b)

Figure 5.2: Wavelength vs. reflectance for laboratory sublimation experiments of the mixtures HypMoCa (a) and HypMur (b).

In another set of measurements, without heating or sublimation experiments, I investigated the effects of both variations in grain size and abundance of dark, reflectance lowering components. For this series of measurements, I solely used hypersthene and the Phobos Simulant (i.e., Phobos Simulant as 'dark material') as mixture endmembers for the samples H98P02, H95P05, H92P08 and H90P10. These samples, first of all, have different abundances of the Phobos Simulant with respect to hypersthene (see also Table 2.1). Additionally, these samples were prepared repeatedly with different hypersthene grain sizes. As grain size variations of hypersthene are vastly dominating the spectral characteristics, the grain size of the Phobos Simulant remained the same, <25-63 µm). Hypersthene grains were added either as 25-250 µm (medium), <25-63 µm (small) or 125-250 µm (large). Spectral parameters will be shown from this section on in a Table format as they include more parameters.

Figure 5.3 shows the spectra of the different samples with different grain sizes followed by Table 5.1 with the spectral parameters pyroxene band strength, band position, visible spectral slope and reflectance at 750 nm. These values are calculated with the same method used to resample the meteorite spectra (to match the Dawn FC format) as shown in section 2.4, equation (1). The subsequent Figure 5.4 shows the spectra in combination with each other according to my observations of the Vestan PIDs: Displayed is a gradual series of smaller grain sizes of hypersthene

(this favors higher reflectance) with smaller contents of dark material (this favors higher pyroxene band strength with respect to materials with higher dark material abundance) to larger grain sizes with higher contents of dark material.

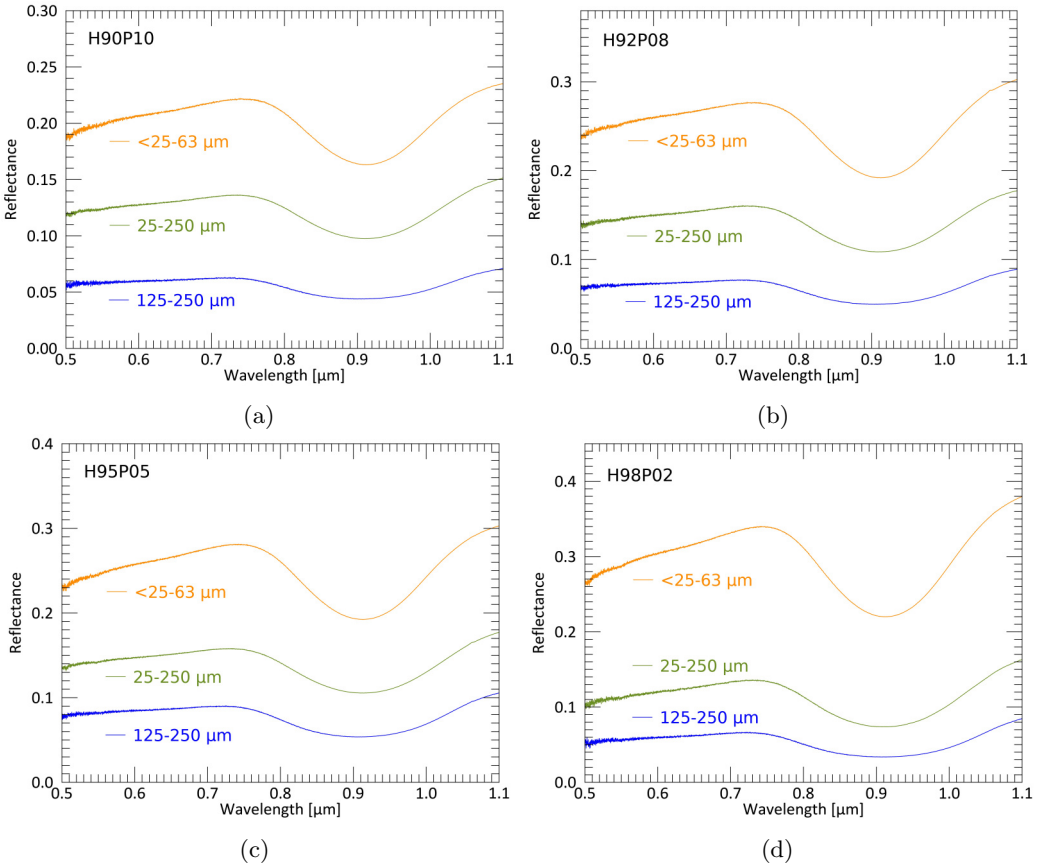


Figure 5.3: Reflectance spectra of H90P10 (a), H92P08 (b), H95P05 (c) and H98P02 (d) and different hypersthene grain sizes.

Table 5.1 illustrates that with increasing grain size, pyroxene band strengths gradually increase while reflectance at 750 nm significantly decrease. The visible spectral slope ratio generally decreases from small to large grain sizes except for H98P02. The band position parameter does not appear to show any systematics with respect to increasing grain sizes. The observations of pyroxene band strength and reflectance are consistent with every mixture and in accordance to literature review and the grain size comparisons with HEDs as presented in section 7. The observed differences between spectra of the different grain size aliquots generally grow larger with less dark material abundance and higher hypersthene abundance.

Now, the combined modification of grain size AND dark material abundance yields different results. Figure 5.4 shows the differences between spectra with smaller grain sizes and less dark material and spectra with larger grain sizes and more dark material. The addition of dark, CC-like material to HEDs generally results in the reduction of overall reflectance and diminishment of spectral features like absorption bands (Cloutis et al., 2013a). According to Table 5.1, Figure 5.4a shows that H98P02, >25-63 µm shows higher reflectance and pyroxene absorption strength with respect to H95P05, 25-250 µm and this sample also shows higher reflectance and pyroxene band strength than H90P10, 125-250 µm. The differences in reflectance are very large (10-20%), which shows that little variations to grain size and dark material abundance can generally lead to the observed spectral characteristics of PIDs and their surroundings. This is emphasized in Figure 5.4b where the small grain size fraction of H92P08 exhibits both higher pyroxene band strength and reflectance at 750 nm with respect to the medium grain size fraction of H90P10; thus a little variation of 2 wt% more hypersthene or less dark material, respectively, can lead to the general

Table 5.1: Spectral parameters for pyroxene band strength, band position, visible spectral slope and reflectance at 750 nm for the surface and interior of H90P10, H92P08, H95P05 and H98P02 for different hypersthene grain sizes.

| Grain Size [µm] | 750/917 [nm] | 965/917 [nm] | 750/430 [nm] | 750 nm |
|---|---|---|---|---|
| H90P10 | | | | |
| <25-63 | 1.338 | 1.095 | 1.312 | 0.221 |
| 25-250 | 1.373 | 1.094 | 1.255 | 0.135 |
| 125-250 | 1.377 | 1.085 | 1.059 | 0.061 |
| H92P08 | | | | |
| <25-63 | 1.416 | 1.117 | 1.312 | 0.275 |
| 25-250 | 1.442 | 1.109 | 1.297 | 0.158 |
| 125-250 | 1.491 | 1.107 | 1.175 | 0.075 |
| H95P05 | | | | |
| <25-63 | 1.437 | 1.116 | 1.367 | 0.280 |
| 25-250 | 1.466 | 1.102 | 1.241 | 0.156 |
| 125-250 | 1.607 | 1.121 | 1.168 | 0.087 |
| H98P02 | | | | |
| <25-63 | 1.516 | 1.137 | 1.432 | 0.338 |
| 25-250 | 1.777 | 1.174 | 1.451 | 0.133 |
| 125-250 | 1.850 | 1.155 | 1.326 | 0.064 |

trend observed for PIDs vs. their surroundings.

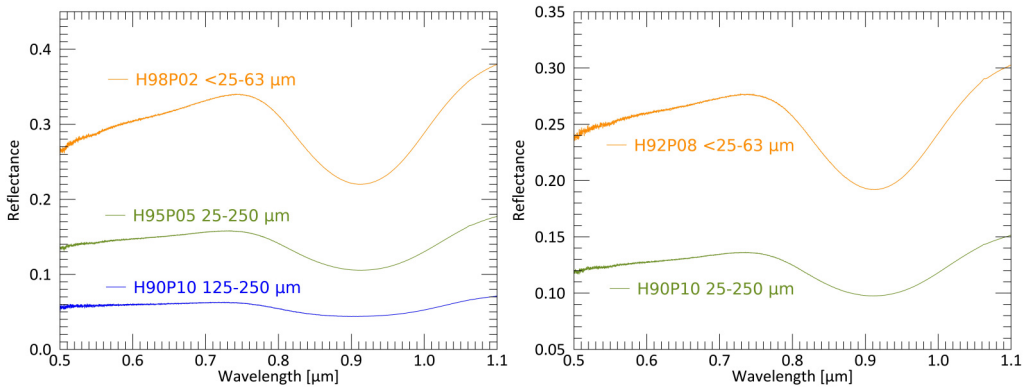


(a) (b)

Figure 5.4: Reflectance spectra of smaller grain size fractions and lower abundance of dark material in comparison with spectra of larger grain sizes and higher abundances of dark material.

## 5.2 Results from Temperature Variations

### 5.2.1 Temperature increase

In the following, experimental results of low to moderate temperature increases of the samples are shown. Samples were heated to 200, 400 and 600 °C for durations of 2, 72 and 168 h according to Table 2.1. It is worth noting that degassing events were not observed during this suite of heating experiments and emerging grains were non-existent or only minor and not retrievable. I use specified colors to illustrate the different sequences. The unheated samples are represented by black lines. The 200 °C, 2 h experiments, are displayed in *forest green*, 400 °C, 2 h in *light coral* and 600 °C, 2 h in *dark magenta*. The 200 °C, 72h experiments are displayed in *deep sky blue*, 400 °C, 72 h in *dark orange* and 600 °C, 72 h in *deep pink*. When showing spectra of the same temperature yet different durations, the color *royal blue* is used for the 2 h spectra and *crimson* for the 72 h spectra in order to facilitate the perception. The colors are named according to the official IDL !COLOR system variable.

Furthermore, the pyroxene band strength (750/917 [nm]), the band position (965/917 [nm]), the visible spectral slope (750/430 [nm]), and the reflectance at 750 nm are calculated with the same method used to resample the meteorite spectra (to match the Dawn FC format) as shown in section 2.4, equation (1).

The first presentation of results regard the meteoritic sample NWA5748M as this sample has the most complete data set. Other meteoritic samples were heated mostly for comparisons and not to the same extent. Table 5.2 displays the described calculated values and the following figures illustrate these as whole reflectance spectra obtained in the PSL.

Figure 5.5 shows the reflectance spectra from 0.5 to 1.1 µm of NWA5748M: unheated and heated to the described temperatures for (a) 2 and (b) 72 hours. Figure 5.5c illustrates the normalized spectra in order to evaluate the different band strengths and visible spectral slopes. The y-axis will keep the same values for an easier absolute comparison and all legends in this section are sorted after the spectra's reflectance values at 0.5 µm.

Figure 5.5 shows that the overall reflectance levels are higher for the 2 h experiments and less intuitive (decrease of reflectance from 200 °C to 400 °C and a steep increase for 600 °C) than the 72 h experiments. However, band strength values steadily increase from 200 °C to 600 °C (Table 5.2) for the 2 h experiments. For the 72 h experiments, reflectance levels are generally lower yet the heating sequence behaves more linear in the way that higher temperatures yield a larger visible spectral slope and higher reflectance values at 750 nm. However, band strengths steadily decrease in this sequence. The normalized spectra show that the visible spectral slope steadily increases with temperature and time (except for 600 °C and 72 h) and that band strengths are stronger for the 2 h experiments than for the 72 h experiments (for 200 °C, there appears to be no significant difference). Thus, a longer duration of heating appears to lead to reduced band strengths. Band positions appear to slightly shift to shorter wavelengths (indicated by higher 965/917 [nm] values).

It is also worth to directly compare samples that were heated to the same temperature for different durations in order to see if time plays a role. For NWA5748M, this is displayed in Figure 5.6. At 200 °C, the longer duration of heating leads to a decrease of reflectance, about the same band strength, and elevated slope (Table 5.2). At 400 °C, heating of NWA5748M leads to a slight increase of reflectance at 750 nm and visible spectral slope but decrease of band strength. At 600 °C, longer heating results in decrease of reflectance at 750 nm and decrease of band strength as well as visible spectral slope. Thus, all temperature variations show different patterns. However, as mentioned earlier, in all cases the band position slightly increases from 2 h to 72 h. These experiments were partly repeated for other meteoritic mixtures and yielded different results which will be shown later on.

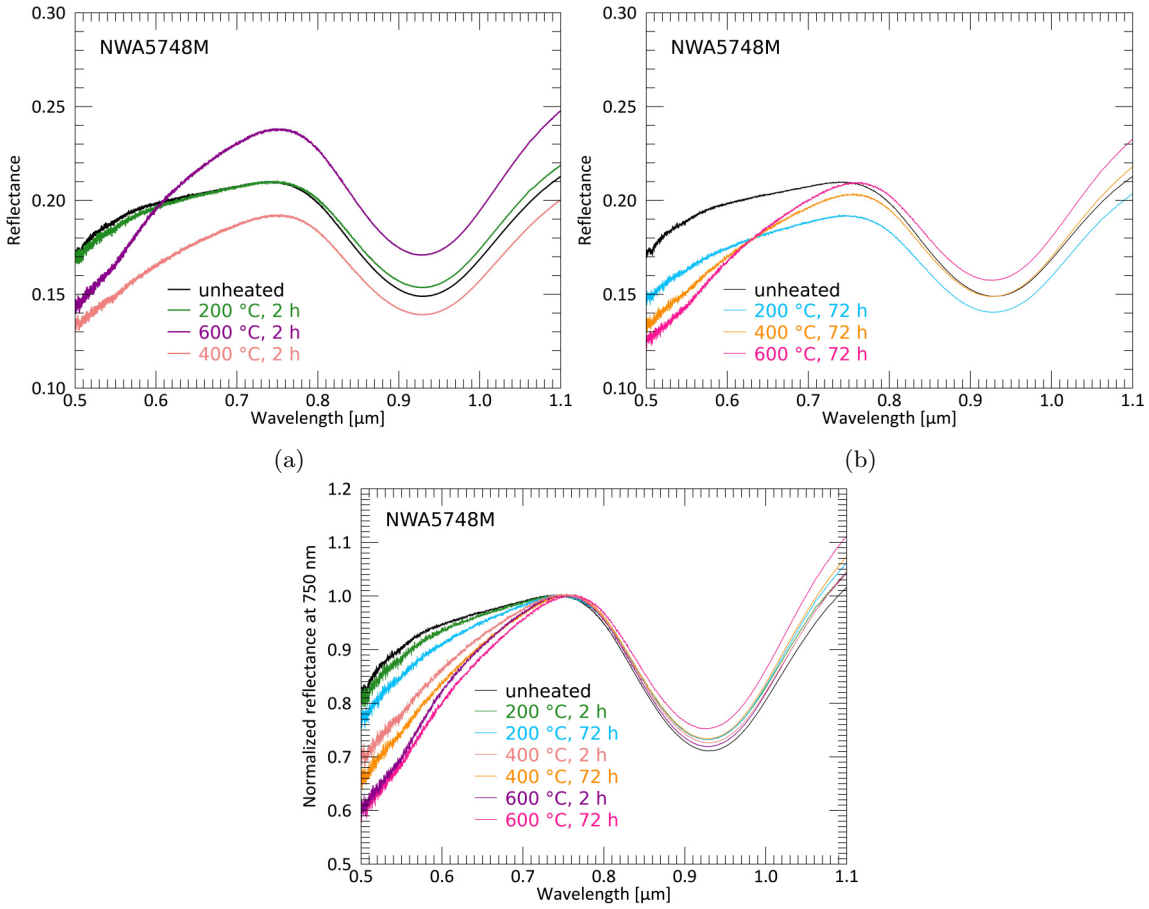


Figure 5.5: Reflectance spectra of NWA5748M after heating to 200, 400 and 600 °C for 2 (a) and 72 (b) hours and all spectra together as normalized reflectance at 750 nm (c) to visualize the differences in visible spectral slope and band strength.

Table 5.2: Spectral parameters for pyroxene band strength, band position, visible spectral slope and reflectance at 750 nm for NWA5748M aliquots heated to different temperatures (T) and durations (t), calculated using the resampling method presented in section 2.4.

| T [°C] & t [h] | 750/917 [nm] | 965/917 [nm] | 750/430 [nm] | 750 nm |
|---|---|---|---|---|
| unheated | 1.388 | 1.046 | 1.380 | 0.209 |
| 200, 2 | 1.348 | 1.047 | 1.370 | 0.209 |
| 200, 72 | 1.349 | 1.049 | 1.432 | 0.191 |
| 400, 2 | 1.362 | 1.045 | 1.643 | 0.191 |
| 400, 72 | 1.348 | 1.052 | 1.649 | 0.202 |
| 600, 2 | 1.374 | 1.049 | 1.866 | 0.237 |
| 600, 72 | 1.313 | 1.055 | 1.817 | 0.208 |

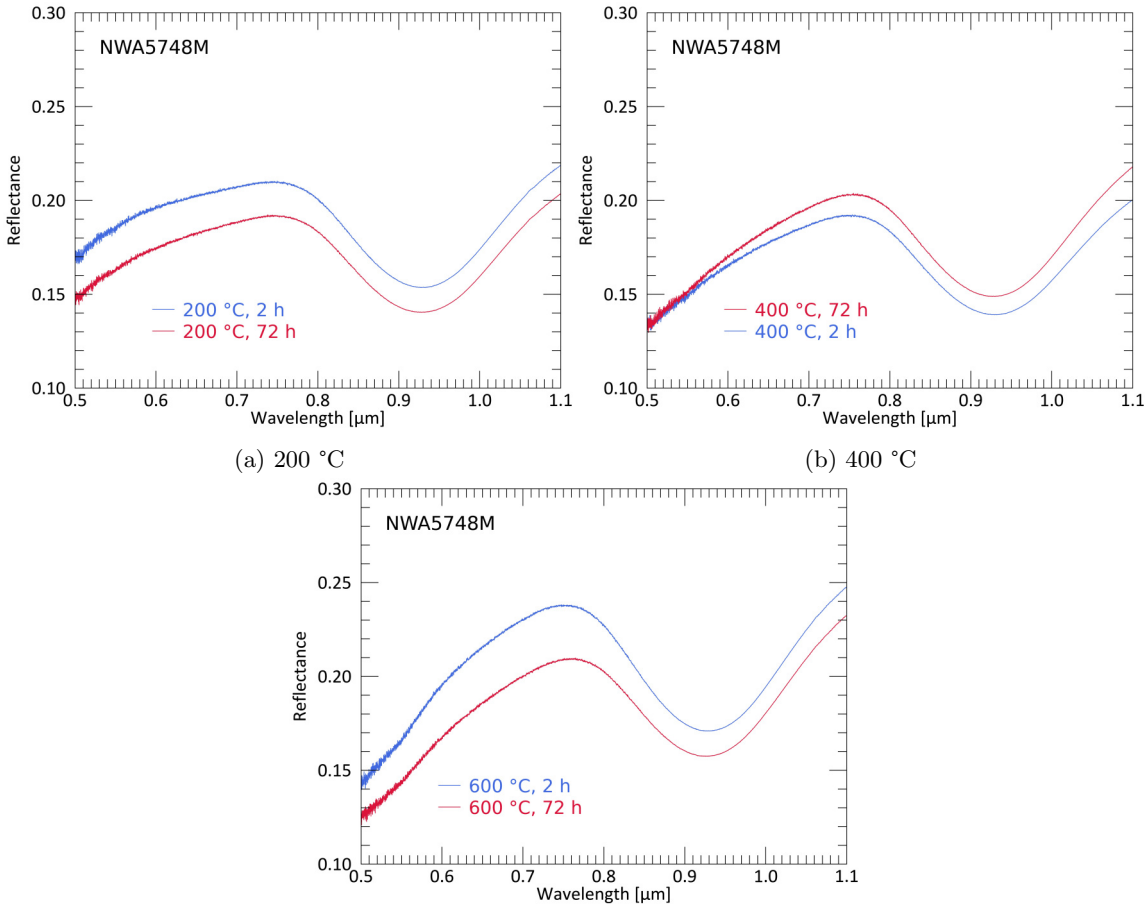


(a) 200 °C

(b) 400 °C

(c) 600 °C

Figure 5.6: Reflectance spectra of NWA5748M after heating to 200 °C (a), 400 °C (b) and 600 °C (c) for 2 (blue) and 72 (red) hours.

The same temperatures and durations were applied to the terrestrial analog H90P10 (90 wt% hypersthene and 10 wt% Phobos Simulant), which is shown in Figure 5.7. Here, the increase of temperature does not yield the same elevated reflectance and visible spectral slope patterns. The 2 h experiments steadily decrease in reflectance and pyroxene band strength. This is true for the 200 °C and 400 °C experiments at 72 h, as well. At 600 °C and 72 h, a significantly increased visible spectral slope is observable. Moreover, the reflectance at 750 nm increases to levels of the unheated sample and the pyroxene band strength exceeds that of 600 °C, 2 h and of 400 °C, 72 h. This indicates a mechanism taking place between 400 °C and 600 °C when the sample is heated for longer durations.

The pyroxene absorption band of EA90P10 (Fig. 5.7d) is significantly reduced with respect to all other analogs (compare the y-axis range). This is probably due to the addition of plagioclase and therefore, the reduction of pyroxene. A similar effect can be seen through spectra of diogenites and eucrites (Figure 2.5), as diogenites contain significantly more pyroxene than eucrites which contain more plagioclase (e.g., Mittlefehldt, 2015 and references therein). Heating of EA90P10 generally also results in the reduction of overall reflectance and pyroxene band strength and it is notable that the sample heated to 400 °C for 72 h exhibits a significantly shallower pyroxene absorption band. This significant reduction (to values <1) is not observed for other regolith analogs (only for the dark material analog endmembers seen in Figure 5.10 and Table 5.6).

For H80P20 and H70P30, only limited data could be acquired. All heated spectra show lower pyroxene band strength with respect to the unheated aliquot. The H80P20 aliquot heated to 400 °C for 72 h shows lower pyroxene band strength than the one heated to 400 °C for 2 h. The reduction of pyroxene band strength and reflectance at 750 nm is significantly higher for H80P20 than for H70P30.

Table 5.3: Spectral parameters for pyroxene band strength, band position, visible spectral slope and reflectance at 750 nm for H90P10 and EA90P10 aliquots heated to different temperatures (T) and durations (t), calculated using the resampling method presented in section 2.4.

| T [°C] & t [h] | 750/917 [nm] | 965/917 [nm] | 750/430 [nm] | 750 nm |
|---|---|---|---|---|
| H90P10 | | | | |
| unheated | 1.373 | 1.094 | 1.255 | 0.135 |
| 200, 2 | 1.320 | 1.090 | 1.328 | 0.129 |
| 200, 72 | 1.321 | 1.092 | 1.202 | 0.128 |
| 400, 2 | 1.268 | 1.077 | 1.257 | 0.107 |
| 400, 72 | 1.251 | 1.079 | 1.232 | 0.121 |
| 600, 2 | 1.245 | 1.087 | 1.322 | 0.104 |
| 600, 72 | 1.259 | 1.096 | 1.547 | 0.136 |
| EA90P10 | | | | |
| unheated | 1.039 | 0.997 | 1.137 | 0.115 |
| 200, 2 | 1.021 | 0.998 | 1.161 | 0.114 |
| 400, 2 | 1.026 | 0.997 | 1.194 | 0.103 |
| 400, 72 | 0.995 | 1.003 | 1.294 | 0.103 |
| H80P20 | | | | |
| unheated | 1.248 | 1.062 | 1.100 | 0.080 |
| 400, 2 | 1.246 | 1.060 | 1.186 | 0.084 |
| 400, 72 | 1.133 | 1.054 | 1.204 | 0.059 |
| H70P30 | | | | |
| unheated | 1.176 | 1.049 | 1.050 | 0.068 |
| 400, 72 | 1.131 | 1.043 | 1.092 | 0.062 |

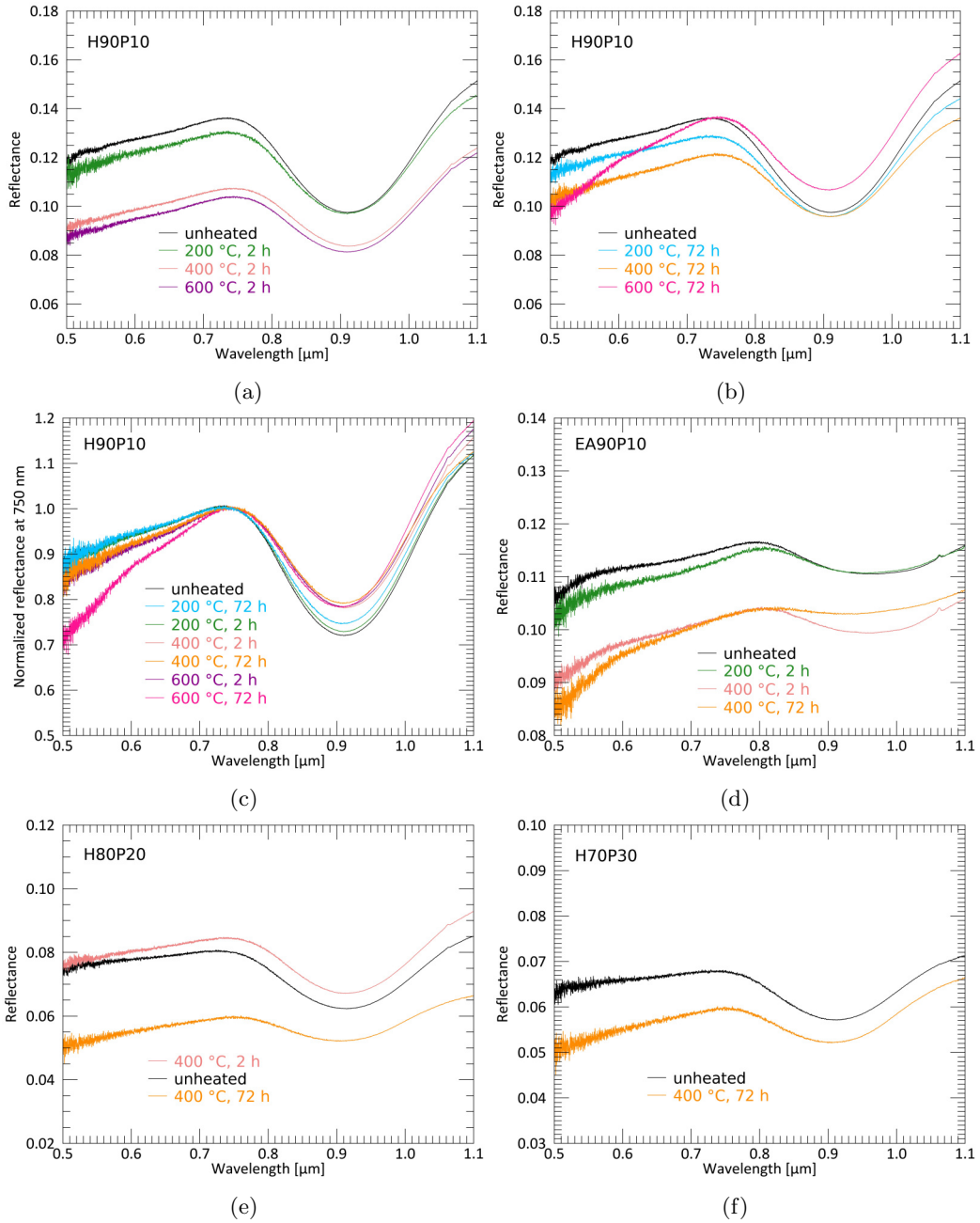


Figure 5.7: Reflectance spectra of H90P10 after heating to 200, 400 and 600 °C for 2 (a) and 72 (b) hours as well as spectra of EA90P10, H80P20 and H70P30. C) shows normalized reflectance at 750 nm to visualize the differences in visible spectral slope and band strength. D) presents the spectra of EA90P10, where instead of only hypersthene, a mixture of pigeonite, labradorite, anorthite is used as HED analog. E) and f) show the (limited) spectra acquired from H80P20 and H70P30.

Direct comparisons between H90P10 aliquots heated to the same temperature yet different durations are shown as whole reflectance spectra in Figure 5.8. At 200 °C, the spectral characteristics of H90P10 remain very similar for both durations, yet for 400 °C and 600 °C, the aliquots heated for 72 h yield significantly higher reflectance and for 600 °C even a slightly larger pyroxene band strength (Table 5.3). Also note that the visible spectral slope significantly increases at 600 °C from 2 h to 72 h.

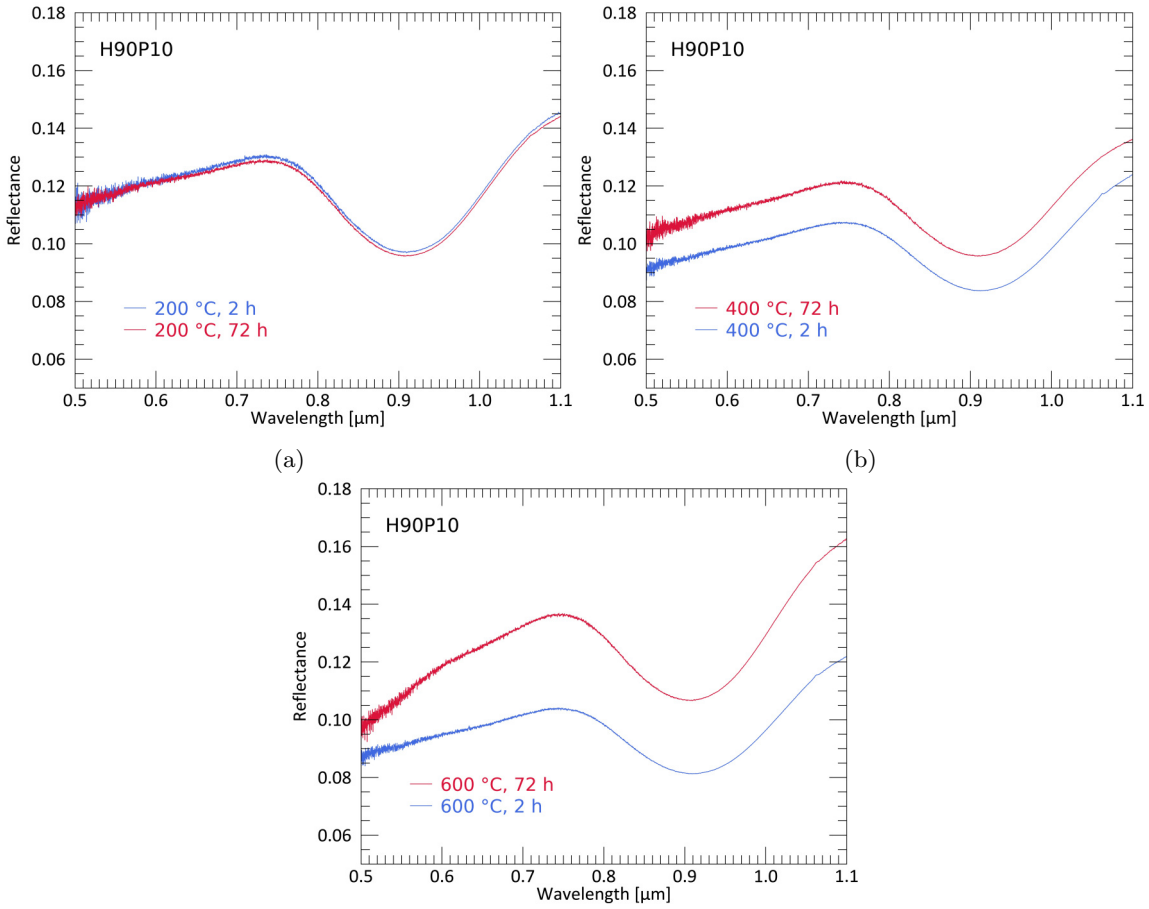


Figure 5.8: Reflectance spectra of H90P10 after heating to 200 °C (a), 400 °C (b) and 600 °C (c) for 2 and 72 hours.

In the following, I present more data of meteoritic and terrestrial samples that do not cover the whole temperature and/or duration range as for NWA5748M and H90P10. They still provide important data for comparisons and an evaluation based on multiple data sets. I start with meteoritic samples and then present data of the terrestrial samples.

NWA5230M was heated to 300, 400 and 600 °C while JaH626M was heated to 200 and 600 °C. Both were heated to 400 °C for 168 h (one week). This is displayed in Figure 5.9, where NWA5230M is displayed in the upper row (a and b) and JaH626 in the lower row (c and d). The data is displayed in a lesser extent as for NWA5748M and H90P10 and includes the Figures for the 2 h and 72 h experiments, including the 168 h experiment (colored in "maroon")). For other considerations like differences between short and long durations, the previously described spectral parameters are given in Tables 5.4 and 5.5. Pyroxene band position values for JaH626 are below one, which is a result of its generally shifted absorption band to longer wavelenghts. Then, the 965 nm reflectance value becomes smaller than the one at 917 nm.

The heating experiments with NWA5230M and JaH626 yield similar results to NWA5748M. Especially for the 600 °C experiments, the visible spectral slope changed significantly to higher values. The aliquots that were heated to 400 °C, 168 h (one week) likewise resulted in a very steep visible spectral slope like those heated to 600 °C. Heating to lower temperatures did not result in such significant changes of the visible spectral slope. In general, the higher temperature samples exhibit the highest reflectances at 750 nm while the pyroxene band strength values do not increase for these experiments. Interestingly, the 300 °C, 2 and 72 h experiments of NWA5230M yield higher reflectance and pyroxene band strength than the 400 °C, 2 and 72 h of the same meteoritic mixture.

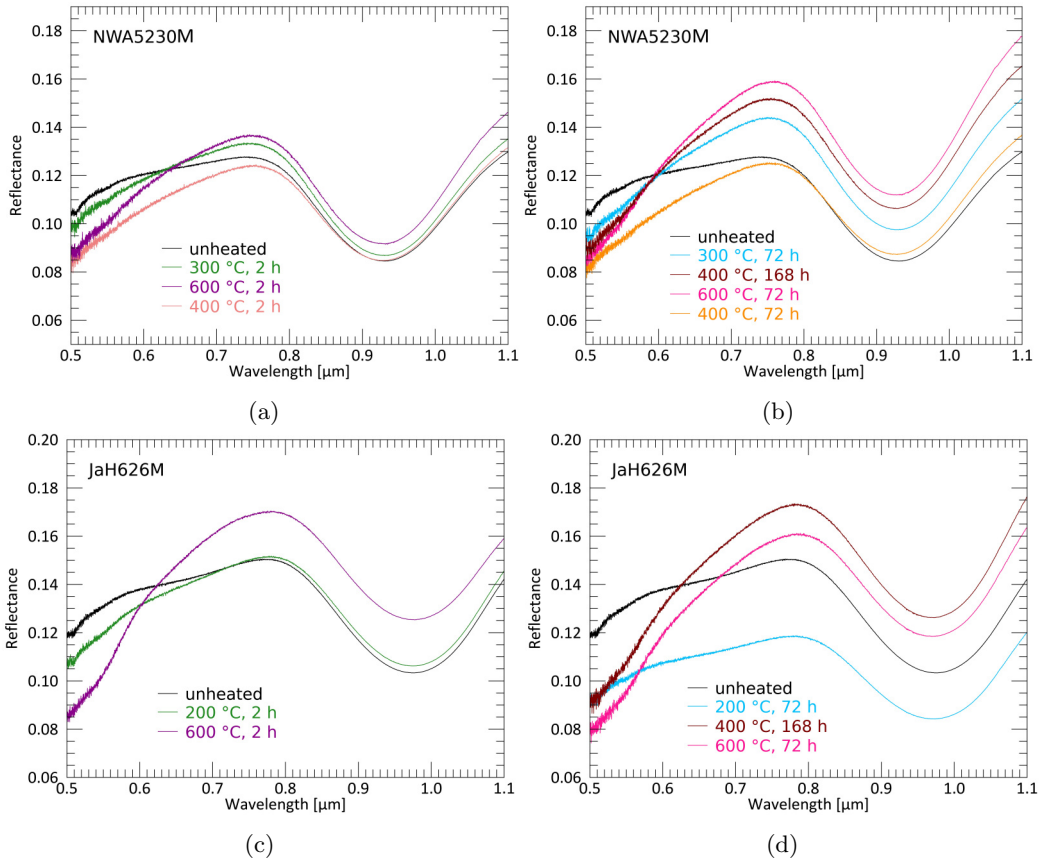


Figure 5.9: Reflectance spectra of NWA5230M (upper row) and JaH626 (lower row) for the 2 (a and c), 72, and 168 h (b and d) experiments.

Table 5.4: Spectral parameters for pyroxene band strength, band position, visible spectral slope and reflectance at 750 nm for NWA5230M aliquots heated to different temperatures (T) and durations (t), calculated using the resampling method presented in section 2.4.

| T [°C] & t [h] | 750/917 [nm] | 965/917 [nm] | 750/430 [nm] | 750 nm |
|---|---|---|---|---|
| unheated | 1.485 | 1.056 | 1.390 | 0.127 |
| 300, 2 | 1.508 | 1.057 | 1.616 | 0.133 |
| 300, 72 | 1.452 | 1.060 | 1.610 | 0.143 |
| 400, 2 | 1.439 | 1.061 | 1.663 | 0.123 |
| 400, 72 | 1.412 | 1.065 | 1.706 | 0.124 |
| 400, 168 | 1.406 | 1.066 | 1.943 | 0.151 |
| 600, 2 | 1.466 | 1.065 | 1.766 | 0.136 |
| 600, 72 | 1.398 | 1.068 | 2.257 | 0.158 |

Table 5.5: Spectral parameters for pyroxene band strength, band position, visible spectral slope and reflectance at 750 nm for JaH626 aliquots heated to different temperatures (T) and durations (t), calculated using the resampling method presented in section 2.4.

| T [°C] & t [h] | 750/917 [nm] | 965/917 [nm] | 750/430 [nm] | 750 nm |
|---|---|---|---|---|
| unheated | 1.337 | 0.943 | 1.411 | 0.149 |
| 200, 2 | 1.309 | 0.945 | 1.581 | 0.150 |
| 200, 72 | 1.300 | 0.949 | 1.436 | 0.117 |
| 400, 168 | 1.264 | 0.954 | 2.403 | 0.170 |
| 600, 2 | 1.256 | 0.951 | 2.358 | 0.168 |
| 600, 72 | 1.253 | 0.957 | 2.077 | 0.157 |

In the following, I will display results of heating endmember materials, namely Murchison, the Phobos Simulant, Hypersthene as well as NWA5748 and NWA3359. The former two represent the dark material (CC) mixed into the Vestan regolith and the latter three represent the endogenic pyroxene-rich components of the Vestan regolith. The results of heating these samples to 400 °C, 72 h are displayed in Figure 5.10. This temperature and duration appears to be one of the likeliest candidates for the conditions that Vestan PID material underwent (see Michalik et al., 2021 and section 6).

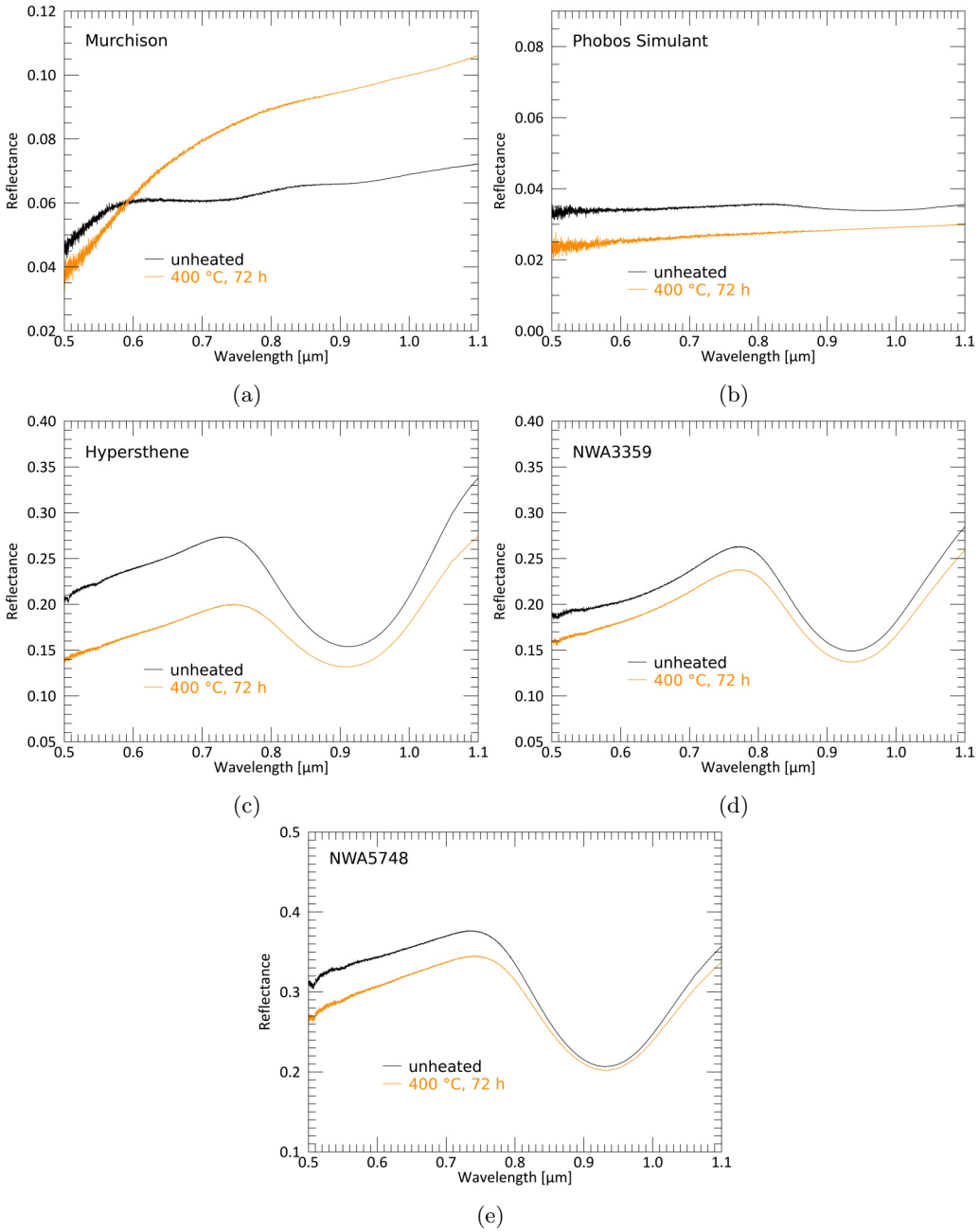


Figure 5.10: Reflectance spectra of Vestan regolith endmember samples, displayed in unheated condition and after 400 °C and 72 h: a) Murchison, b) Phobos Simulant, c) Hypersthene, d) NWA3359, e) NWA5748.

The most notable result of this heating suite is that the heated Murchison sample shows a significant increase of reflectance with respect to the unheated sample. This effect is not observed for the Phobos Simulant or for Hypersthene and the pure HEDs NWA3359 and NWA5748. While the reflectance of all other heated spectra in Figure 5.10 remain below their unheated counterpart for all wavelengths – though partly increasing in overall slope as well – Murchison exceeds its unheated aliquot by far beyond ~0.6 µm. Furthermore, Murchison is the only sample that experiences a significant reddening in the VIS wavelength region.

Table 5.6 gives the spectral parameters for the endmember samples displayed in Figure 5.10. It shows that the observations of the whole spectra translate into the resampled values of the spectral parameters. The visible spectral slope (750/430 [nm]) increases drastically for Murchison, comparable to some of the meteoritic mixtures heated at 600 °C or 400 °C for 168 hours. This strongly indicates that Murchison is responsible for the observed spectral change for the meteoritic analog samples. However, I note that heating of the terrestrial sample H90P10 could also produce higher visible spectral slopes and (beyond 750 nm) reflectance with respect to the unheated aliquot.

Table 5.6: Spectral parameters for pyroxene band strength, band position, visible spectral slope and reflectance at 750 nm for Murchison, Phobos Simulant, Hypersthene, NWA5748 and NWA3359 heated to 400 °C for 72 h, calculated using the resampling method presented in section 2.4.

| T [°C] & t [h] | 750/917 [nm] | 965/917 [nm] | 750/430 [nm] | 750 nm |
|---|---|---|---|---|
| Murchison | | | | |
| unheated | 0.929 | 1.022 | 1.524 | 0.061 |
| 400, 72 | 0.890 | 1.027 | 2.614 | 0.085 |
| Phobos Simulant | | | | |
| unheated | 1.029 | 0.995 | 1.023 | 0.035 |
| 400, 72 | 0.953 | 1.016 | 1.058 | 0.027 |
| Hypersthene | | | | |
| unheated | 1.724 | 1.152 | 1.493 | 0.269 |
| 400, 72 | 1.482 | 1.156 | 1.615 | 0.198 |
| NWA5748 | | | | |
| unheated | 1.770 | 1.064 | 1.320 | 0.373 |
| 400, 72 | 1.665 | 1.059 | 1.442 | 0.342 |
| NWA3359 | | | | |
| unheated | 1.682 | 1.058 | 1.480 | 0.257 |
| 400, 72 | 1.656 | 1.057 | 1.596 | 0.233 |

### 5.2.2 Comparison between Sample Surface and Sample Interior after Heating

As mentioned in section 2.5.3, I observed that the spectral characteristics of the sample surface was different from the characteristics of the interior sample. Moreover, the geomorphologic observations of the PIDs on Vesta suggest that both the material of the PIDs and their immediate surrounding belong to the same host deposit, indicating a similar initial temperature they were exposed to (due to the Marcia impact). To investigate this systematically, I measured both the sample surface reflectance and the reflectance of the 'interior material by mechanically mixing the samples. Thus, interior particles were mixed with surface particles. A clear separation of interior and surface particles was not feasible. In the following images, I refer to these mechanically mixed samples as "interior", which is highly simplified as it is a mixture between surface and interior particles. With this said, it is important to note that the reflectance spectra of the 'real' interior particles would yield even larger differences with respect to the surface measurements. Moreover, I note that I used the "interior", mechanically mixed reflectance spectra in the previous section 5.2.1 for all representative spectra of the heated aliquots as they appear to best represent the *true* behavior of the sample in consequence of the heating process. However, I acknowledge that especially in vacuum, this might not be the case which I will elaborate on in section 7.

Figure 5.11 shows reflectance spectra of the surface and the interior of the heated NWA5748M aliquots. Again, the y-axis is displayed at the same range in order to facilitate direct comparisons. Table 5.7 gives the spectral parameters presented in the previous section for the surface and interior of heated NWA5748M aliquots.

With the exception of the 200 °C, 2 h experiment, all depicted spectra of the interior NWA5748M samples show systematically higher reflectance at 750 nm and stronger pyroxene band depths. This is also illustrated by the calculated spectral parameters in Table 5.7. The largest difference between surface and interior is achieved for the 600 °C experiments. Visible spectral slopes (750/430 [nm]) steepen for all considered temperatures and durations. The band position parameter 965/917 [nm] slightly increases for four out of the six comparisons (exceptions for 200 °C, 2 h and 400 °C, 2 h).

Table 5.7: Spectral parameters for pyroxene band strength, band position, visible spectral slope and reflectance at 750 nm for the surface and interior of NWA5748M aliquots.

| Condition | T [°C] & t [h] | 750/917 [nm] | 965/917 [nm] | 750/430 [nm] | 750 nm |
|---|---|---|---|---|---|
| Surface | 200, 2 | 1.386 | 1.048 | 1.354 | 0.212 |
| Interior | 200, 2 | 1.348 | 1.047 | 1.370 | 0.209 |
| Surface | 200, 72 | 1.324 | 1.046 | 1.321 | 0.185 |
| Interior | 200, 72 | 1.349 | 1.049 | 1.432 | 0.191 |
| Surface | 400, 2 | 1.357 | 1.047 | 1.500 | 0.188 |
| Interior | 400, 2 | 1.362 | 1.045 | 1.643 | 0.191 |
| Surface | 400, 72 | 1.328 | 1.049 | 1.526 | 0.194 |
| Interior | 400, 72 | 1.348 | 1.052 | 1.649 | 0.202 |
| Surface | 600, 2 | 1.296 | 1.048 | 1.504 | 0.195 |
| Interior | 600, 2 | 1.374 | 1.049 | 1.866 | 0.237 |
| Surface | 600, 72 | 1.192 | 1.048 | 1.520 | 0.183 |
| Interior | 600, 72 | 1.313 | 1.055 | 1.817 | 0.208 |

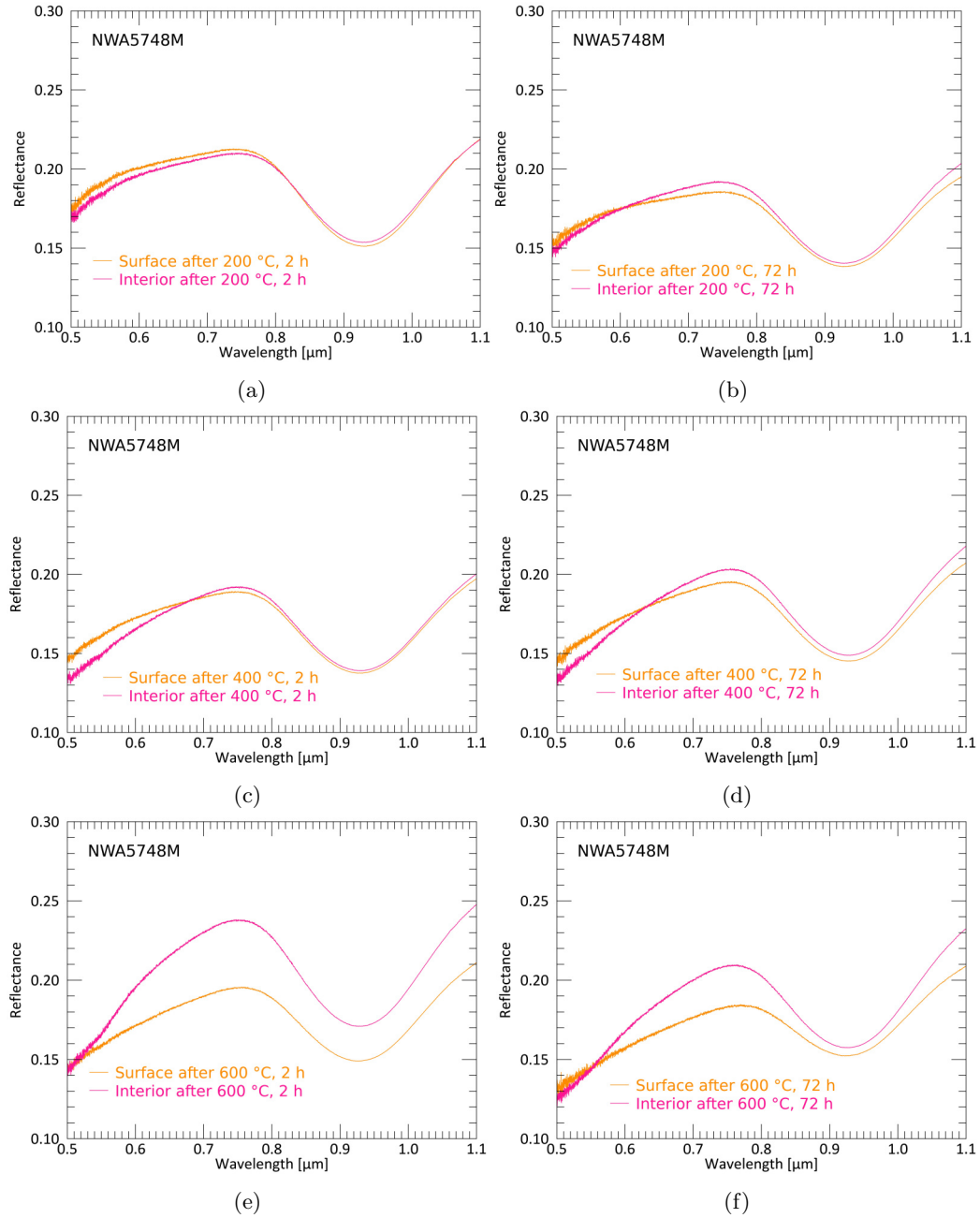


Figure 5.11: Reflectance spectra of the surface (orange) and interior (deep pink) of NWA5748M after heating to 200 °C (a and b), 400 °C (c and d) and 600 °C (e and f) for 2 (left column) and 72 (right column) hours.

The presented sequences for NWA5748M are partly also available for the terrestrial analog H90P10 which is presented in the following Figure 5.12 and Table 5.8. For this sample, the reflectance at 750 nm of the interior of the sample almost never exceeds the reflectance of the surface. The only experiment where this happens similarly to NWA5748M is at 600 °C and 72 h, which is displayed in Figure 5.12e. For all other comparisons, the interior of the heated H90P10 aliquots show a decrease of reflectance and pyroxene band strength with respect to the surface (Table 5.8).

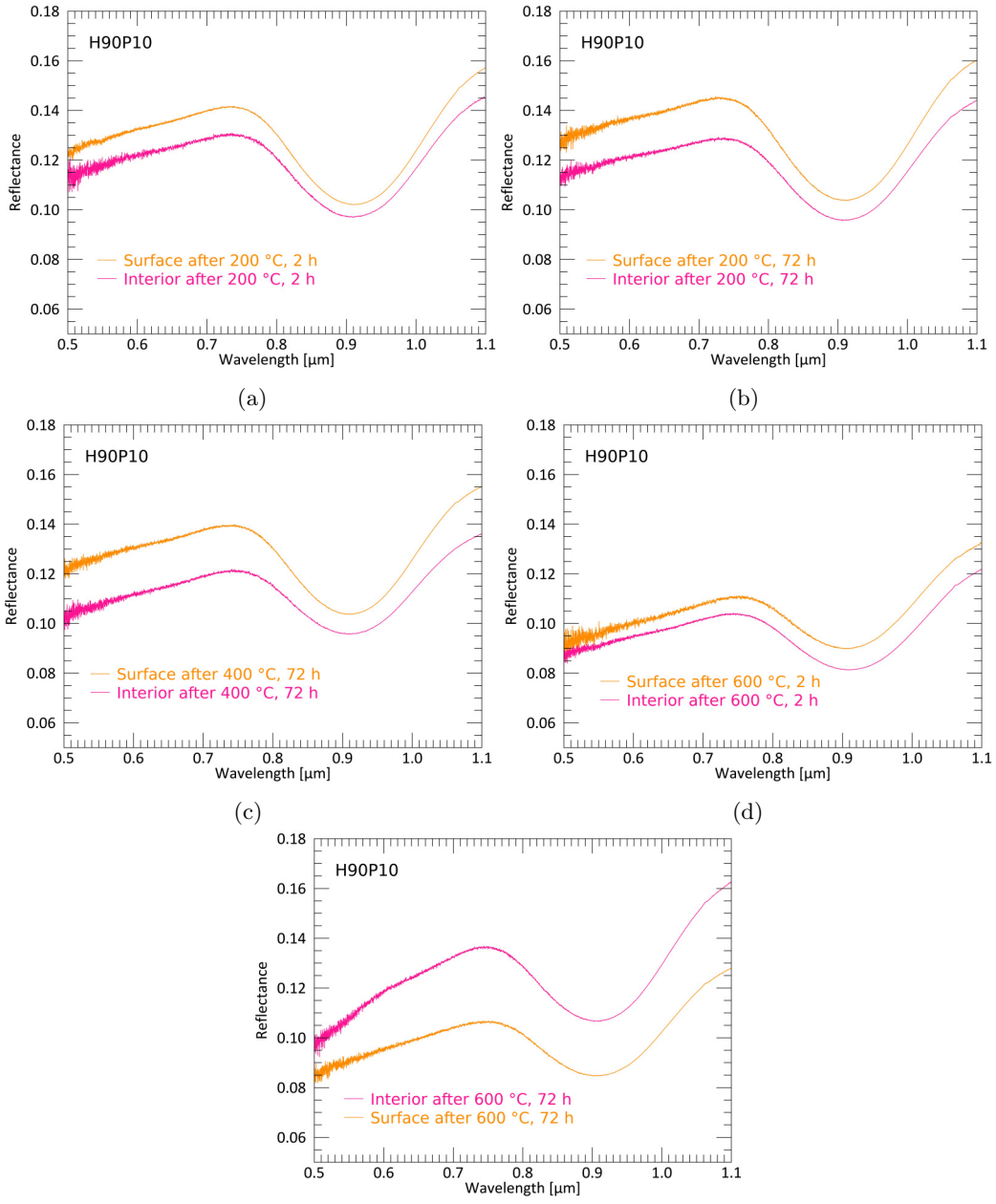


Figure 5.12: Reflectance spectra of the surface (dark orange) and interior (deep pink) of H90P10 after heating to 200 °C (a and b), 400 °C (c) and 600 °C (d and e) for 2 and 72 hours.

Table 5.8: Spectral parameters for pyroxene band strength, band position, visible spectral slope and reflectance at 750 nm for the surface and interior of H90P10 aliquots.

| Condition | T [°C] & t [h] | 750/917 [nm] | 965/917 [nm] | 750/430 [nm] | 750 nm |
|---|---|---|---|---|---|
| Surface | 200, 2 | 1.362 | 1.094 | 1.217 | 0.140 |
| Interior | 200, 2 | 1.320 | 1.090 | 1.328 | 0.129 |
| Surface | 200, 72 | 1.369 | 1.096 | 1.232 | 0.144 |
| Interior | 200, 72 | 1.321 | 1.092 | 1.202 | 0.128 |
| Surface | 400, 72 | 1.324 | 1.095 | 1.252 | 0.139 |
| Interior | 400, 72 | 1.251 | 1.079 | 1.232 | 0.121 |
| Surface | 600, 2 | 1.214 | 1.090 | 1.232 | 0.110 |
| Interior | 600, 2 | 1.245 | 1.087 | 1.322 | 0.104 |
| Surface | 600, 72 | 1.240 | 1.094 | 1.353 | 0.106 |
| Interior | 600, 72 | 1.259 | 1.096 | 1.547 | 0.136 |

These surface and interior measurements were also acquired for other meteoritical and terrestrial samples. In the following, I will display results for meteoritic regolith analogs, followed by more terrestrial analogs and again some of the analog endmembers. Figure 5.13 shows the surface and interior measurements of sample NWA5230M and Figure 5.14 shows the results for JaH626M, EA90P10, H80P20 and H70P30.

For NWA5230M, all reflectance spectra of the interior exceed the reflectance of the surface at 750 nm. Likewise, all reflectance spectra of the interior show visible spectral slopes larger than the ones of the surface. However, the pyroxene band strength only increases for the two aliquots heated to 600 °C as seen in Table 5.9.

The interior of both comparisons for JaH626 (400 °C, 168 h and 600 °C, 72 h) show significantly increased reflectance at 750 nm and visible spectral slopes, increased pyroxene band strengths and slightly reduced 965/917 [nm] values, indicating a small shift of the band position to longer wavelengths. EA90P10 and H80P20 do not show an increase in reflectance at 750 nm or pyroxene band strength. Visible spectral slope increases for the interior of EA90P10 and decreases for the interior of H80P20. 965/917 [nm] values slightly decrease for EA90P10 and slightly increase for H80P20. Interestingly, H70P30 shows a slight increase in reflectance at 750 nm and pyroxene band strength as well as visible spectral slope and a slight reduction of 965/917 [nm] values.

The results of surface and interior measurements of the endmember suite of samples are displayed in Figures 5.15 and Table 5.10. Similar to the results of the previous section, Murchison is the only endmember which exhibits an increased reflectance at 750 nm as well as a significantly larger visible spectral slope.

There is another approach to take if we assume that on Vesta, the surrounding deposit of PIDs has not been mechanically mixed with the interior and was subject to heating for a shorter period of time. Then the results can be compared by displaying, at the same temperature, the surface of a sample at 2 hours and the interior of a sample at 72 hours (and for NWA5230M also for 168 h). I will display the results of NWA5748M, NWA5230M and H90P10, which cover these experiments. Figure 5.16 shows spectra of the surface after 2 h and interior after 72 h of NWA5748M for various temperatures. Reflectance at 750 nm increases for the 400 °C and 600 °C interior spectra. Pyroxene band strength only increases for the interior after 72 h with respect to the surface after 2 h at 600 °C (Table 5.7). Visible spectral slopes increase gradually with temperature and time in this series.

Figure 5.17 shows these series of spectra for NWA5230M and H90P10. The heated aliquots of NWA5230M suggest that heating for longer durations results in a significant increase of visible spectral slope, reflectance at 750 nm and pyroxene band strength. For H90P10 at 600 °C, the visible spectral slope, reflectance at 750 nm and pyroxene band strength are likewise significantly larger for the interior after 72 h than for the surface after 2 h. At 200 °C, no such effect is present. 965/917 [nm] values tend to minimally increase for both samples.

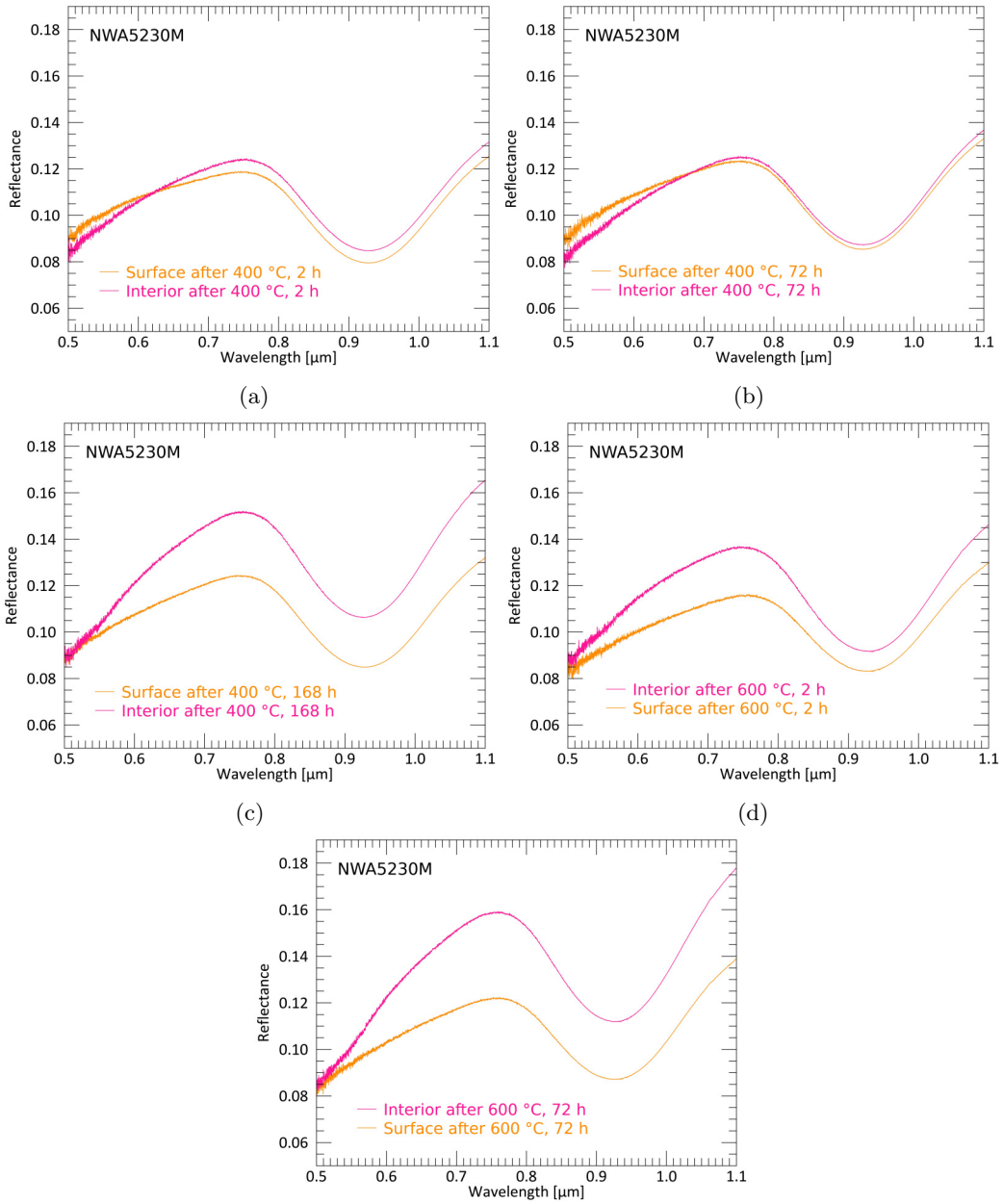


Figure 5.13: Reflectance spectra of the surface (dark orange) and interior (deep pink) of NWA5230M after heating to 400 °C (a-c) and 600 °C (d and e) for 2 h (a and d), 72 h (b and e), and 169 h (c) .

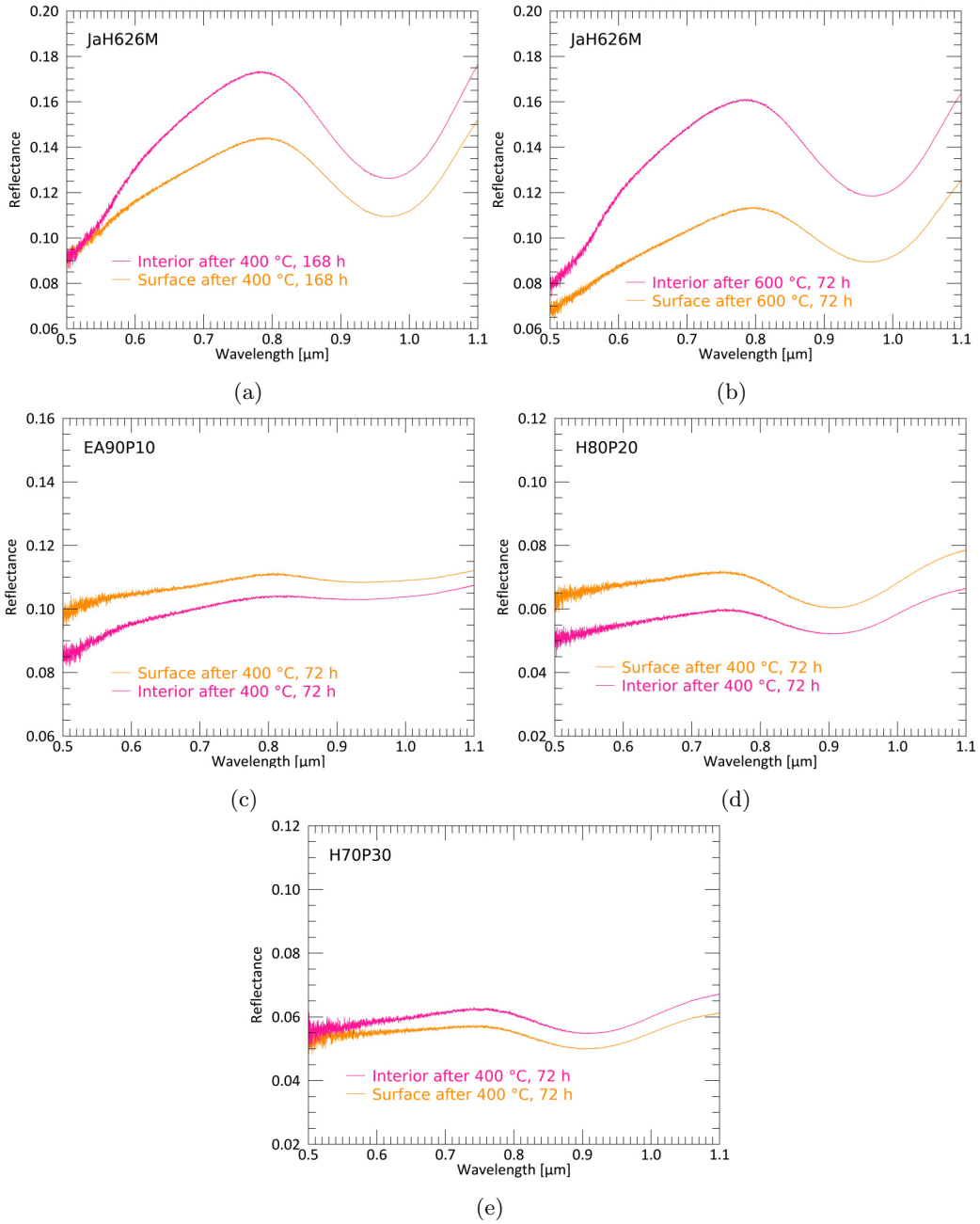


Figure 5.14: Reflectance spectra of the surface (dark orange) and interior (deep pink) of JaH626, EA90P10, H80P20 and H70P30 after heating to 400 °C (a, c, d, e) and 600 °C (b) 72 h (b-e) and 168 h (a).

Table 5.9: Spectral parameters for pyroxene band strength, band position, visible spectral slope and reflectance at 750 nm for the surface and interior of NWA5230M, JaH626M, EA90P10, H80P20 and H70P30 aliquots.

| Condition | T [°C] & t [h] | 750/917 [nm] | 965/917 [nm] | 750/430 [nm] | 750 nm |
|---|---|---|---|---|---|
| NWA5230M | | | | | |
| Surface | 400, 2 | 1.468 | 1.064 | 1.484 | 0.118 |
| Interior | 400, 2 | 1.439 | 1.061 | 1.663 | 0.123 |
| Surface | 400, 72 | 1.425 | 1.066 | 1.502 | 0.123 |
| Interior | 400, 72 | 1.412 | 1.065 | 1.706 | 0.124 |
| Surface | 400, 168 | 1.441 | 1.062 | 1.559 | 0.124 |
| Interior | 400, 168 | 1.406 | 1.066 | 1.943 | 0.151 |
| Surface | 600, 2 | 1.375 | 1.067 | 1.452 | 0.115 |
| Interior | 600, 2 | 1.466 | 1.065 | 1.766 | 0.136 |
| Surface | 600, 72 | 1.378 | 1.071 | 1.665 | 0.121 |
| Interior | 600, 72 | 1.398 | 1.068 | 2.257 | 0.158 |
| JaH626M | | | | | |
| Surface | 400, 168 | 1.215 | 0.958 | 1.694 | 0.141 |
| Interior | 400, 168 | 1.264 | 0.954 | 2.403 | 0.170 |
| Surface | 600, 72 | 1.170 | 0.966 | 1.835 | 0.110 |
| Interior | 600, 72 | 1.253 | 0.957 | 2.077 | 0.157 |
| EA90P10 | | | | | |
| Surface | 400, 72 | 1.008 | 1.001 | 1.256 | 0.109 |
| Interior | 400, 72 | 0.995 | 1.003 | 1.294 | 0.103 |
| H80P20 | | | | | |
| Surface | 400, 72 | 1.174 | 1.060 | 1.220 | 0.071 |
| Interior | 400, 72 | 1.133 | 1.054 | 1.204 | 0.060 |
| H70P30 | | | | | |
| Surface | 400, 72 | 1.129 | 1.046 | 1.090 | 0.057 |
| Interior | 400, 72 | 1.131 | 1.043 | 1.092 | 0.062 |

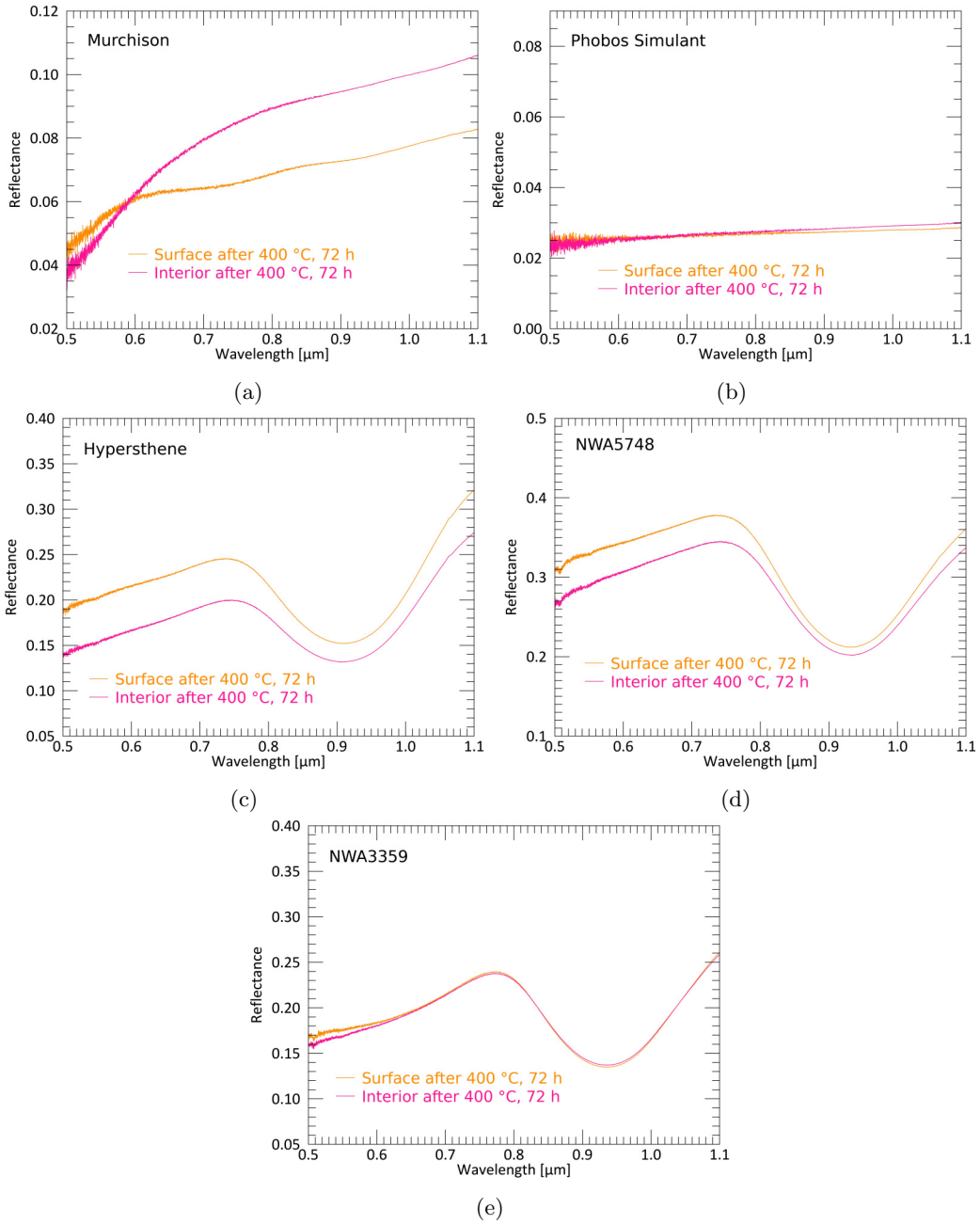


Figure 5.15: Reflectance spectra of the surface (dark orange) and interior (deep pink) of Murchison (a), Phobos Simulant (b), Hypersthene (c), NWA5748 (d) and NWA3359 (e) after heating to 400 °C for 72 h.

Table 5.10: Spectral parameters for pyroxene band strength, band position, visible spectral slope and reflectance at 750 nm for the surface and interior of Murchison, Phobos Simulant, Hypersthene, NWA5748 and NWA3359 aliquots.

| Condition | T [°C] & t [h] | 750/917 [nm] | 965/917 [nm] | 750/430 [nm] | 750 nm |
|---|---|---|---|---|---|
| Murchison | | | | | |
| Surface | 400, 72 | 0.898 | 1.031 | 1.946 | 0.066 |
| Interior | 400, 72 | 0.890 | 1.027 | 2.614 | 0.085 |
| Phobos Simulant | | | | | |
| Surface | 400, 72 | 0.970 | 1.011 | 1.036 | 0.027 |
| Interior | 400, 72 | 0.953 | 1.016 | 1.058 | 0.027 |
| Hypersthene | | | | | |
| Surface | 400, 72 | 1.574 | 1.155 | 1.427 | 0.243 |
| Interior | 400, 72 | 1.482 | 1.156 | 1.615 | 0.198 |
| NWA5748 | | | | | |
| Surface | 400, 72 | 1.735 | 1.062 | 1.352 | 0.375 |
| Interior | 400, 72 | 1.665 | 1.059 | 1.442 | 0.342 |
| NWA3359 | | | | | |
| Surface | 400, 72 | 1.694 | 1.060 | 1.495 | 0.234 |
| Interior | 400, 72 | 1.656 | 1.057 | 1.596 | 0.233 |

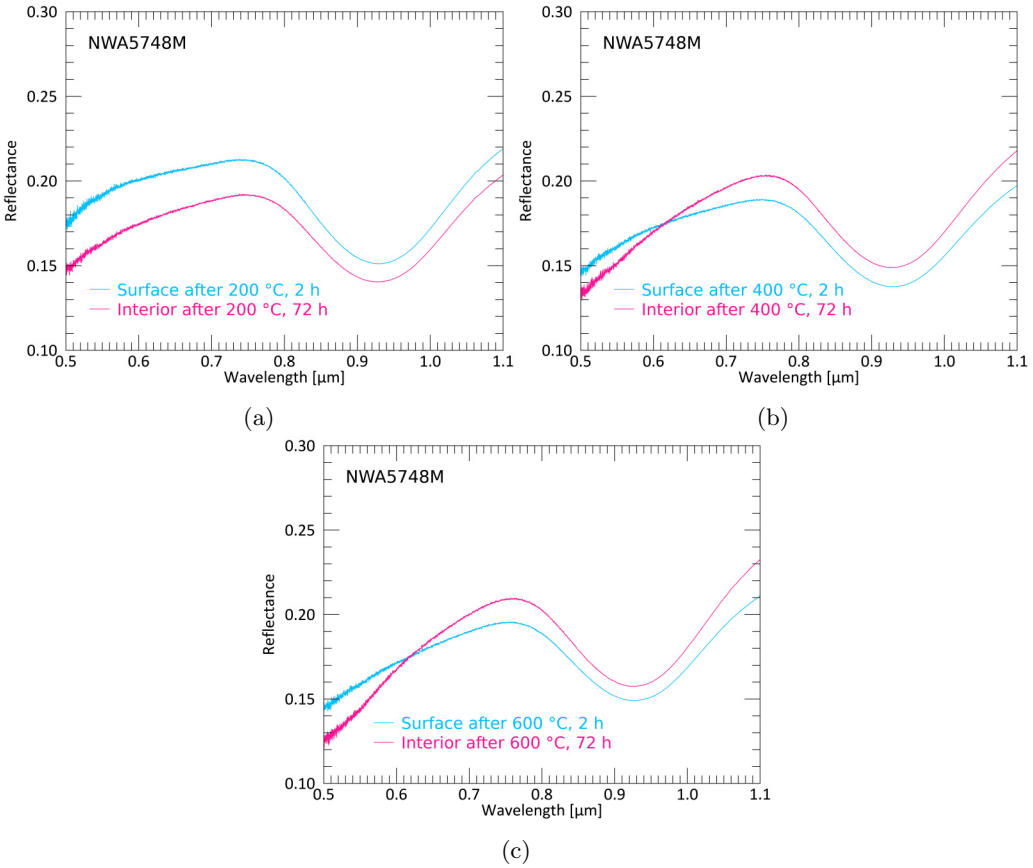


Figure 5.16: Reflectance spectra of the surface after 2 h (deep sky blue) and interior after 72 h (deep pink) of NWA5748M after 200 °C (a), 400 °C (b) and 600 °C (c).

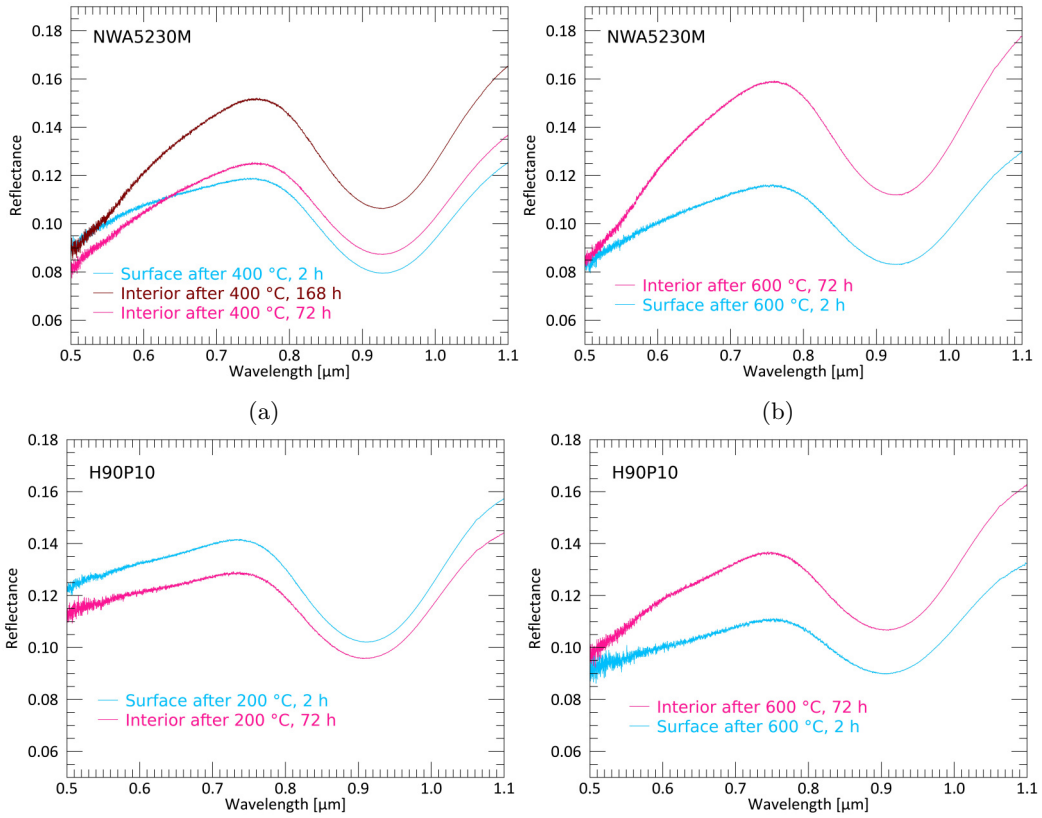


Figure 5.17: Reflectance spectra of the surface after 2 h (deep sky blue) and interior after 72 h (deep pink) of NWA5230 (a and b) and H90P10 (c and d) after 200 °C (c), 400 °C (a) and 600 °C (b and d).

## 5.3 Near-InfraRed measurements of heated samples

For some of the heated samples, near-infrared (NIR) measurements at longer wavelength were acquired (requires another detector within the spectrometer). Shown will be the range between 1.1 and 2.5 µm, which covers the second pyroxene absorption band centered at around 1.9 µm. Beyond this range, a prominent water band is present that is not comparable to Vestan data as the water is likely adsorbed from the laboratory environment.

In the previous sections, the most systematic effect of increasing reflectance and pyroxene band strength (as for PIDs on Vesta) is shown to result as a difference of heated interior and heated surface particles. In the following, the spectra and spectral parameters are shown for the mentioned wavelength region for the samples NWA5748, NWA5748M, NWA5230M, H90P10, H80P20 and H70P30 for 400 °C and 72 h (for H90P10, a measurement of the interior particles after 600 °C and 72 h is shown as well). The spectral parameters were computed by smoothing the laboratory spectra (as they show high degrees of distortion) with the IDL smooth function and a convolution width of 40. Then, the reflectance at 1.44602 and 1.90992 are used to generate the spectral parameters shown in Table 5.11, which represent the closest values to the wavelengths reported for VIR data in section 4.9.

Figure 5.18 shows the spectra of NWA5748M (includes Murchison) and NWA5748. Table 5.11 gives the according spectral parameters (reflectance at 1.44602 µm and 1.44602/1.90992 [µm]) for all samples. it can be seen that the general trend of increasing reflectance and pyroxene band depth continues in the NIR region for the second pyroxene absorption band. NWA5748 (without Murchison) likewise shows a slight increase in reflectance between surface particles and interior particles, yet with no increase in pyroxene band strength. It must always be kept in mind that interior particles alone could not be measured, instead the mixture between surface and interior particles was measured.

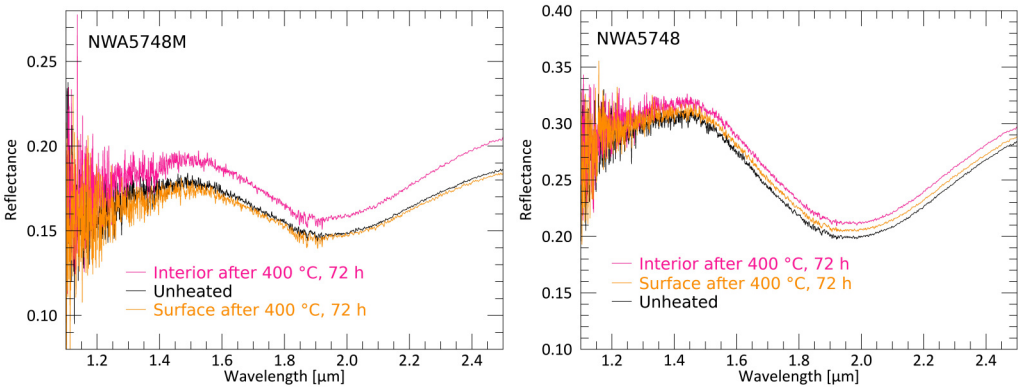


(a) (b)

Figure 5.18: NIR reflectance spectra of NWA5748M (a) and NWA5748 (b).

The same measurement was conducted for NWA5230M (Fig. 5.19), which visibly shows only marginal differences between the spectra yet the values in Table 5.11 reveal that a slight increase in reflectance and pyroxene band strength might also be present, though the spectra are still distorted despite smoothing them. The increase in pyroxene band strength is comparable to that of NWA5748M. However, NWA5230M does not show an increased pyroxene band strength at 400 °C in VIS measurements. Figure 5.19 also shows MIR data of Murchison (values in Table 5.11) and its aliquot heated to 400 °C, 72 h. The increased reflectance continues in the whole depicted wavelength range, thus likely affecting the spectra of analog samples that were mixed with Murchison.

Figure 5.20 shows the NIR reflectance spectra of H90P10, H80P20 and H70P30. H90P10 and H80P20 do not show increased pyroxene band strength of the interior particles with respect to surface particles, which is according to the results from VIS measurements (Tables 5.8 and 5.9). However, the 600 °C, 72 h data for H90P10 show that as least the increased reflectance translate into the NIR region and probably the pyroxene band strength as well, as the pyroxene band strength is higher than for both of the 400 °C measurements. Nevertheless, it is an assumption as the spectra of

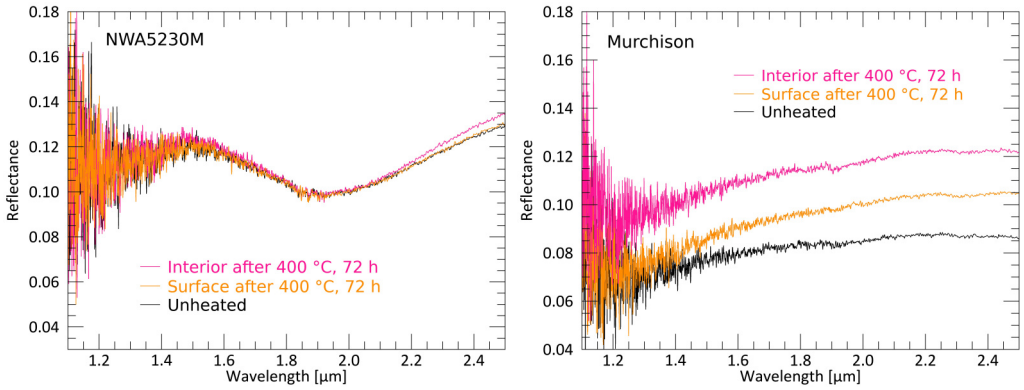


(a) (b)

Figure 5.19: a) NIR reflectance spectra of NWA5230M, b) NIR reflectance spectra of Murchison.

the surface at 600 °C, 72 h was not measured. H70P30 shows a very slight increase in pyroxene band strength for VIS measurements and an increase in reflectance for both VIS and NIR measurements.

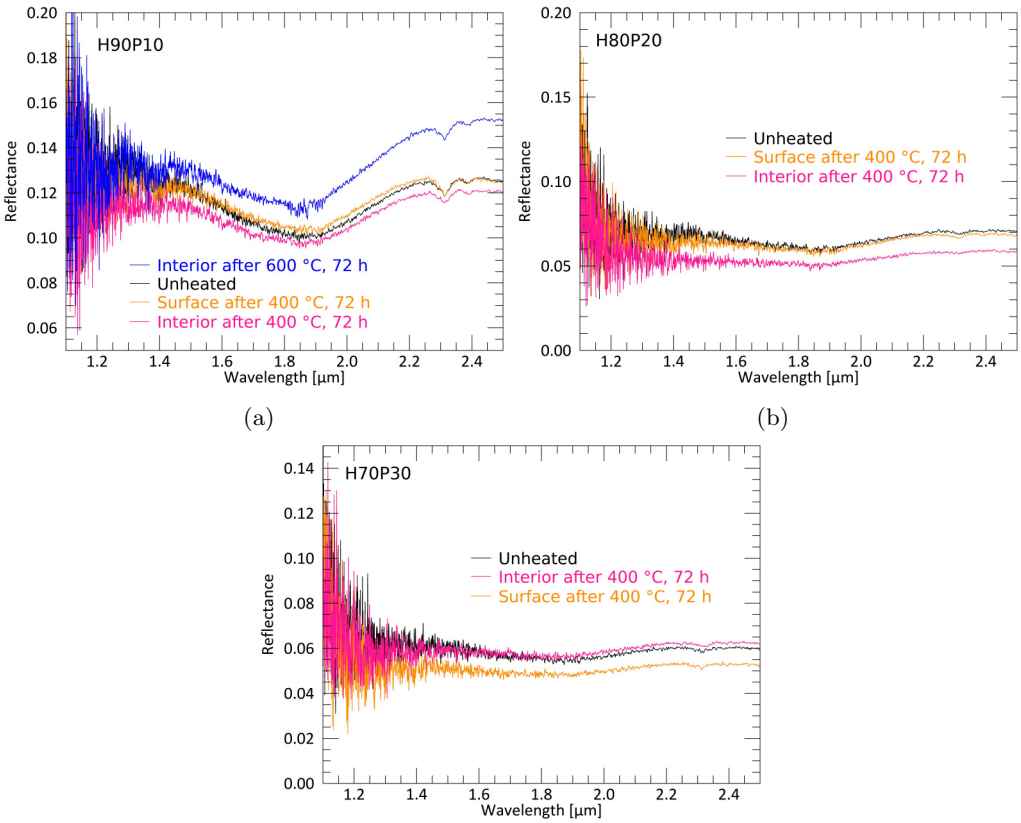


(a) (b)

(c)

Figure 5.20: NIR reflectance spectra of H90P10 (a), H80P20 (b) and H70P30(c).

Table 5.11: Spectral parameters of laboratory NIR measurements: Reflectance at 1.44602 µm and pyroxene band strength ratio 1.44602/1.90992 [µm].

| Condition | T [°C] and duration [h] | refl. at 1.44602 µm | 1.44602/1.90992 [µm] |
|---|---|---|---|
| NWA5748M | | | |
| Unheated | - | 0.176 | 1.200 |
| Surface | 400, 72 | 0.173 | 1.201 |
| Interior | 400, 72 | 0.192 | 1.233 |
| NWA5748 | | | |
| Unheated | - | 0.304 | 1.521 |
| Surface | 400, 72 | 0.309 | 1.499 |
| Interior | 400, 72 | 0.319 | 1.498 |
| NWA5230M | | | |
| Unheated | - | 0.119 | 1.209 |
| Surface | 400, 72 | 0.118 | 1.204 |
| Interior | 400, 72 | 0.121 | 1.233 |
| Murchison | | | |
| Unheated | - | 0.074 | 0.893 |
| Surface | 400, 72 | 0.083 | 0.853 |
| Interior | 400, 72 | 0.102 | 0.894 |
| H90P10 | | | |
| Unheated | - | 0.124 | 1.228 |
| Surface | 400, 72 | 0.122 | 1.178 |
| Interior | 400, 72 | 0.115 | 1.167 |
| Interior | 600, 72 | 0.132 | 1.146 |
| H80P20 | | | |
| Unheated | - | 0.069 | 1.153 |
| Surface | 400, 72 | 0.065 | 1.113 |
| Interior | 400, 72 | 0.053 | 1.044 |
| H70P30 | | | |
| Unheated | - | 0.062 | 1.136 |
| Surface | 400, 72 | 0.052 | 1.084 |
| Interior | 400, 72 | 0.058 | 1.016 |

## 5.4 Microscopy of NWA5748M

While investigating how elevated reflectance and pyroxene band strength develop, optical microscopy of the above mentioned samples was undertaken. The most apparent difference between the unheated and heated NWA5748M aliquot (600 °C, 72h) is that the heated aliquot ("interior", i.e. mechanically mixed after heating was terminated) exhibits vast amounts of tiny to small (<10-100 µm), red phases throughout the sample. This is not seen in the unheated sample. Figure 5.21 shows images of the samples at various zoom levels under the same illumination conditions.

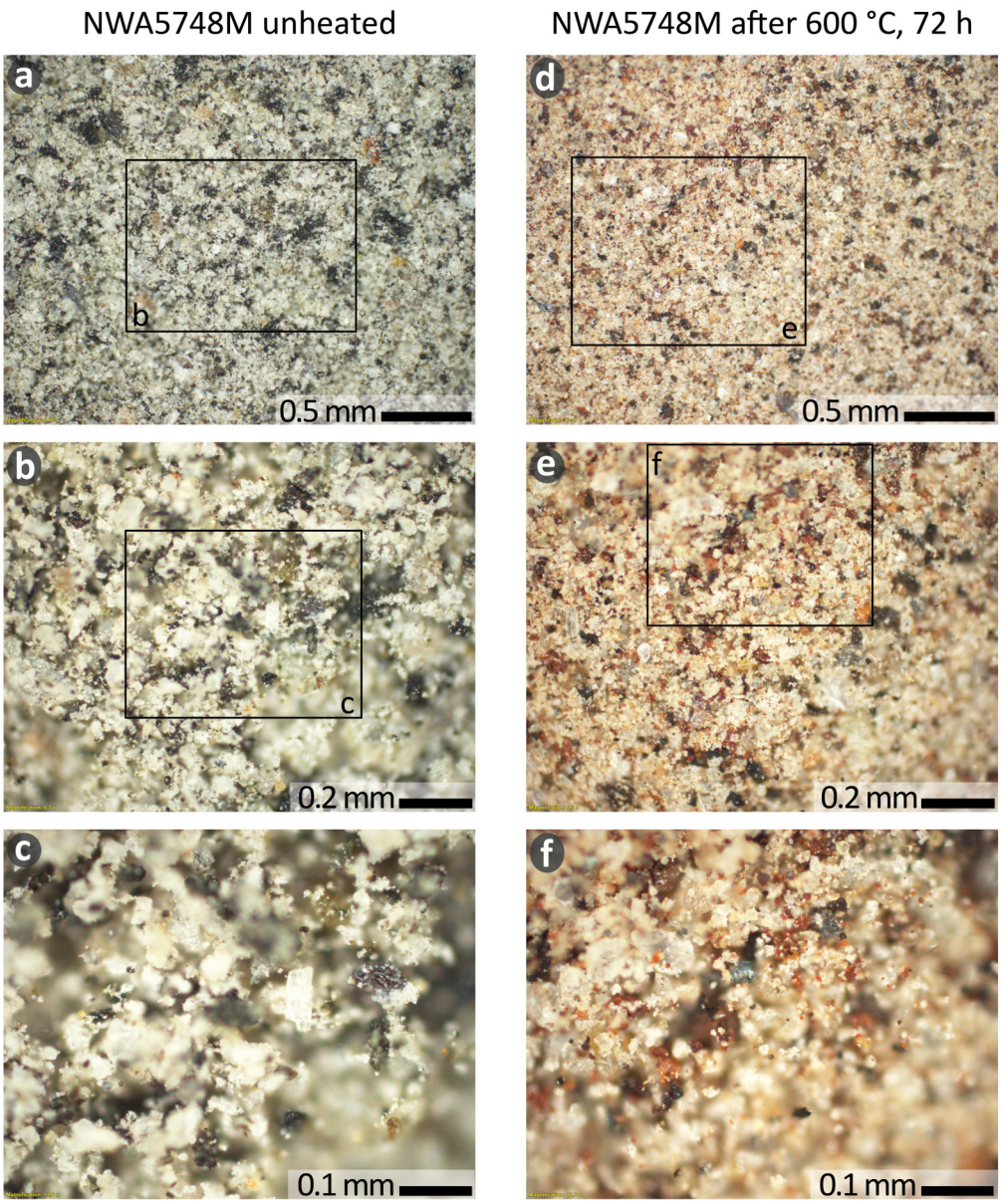


Figure 5.21: Microscopy images of an unheated (a-c) and a heated (d-f) aliquot of NWA5748M. Images were aquired in Dark Field mode (DF) with an Olympus DP26 microscope.

## 5.5 Results from Electron Probe Microanalysis

Finally, I present results of EPMA analysis of Murchison and NWA5748M. As seen in Figure 5.10, Murchison is the only endmember experiencing significant reddening after 400 °C, 72 h which is likely the cause for the changes of the meteoritic analogs, as well. Thus, Murchison is included here for analysis, as well. NWA5748M is, in this study, the meteoritic analog with the largest data set and a clear systematic increase in visible spectral slope, reflectance and band strength (the latter two only with respect to the initial heated surface). The 600 °C, 72 h aliquot was chosen for EPMA due to the most pronounced development of these spectral characteristics. The unheated aliquots were analyzed as well. Several spots that showed the presence of iron oxides with the EDS were analyzed via WDS in order to evaluate the species (hematite/magnetite). All selected locations had values typical for hematite (below 90 wt% FeO). The according hematite wt% of the numbered locations within the BSE (backscattered electrons) images shown in the following are given in Table

5.12. Other very minor oxide constituents were found to be $SiO_2$ and $Cr_2O_3$, which is given in detail in the Appendix (12.5).

Hematite was only identified within the heated aliquots of Murchison and NWA5748M. It often occurs as "coatings" or rims around sulfide or metal grains (especially for NWA5748M, Fig. 5.24). However, inclusions of iron metal within pyroxene host grains did not transform or build a hematite coating (example in Fig. 5.24A). Such appearances were not found in the unheated aliquots of both samples. Figure 5.22 shows BSE images of the heated aliquot of Murchison, depicting an accumulation of hematite droplets within a larger grain of likely phyllosilicates and partly olivine.

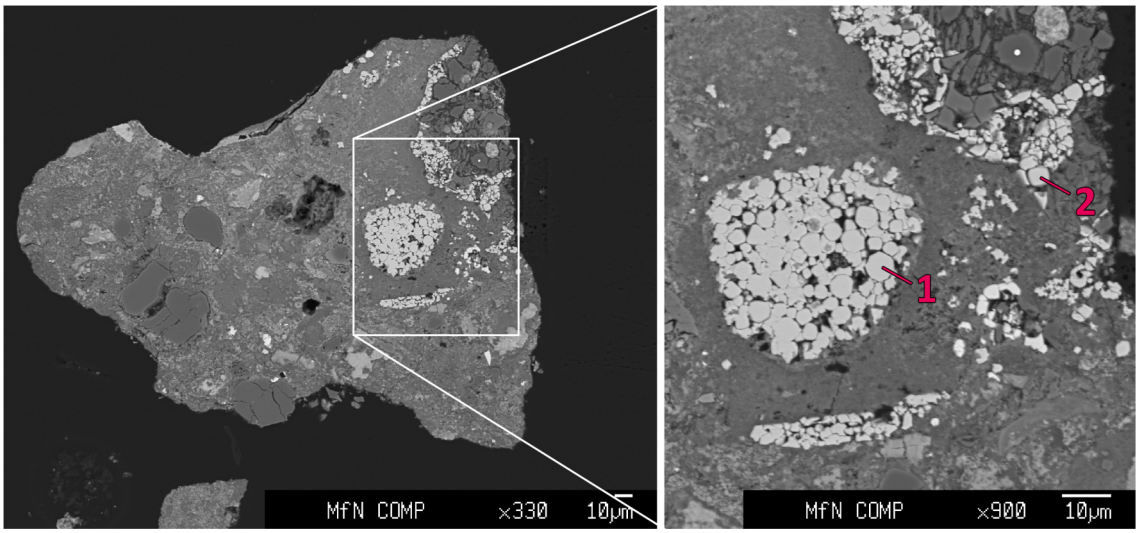


Figure 5.22: BSE image of a grain from Murchison heated to 400 °C, 72 h. The enlargement image depicts the locations of WDS analysis shown in Table 5.12.

Such hematite occurrences were not found within the unheated aliquot, although some sulfides exist (Fig. 5.23A). Likewise, sulfides were also found within NWA5748M (Fig. 5.23B and D). Within the unheated sample of NWA5748M, no hematite surroundings were found, yet in the heated sample, hematite was identified surrounding pure iron metal, iron sulfides and partly pyroxene which is shown in Figure 5.24 and Table 5.12. The $Fe_2O_3$ do not always add up to 100% and can be affected by various effects: 1) Hematite phases were often quite narrow, possibly not covering the whole measurement spot size, 2) Hematite phases also exhibited small inhomogeneities, inclusions and pores, possibly also affecting the WDS result and 3) The samples were prepared as polished grains embedded in epoxy. As the grains possess very different properties regarding their hardness and constitution, an ideal polish of all grains could not be achieved.

Table 5.12: WDS analysis of $Fe_2O_3$ (hematite) of the numbered locations in Figures 5.22 and 5.24.

| Location | $Fe_2O_3$ wt% |
|---|---|
| 1 | 99.97 |
| 2 | 98.90 |
| 3 | 98.52 |
| 4 | 92.45 |
| 5 | 95.86 |

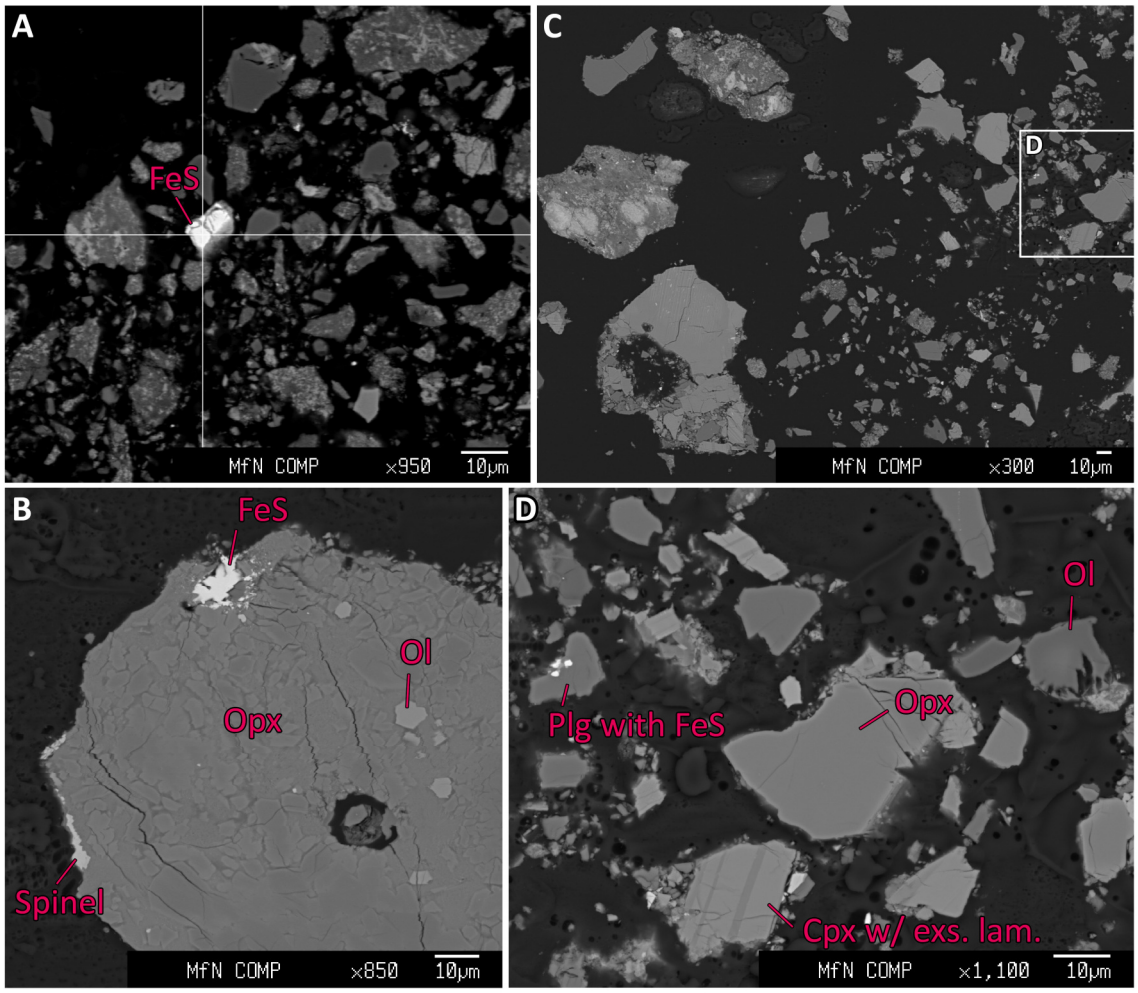


Figure 5.23: A: BSE image of a grain from unheated Murchison, depicting a bright iron sulfide in the center. B: BSE image of a grain from unheated NWA5748M depicting a pyroxene grain with olivine inclusions as well as iron sulfide and spinel as additional phases. No hematite visible. C and D: BSE image of multiple grains from unheated NWA5748M with no signs of hematite coatings or rims. D shows typical howarditic compositions with orthopyroxenes and clinopyroxenes including Ca-rich exsolution lamellae as well as olivine and plagioclase showing inclusions of iron sulfide. Legend: Ol-olivine, Cpx: clinopyroxene, Opx: orthopyroxene, exs. lam.-exsolution lamellae, Plg-plagioclase.

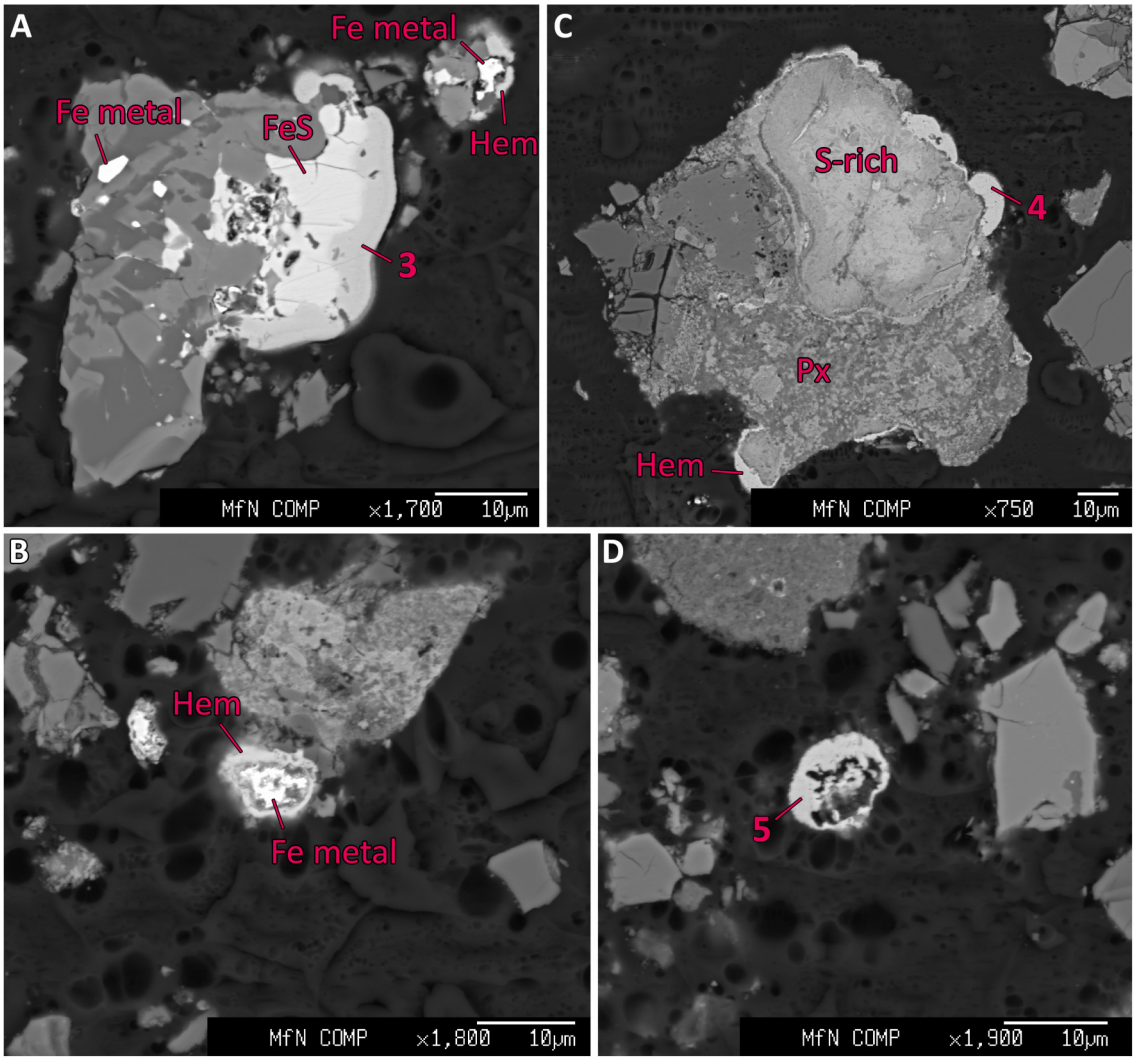


Figure 5.24: BSE images of NWA5748M, heated to 600 °C for 72 h. A: Grain with hematite coating (location 3) over iron sulfide phase. Larger grain also includes metallic iron that has not been oxidized. Nearby small grain (upper right) shows hematite rims to iron metal. B: Hematite rim around iron metal. C: Hematite coating around sulfur-rich phase (upper right) and pyroxene (bottom). The sulfur-rich phase could not be identified and a corresponding EDS spectrum is given in the Appendix (12.6). D: hematite grain not attached to another grain. Legend: Hem-hematite, Px-pyroxene.

# 6 Discussion I: Origin of Pitted Impact Deposits from Geomorphological Evidence and Spectral Characteristics

## 6.1 Origin of the Pitted Impact Deposits

On Mars, Ceres and Vesta, PIDs occur within smooth impact deposits (Denevi et al., 2012; Pasckert et al., 2018; Sizemore et al., 2017; Tornabene et al., 2012), implying that smooth and pitted surfaces share the same host deposit and originate from the same event. My analysis adds more occurrences of PIDs to the already existing data on Vesta (Denevi et al., 2012) and further confirms the relationship of the pitted and smooth ejecta deposits. The spectral characteristics of these two deposit surface types are different from each other, yet their analysis also confirms a relationship of the two: PIDs show higher reflectance and pyroxene band strength with respect to the smooth deposit surroundings and the absolute values of PID reflectance and pyroxene band strength are directly related to those of their surroundings; i.e., where the surrounding host material has less pronounced pyroxene characteristics and lower reflectance (ejecta unit E2), the PIDs' material likewise exhibits a less pronounced 'enhancement' of these properties (PIDs type 2) and vice versa. This confirms a simultaneous emplacement of the original material before pits formed on some of the deposits surface, as was shown in detail by Tornabene et al. (2012) for Mars. Therefore, it can be excluded that the material of the PIDs was introduced later, e.g. by some sort of extraordinary secondary impact process at a later stage of Marcia's formation. As a result, differences in age and exposure to the various kinds of space weathering processes (Pieters et al., 2012) are very unlikely causes for the spectral differences.

I furthermore observe that the spectral characteristics of PIDs reach several tens of meters outward into the smooth zones of the host deposits, building another sort of halo around the PIDs. This indicates that the formation of the individual pits inside a PID is linked to ejection of material, not e.g. the loss of material through subsurface voids, which was also shown for Mars (Tornabene et al., 2012). Thus, solid material was likely ejected along with volatile phases. This is consistent with the interpretation of Denevi et al. (2012).

I observe several PIDs occurring in pre-existing craters and with positive local topographies, facing Marcia crater. Their origin therefore appears to be linked to the accumulation of ejecta (Fig. 6.1). Accumulation of material is accompanied by an increase of impact deposit thickness and an increase in the amount of internal heat. The volume of heat-bearing material increases significantly whereas the surface area – where heat can freely radiate into space – remains small. This possibly results in the liberation of hydroxyl groups from their host minerals as well as the buildup of pressure within the pore spaces. The crater-fill PIDs do not feature a positive topography, yet they naturally represent accumulated, possibly partially melted impact material within a large cavity, likewise leading to an increased volume of volatiles per surface area and an increased internal amount of heat.

Furthermore, I identified several locations where PIDs reside along scarps and crater walls (Fig. 6.1b), likewise indicating a structural control facilitating the liberation of volatiles along contacts between the host deposits and bedrock. Although a relationship to pre-existing topography is only observed for a minor population of the PIDs, it is reasonable to assume that this mechanism also plays a role for other PIDs where pre-existing topography cannot be determined anymore, especially within E2b and E2a, where the pre-existing topography has been largely obscured by overlying ejecta. In summary, I present evidence that the formation of PIDs is controlled by the geomorphological setting into which the impact deposit was placed. This is consistent with what Denevi et al. (2012) already suggested (i.e., 'topographic lows') and what Tornabene et al. (2012) found for Martian PIDs.

Stubbs and Wang (2012) suggested the long-term survivability of water ice a few meters below the surface of Vesta and therefore Scully et al. (2015) suggested that the heating of heterogeneously distributed subsurface ice deposits could also have caused the formation of PIDs. However, it

is unlikely that subsurface ice would coincidentally be present within pre-existing craters, facing the excavation direction of a non-existent crater at that point in time. The redistribution of icy material by the impact and preferred deposition within craters is also questionable. Considering the spectral characteristics this possibility likewise seems implausible as the sublimation of water ice would not result in a spectral change of the rocky material considering a rapid degassing within hours. In conclusion, my observations do not favor a role of (water) ice in the formation process which instead is controlled by accumulation of ejecta and therefore the possibility of the material to liberate volatile species (i.e., increased amount of internal heat) and to build up the necessary pressure and vent pipes.

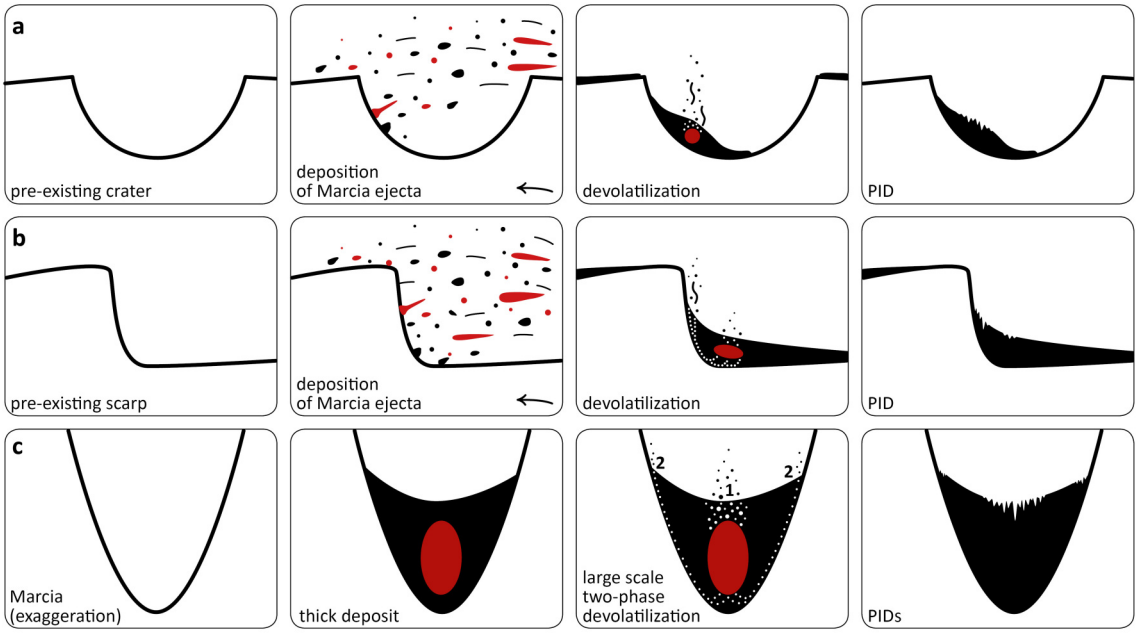


Figure 6.1: Simplified schematic depiction of the mechanism leading to the formation of PIDs according to profiles shown in Figure 4.8: a) within pre-existing small craters, b) at topographic highs, c) within Marcia (deposit thickness >500 m). White circles indicate paths for volatile escape. Red color within a deposit indicates the thickest part which likely retains heat for the longest time spans (highly simplified).

Our analysis of topographic profiles indicates that PIDs both form where their host deposit is thickest, but also on the margins of a host deposit. In the former case, this indicates an internal volatile source as such that the volatiles directly originate from the impact ejecta, which is likely a melt-bearing breccia (Denevi et al., 2012; Tornabene et al., 2012). In the latter case (formation on the margins of a deposit), pit formation occurs close to the colder target rock, which could indicate a contribution of target rock volatiles. However, an easier explanation consistent with observations by Tornabene et al. (2012) is that the contact provides a zone of weakness or conduit that would provide a path for volatile release and thus concentrate pits along those margins (Fig. 6.1b and c, white circles). PID formation on margins of a host deposit is especially present within Calpurnia, Minucia and also Marcia, where host deposit thicknesses are considerably larger than in other areas. The heavier overburden could additionally lead to the preferred release of volatiles along pathways adjacent to the colder target rock. Within Marcia, it is astonishing to observe very large PIDs in the center of the host deposit and very small PIDs located on the margins within the spectrally distinct halo. This might suggest more than one phase of devolatilization where the largest number of volatiles is released very rapidly through the direct pathways within the deposit and residual volatiles from deeper regions within the host deposit ascend along the margins to form smaller PIDs (Fig. 6.1c). The presence of the spectral halo itself as well as signs of subsidence within the crater-fill deposit (Fig. 4.11 in this study and Denevi et al., 2012) might support this hypothesis of different devolatilization phases. The majority of PIDs (~73%) occur within 30 km (i.e., one

crater radius) of the Marcia rim. This correlates well with the positive correlation of ejecta deposit thickness and PID occurrence as ejecta thicknesses gradually become lower with distance from the crater (e.g., Melosh, 1989). I observe the largest and thickest PIDs within the parent crater (Marcia) and a decrease of pit occurrences (i.e., dependent on deposit thickness) with distance from the parent crater. However, I did not observe a correlation of deposit thickness and PID size (area) within the 13 identified pre-existing small craters that host PIDs. This could be due to an erroneous estimation of pre-Marcia topography but also to compositional inhomogeneities within the ejecta (especially in terms of volatile content). Tornabene et al. (2012) present evidence for Tooting crater on Mars that shows that volatile contents of the target rock might vary in different portions of the crater, resulting in pit-poor and densely pitted regions within this crater. Given the possibility that Marcia crater was formed by an oblique impact (oval shape), heterogeneities within the ejecta deposits appear likely and could cause various pit size:deposit thickness ratios not dependent on each other.

## 6.2 Origin of the PIDs' spectral characteristics

PIDs are characterized by an increase in reflectance as well as pyroxene band strength with respect to their immediate smooth surroundings (excluding the crater-fill PIDs), yet to a varying degree (Fig. 4.10). This spectral change occurred after deposition and could result from changes in grain size, structure or composition. Regarding grain size, higher reflectance of a pyroxene-bearing material can be attributed to a smaller grain size (e.g., Clark, 1999) as the larger number of reflective surfaces (crystal faces) increases the probability of light scattering. In contrast, stronger pyroxene absorptions can be attributed to larger grain sizes as absorption of light is more likely with lower numbers of reflective surfaces and larger crystal bodies. Harloff and Arnold (2001) have shown that differences in roughness behave similar to differences in grain size. Therefore, the spectral characteristics of PIDs do not conform to general grain size or roughness effects. I nevertheless evaluate the effect of grain size variations specifically for HED meteorites in order to evaluate whether grain size might still have an influence on the spectral appearance of the PIDs.

Figure 6.2 shows the same spectral parameters as Figures 2.5 & 4.12 but for 16 individual HED meteorites which were ground and separated into different grain size fractions. For 14 of these HEDs the largest grain size fraction exhibits the lowest 965/917 [nm] values which probably results – in contrast to a compositional difference due to different band centers –from the decrease of pyroxene band depth with larger grain sizes (e.g., Clark, 1999; Cloutis et al., 2013a). Absorption band saturation for the first pyroxene band of HEDs commonly starts around grain sizes of 67 µm on average (Cloutis et al., 2013a). The spectra of grain sizes beyond that average value show more similar reflectance for 965 and 917 nm which reduces 965/917 [nm] values. Vice versa, the smaller grain sizes show the highest 965/917 [nm] values.

Except for JAH626, the finest fractions of all HED's exhibit the lowest 750/917 [nm] values, yet the largest grain size fractions exhibit the second lowest values for 12 of these meteorites. A possible reason for this is also the saturation of the absorption band. As grain sizes get larger, pyroxene band depth and reflectance become lower. Once a maximum of band depth is reached, reflectance can continue to decrease while the band depth cannot, causing 750/917 [nm] values to decrease again (e.g., Clark, 1999; Harloff and Arnold, 2001). PRA04401 contains carbonaceous chondrite clasts but does not exhibit any distinct spectral properties in terms of grain size. In summary, the presented spectra of different grain size fractions of HED meteorites are consistent with general grain size-related observations which do not conform with those of the PIDs on Vesta.

As I have just described, he difference of the PIDs associated with Marcia with respect to their surroundings is very systematic (higher 750/917 [nm] values, almost no change for 965/917 [nm]), indicating no observable consistency of spectral characteristics related to particle size or roughness. Zambon et al. (2014) also found that the bright material on Vesta does not result from differences in grain size. In their spectral study on HED meteorites mixed with CM2-type chondrites, Cloutis et al. (2013a) also found that contamination with carbonaceous chondrite material is the most plausible explanation for the 'dark material' on Vesta and the diminishment of spectral features. Other studies also investigated the 'dark material' on Vesta (McCord et al., 2012; Reddy et al., 2012a). They likewise concluded that the occurrence of 'dark material' is most likely caused by contamination with carbonaceous chondrite material and did not find consistencies with other possible explanations like shock effects, opaque phases and plagioclase content.

The differences between the PIDs and their surroundings follow the same systematics like the difference between HED properties and 'dark material': a positive correlation between reflectance and pyroxene band strength. In the present case, this is furthermore supported by the slight depletion in OH that I observe for the PIDs (Fig. 4.10) consistent with devolatilization of exogenic, OH-bearing minerals. Therefore, I find the differences between PIDs and their surroundings with respect to reflectance and pyroxene band strength to likely result from a small difference in composition, i.e. due to the loss and/or decomposition of dark, volatile-bearing phases.

Regarding the spectral analysis of HED grain size fractions, it is important to note that terrestrial weathering, especially of Antarctic meteorites, can alter the grinding behavior of meteorites and thus result in unrealistic spectra for different grain sizes with respect to material still residing on an airless body. Most of the presented Antarctic meteorites have weathering grade A or

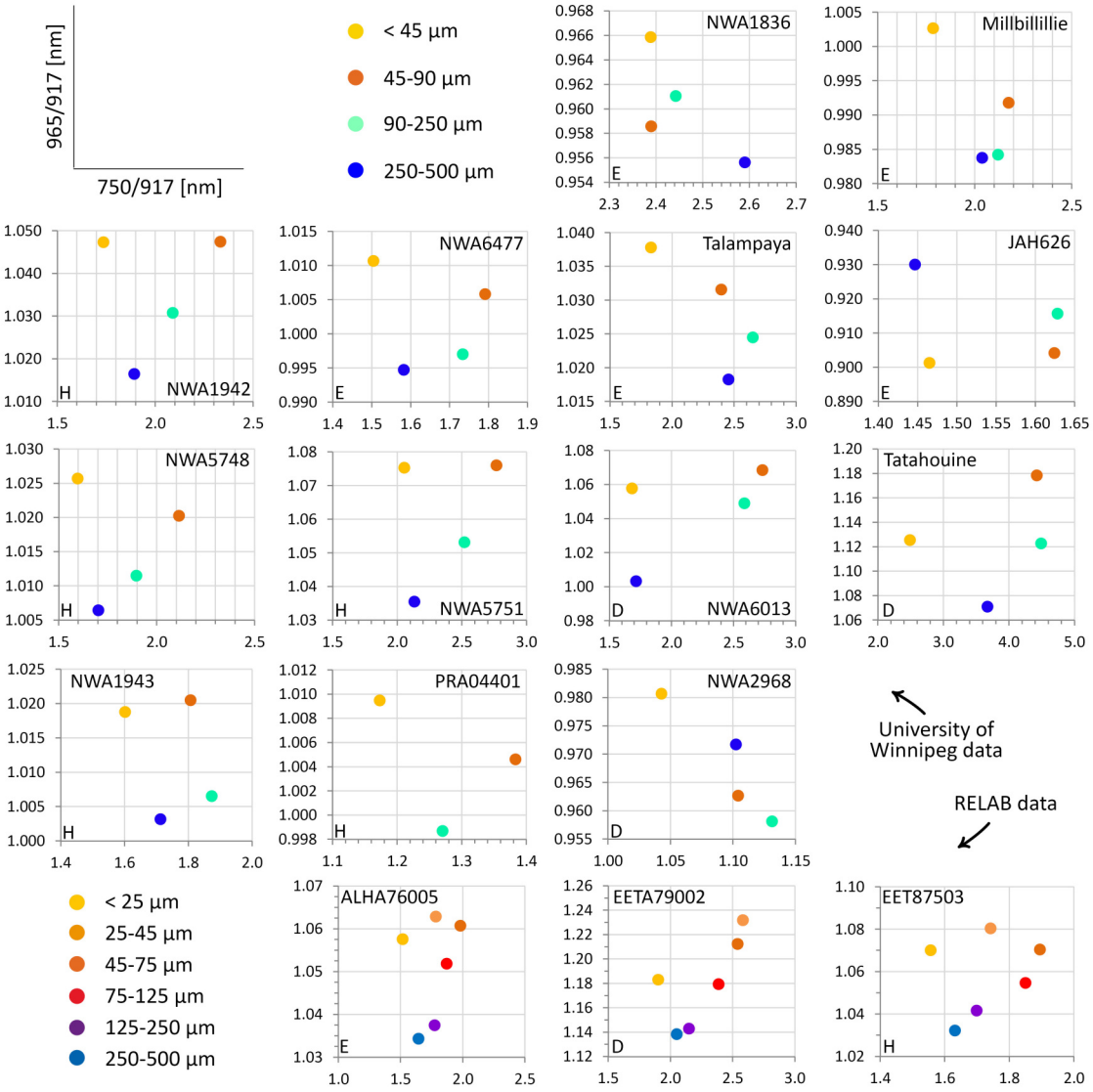


Figure 6.2: 750/917 [nm] vs. 965/917 [nm] for 16 different HED's that have been separated in several grain size fractions. Note that for PRA04401, only three size fractions were available and that for the three RELAB HED's, six grain size fractions were available. The small letters in the lower left corners indicate the HED species. The first 13 sample spectra were provided by Dr. Edward Cloutis and measured at the University of Winnipeg's Planetary Spectrophotometer Facility (e.g., Cloutis et al., 2013a,b).

W0/W1 which are the least altered grades, thus I assume – in agreement with my observations regarding basic spectral behavior of absorption bands and reflectance with respect to grain size – that these weathering effects do not or minorly affect the visible and near infrared analysis undertaken here. JAH626 is considered an outlier in the analysis. The meteorite is shocked (e.g., Ruesch et al., 2015) with little signs of terrestrial weathering. NWA2968 is a find and not characterized regarding its weathering grade in the Meteoritical Bulletin so far, so it is possible that the largest grain size fraction behaves anomalous with respect to the other grain size fractions of this meteorite due to terrestrial weathering. Additionally, this meteorite is officially regarded as an ungrouped olivine-rich achondrite, so it might not be representative for Vesta.

Tornabene et al. (2012) present evidence of outcropping meter to decameter-sized rock fragments within the walls of the pits with significantly "brighter" albedo which they do not observe for the smooth surroundings. They interpret this finding as evidence for the deposit being an impact

melt-bearing breccia. For a suevite outcrop at Ries crater in Germany, Newsom et al. (1986) similarly report on coarse-grained surfaces of a degassing pipe system, devoid of soil/matrix. Boyce et al. (2012) additionally suggest that the high escape rates can also eject cm-sized clasts into the surrounding of the PIDs which could represent the spectral halo presented in this study. If Vestan PIDs also show outcropping rock fragments – which is not determinable with the given image resolutions – then the spectral differences could originate from this exposure. These spectral signatures might additionally differ from typical Vestan lithologies as Marcia is the largest well-preserved crater and might have excavated deeper materials not seen anywhere else beyond the Rheasilvia basin. Within Marcia's impact melt-bearing breccia, larger clasts and rock fragments would predominantly be of HED lithology due to their higher internal strength with respect to carbonaceous chondrite material and could therefore dominate the reflectance spectrum. However, if this is true, other materials in the vicinity of Marcia like small post-impact craters or 'fresh' crater wall material still subject to modification should experience similar spectral characteristics. Yet as I have presented here, PIDs are characterized by stronger pyroxene absorptions (750/917 [nm] values) with respect to other Marcia-related materials with similar reflectance at 750 nm. I have shown that a 'younger' crater (i.e., post-Marcia) that impacted into the smooth part of the host deposit right next to a PID shows similar reflectance values but lower pyroxene band strength. Thus, the younger crater shows less pronounced pyroxene characteristics than the older PID within the same host deposit. This strongly indicates that another process changed the typical spectral nature of the original material at the PIDs' sites which is not related to differences in pyroxene proportions.

A significant shift of the pyroxene band center towards shorter wavelength and therefore to more Mg-rich pyroxene is not observed (Fig. 4.12), although the 965/917 [nm] ratio is sensitive to this mineralogical difference. Hence, there is no difference in the proportion of diogenitic/eucritic lithologies with respect to PIDs and their surroundings which favors the theory of carbonaceous contamination in addition to a unique process related to accumulation and heat retention. The more endogenic and OH-depleted nature of the PIDs could theoretically also arise from phase transitions of phyllosilicates to olivine and pyroxene due to shock metamorphism and heating to >500°C and 750°C, respectively (e.g., Akai, 1992; Nakamura, 2005 and references therein). However, as Sizemore et al. (2017) similarly describe for Ceres, average impact velocities of ~5 km/s in the asteroid belt (Bottke et al., 1994) would generate maximum target temperatures of ~800 K (Marchi et al., 2013; Supplementary Fig. S3 (11)) which suggests that for average projectiles impacting on Vesta, no phase transitions of phyllosilicates would occur. Furthermore, even if Marcia was a result of a high velocity impact, no olivine has been detected in the Marcia area (Ammannito et al., 2013b; Palomba et al., 2015; Thangjam et al., 2014). Yet I again note that detection of olivine might not be possible with the given instrumentation below 30 wt% (Beck et al., 2013; Le Corre et al., 2013).

Liberation of hydroxyl groups in phyllosilicates of carbonaceous chondrites starts around 400 °C (Garenne et al., 2014) implicating that the formation of PIDs can result from devolatilization of phyllosilicates at average main belt impact velocities. However, the spectral characteristics of PIDs do not conform to devolatilization studies that investigated the spectral properties of mixtures containing volatile-bearing phases upon heating and sublimation. The different mixtures (cometary analogs with silicate components) used in Poch et al. (2016) exhibited lower reflectance and diminishment of spectral features after sublimation occurred (>-70 °C). Moderate heating of a Ceres analog material (maximum of 300 K, Galiano et al., 2020) likewise resulted in darkening of spectral properties in the VIS-NIR wavelength region as does heating of phyllosilicates (up to 700 °C, e.g., Alemanno et al., 2020; Hiroi and Zolensky, 1999). The water-related band near 3 µm of the CM2 meteorite Murchison vanishes around 500-700 °C (Hiroi et al., 1996; Miyamoto, 1991) which indicates that the PIDs' materials have not seen temperatures above those values (as VIR data show absorption bands there). Below this temperature, Murchison has been reported to show a decrease in reflectance upon heating (Cloutis et al., 2012). Cloutis et al. (2012) also showed that prolonged heating (72h) of a subbituminous coal at 450 °C results in an increase of reflectance. In this example, organics are lost or aggregated which changes the phyllosilicate-organic ratio and makes the phyllosilicates spectrally more dominant. Hence, the loss of organic compounds might trigger the change in reflectance and pyroxene band strength for the PIDs' material; yet this effect has not been shown on carbonaceous chondrite material unless fully melted and recrystallized (Clark

et al., 1993a). There are no studies that reflect the situation on Vesta; yet the studies reported here show that most heating/sublimation experiments with different planetary analogs result in the darkening of overall reflectance and diminishment of spectral features, in contrary to what we observe for the PIDs.

Differences in glass content can also affect a material's spectral characteristics. For pyroxene-rich lunar impact-melt-bearing deposits, Neish et al. (2021) found a possible contribution of glass to explain a smooth optical appearance of certain melt deposits while showing high roughness from radar observations. Given the high likelihood that the PID host material is an impact melt-bearing breccia (Denevi et al., 2012; Tornabene et al., 2012), glass content could also play a role during the formation process of PIDs (i.e., the PIDs' surface might be devoid of glass due to the destruction of the surface layer through devolatilization). Tompkins and Pieters (2010) analyzed the effects of glass content in lunar Apollo samples and observed 'redder' spectra for the quenched glass samples vs. their crystalline counterpart as well as an inconsistent dependency of the reflectance at 750 nm. They found that higher glass contents shift the mafic absorption band position near 1 µm towards longer wavelength which decreases the 750/917 [nm] ratio of a glassy-crystalline mixture. Thus, the surrounding material of the PIDs could indeed contain higher glass contents, yet there is no difference regarding pyroxene band positions for PIDs and their surroundings. The observations of Tompkins and Pieters (2010) regarding the spectral properties of glass-crystalline mixtures are not consistent with my observations of PID-related material so differences in glass content do not seem to play a role in the context of the PIDs either.

I conclude that the most likely explanation for the spectral distinctness of the PIDs is the effect of prolonged internal heating due to the accumulation of material and the devolatilization accompanied by the possible loss of organics and decomposition of darkening agents, although heating studies of meteorites have only shown a general loss of spectral features and reflectance upon heating. Other processes might enhance this effect, like the ejection of entrained pyroxene-rich clasts during the rapid release of steam. Experimental work could refine this hypothesis which is beyond the scope of this study. Lastly, I note that the 'hollows' identified on Mercury (Blewett et al., 2011, 2013) likewise exhibit an increase in reflectance and are linked to a loss of volatiles. While their origin is likely not impact-related (Blewett et al., 2013), the process of volatile release might share similar aspects as the PIDs on Vesta.

## 6.3 The crater-fill PIDs of Marcia

The crater-fill PIDs of Marcia are slightly lower in reflectance than the average Vesta but exhibit the lowest OH abundance of all observed PIDs including the much brighter ones (see Tables 4.4 & 4.5 and Figs. 3.10, 4.10 and 4.13). This is contrary to the general negative correlation between reflectance/pyroxene band strength and OH abundance. Very few exceptions to this observation (e.g., Oppia's ejecta) on Vesta were reported by Combe et al. (2015a) and Le Corre et al. (2013). De Sanctis et al. (2015c) report higher OH abundances for the pitted material on the floor (with respect to the western crater wall material) and conclude that this material is linked to volatile-rich exogenic material. However, our observations including the brighter halo of the PIDs and newly calibrated VIR data from Combe et al. (2015a) do not confirm their conclusion entirely.

The crater-fill PIDs are depleted in OH with respect to other typical Vestan materials with the same reflectance and pyroxene band strength values. The 2.8 µm band absorption depth values are even lower than for the bright PIDs west and north of the crater. The presence of the halo (Fig. 4.11), which comprises very small pits, shows that the crater-fill PIDs of Marcia are not homogeneously darker and that there is compositional diversity among this material. The halo shows the same trend regarding reflectance and pyroxene band strength (Fig. 4.13) as the external PIDs. We therefore propose that for the central PIDs, their darker appearance in the VNIR range could result from the infall of 'dark material' from the crater rim due to space weathering mechanisms (Pieters et al., 2012) and mass wasting processes (Krohn et al., 2014b; Otto et al., 2013) that prevail on Vesta. Especially on the eastern crater wall inflow of dark and partly also OH-rich material is observable (see Figure 3.10b & d, 4.11b and Scully et al., 2015). Thus, we speculate that the OH-depleted pitted floor originally exhibited high reflectance and pyroxene band strength similar to the halo at the margins of the crater-fill PIDs as well as to the area around the central peak. This would also be consistent with the spectral characteristics of the external PIDs. The crater-fill PIDs would then have gradually lost these spectral characteristics due to the input of dark material from the rim. As presented with DTM data (Fig. 4.8), the halo reaches higher slopes at the NW crater wall and might thus not be affected by the input of darker material. Moreover, the crater wall in the NW is much more pyroxene-dominated than other areas of the crater wall, possibly also leading to less input of dark material and/or more input of pyroxene-rich material from the walls. The large depletion of OH within the crater is consistent with the presence of the largest PIDs, i.e., the crater-fill deposit has been subject to higher temperatures and constitutes the most voluminous impactite deposit associated with craters. They are thereby the most prolonged heat source and continued to lose volatiles long after the smaller external deposits had cooled.

The observations by Tosi et al. (2014) might support this hypothesis. They found a higher thermal inertia for the crater-fill deposits of Marcia indicating a larger component of less porous material (De Sanctis et al., 2015c; Scully et al., 2015; Tosi et al., 2014). Furthermore, there is no indication of a heterogeneous subsurface where the crater-fill PIDs reside. Instead, the surrounding bedrock exposed north and west of the crater-fill PIDs shows a eucritic signature with only a very small spectral indication of contamination (see supplementary Fig. S4 (11)) which is likely due to surficial processes (e.g., Pieters et al., 2012). The crater is currently roughly 8-9 km deep (from the current rim) while the excavation depth ranges from 3-7 km depending on the estimation method (one third of the transient cavity depth, Melosh, 1989; estimates based on lower ballistic and upper melt-rich ejecta for Haughton crater on Earth, Osinski et al., 2011). Jaumann et al. (2014) reported the regolith layer in that region to be about 1 km thick, therefore it furthermore seems unlikely to find exogenic material at these depths as hypothesized by Scully et al. (2015). Given that typical crustal lithologies are expected beneath the regolith (i.e., eucrites; e.g., Binzel and Xu, 1993; Keil, 2002; McSween et al., 2013b, 2011 and references therein) it seems even more intriguing that the Marcia impact mobilized such a large volume of volatiles shaping the surrounding geology while excavation depths might have reached deep below the surface regolith into a differentiated body. However, estimation of regolith thickness around Marcia by Jaumann et al. (2014) is based on visual observations of dark material while Denevi et al. (2016) assume regolith depths greater than 1 km based on blocky crater population. Thus, ejecta could possibly still be regolith-dominated. Modelling the formation of this crater could perhaps greatly enhance the understanding of volatiles involved in such a large low-gravity collision, especially given the observation that Marcia might

have been an oblique impact and that oblique impacts favor survivability of impactor materials (e.g., Pierazzo and Melosh, 2000).

Ejecta and crater fill materials can differ greatly due to the provenance of the materials they are comprised of, so the spectral characteristics of the crater-fill PID could also be a result of a different composition due to shed crater wall material, adding higher reflectance and pyroxene band strength materials (i.e., crustal material), especially to the margins of the crater-fill. The halo of the crater-fill on the margins and the central peak could therefore also represent added slumped and uplifted material with similar spectral characteristics. However, the halo is characterized by lower reflectance and similar 750/917 [nm] ratios with respect to the crater-wall material, indicating that it is not derived from this compositional variation. Instead, the halo plots on the same unique trend presented in Figure 4.13, indicating that crater-fill and external PIDs share a common origin, independent of compositional differences.

## 6.4 Distribution of Volatiles

Ejecta units E1 and E2 significantly differ in their overall OH content (Fig. 3.10d). The VIR and GRaND instruments have detected higher concentrations of eucritic lithologies in and around Marcia (as opposed to diogenitic and howarditic lithologies, Ammannito et al., 2013a; De Sanctis et al., 2015b; Prettyman et al., 2012) indicating that the Marcia impact excavated eucritic crustal material. This generally conforms to the estimated excavation depth (3 to 7 km) and the estimated regolith thickness in this region (1 km, Jaumann et al., 2014). This higher eucritic concentration appears in both E1 and E2 as presented here (mainly east and west of Marcia, best illustrated in Russell et al., 2015) which could suggest that Calpurnia is not the source of ejecta unit E2a. If these eucrite-dominated lithologies were to source from the Calpurnia event, they would broadly occur around Calpurnia crater as well, which cannot be observed (Prettyman et al., 2013; Russell et al., 2015) though the data presented do not have a high spatial resolution. The Marcia region displays both large differences in OH contents but also increased eucritic lithologies, implying complex relationships between the observed materials. We have presented evidence that pitted surfaces do not form as a result of an especially high volatile content or the presence of ice at this location but rather through structural control. Nevertheless, volatiles are naturally required in the formation of PIDs, which is why we discuss the distribution of volatiles (i.e., the distribution of carbonaceous material) in the Marcia region in more detail.

Our estimates of volatiles that were lost through the PIDs range around $10^8$-$10^9$ m3 (Table 4.3). As E2a is still very OH-rich (Figs. 3.10 and 3.12) clearly not all volatiles were lost during the impact, be it Marcia or Calpurnia. Reddy et al. (2012a) suggest that on average 1-6 vol% of CM2 chondrite material is mixed within the regolith of Vesta and that up to 50 vol% are locally possible. They present three equations (section 5.2) to calculate the CM2 content (vol%) of which the first two were derived by Le Corre et al. (2011) and are based on the reflectance at 750 nm and the parameter for pyroxene band strength (750/917 [nm]). The third equation was developed by Reddy et al. (2012a) and uses the ratio 750/965 [nm]. We calculated the CM2 content for all of our regions of interest and for all three equations. The three equations and all calculated values can be found in the supplements (S6, 11). Equation (1) which is based on the 750 nm reflectance gives the highest contents and equation (2) using the 750/917 [nm] ratio gives the lowest values. The third equation has similar values as equation (2) with slightly higher estimates (typically 2 to 4 vol%). Results of equation (1) yield similar values like (2) and (3) for low reflectance regions but significantly higher values for higher reflectance regions which seems unrealistic. In the following, we use equation (3) as it appears to yield the most realistic results. We note at this point that the calculated values most likely do not represent the 'true' values as PIDs do not follow the 'typical' Vestan trend regarding their pyroxene band strength values (Fig. 4.13), which also affects the 750/965 [nm] ratio.

We calculate the difference in CM2 chondrite material between PIDs and their surroundings (based on values in Table 4.5) to be about 9 to 12 vol% which is slightly higher than Reddy et al. (2012a) suggest for the average abundance of CM2 chondrite material on a global scale. This difference corresponds to a difference of volatile material of roughly 1 wt% (assuming 11% of mass loss during devolatilization, Garenne et al., 2014). The smooth surroundings of PIDs contain about 19 to 26 vol% CM2 material while the PIDs contain about 7 to 17 vol% of CM2 material. The volatile content of the surrounding of PIDs corresponds to about 2-3 wt%. Boyce et al. (2012) show for Tooting crater on Mars that a relatively low volume of volatiles can lead to extensive pitting as well. They estimate 12 wt% of volatiles for Tooting crater target material but also acknowledge that for the Ries crater in Germany, Engelhardt et al. (1995) and Osinski (2003) observed that roughly half of the target volatiles were still present in impact glasses, reducing the released volume. This corresponds well to our calculations of volatiles lost (i.e., 1 wt% lost with host material volatile abundances of 2-3 wt%) based on the approaches by Reddy et al. (2012a) and Garenne et al. (2014) and is also consistent with the generally dryer nature of Vesta (i.e., no subsurface ice as opposed to Mars).

Based on an average of 10 vol% of CM2 material loss, we calculated the volume of CM2 material now lost at the PIDs' sites (excluding the crater-fill) using the total size of PIDs (212 km2, Table 4.3), average thicknesses of the PIDs' material (50 m, 100 m, 200 m, see section 4.5) and a porosity

of 25% which results in approximate total volumes of $0.9*10^9$ m3, $1.8*10^9$ m3 and $3.5*10^9$ m3, respectively. We roughly estimate the regolith porosity (i.e., 25%) from macro porosity estimates for the silicate portion of Vesta (8%) by Ermakov et al. (2014), average howardite and eucrite porosities (11%) given in Macke et al. (2011a) and the decline in porosity near the surface from 55% at the surface to 37% at one meter depth (Palmer et al., 2015).

Garenne et al. (2014) observe a mass loss of around 11% between 200 and 700 °C (attributed to (oxy) hydroxides and the dehydroxylation of phyllosilicates) for their studied CM chondrites on which they performed thermogravimetric analysis combined with infrared spectroscopy in order to quantify the chondrite's water content. We assume here that the molecular waters lost between 0 and 200 °C are already gone within the whole ejecta (i.e., both PIDs and their smooth surroundings). Assuming the same percentage of volatiles lost during the devolatilization process occurring at the PIDs' sites, a grain density of 2900 kg/m3 for the CM2 material (Macke et al., 2011b) and the assumption that the density of lost volatiles roughly equals 1000 kg/m$^3$ (the density of water vapor, upper limit), resulting volatile volumes are $2.8*10^8$ m$^3$, $5.7*10^8$ m$^3$ and $1.1*10^9$ m$^3$, respectively. These values are in very good agreement with the estimated values in Table 4.3 from pit statistics. For the crater-fill PIDs in Marcia, we assume a material thickness of 500 m and a lower porosity (15%) accounting for more compacted material (De Sanctis et al., 2015c; Scully et al., 2015; Tosi et al., 2014). The volume of lost volatiles is then $8.5*10^9$ m$^3$ which is one order of magnitude higher than our estimates in Table 4.3, possibly resulting from underestimated pit depths in section 4.5, underestimated porosity or overestimated material thickness in this calculation.

With the same equation derived in Reddy et al. (2012a), we furthermore calculate the average CM2 content of E2a to be around 31 vol%. If we assume that this ejecta part formed exclusively from a 1 km thick contaminated regolith layer (Jaumann et al., 2014; neglecting the possibility E2a originates from the Calpurnia impact) and a crater radius of roughly 30 km, a volume of 2800 km$^3$ of regolith material was redistributed by the impact. Assuming a symmetric distribution around Marcia with a radius of about 100 km (the farthest PID is 69 km off the crater rim) we calculate the average thickness of contaminated Marcia ejecta to be roughly 100 m, which is consistent with ejecta thicknesses estimated with the approach by McGetchin et al. (1973) for ejecta about 15 km off the Marcia rim. We acknowledge that this is a rough estimate with high variations between regions closer and farther from the rim and it does also not include Calpurnia as the possible origin of E2a. It is difficult to estimate the thickness of E2a as it is located right on the slopes of Vestalia Terra (mountains rising to 10 km above the Marcia rim). Ejecta accumulated there and obscured much of the underlying topography. If we assume an average of 200 m thickness roughly accounting for this accumulation for an area of about 13,000 km$^2$ (E2a, Fig. 3.11), a regolith porosity of roughly 25% and a CM2 content of 31 vol%, roughly $6*10^{11}$ m$^3$ of CM2 material are still present within E2a which corresponds to $1.9*10^{11}$ m$^3$ of volatiles. This is a lower limit as there are possibly more E2-type ejecta below E1 ejecta (as seen at Laeta crater and possibly even at Aricia Tholus, Fig. 3.11). For E1 and E2b, the average CM2 content is 16 vol% and 24 vol%, respectively. For E1, with an assumed average thickness of 50 m and an extent of 11,000 km$^2$, the volume of still-present volatiles is $2*10^{10}$ m$^3$. For E2b (100 m and 12,000 km$^2$), still-present volatiles are in the order of $7*10^{10}$ m$^3$. The estimated value of $1.9*10^{11}$ m$^3$ of volatiles still present in E2a is two to three orders of magnitude higher than our estimates of lost volatiles through volatile degassing at the PIDs' sites. Most of the hydroxyl groups bound in minerals/phyllosilicates were therefore not liberated during the impact (be it Marcia or Calpurnia) and the volatiles lost by rapid vent-forming devolatilization represent a small fraction (<2%) of volatiles still present in the whole area. This furthermore illustrates that PID formation does not depend on the volatile content at their specific location as volatiles are still ubiquitous in the ejecta blanket. They were lost at the PIDs' sites due to topography-dependent ejecta accumulation and the resulting increase in deposit thickness and internal heat.

Independent of whether Marcia or Calpurnia generated the ejecta unit E2a, the regolith where the Marcia impactor hit held at least 31 vol% of CM2 material which is an unreasonably high amount (Reddy et al., 2012a) for a large regional area like the ~30 km radius of pre-Marcia or 25 km radius of pre-Calpurnia regolith, yet the three equations to calculate CM2 content by Le Corre et al. (2011) and Reddy et al. (2012a) generate similar values for E2a (see S6) and E2a furthermore

shows the highest large-scale abundance of OH (i.e., strongest absorptions at 2.8 µm, Combe et al., 2015a). The Veneneia impact basin which is thought to have delivered most of the dark material is close to Marcia (e.g., Jaumann et al., 2014; Schenk et al., 2012) which could be the reason for this abnormally high amount of carbonaceous chondrite material within the regolith, yet does not entirely explain the strong dichotomy of the ejecta units which remains an open question.

## 6.5 Insights from Dawn VIR data

This subsection is not part of Michalik et al. (2021) and relates to the new analysis of VIR data presented in section 4.9.

In section 4.9, I have shown that the PIDs' distinct spectral characteristics as seen by FC data for the first pyroxene absorption band likewise occur for the second pyroxene absorption band around 2 µm. Values of the ratio 1.446/1.910 [µm] are prominent for PIDs associated with Marcia, although their reflectance at 1.446 or 1.910 µm are not particularly elevated with respect to other regions. Thus, PIDs can also be identified by the spatially lower resolved VIR instrument. This emphasizes that the effect is real as we observe it with two separate science instruments. Moreover, the prominent spectral characteristics of the halo on the margins of the crater-fill PID are as apparent as in FC data. PIDs in the crater-fill deposits of the smaller craters Cornelia and Licina show lower reflectance and pyroxene band strength, resembling the results from FC data. This indicates that either the observed process did not occur for Cornelia and Licinia crater-fill PIDs or that the 'real' spectral characteristics of these PIDs are obscured, possibly by mass wasting and inflow of material, as we speculate for Marcia as well.

The observation of the second pyroxene band has also implications on the cause of these spectral characteristics, as they occur to both pyroxene absorptions. Some possible explanations for this phenomenon only occur in the UV or VIS region. For example, the $Fe^{2+}$ to $Fe^{3+}$ intervalence charge transfer transition (IVCT) only causes absorptions in the UV and VIS region (e.g., Burns, 1993), so the second pyroxene band should not be affected. Likewise, changes of electronic transitions between oxygen ligands and the central transition metal would effect UV absorptions (i.e., oxygen metal charger transfer transitions, Burns, 1993) The formation of hematite alone can either not affect both pyroxene absorption bands. Hematite shows one prominent absorption band around 860 nm yet none in the region around 2 µm. The pyroxene absorptions at 1 and 2 µm are caused by the crystal field effect of $Fe^{2+}$ in the M2 site, hence the most likely explanation is that something changes this particular light absorption mechanism, which will be elaborated on further in section 7.3.

# 7 Discussion II: Insights from Laboratory Experiments

## 7.1 Grain size

Similar to the aspects and data discussed in the previous section 6, the results of the presented grain size experiments (section 5.1) did not show similarities to the Vestan PIDs. Smaller grain sizes and dust emerging from a sublimating material yield higher overall reflectance but lower pyroxene band strength, even when containing dark particles. In contrast, the larger remainders of the sublimation experiments exhibit higher pyroxene band strengths but significantly lower overall reflectance. This is in strong contrast to what we observe on Vesta for the PIDs (higher reflectance and band strength). Furthermore, the laboratory experiments regarding grain size are likely not robust due to the use of a lid and limited recovering option from the vacuum chamber. Fine-grained material became stuck on the lid, yet the material recovered from the chamber also contained larger grains, indicating that larger grain sizes were also ejected yet did not become stuck on the lid. This presents two problems: 1) The fine-grained fraction is not representative of the material that would have been ejected without the lid, and 2) the fraction recovered from the chamber is likewise not representative of the ejected material as a significant part of the fine-grained fraction was removed from the material (and stuck on the lid). In summary, although the undertaken experiments are not robust, other considerations as presented in section 6 strongly speak against a role of grain size.

## 7.2 Abundance of carbonaceous chondrite material

A combination of varying grain sizes and compositions (abundance of 'dark material'), however, yields different results. A material containing smaller grain sizes and less dark material shows spectra with higher overall reflectance and pyroxene band strength with respect to materials with larger grain sizes and more dark material. Moreover, likewise do similar grain sizes but different abundances of CC-material yield similar characteristics. Thus, the loss of darkening agents and possibly grain size variations could yield to the PID spectral characteristics. However, when comparing the absolute differences between the spectra's reflectance at 750 nm and pyroxene band depths, the experimental data do not conform to the PID characteristics, i.e. the differences in reflectance (at 750 nm) have to be quite high (at least >0.05) in order to achieve similar pyroxene band strength differences (~0.15; see section 4.10) as for PIDs and their surroundings (see also Table 5.1), where the difference in reflectance is on average only (~0.024). Thus, it remains challenging to artificially create the spectral characteristics of PIDs and their surroundings with solely 'dark material' and grain size variations.

The abundance of dark material within the regolith analog also appears to play a role regarding the heating experiments, which will be described in the next section.

## 7.3 Temperature Effects

The experiments undertaken in the PSL facility at DLR clearly show that temperature plays an important role in changing the spectral characteristics of the considered samples. However, these changes do not appear to be entirely systematic, neither within a given sample or within a whole suite (meteoritic/terrestrial) or temperature range.

A mere temperature increase for a particular duration rarely results in higher reflectance and band strength (as seen for PIDs on Vesta). With respect to the unheated sample, all heated aliquots show lower pyroxene band strength, even when reflectance at 750 nm is higher (e.g., at 600 °C, 2h for the meteoritic samples). However, it is important to understand the concept on Vesta: The PIDs are part of a larger impact deposit whose surface is not entirely pitted. Hence, it can be assumed that the surrounding impact deposit likewise experienced higher temperatures, but possibly not reaching the same peak temperature and/or the same duration of elevated temperatures. Moreover, the surface of the unpitted deposit was not disturbed after deposition (except the exposure to space weathering). Instead, the pitted deposit's surface was likely modified after deposition through the release of volatiles and particles at the PIDs' sites. With that said, it is critical to observe the changes not with respect to the unheated sample but to the other heated aliquots.

The only samples where a temperature increase yielded higher reflectance and pyroxene band strength for a reasonable situation comparable to Vesta (higher temperature and/or longer duration) were for: H90P10 at 600 °C for 72 h with respect to H90P10 at 600 °C for 2 h. Interestingly, for JaH626M and NWA5748M, the 600 °C, 2 h aliquot yielded higher reflectance and band strength than the 600 °C, 72 h aliquot, which is counterintuitive to the situation on Vesta (the less voluminous surrounding deposit would not be heated for longer durations).

Heating of samples furthermore mostly resulted in the increase of the visible spectral slope with higher temperatures and durations, which is especially apparent in meteoritic samples. 965/917 [nm] values also tend to increase (with exceptions) with temperature and duration which could correspond to a slightly shifted band position to shorter wavelengths, but possibly also to the change of the band intensity (with 965 nm values increasing and 917 nm values decreasing for a more intense absorption). The same is observed for Vestan PIDs (see section 4.10). The change in 965/917 [nm] and 750/430 [nm] values was not observed in Michalik et al. (2021) and presents an addition in this dissertation. Visible spectral slope (750/430 [nm]), however, does not increase dramatically for PIDs vs. their surroundings (0.02-0.08 in absolute values), whereas the laboratory heating results in significantly higher differences for the mentioned samples (0.225 for the considered H90P10 aliquots). The change in 965/917 [nm] for the considered H90P10 aliquots is 0.009 which is in good agreement with changes for PIDs vs. their surroundings (~0.000-0.020).

Heating (400 °C, 72 h) of the analog endmembers mostly results in a decrease of overall reflectance and pyroxene band strength (for pyroxene-bearing endmembers), except for Murchison (Fig. 5.10). The reflectance spectrum of the heated Murchison aliquot is significantly increased in visible spectral slope and overall reflectance beyond ~0.6 µm. The Phobos Simulant, which is supposed to represent a CC analog, does not experience similar effects at this temperature. However, it can be assumed that a related mechanism occurs at 600 °C, where we see significant changes in the H90P10 sample. For the terrestrial sample H70P30 with a higher CC analog content, this effect appears to start already at 400 °C, seen in both VIS and NIR measurements for both pyroxene absorptions. This indicates that a higher CC content in these analog samples facilitates the onset of the process. This in turn could explain why PIDs in ejecta units E2a and E2b (they show higher overall OH contents) also occur at sites where no pre-existing craters or ridges are readily identifiable and/or present.

The remarkable change of the Murchison reflectance spectrum is not in accordance with observations by Cloutis et al. (2012), who show the absolute reflectance in the VIS and NIR range of heated Murchison. Their data for Murchison were initially presented by Hiroi et al. (1993) and Hiroi et al. (1994), who heated the samples for one week in a low pressure hydrogen atmosphere. This is a different procedure from the one presented here and therefore likely produces different results. The heating of Murchison was also performed in other studies (not focusing on spectral characteristics) (e.g., Zolensky et al., 1994, Yamashita et al., 2015) which report on the decom-

position of tochilinite, a hydroxysulfide mineral and major constituent of the Murchison matrix. Tochilinite is a brown to black mineral, thus darkening an overall spectrum. The loss of tochilinite would increase the overall reflectance, however, this would also be true for regions devoid of CC material on Vesta, as discussed already in section 6.

Few studies exist on the heating of HED material (e.g., Hinrichs and Lucey, 2002; Miyamoto and Mikouchi, 2001). These studies report that the spectra of heated HED samples generally do not change significantly but tend to lose spectral contrast and band strength after heating, which is identical to what is observed in this thesis for the HEDs NWA3359 and NWA5748. Hinrichs and Lucey (2002) observe a shift of band minima to longer wavelengths, though they measure the sample during the heating process. Nevertheless, NWA3359 and NWA5748 accordingly show slight decreases in 965/917 [nm] values, which could indicate a slight shift to longer wavelengths, as well.

The most systematic and distinct changes for the here presented laboratory heating experiments were observed when comparing heated surfaces and heated interiors (section 5.2.2). All meteoritic samples showed that for a certain threshold temperature, both reflectance and pyroxene band strength become higher for interior vs. surface particles. The most likely explanation is that volatiles lost from Murchison cause the oxidation of the interior analog sample, yet are quickly lost to the vacuum on the surface. In the interior, volatiles are more likely to interact with the material without escaping. The mentioned threshold temperatures of the experiments were mostly around 400 °C, suggesting that the ejecta deposits on Vesta likely experienced similar temperatures at or above 400 °C.

This observation of changes between the interior and surface of the analog samples is in agreement with the concept on Vesta, where particles were likely ejected through the degassing pipes from the interior of the ejecta deposit to the surface (Boyce et al., 2012; Denevi et al., 2012; Michalik et al., 2021; Tornabene et al., 2012). Interior material therefore appears more affected by the process inducing the observed spectral changes. For NWA5748M, this already starts at 200 °C and 72h, whereas for NWA5230M, it starts at 600 °C. For JaH626, no spectra of interior and surface particles were acquired below 400 °C, so the only data available is the one in Table 5.9, showing that for both 400 °C, 168 h and 600 °C, 72 h, both reflectance and pyroxene band strength increase for interior particles with respect to surface particles.

The absolute changes for the pyroxene band strength indicator 759/917 [nm] (0.055 ±0.038) are less for the meteoritic samples heated in the laboratory environment than for PIDs vs. their surroundings (0.149 ±0.057). However, one has to keep in mind that interior particles could not be measured separately (they were mechanically mixed with surface particles). Thus, the 'true' values would be higher. Nevertheless, changes in 750/430 [nm] values (~0.1-0.3) by far exceed the values for PIDs (~0.02-0.08), whereas 965/917 [nm] values (~0.003-0.007, but negative values exist) are again in agreement with Vestan PIDs' values (~0-0.02, negative values also exist).

Interestingly, the effects between surface and interior enhance with temperature and duration, yet the overall level of absolute values decreases, which is why an aliquot heated to 600 °C, 72 h (interior) still exhibits lower pyroxene band strength than for example an aliquot heated to 400 °C, no matter the duration or interior/surface condition.

The terrestrial samples do not show these extensive differences between surface and interior particles. H90P10 only shows an increased reflectance and pyroxene band strength for the interior vs. surface for the 600 °C, 72 h experiment, indicating a change in behavior of the sample mineralogy at this temperature (or slightly lower). H80P20 does not show any such increase for the acquired temperature at 400 °C, 72 h. Interestingly though, H70P30 shows a slight increase in reflectance and pyroxene band strength for interior vs. surface particles for the 400 °C, 72 h aliquot, which was mentioned earlier.

The more pronounced spectral changes in the meteoritic analogs appear to arise due to the use of Murchison as a dark material/CC analog. Figures 5.10 and 5.15 show that Murchison significantly increases its visible spectral slope upon temperature. Murchison and its terrestrial counterpart (Phobos Simulant) were heated to 400 °C and 72 h in order to observe any changes of these endmembers. It can be assumed that the Phobos Simulant behaves similar to Murchison for higher temperatures, as related changes occur to H90P10 after 600 °C. Moreover, as similar changes

to H70P30 already occur at 400 °C, an increased effect with increasing Phobos Simulant-abundance can be assumed. A similar observation can be made for meteoritic samples, as NWA5748M contains 20 wt% Murchison and NWA5230M 15 wt%. The difference is small, yet NWA5748M shows an earlier onset of the development of higher reflectance and band strength for interior vs. surface particles (at 200 °C, 72 h, vs. for NWA5230M at 600 °C). This might arise from the difference of Murchison abundance, yet it cannot be excluded that the individual meteorite properties also play a role.

The reddening of the samples (increased visible spectral slope) is the most characteristic change of the heated samples, which is significantly larger than seen for the PIDs and their surroundings. One thing that distinguishes the two settings, of course, is time and scale. The PIDs associated with Marcia have been exposed to the space environment for at least 40 Ma (Williams et al., 2014b), which the meteoritic samples, after heating, have not. It is possible that large visible spectral slopes degrade over time, which is characteristic for space weathering on Vesta (Pieters et al., 2012). Pieters et al. (2012) have shown that typical soil maturation characteristics (like reddening of spectrum and loss of spectral features) prevailing on the moon and some asteroids do not prevail on Vesta. Instead, freshly exposed bright areas are relatively redder than background soil.

The most likely explanation for the reddening of laboratory samples is the formation of ferric iron compounds, i.e., hematite. Microscope images have shown that very small red phases are present in the heated sample NWA5748M (600 °C, 72 h), scattered throughout grains and attached to grains. EPMA analysis confirmed that hematite coatings formed around iron sulfide, iron metal and pyroxene grains. The development of hematite explains the strong reddening of the laboratory heated samples. However, we do not observe the typical absorption features at 0.66 µm and 0.85 µm (Morris et al., 1985), which might be completely masked by the spectral predominance of pyroxene or might be due to poor crystallinity of the hematite (EPMA images show roundish, amorph-like shapes of the found hematite, see Fig. 5.24). However, some samples might indicate the development of another typical absorption at around 0.5 µm (Morris et al., 1985), indicated by a prominent kink or sudden near-VIS reflectance loss of spectra of relatively high-temperature interior aliquots (e.g., 600 °C for NWA5748M, 600 °C for H90P10, 400 °C, 168 h and 600 °C for NWA5230, 400 °C, 168 h and 600 °C, 72 h for JaH626) at about 0.6 µm towards shorter wavelengths.

Development of hematite during oxidation/heating is a commonly observed process and was also observed for extraterrestrial materials. Dixit et al. (2021) show that hematite develops after heating several ordinary chondrites in air (here, 600 °C is the lowest of the studied temperatures). It is moreover well-known for Mars and SNC meteorites that (nanophase) hematite is a common weathering product (e.g., Minitti et al., 2002; Morris et al., 1989, 2000). Morris et al. (1994) show that relatively unoxidized pyroxene-bearing impact melt samples from the terrestrial crater Manicouagan (Quebec, Canada) develop hematite when heated and oxidized. This oxidation occurs subsolidus and the spectra gradually change from well-pronounced pyroxene spectra to essentially hematite spectra at 1000 °C. At 400 °C and 500 °C, the spectra are already significantly reddened (Morris et al., 1994) but still exhibit distinct pyroxene absorptions, very similar to the results shown here. Furthermore, the development of hematite was seen when oxidizing various pyroxenes when heated to 600 °C in air (Cutler et al., 2020) to infer Venus surface alteration (see also Dyar et al., 2021 for surface alteration of Venus). Straub et al. (1991) also observed the formation of nanophase hematite when heating pyroxenes in air.

Li et al. (2020) presented evidence for the presence of hematite on the Moon and compare laboratory acquired hematite data to those of the Moon (Fig. 7.1). The moon surface is highly reduced and shows only up to 1 wt% of ferric iron (Li et al., 2020). Some pixels of $M^3$ (Moon Mineralogy Mapper) spectra suggesting the presence of hematite show significantly shallower visible spectral slopes than those of pure hematite, possibly resulting from exposure to the space environment, or differences in particle size and abundance (Li et al., 2020). However, no studies exist on the space weathering of hematite, which the authors likewise point out. The EPMA analysis presented in section 5.5 shows that hematite forms as very thin coatings (about $\leq$2 µm), so these coatings might be prone to weathering of any kind. Pieters et al. (2012) point out that mechanical brecciation dominates space weathering processes on Vesta, so the hematite might be quickly removed from its host grains.

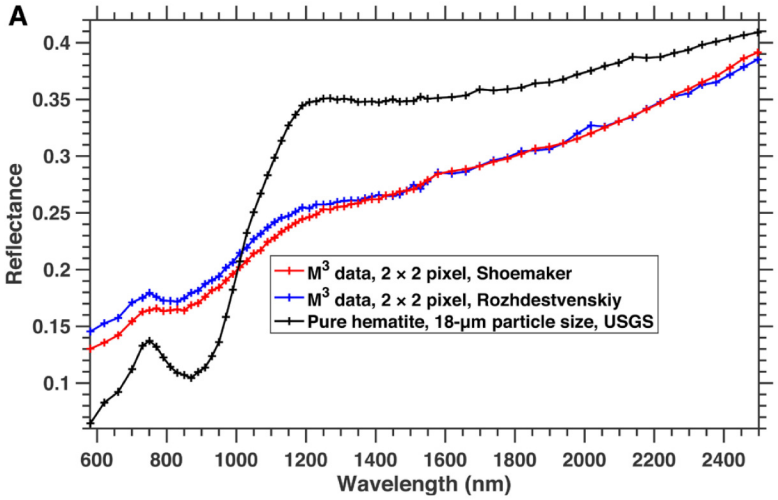


Figure 7.1: Caption adapted from Li et al. (2020): Examples of $M^3$ spectra at hematite-rich pixels. The hematite-rich M3 spectra are compared with laboratory spectra of pure hematite.

We do not observe this strong reddening for PIDs, although other distinct red areas on Vesta exist (Le Corre et al., 2013). However, we do see a small kink at 650 nm for both PIDs and their surroundings, which might tentatively indicate the typical hematite absorption at 0.66 µm. More work is needed to evaluate this kink. Le Corre et al. (2013) concluded that the "orange material" (it appears orange in the Clementine-type RGB as the visible spectral slope is large), is most likely impact melt, yet did not consider hematite formation as a possibility. They determined an age of >200 Ma for Oppia, which is either older or similar-aged as Marcia. We do not know whether hematite could also be a possibility for this orange appearing material, yet if it would, the large visible spectral slope would not have significantly degraded over time.

Even if hematite was proven to exist on Vesta, it cannot explain the strengthening of pyroxene band strengths for both of the pyroxene crystal field transitions which is observed for PIDs on Vesta and can be beautifully seen in the comparisons between surface and interior in section 5.2.2. Hematite is generally darker than pyroxene in the VIS range and lowers band strengths and reflectance of pyroxene as it absorbs more light and can scatter it before it encounters the pyroxene grain. Data provided by Edward Cloutis from the University of Winnipeg of powdered pyroxene and hematite mixtures strengthen this concept, which is illustrated in Figure 7.2. The nanophase hematite lowers pyroxene band strength of both pyroxene bands at 0.9 and 1.9 µm, lowers the reflectance below ~0.8 µm yet increases reflectance of the mixtures beyond 0.8 µm. Moreover, the band position moves towards shorter wavelengths with increasing hematite proportions in the mixture. This is likely due to the overlapping of the shallower hematite absorption band near 0.86 µm. A shift to (slightly) shorter wavelengths is also seen for the majority of PIDs on Vesta and for the majority of the heated samples presented in section 5. However, no heating was involved in acquiring the data shown in Figure 7.2.

Cutler et al. (2020) heated several pyroxenes for various amounts of time under Earth atmospheric conditions. As mentioned before, they likewise observed the formation of hematite for their considered samples basalt, diopside, augite, pyroxenite and olivine. They note that hematite took longer to form from pyroxenes than from olivine (about an order of magnitude) and that pyroxene signatures are still recognizable after two months of alteration. The authors chose much longer durations for their experiments (one to seven weeks), yet interestingly likewise observe an increase of reflectance and pyroxene band strength even with respect to the unheated sample (see Fig. 7.3 taken from Cutler et al., 2020). The orthopyroxenite sample showed an increase of 20% in pyroxene band depth and a slight increase in overall reflectance which the authors attribute to the formation of the relatively brighter hematite. The diopside sample even shows larger increases in band depth. The increase of band depth is suggested to form due to two possible mechanisms: 1) The migration of iron from the inner pyroxene grains to form hematite brings more Fe near or to the surface of

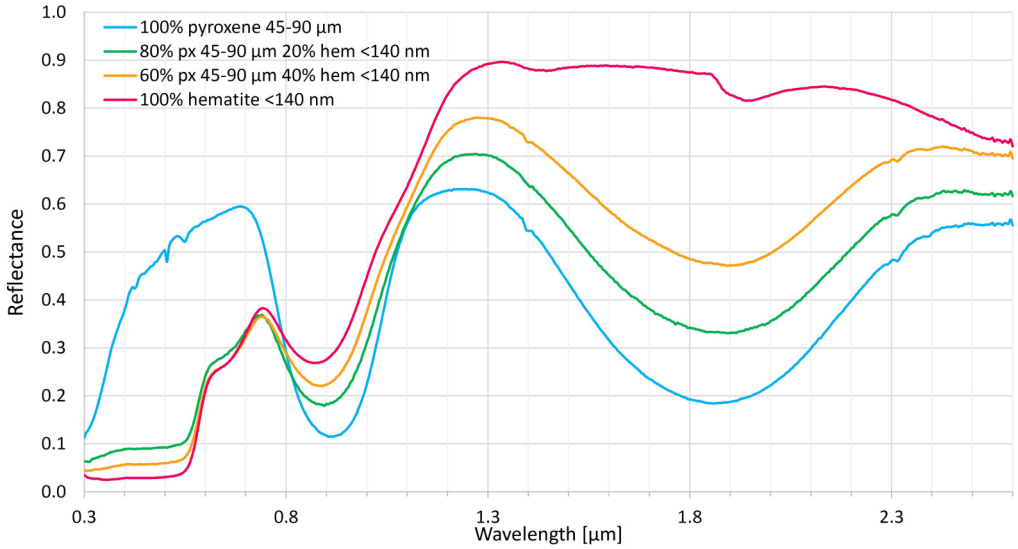


Figure 7.2: Wavelength vs. reflectance for nanophase hematite and pyroxene mixtures. Data provided by Edward Cloutis in personal communication. Corresponding RELAB file are: cahe01 for 100% hematite <140 nm, cbpp47 for 100% pyroxene 45-90 µm, c1mx17 for 80% pyroxene 45-90 µm and 20% hematite <140 nm, and c1mx18 for 60% pyroxene 45-90 µm and 40% hematite <140 nm.

the grains which results in the appearance of an increased iron abundance, and 2) the cations in the initial pyroxene might be disordered and at elevated temperatures, more Fe can migrate to the preferred M2 sites which causes a strengthening of the pyroxene absorption (Cutler et al., 2020). However, for the diopside sample, the authors observe a shift to longer wavelength with increasing durations. They attribute this to the possibly higher iron abundance in the M2 site or the iron migration towards the grain surfaces. However, the pyroxene band position of their orthopyroxenite sample appears to slightly shift to shorter wavelength, which they do not describe but is observable in their Figure 1 (here Fig. 7.3). The pyroxene absorption band also appears to narrow towards shorter wavelengths.

Straub et al. (1991) also exposed pyroxenes to oxidation and observed the obscuring of the prominent pyroxene crystal field bands as well as the intensification of the $Fe^{2+}$ to $Fe^{3+}$ IVCT transition, yet they did not heat their pyroxenes simultaneously. They state that the $Fe^{3+}$ cation can both remain within the pyroxene structure or leave the structure to form nanophase hematite.

The shift of 965/917 [nm] (pyroxene band position) appears subtle, both for most of the heated samples presented here and for most of the presented PIDs with respect to their surrounding. McCanta and Dyar (2020) show that increased oxidation (higher $Fe^{3+}$) of pyroxenes lead to band minima at shorter wavelengths, although they did not observe a hematite formation. They either did not observe an increase in reflectance and pyroxene band strength with progressive oxidation, in contrast to what Cutler et al. (2020) showed. However, Cutler et al. (2020) applied significant temperatures to the samples while exposing them to an oxidizing environment, which likely plays a key role in the observed increase in reflectance and band strength.

A pyroxene band position shift to lower or higher values is not systematic, neither for the laboratory acquired spectra of heated samples nor for PIDs. In both datasets, marginal shifts to longer wavelengths also occur. This might indicate that various processes play a role, each of which might prevail in a given environment, depending on the temperature and composition of the material. A shift to shorter wavelengths as oxidation progresses is a reasonable assumption but a shift to longer wavelengths due to the concentration of Fe either on the grains' surfaces or in the M2 sites is likewise a reasonable explanation. Possibly, both mechanisms occur at the same time, leading to the observed subtle shifts of 965/917 [nm] values.

PIDs might not show hematite indications as the process of oxidation had just started. Boyce

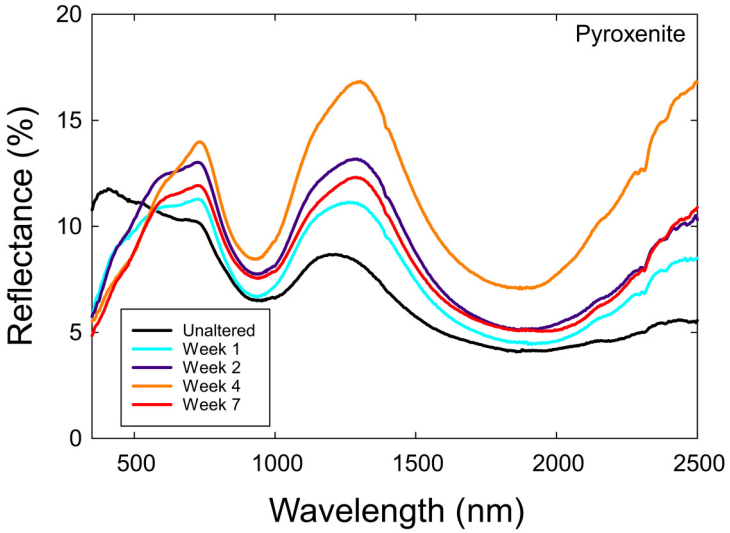


Figure 7.3: Wavelength vs. reflectance for orthopyroxenite before and after oxidation at 600 °C for various durations. Figure taken from Cutler et al. (2020), Figure 1.

et al. (2012) show that for Tooting crater and an estimated volatile content of 10% by mass of water, the devolatilization process and/or pit formation ceased after ~96 days. For an estimated volatile content of 4%, this value decreases to ~38 days. Another decrease of devolatilization time could occur due to the decrease of median clast size in their calculations, leading to a cease of steam release after 16 days. As the Vestan regolith holds significantly less volatile contents, this value might decrease even more. In addition, the lower gravity regime might increase steam escape velocities further (Boyce et al., 2012).

This results in possibly just hours to days of volatile release at PID sites on Vesta. Our experiments showed that hematite can already form at low temperature and durations, yet our analog samples are homogeneously mixed particulate materials, whereas the impact deposits on Vesta probably contain both melt and rock fragments, inhomogeneously mixed with CC-material. Jaumann et al. (2014) have shown that the 'dark material' on Vesta often occurs as inhomogeneously distributed lenses in the subsurface/regolith. Furthermore, we have no way of knowing the *real* composition of the CC-material within the regolith around Marcia. Different CCs could alter the oxidation behavior, which the presented laboratory experiments have likewise shown. Thus, the oxidation process appears highly sensitive to the species of CC material and to the abundance.

In summary, the presented heating experiments show that an oxidizing environment in addition to heating might be capable of creating the spectral effects seen for PIDs in Marcia's ejecta (and the halo within Marcia). This simple subsolidus thermal oxidation process is the most likely explanation for the distinct spectral characteristics of PIDs which deviate from typical Vestan values. Hematite detection is tentative or non-existent on Vesta, yet the formation of hematite might not have yet been in place, or not been pronounced enough to create strong reddening effects and the typical light absorptions.

This work is the first to describe a possible surficial oxidation process on Vesta with potential implications to other solar system objects and even astrobiological considerations. Oxidation in combination with the presence of iron oxides and presence of organics (due to influx of various meteoritic and possibly cometary material) might influence the search for organic matter on Mars (Royle et al., 2021). Gaidos and Selsis (2006) argue to not underestimate the potential role of small bodies in the development and distribution of life or its precursors within the solar system and this work and previous Dawn works show that even differentiated, thought-to-be-dry asteroids enable diverse mechanism (mostly due to the influx of carbonaceous chondrite material) like the here suggested oxidation of iron.

# 8 Summary and Conclusions

This Summary and Conclusions section partly contains paragraphs that were published in Michalik et al. (2021).

This thesis studies the Pitted Impact Deposits (PIDs) on Vesta. In Michalik et al. (2021), we have reported on the spectral and geomorphologic properties of pitted impact deposits related to the young, large impact crater Marcia (and Calpurnia) on Vesta. By analyzing FC data, we find that volatile release shaping the characteristic pits within the PIDs is linked to topography-controlled accumulation of ejecta and the accompanied increase of deposit thickness and internal amount of heat, resulting in the prolonged retention of heat within the material and larger volumes of heat-bearing material with respect to the deposit's surface area. Pitted surfaces on impact deposits are often found within pre-existing craters and along scarps and crater-walls, enabling the estimation of pre-existing topography and deposit thickness. PID formation is therefore most likely not linked to exceptionally high, location-specific volatile contents or subsurface ice deposits as suggested by Scully et al. (2015).

PIDs occur within spectrally distinct ejecta units and accordingly hold different spectral and morphological properties, likely related to the initial abundance of volatiles/chondritic material in each ejecta unit. Based on equation (3) in Reddy et al. (2012a) we calculate the difference in CM2 chondrite material between PIDs and their surroundings to be about 8 to 12 vol% which would correspond to a difference of ~1 wt% volatiles. We roughly estimated the volume of volatiles that were lost through the explosive devolatilization within the PIDs material as well as the volume of volatiles still present in the ejecta. We find that volatiles lost from PIDs likewise represent only a small fraction of the volatiles still present in the ejecta (¡2%). This furthermore illustrates that PID formation is not tied to an exceptionally high availability of volatiles (i.e., carbonaceous chondrite material), but that topography related accumulation of ejecta material plays a key role. The inferred volumes of now lost volatiles from these calculations are in good agreement with volumes calculated from pit statistics presented here.

The pitted surfaces of PIDs display an 'enhancement' of eucritic characteristics, i.e. higher reflectance at 750 nm and higher pyroxene band strength (750/917 [nm]), which is presented in Michalik et al. (2021). At the time of writing this published study, these spectral characteristics most likely corresponded to less contamination by carbonaceous chondrite material in contrast to grain size, roughness or glass content. Yet we noted that the observed changes to the deposit material do not conform entirely with the trend given by carbonaceous contamination. We observe a unique spectral trend for PIDs with respect to their smooth surroundings and/or other typical Vestan materials regarding reflectance, pyroxene band strength and 2.8 µm absorptions. At the time of publication, the most likely explanation for this spectral enhancement of eucritic characteristics was the loss and decomposition of exogenic volatile-rich material upon prolonged heating. This is consistent with the hypothesis presented by Denevi et al. (2012) (which was based on findings from Tornabene et al., 2012 and Boyce et al., 2012 for Martian PIDs).

The spectral characteristics of the crater-fill PIDs within Marcia, which are by far the largest of all PIDs observed, are heterogeneous. Most of the PIDs' surface show lower reflectance and pyroxene band strength than their surroundings (i.e., the crater walls) but also the lowest 2.8 µm band depth values among PIDs. This contradicts the general anti-correlation between OH abundance and reflectance/pyroxene band strength as observed for all other PIDs related to Marcia. In Michalik et al. (2021), we speculate this might result from inflow of dark material from the crater rim by mass wasting processes. The original surface of the crater-fill PIDs likely exhibited higher reflectance and pyroxene band strength similar to the halo observed on the margins of the crater-fill PIDs and close to the central peak. This halo shows the same unique spectral characteristics as the external PIDs regarding reflectance and pyroxene band strength and therefore, the crater-fill PIDs might still have experienced the same unique process. However, the halo moreover comprises much smaller individual pits as does the immediate surrounding of the central peak which additionally shows signs of subsidence. This might indicate a secondary devolatilization process within the crater-fill deposit, occurring after an initial devolatilization phase and thus having had more time for material changes to occur.

This thesis additionally includes analysis of Dawn VIR data at lower spatial but higher spectral resolution. VIR-IR data show that the second pyroxene absorption is likewise affected and shows higher reflectance and pyroxene band strength with respect to the immediate surrounding. Similar to FC observations, some PIDs stand out exceptionally while others do not, indicating different levels of material alteration. VIR-IR data also show the beautiful halo around the crater-fill PID of Marcia, again with analogous observations to FC data presented in Michalik et al. (2021). This observation clearly shows that some mechanism is affecting the two $Fe^{2+}$/M2 crystal field absorptions, instead of metal-metal or oxygen-metal charger transfer transitions that occur solely in the UV and VIS region.

Heating studies of meteorites and analog materials generally show a loss of reflectance and spectral features upon heating, which is why it remained difficult to explain this spectral phenomenon, especially the increase of pyroxene band strength with respect to other Marcia-related materials with similar reflectance values. Vesta-related experiments have not yet been undertaken so far. Few heating studies on HED material likewise reported on the diminishment of absorption features and lowering of overall reflectance, analogous to what has been shown in this thesis for HEDs NWA3359 and NWA5748.

The unique PID-forming process on Mars includes excavation of entrained particles/clasts/fragments through the devolatilization conduits (Boyce et al., 2012; Tornabene et al., 2012) which we thought might play an additional role on Vesta if these clasts were eucrite-dominated. This might enhance the effect of the loss of CM2 compounds and explain the unique spectral trend. This is also consistent with the observed spectral halo around the pitted surfaces, covering smooth surfaces beyond the pits. Nevertheless, it remained challenging to judge whether the expected spectral effects from such an excavation of eucrite-dominated clasts could really conform to the observed deviation from the typical Vestan spectral trend which is especially related to the higher band strength values of the PIDs. Thus, the petrologic and geochemical details of PID formation remained uncertain.

The presented laboratory measurements and experiments provide more insights into the development of the spectral characteristics seen on Vesta. First, they fortify that variations in grain size cannot account for the spectral characteristics seen for PIDs with respect to their surroundings. Second, the heating experiments involving meteoritic analog samples (HEDs + Murchison) and terrestrial analog samples (mostly hypersthene + CC analog) show that applying heat can have enormous effects on the spectral characteristics. I observed a strong reddening of the meteoritic samples in the VIS range and the formation of hematite aggregates, likely due to the presence of the Murchison CM2 chondrite, which showed a strong reddening by itself upon heating. They might not be crystalline as the typical hematite absorptions (except for the potential 0.5 µm absorption) do not appear in the measured reflectance spectra. Comparing the sample surface and sample interior after heating revealed that the interior reacted differently to the heat than the surface, showing higher reflectance and pyroxene absorption strengths. The most likely explanation for this observation is that volatiles within the sample could not escape into the vacuum while they did on the surface and thus were not able to react.

Numerous studies have shown that hematite forms within extraterrestrial materials as a result of being exposed to oxidizing conditions. On Vesta, these conditions might have been induced due to the heating of the carbonaceous chondrite material within the regolith. However, few studies exist on the development of higher reflectance and pyroxene band strength in combination with oxidation. Hematite cannot be responsible for this change. Instead, the most likely explanation is that the heating enables Fe cations to be more mobile and either move to the grains' surfaces to form hematite or preferably move to the M2 sites (as suggested by Cutler et al., 2020), in both ways increasing the absorption strength. Hematite is not (readily) identified on Vesta, yet possibly did not have the time to fully form due to the short process of devolatilization of only a few hours to days. In our experiments, hematite formed within very short timescales of only two hours, yet the constitution of the analog samples might have facilitated the oxidation process in contrast to the possibly melt-rich breccia on Vesta, where carbonaceous chondrite material is likely heterogeneously distributed on larger scales. Nevertheless, the presence of free volatiles probably enhanced the movement of Fe cations within the pyroxenes, creating the spectral patterns we see

today.

Oxidation experiments without heating have been shown to shift band positions of pyroxene absorptions to shorter wavelengths (McCanta and Dyar, 2020). In contrast, oxidation experiments with accompanied heating of pyroxene-bearing samples showed a shift of band positions to longer wavelengths (yet for calcic pyroxenes) (Cutler et al., 2020). An increase of $Fe^{2+}$ in the M2 site is generally linked to the shift of band positions to longer wavelengths. In both the heating experiments presented here and on Vesta we observe a subtle shift of band position towards shorter wavelengths, although this is not occurring universally for all PIDs/analog samples. I suggest this might arise from both mechanisms counterbalancing each other, with the oxidizing effect being slightly more dominant.

This work indicates that a subsolidus thermal oxidation occurs on the atmosphereless asteroid Vesta, which is known to be moderately reduced and depleted in volatiles. This oxidation occurs within regolith/ejecta and can be observed today because its products were transported to the surface by means of devolatilization and accompanying particle transport. As large areas of Vesta's regolith contain OH-bearing CC material, this oxidation process might be more widely distributed than seen via spacecraft analysis. Especially areas featuring ejecta that were heated to higher temperatures might have experienced oxidation underneath the immediate surface. These results then also indicate that the surface is not always representative of the interior, aside from the effects of space weathering. If this is true for the reduced asteroid Vesta, this can have implications to other asteroids and planetary surfaces, as well.

# 9 Outlook

## 9.1 Open Questions

The analysis presented in this thesis have raised questions that could not be answered yet: 1) As the PIDs on Vesta do not indicate the formation of hematite, it would be helpful to investigate this further, either via more specialized laboratory experiments accompanied by more detailed mineralogical analysis or by more detailed investigations of the VIR data on Vesta. So far, no study exists on the combined effect of heat and an oxidizing environment (not air) for Vesta regolith analogs. Publishing the VIR and laboratory results of this work (planned within the upcoming weeks) will give the scientific community more insights into the processes occurring on Vesta and implications for other objects/materials, hopefully initiating follow-up studies. The VIR-VIS data might give hints toward a possible formation of hematite either for the PIDs or possibly for the outstanding orange material (Le Corre et al., 2013), which should be revisited.

Space weathering of hematite is poorly understood (e.g., Li et al., 2020). Additional work is needed to study the process of hematite (/iron oxide) weathering on airless bodies, especially now that hematite has been identified on the moon (Li et al., 2020) and appears to be more wide-spread on the surfaces of asteroids as well (e.g., Kleer et al., 2021; Vilas et al., 1994 and this study).

Another open question regards the exact process by which the pyroxene band strength is increased in the experiments. This work contains only suggestions adopted from the literature whereas a more detailed mineralogical analysis could provide more insights into this important process. It is obvious that oxidation in combination with heat somehow affects the M2 site of the pyroxene crystal, which needs more attention as this phenomenon might be more widely distributed in the solar system than previously thought.

## 9.2 Applications to Upcoming Space Missions

Several upcoming missions will explore either unknown asteroid or planet worlds. For example, BepiColombo (e.g., Benkhoff, 2021; Benkhoff et al., 2015) is set to explore Mercury in more detail. On Mercury, the so-called *hollows* are an intriguing geomorphological feature, likewise thought to represent some sort of devolatilization, described initially in detail by Blewett et al. (2011, 2013). Figure 9.1 shows an example, taken from Blewett et al. (2011). These hollows are similarly characterized by closely-spaced clusters of pits/depressions and they exhibit higher reflectance and a bright halo. However, it remains difficult to explain these features. Barraud et al. (2020) and other studies have accordingly concluded sublimation and volatile release as the origin of these features. They also report on more specific spectral characteristics of hollows, e.g. a higher reflectance at 750 nm with respect to the VIS and VISNIR slope. Hollows are likely not solely impact deposits like on Mars, Vesta and Ceres as they also occur far from ejecta deposits (Blewett et al., 2011, 2013). Helbert et al. (2013) undertook laboratory experiments and suggested that sulfides and their possible decomposition might be responsible for the volatile release at these cites. Hollows appear bluish (e.g., Blewett et al., 2011) in contrast to common oxidized iron-compounds like hematite. However, Mercury's surface is supposed to be iron-poor due to missing characteristic absorption features, so hematite is not expected as a product. These feature still share similarities to the pitted impact deposits and I hope this work can additionally help to identify the exact mechanisms behind the formation of hollows.

The missions Lucy (e.g., Marchi et al., 2020) and Psyche (e.g., Polanskey et al., 2020) are soon starting their journey to new asteroid worlds. The mission Psyche will explore the asteroid Psyche, thought to represent a metal-rich world, possibly representing an ancient planetesimal or planetary core. Psyche is likewise located in the asteroid belt (at around 2.9 AU) and is likely subject to influx of CC material as well. Hence, the formation of iron oxide appears plausible, which was also interpreted by Kleer et al. (2021) via thermal emission data. The Lucy spacecraft has recently started its journey towards the Trojan asteroids, which are separated in two groups and located in Jupiter's orbit. Lucy is the first mission to explore the Trojan asteroids and as some C-type (and

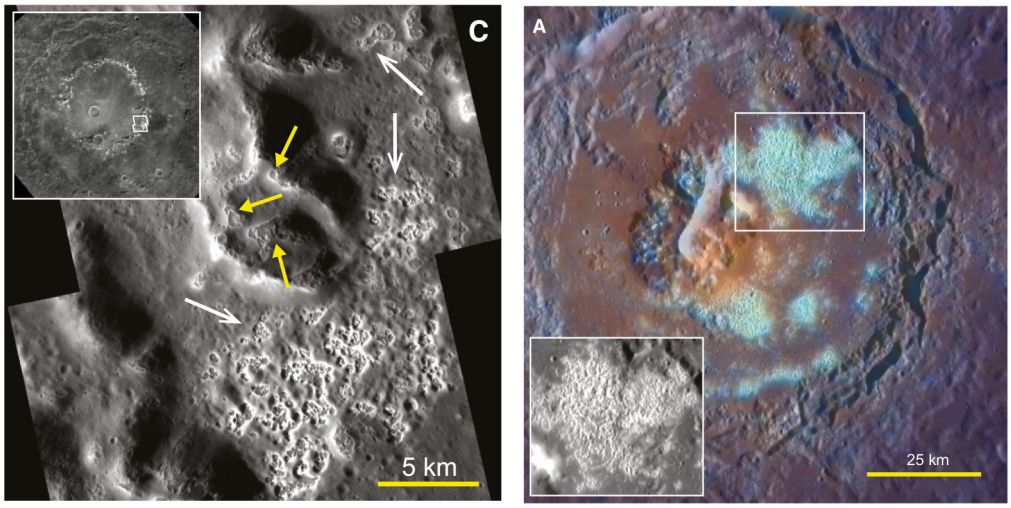


(a) (b)

Figure 9.1: a) Portion of the peak ring of the 265-km-diameter Raditladi basin (inset). White arrows indicate hollows on the basin floor; yellow arrows show those on the peak mountains. Images EN0220979987M and -9993M, 17 m/pixel, caption taken from Figure 1 in Blewett et al. (2011), b) Tyagaraja crater, 97 km in diameter. Bright areas with blue color and etched texture correspond to a high density of hollows (inset). The central pit surrounded by reddish material is probably a pyroclastic vent. From monochrome image EN0212327089M, 111 m/pixel, with enhanced color from the eight-filter set EW0217266882I (34), caption taken from Figure 2 in Blewett et al. (2011).

other opaque-rich) asteroids likewise occur in their path (see Fig. 1.1), they might also show some evidence of devolatilization and/or surficial oxidation.

Volatiles and devolatilization processes have been discovered in all parts of our solar system, so any future space mission will need to explore devolatilization and oxidation evidence, shedding more light into the evolution of the solar system objects and the development of the water-rich world Earth is today.

## 9.3 Spectral Properties of Pitted Impact Deposits on Mars and Ceres

The currently existing studies about pitted impact deposits and Mars (Boyce et al., 2012; Tornabene et al., 2012 and Ceres (Sizemore et al., 2017) do not include spectral observations. Orbital spectral data is already available: for Mars via the CRISM instrument onboard the Mars Reconaissance Orbiter (MRO) and for Ceres via the VIR instrument from the Dawn mission. Both data sets need to be investigated in order to understand whether the spectral characteristics of PIDs on Mars and Ceres share similarities with Vestan PIDs and therefore, if the mineralogical aspects presented here are analogous to those bodies or not. Both Mars and Ceres are dominated by different regolith components, possibly resulting in a different devolatilization/oxidation behavior accordingly. If iron oxides form alongside with Martian PIDs, they might also represent a potential target for the search of organic matter (Royle et al., 2021).

# 10 References


Adams, J. B. and T. B. McCord (Jan. 1973). "Vitrification darkening in the lunar highlands and identification of Descartes material at the Apollo 16 site". In: *Lunar and Planetary Science Conference Proceedings* 4, p. 163.

Akai, Junji (Mar. 1992). "T-T-T diagram of serpentine and saponite, and estimation of metamorphic heating degree of Antarctic carbonaceous chondrites". In: *Antarctic Meteorite Research* 5, p. 120.

Alemanno, G., A. Maturilli, J. Helbert, and M. D'Amore (Sept. 2020). "Laboratory studies on the 3 µm spectral features of Mg-rich phyllosilicates with temperature variations in support of the interpretation of small asteroid surface spectra". In: *Earth and Planetary Science Letters* 546, p. 116424. ISSN: 0012-821X. DOI: 10.1016/j.epsl.2020.116424.

Amelin, Yuri, Angela Kaltenbach, Tsuyoshi Iizuka, Claudine H. Stirling, Trevor R. Ireland, Michail Petaev, and Stein B. Jacobsen (Dec. 2010). "U–Pb chronology of the Solar System's oldest solids with variable 238U/235U". en. In: *Earth and Planetary Science Letters* 300.3, pp. 343–350. ISSN: 0012-821X. DOI: 10.1016/j.epsl.2010.10.015. URL: https://www.sciencedirect.com/science/article/pii/S0012821X10006497 (visited on 09/14/2021).

Ammannito, E., M. C. De Sanctis, F. Capaccioni, M. T. Capria, F. Carraro, J. P. Combe, S. Fonte, A. Frigeri, S. P. Joy, A. Longobardo, G. Magni, S. Marchi, T. B. McCord, L. A. McFadden, H. Y. McSween, E. Palomba, C. M. Pieters, C. A. Polanskey, C. A. Raymond, J. M. Sunshine, F. Tosi, F. Zambon, and C. T. Russell (Nov. 2013a). "Vestan lithologies mapped by the visual and infrared spectrometer on Dawn". English. In: *Meteorit Planet Sci* 48.11, pp. 2185–2198. ISSN: 1086-9379. DOI: 10.1111/maps.12192.

Ammannito, E., M. C. de Sanctis, E. Palomba, A. Longobardo, D. W. Mittlefehldt, H. Y. McSween, S. Marchi, M. T. Capria, F. Capaccioni, A. Frigeri, C. M. Pieters, O. Ruesch, F. Tosi, F. Zambon, F. Carraro, S. Fonte, H. Hiesinger, G. Magni, L. A. McFadden, C. A. Raymond, C. T. Russell, and J. M. Sunshine (Dec. 2013b). "Olivine in an unexpected location on Vesta's surface". In: *Nature* 504, p. 122. ISSN: 0028-0836.

Barraud, O., A. Doressoundiram, S. Besse, and J. M. Sunshine (2020). "Near-Ultraviolet to Near-Infrared Spectral Properties of Hollows on Mercury: Implications for Origin and Formation Process". en. In: *Journal of Geophysical Research: Planets* 125.12. _eprint: https://onlinelibrary.wiley.com/doi/pdf/10.1029/2020JE006497, e2020JE006497. ISSN: 2169-9100. DOI: 10.1029/2020JE006497. URL: https://onlinelibrary.wiley.com/doi/abs/10.1029/2020JE006497 (visited on 11/15/2021).

Beck, A. W., T. J. McCoy, J. M. Sunshine, C. E. Viviano, C. M. Corrigan, T. Hiroi, and R. G. Mayne (Nov. 2013). "Challenges in detecting olivine on the surface of 4 Vesta". English. In: *Meteorit Planet Sci* 48.11, pp. 2155–2165. ISSN: 1086-9379. DOI: 10.1111/maps.12160.

Benkhoff, J. (Mar. 2021). "The BepiColombo Mission to Explore Mercury — Status Update and First Results from Science Activities During Cruise". In: *52nd Lunar and Planetary Science Conference*. Lunar and Planetary Science Conference, p. 2734.

Benkhoff, J., M. Fujimoto, and J. Zender (Oct. 2015). "BepiColombo - a joint ESA/JAXA mission to explore Mercury". In: *European Planetary Science Congress*, EPSC2015–184.

Binzel, R. P. and S. Xu (Apr. 1993). "Chips off of Asteroid 4 Vesta: Evidence for the Parent Body of Basaltic Achondrite Meteorites". In: *Science* 260, p. 186. ISSN: 0036-8075. DOI: 10.1126/science.260.5105.186.

Binzel, Richard P., Michael J. Gaffey, Peter C. Thomas, Benjamin H. Zellner, Alex D. Storrs, and Eddie N. Wells (July 1997). "Geologic Mapping of Vesta from 1994 Hubble Space Telescope Images". In: *Icarus* 128.1, pp. 95–103. ISSN: 0019-1035. DOI: 10.1006/icar.1997.5734.

Bland, Philip A., Gordon Cressey, and Olwyn N. Menzies (Jan. 2004). "Modal mineralogy of carbonaceous chondrites by X-ray diffraction and Mössbauer spectroscopy". en. In: *Meteoritics & Planetary Science* 39.1, pp. 3–16. ISSN: 10869379, 19455100. DOI: 10.1111/j.1945-5100.2004.tb00046.x. URL: https://onlinelibrary.wiley.com/doi/10.1111/j.1945-5100.2004.tb00046.x (visited on 09/07/2021).

Blewett, David T., Nancy L. Chabot, Brett W. Denevi, Carolyn M. Ernst, James W. Head, Noam R. Izenberg, Scott L. Murchie, Sean C. Solomon, Larry R. Nittler, Timothy J. McCoy, Zhiyong Xiao, David M. H. Baker, Caleb I. Fassett, Sarah E. Braden, Jürgen Oberst, Frank Scholten, Frank Preusker, and Debra M. Hurwitz (Sept. 2011). "Hollows on Mercury: MESSENGER Evidence for Geologically Recent Volatile-Related Activity". In: *Science* 333, p. 1856. ISSN: 0036-8075.

Blewett, David T., William M. Vaughan, Zhiyong Xiao, Nancy L. Chabot, Brett W. Denevi, Carolyn M. Ernst, JöRn Helbert, Mario D'Amore, Alessandro Maturilli, James W. Head, and Sean C. Solomon (May 2013). "Mercury's hollows: Constraints on formation and composition from analysis of geological setting and spectral reflectance". In: *Journal of Geophysical Research (Planets)* 118, pp. 1013–1032. ISSN: 0148-0227.

Bottke, W. F., M. Brož, D. P. O'Brien, A. Campo Bagatin, A. Morbidelli, and S. Marchi (2015). "The Collisional Evolution of the Main Asteroid Belt". en. In: *Asteroids IV*. Ed. by Patrick Michel, Francesca E. DeMeo, and William F. Bottke. University of Arizona Press. ISBN: 978-0-8165-3213-1. DOI: 10.2458/azu_uapress_9780816532131-ch036. URL: http://muse.jhu.edu/chapter/1705193 (visited on 07/19/2021).

Bottke, W. F., M. C. Nolan, R. Greenberg, and R. A. Kolvoord (Feb. 1994). "Velocity Distributions among Colliding Asteroids". In: *Icarus* 107, pp. 255–268.

Boyce, Joseph M., Lionel Wilson, Peter J. Mouginis-Mark, Christopher W. Hamilton, and Livio L. Tornabene (Sept. 2012). "Origin of small pits in martian impact craters". In: *Icarus* 221, pp. 262–275.

Brouwer, Dirk (Mar. 1951). "Secular variations of the orbital elements of minor planets". In: *aj* 56, p. 9. DOI: 10.1086/106480.

Burbine, T. H., P. C. Buchanan, R. P. Binzel, S. J. Bus, T. Hiroi, J. L. Hinrichs, A. Meibom, and T. J. Mccoy (2001). "Vesta, Vestoids, and the howardite, eucrite, diogenite group: Relationships and the origin of spectral differences". en. In: *Meteoritics & Planetary Science* 36.6. _eprint: https://onlinelibrary.wiley.com/doi/pdf/10.1111/j.1945-5100.2001.tb01915.x, pp. 761–781. ISSN: 1945-5100. DOI: 10.1111/j.1945-5100.2001.tb01915.x. URL: https://onlinelibrary.wiley.com/doi/abs/10.1111/j.1945-5100.2001.tb01915.x (visited on 08/03/2021).

Burbine, Thomas, T. McCoy, Anders Meibom, Brett Gladman, and K. Keil (Jan. 2002). "Meteoritic Parent Bodies: Their Number and Identification". In: *Asteroids III*.

Burns, Roger G. (1993). *Mineralogical Applications of Crystal Field Theory*. Cambridge Topics in Mineral Physics and Chemistry. New York: Cambridge University Press. ISBN: 0-521-43077-1.

Carrozzo, F. G., A. Raponi, M. C. De Sanctis, E. Ammannito, M. Giardino, E. D'Aversa, S. Fonte, and F. Tosi (Dec. 2016). "Artifacts reduction in VIR/Dawn data". In: *Review of Scientific Instruments* 87.12. Publisher: American Institute of Physics, p. 124501. ISSN: 0034-6748. DOI: 10.1063/1.4972256. URL: https://aip.scitation.org/doi/full/10.1063/1.4972256 (visited on 10/11/2021).

Clark, Beth E., Fraser P. Fanale, and Mark S. Robinson (1993a). *Simulation of possible Regolith Alteration Effects on Carbonaceous Chondrite Meteorites*. Lunar and Planetary Science Conference XXIV, p.301.

Clark, R. N. (1999). "Spectroscopy of Rocks and Minerals, and Principles of Spectroscopy". In: *Remote Sensing for the Earth Sciences: Manual of Remote Sensing*. Ed. by Andrew N. Rencz. Vol. 3. John Wiley & Sons, Inc. ISBN: 0-471-29405-5.

Clark, R. N., Gregg A. Swayze, Andrea J. Gallagher, Trude V.V. King, and Wendy M. Calvin (1993b). *The U. S. Geological Survey, Digital Spectral Library: Version 1 (0.2 to 3.0um)*. ENGLISH. Report 93-592. Edition: -. DOI: 10.3133/ofr93592. URL: http://pubs.er.usgs.gov/publication/ofr93592.

Cloutis, E. A. and M. J. Gaffey (Apr. 1991). "Spectral-compositional variations in the constituent minerals of mafic and ultramafic assemblages and remote sensing implications". English. In: *Earth Moon and Planets* 53.1, pp. 11–53. ISSN: 0167-9295. DOI: Doi10.1007/Bf00116217.

Cloutis, E. A., P. Hudon, T. Hiroi, and M. J. Gaffey (Aug. 2012). "Spectral reflectance properties of carbonaceous chondrites 4: Aqueously altered and thermally metamorphosed meteorites". In: *Icarus* 220, p. 586. ISSN: 0019-1035. DOI: 10.1016/j.icarus.2012.05.018.

Cloutis, E. A., M. R. M. Izawa, L. Pompilio, V. Reddy, H. Hiesinger, A. Nathues, P. Mann, L. Le Corre, E. Palomba, and J. F. Bell (Apr. 2013a). "Spectral reflectance properties of HED meteorites + CM2 carbonaceous chondrites: Comparison to HED grain size and compositional variations and implications for the nature of low-albedo features on Asteroid 4 Vesta". In: *Icarus* 223, pp. 850–877. ISSN: 0019-1035.

Cloutis, E. A., P. Mann, M. R. M. Izawa, A. Nathues, V. Reddy, H. Hiesinger, L. Le Corre, and E. Palomba (July 2013b). "The 2.5-5.1 µm reflectance spectra of HED meteorites and their constituent minerals: Implications for Dawn". In: *Icarus* 225, pp. 581–601.

Cochran, Anita L., Faith Vilas, Kandy S. Jarvis, and Michael S. Kelley (Feb. 2004). "Investigating the Vesta-vestoid-HED connection". In: *Icarus* 167, pp. 360–368. ISSN: 0019-1035. DOI: 10.1016/j.icarus.2003.10.007.

Combe, Jean-Philippe, Eleonora Ammannito, Federico Tosi, Maria Cristina De Sanctis, Thomas B. McCord, Carol A. Raymond, and Christopher T. Russell (Oct. 2015a). "Reflectance properties and hydrated material distribution on Vesta: Global investigation of variations and their relationship using improved calibration of Dawn VIR mapping spectrometer". In: *Icarus* 259, pp. 21–38. ISSN: 0019-1035.

Combe, Jean-Philippe, Thomas B. McCord, Lucy A. McFadden, Simone Ieva, Federico Tosi, Andrea Longobardo, Alessandro Frigeri, Maria Cristina De Sanctis, Eleonora Ammannito, Ottaviano Ruesch, Ernesto Palomba, Marcello Fulchignoni, Carol A. Raymond, and Christopher T. Russell (Oct. 2015b). "Composition of the northern regions of Vesta analyzed by the Dawn mission". In: *Icarus* 259, p. 53. ISSN: 0019-1035. DOI: 10.1016/j.icarus.2015.04.026.

Combe, Jean-Philippe, Thomas B. McCord, Federico Tosi, Eleonora Ammannito, Filippo Giacomo Carrozzo, Maria Cristina De Sanctis, Andrea Raponi, Shane Byrne, Margaret E. Landis, Kynan H. G. Hughson, Carol A. Raymond, and Christopher T. Russell (Sept. 2016). "Detection of local $H_2O$ exposed at the surface of Ceres". In: *Science* 353, aaf3010. ISSN: 0036-8075. DOI: 10.1126/science.aaf3010.

Connelly, James N., Martin Bizzarro, Alexander N. Krot, Åke Nordlund, Daniel Wielandt, and Marina A. Ivanova (Nov. 2012). "The Absolute Chronology and Thermal Processing of Solids in the Solar Protoplanetary Disk". In: *Science* 338.6107. Publisher: American Association for the Advancement of Science, pp. 651–655. DOI: 10.1126/science.1226919. URL: https://www.science.org/lookup/doi/10.1126/science.1226919 (visited on 09/14/2021).

Cutler, K. S., J. Filiberto, A. H. Treiman, and D. Trang (June 2020). "Experimental Investigation of Oxidation of Pyroxene and Basalt: Implications for Spectroscopic Analyses of the Surface of Venus and the Ages of Lava Flows". en. In: *Planet. Sci. J* 1.1, p. 21. ISSN: 2632-3338. DOI: 10.3847/PSJ/ab8faf. URL: https://iopscience.iop.org/article/10.3847/PSJ/ab8faf (visited on 11/09/2021).

Davis, A.M. and K.D. McKeegan (2014). "Short-Lived Radionuclides and Early Solar System Chronology". en. In: *Treatise on Geochemistry*. Elsevier, pp. 361–395. ISBN: 978-0-08-098300-4. DOI: 10.1016/B978-0-08-095975-7.00113-3. URL: https://linkinghub.elsevier.com/retrieve/pii/B9780080959757001133 (visited on 07/30/2021).

De Sanctis, M. C., E. Ammannito, M. T. Capria, F. Tosi, F. Capaccioni, F. Zambon, F. Carraro, S. Fonte, A. Frigeri, R. Jaumann, G. Magni, S. Marchi, T. B. McCord, L. A. McFadden, H. Y. McSween, D. W. Mittlefehldt, A. Nathues, E. Palomba, C. M. Pieters, C. A. Raymond, C. T. Russell, M. J. Toplis, and D. Turrini (May 2012a). "Spectroscopic Characterization of Mineralogy and Its Diversity Across Vesta". eng. In: *Science* 336.6082, pp. 697–700. ISSN: 0036-8075. DOI: 10.1126/science.1219270.

De Sanctis, M. C., E. Ammannito, A. Raponi, S. Marchi, T. B. McCord, H. Y. McSween, F. Capaccioni, M. T. Capria, F. G. Carrozzo, M. Ciarniello, A. Longobardo, F. Tosi, S. Fonte, M. Formisano, A. Frigeri, M. Giardino, G. Magni, E. Palomba, D. Turrini, F. Zambon, J.-P. Combe, W. Feldman, R. Jaumann, L. A. McFadden, C. M. Pieters, T. Prettyman, M. Toplis, C. A. Raymond, and C. T. Russell (Dec. 2015a). "Ammoniated phyllosilicates with a likely outer Solar System origin on (1) Ceres". In: *Nature* 528, p. 241. ISSN: 0028-0836. DOI: 10.1038/nature16172.

De Sanctis, M. C., Eleonora Ammannito, M. Teresa Capria, Fabrizio Capaccioni, Jean-Philippe Combe, Alessandro Frigeri, Andrea Longobardo, Gianfranco Magni, Simone Marchi, Tom B. McCord, Ernesto Palomba, Federico Tosi, Francesca Zambon, Francesco Carraro, Sergio Fonte,

Y. J. Li, Lucy A. McFadden, David W. Mittlefehldt, Carle M. Pieters, Ralf Jaumann, Katrin Stephan, Carol A. Raymond, and Christopher T. Russell (Nov. 2013). "Vesta's mineralogical composition as revealed by the visible and infrared spectrometer on Dawn". In: *Meteoritics and Planetary Science* 48, pp. 2166–2184. ISSN: 1086-9379.

De Sanctis, M. C., J. P. Combe, A. Ammannito, A. Frigeri, A. Longobardo, E. Palomba, F. Tosi, F. Zambon, K. Stephan, C. A. Raymond, and C. T. Russell (2015b). "Eucritic crust remnants and the effect of in-falling hydrous carbonaceous chondrites characterizing the composition of Vesta's Marcia region". In: *Icarus* 259, pp. 91–115. ISSN: 0019-1035. DOI: 10.1016/j.icarus.2015.05.014.

De Sanctis, M. C., J.-Ph Combe, E. Ammannito, E. Palomba, A. Longobardo, T. B. McCord, S. Marchi, F. Capaccioni, M. T. Capria, D. W. Mittlefehldt, C. M. Pieters, J. Sunshine, F. Tosi, F. Zambon, F. Carraro, S. Fonte, A. Frigeri, G. Magni, C. A. Raymond, C. T. Russell, and D. Turrini (Oct. 2012b). "Detection of Widespread Hydrated Materials on Vesta by the VIR Imaging Spectrometer on board the Dawn Mission". In: *The Astrophysical Journal Letters* 758. ISSN: 0004-637X.

De Sanctis, M. C., A. Coradini, E. Ammannito, G. Filacchione, M. T. Capria, S. Fonte, G. Magni, A. Barbis, A. Bini, M. Dami, I. Ficai-Veltroni, and G. Preti (2011). "The VIR Spectrometer". In: *Space Science Reviews* 163.1, pp. 329–369. ISSN: 1572-9672. DOI: 10.1007/s11214-010-9668-5.

De Sanctis, M. C., A. Frigeri, E. Ammannito, F. Tosi, S. Marchi, F. Zambon, C. A. Raymond, and C. T. Russell (Mar. 2015c). "Mineralogy of Marcia, the youngest large crater of Vesta: Character and distribution of pyroxenes and hydrated material". In: *Icarus* 248, pp. 392–406. ISSN: 0019-1035.

DeMeo, F. E., C. M. O'D Alexander, K. J. Walsh, C. R. Chapman, R. P. Binzel, Francesca E. DeMeo, and William F. Bottke (2015). "The Compositional Structure of the Asteroid Belt". In: *Asteroids IV*. Ed. by Patrick Michel, pp. 13–41.

DeMeo, F. E. and B. Carry (Jan. 2014). "Solar System evolution from compositional mapping of the asteroid belt". eng. In: *Nature* 505.7485, pp. 629–634. ISSN: 0028-0836. DOI: 10.1038/nature12908.

Denevi, B. W., A. W. Beck, E. I. Coman, B. J. Thomson, E. Ammannito, D. T. Blewett, J. M. Sunshine, M. C. de Sanctis, J.-Y. Li, S. Marchi, D. W. Mittlefehldt, N. E. Petro, C. A. Raymond, and C. T. Russell (Dec. 2016). "Global variations in regolith properties on asteroid Vesta from Dawn's low-altitude mapping orbit". In: *Meteoritics & Planetary Science* 51, p. 2366. ISSN: 1086-9379. DOI: 10.1111/maps.12729.

Denevi, B. W., D. T. Blewett, D. L. Buczkowski, F. Capaccioni, M. T. Capria, M. C. De Sanctis, W. B. Garry, R. W. Gaskell, L. Le Corre, J.-Y. Li, S. Marchi, T. J. McCoy, A. Nathues, D. P. O'Brien, N. E. Petro, C. M. Pieters, F. Preusker, C. A. Raymond, V. Reddy, C. T. Russell, P. Schenk, J. E. C. Scully, J. M. Sunshine, F. Tosi, D. A. Williams, and D. Wyrick (Oct. 2012). "Pitted Terrain on Vesta and Implications for the Presence of Volatiles". eng. In: *Science* 338.6104, p. 246. ISSN: 0036-8075. DOI: 10.1126/science.1225374.

Dixit, Ambesh, Beena Bhatia, and R. P. Tripathi (Sept. 2021). "Evolution of hematite and/or magnetite iron phases with thermal heating in ordinary chondrites: A generic characteristic". en. In: *J Earth Syst Sci* 130.4, p. 191. ISSN: 0973-774X. DOI: 10.1007/s12040-021-01699-8. URL: https://doi.org/10.1007/s12040-021-01699-8 (visited on 11/08/2021).

Dyar, M. Darby, Jörn Helbert, Reid F. Cooper, Elizabeth C. Sklute, Alessandro Maturilli, Nils T. Mueller, David Kappel, and Suzanne E. Smrekar (Apr. 2021). "Surface weathering on Venus: Constraints from kinetic, spectroscopic, and geochemical data". en. In: *Icarus* 358, p. 114139. ISSN: 0019-1035. DOI: 10.1016/j.icarus.2020.114139. URL: https://www.sciencedirect.com/science/article/pii/S0019103520304802 (visited on 11/15/2021).

Dyar, M. Darby, Rachel L. Klima, Alexandra Fleagle, and Samantha E. Peel (July 2013). "Fundamental Mössbauer parameters of synthetic Ca-Mg-Fe pyroxenes". en. In: *American Mineralogist* 98.7. Publisher: De Gruyter, pp. 1172–1186. ISSN: 1945-3027. DOI: 10.2138/am.2013.4333. URL: https://www.degruyter.com/document/doi/10.2138/am.2013.4333/html (visited on 10/20/2021).

Engelhardt, W. V. (Dec. 1972). "Shock produced rock glasses from the Ries crater". In: *Contributions to Mineralogy and Petrology* 36, p. 265. ISSN: 0010-7999. DOI: 10.1007/bf00444336.

Engelhardt, W. V., J. Arndt, B. Fecker, and H. G. Pankau (1995). "Suevite breccia from the Ries crater, Germany: Origin, cooling history and devitrification of impact glasses". en. In: *Meteoritics* 30.3. _eprint: https://onlinelibrary.wiley.com/doi/pdf/10.1111/j.1945-5100.1995.tb01126.x, pp. 279–293. ISSN: 1945-5100. DOI: https://doi.org/10.1111/j.1945-5100.1995.tb01126.x. URL: https://onlinelibrary.wiley.com/doi/abs/10.1111/j.1945-5100.1995.tb01126.x (visited on 06/04/2021).

Ermakov, A. I., R. R. Fu, J. C. Castillo-Rogez, C. A. Raymond, R. S. Park, F. Preusker, C. T. Russell, D. E. Smith, and M. T. Zuber (Nov. 2017). "Constraints on Ceres' Internal Structure and Evolution From Its Shape and Gravity Measured by the Dawn Spacecraft". In: *JGR Planets* 122, p. 2267. ISSN: 0148-0227. DOI: 10.1002/2017je005302.

Ermakov, A. I., M. T. Zuber, D. E. Smith, C. A. Raymond, G. Balmino, R. R. Fu, and B. A. Ivanov (Sept. 2014). "Constraints on Vesta's interior structure using gravity and shape models from the Dawn mission". In: *Icarus* 240, pp. 146–160. ISSN: 0019-1035. DOI: 10.1016/j.icarus.2014.05.015.

Fendrich, Kim V. and Denton S. Ebel (2021). "Comparison of the Murchison CM2 and Allende CV3 chondrites". en. In: *Meteoritics & Planetary Science* 56.1. _eprint: https://onlinelibrary.wiley.com/doi/pdf/10.1111/maps.13623, pp. 77–95. ISSN: 1945-5100. DOI: 10.1111/maps.13623. URL: https://onlinelibrary.wiley.com/doi/abs/10.1111/maps.13623 (visited on 09/08/2021).

Fu, Roger R., Anton I. Ermakov, Simone Marchi, Julie C. Castillo-Rogez, Carol A. Raymond, Bradford H. Hager, Maria T. Zuber, Scott D. King, Michael T. Bland, Maria Cristina De Sanctis, Frank Preusker, Ryan S. Park, and Christopher T. Russell (Oct. 2017). "The interior structure of Ceres as revealed by surface topography". In: *Earth and Planetary Science Letters* 476, p. 153. ISSN: 0012-821X. DOI: 10.1016/j.epsl.2017.07.053.

Gaffey, M. J. (Feb. 1976). "Spectral reflectance characteristics of the meteorite classes". In: *Journal of Geophysical Research* 81, p. 905. ISSN: 0148-0227.

Gaffey, M. J. and T. B. McCord (Mar. 1978). "Asteroid Surface Materials: Minerological Characterizations from Reflectance Spectra". In: *ßr* 21.5, pp. 555–628. DOI: 10.1007/BF00240908.

Gaidos, Eric and Franck Selsis (Feb. 2006). "From Protoplanets to Protolife: The Emergence and Maintenance of Life". en. In: *arXiv:astro-ph/0602008*. arXiv: astro-ph/0602008. URL: http://arxiv.org/abs/astro-ph/0602008 (visited on 11/16/2021).

Galiano, A., F. Dirri, E. Palomba, A. Longobardo, B. Schmitt, and P. Beck (June 2020). "Spectral investigation of Ceres analogue mixtures: In-depth analysis of crater central peak material (ccp) on Ceres". In: *Icarus* 343, p. 113692. ISSN: 0019-1035.

Garenne, A., P. Beck, G. Montes-Hernandez, R. Chiriac, F. Toche, E. Quirico, L. Bonal, and B. Schmitt (July 2014). "The abundance and stability of "water" in type 1 and 2 carbonaceous chondrites (CI, CM and CR)". In: *Geochimica et Cosmochimica Acta* 137, p. 93. ISSN: 0016-7037.

Greenwood, Richard C., Ian A. Franchi, Albert Jambon, and Paul C. Buchanan (June 2005). "Widespread magma oceans on asteroidal bodies in the early Solar System". en. In: *Nature* 435.7044. Bandiera_abtest: a Cg_type: Nature Research Journals Number: 7044 Primary_atype: Research Publisher: Nature Publishing Group, pp. 916–918. ISSN: 1476-4687. DOI: 10.1038/nature03612. URL: https://www.nature.com/articles/nature03612 (visited on 08/27/2021).

Gupta, Ravi P. (2003). *Remote Sensing Geology*. Heidelberg, Germany: Springer-Verlag Berlin. ISBN: 3-540-43185-3.

Hapke, B. (Apr. 1981). "Bidirectional reflectance spectroscopy. I - Theory". In: *Journal of Geophysical Research* 86, pp. 3039–3054. ISSN: 0148-0227. DOI: 10.1029/JB086iB04p03039.

Hapke, Bruce (2012). *Theory of Reflectance and Emittance Spectroscopy*. 2nd ed. Cambridge: Cambridge University Press. ISBN: 978-0-521-88349-8. DOI: 10.1017/CBO9781139025683. URL: https://www.cambridge.org/core/books/theory-of-reflectance-and-emittance-spectroscopy/C266E1164D5E14DA18141F03D0E0EAB0 (visited on 10/20/2021).

Harloff, J. and G. Arnold (Feb. 2001). "Near-infrared reflectance spectroscopy of bulk analog materials for planetary crust". In: *Planetary and Space Science* 49, p. 191. ISSN: 0032-0633. DOI: 10.1016/s0032-0633(00)00132-x.

Helbert, J. and A. Maturilli (Sept. 2008). *The heat is on - in the Planetary Emissivity Laboratory (PEL) at DLR Berlin*. European Planetary Science Congress 2008, Abstract EPSC2008-A-00357.

Helbert, Jörn, Alessandro Maturilli, and Mario D'Amore (May 2013). "Visible and near-infrared reflectance spectra of thermally processed synthetic sulfides as a potential analog for the hollow forming materials on Mercury". en. In: *Earth and Planetary Science Letters* 369-370, pp. 233–238. ISSN: 0012-821X. DOI: 10.1016/j.epsl.2013.03.045. URL: https://www.sciencedirect.com/science/article/pii/S0012821X13001660 (visited on 11/15/2021).

Hinrichs, John L. and Paul G. Lucey (Jan. 2002). "Temperature-Dependent Near-Infrared Spectral Properties of Minerals, Meteorites, and Lunar Soil". en. In: *Icarus* 155.1, pp. 169–180. ISSN: 0019-1035. DOI: 10.1006/icar.2001.6754. URL: https://www.sciencedirect.com/science/article/pii/S0019103501967545 (visited on 11/04/2021).

Hirayama, K. (Jan. 1922). "Families of Asteroids". In: *Japanese Journal of Astronomy and Geophysics* 1, p. 55.

Hiroi, Takahiro, Carlé M. Pieters, Michael E. Zolensky, and Michael E. Lipschutz (Aug. 1993). "Evidence of Thermal Metamorphism on the C, G, B, and F Asteroids". In: *Science* 261.5124. Publisher: American Association for the Advancement of Science, pp. 1016–1018. DOI: 10.1126/science.261.5124.1016. URL: https://www.science.org/doi/10.1126/science.261.5124.1016 (visited on 11/04/2021).

— (Mar. 1994). "Possible thermal metamorphism on the C, G, B, and F asteroids detected from their reflectance spectra in comparison with carbonaceous chondrites". In: *Antarctic Meteorite Research* 7, p. 230.

Hiroi, Takahiro, Michael E. Zolensky, Carlé M. Pieters, and Michael E. Lipschutz (May 1996). "Thermal metamorphism of the C, G, B, and F asteroids seen from the 0.7 micron, 3 micron and UV absorption strengths in comparison with carbonaceous chondrites". In: *Meteoritics & Planetary Science* 31, p. 321. ISSN: 1086-9379. DOI: 10.1111/j.1945-5100.1996.tb02068.x.

Hiroi, Takahiro and Michael E. %J Antarctic Meteorite Research Zolensky (Mar. 1999). "UV-Vis-NIR absorption features of heated phyllosilicates as remote-sensing clues of thermal histories of primitive asteroids". In: *Antarctic Meteorite Research* 12, p. 108. ISSN: 1343-4284.

Jaumann, R., A. Nass, K. Otto, K. Krohn, K. Stephan, T. B. McCord, D. A. Williams, C. A. Raymond, D. T. Blewett, H. Hiesinger, R. A. Yingst, M. C. De Sanctis, E. Palomba, T. Roatsch, K.-D. Matz, F. Preusker, F. Scholten, and C. T. Russell (Sept. 2014). "The geological nature of dark material on Vesta and implications for the subsurface structure". English. In: *Icarus* 240, pp. 3–19. ISSN: 0019-1035. DOI: 10.1016/j.icarus.2014.04.035.

Jaumann, R., D. A. Williams, D. L. Buczkowski, R. A. Yingst, F. Preusker, H. Hiesinger, N. Schmedemann, T. Kneissl, J. B. Vincent, D. T. Blewett, B. J. Buratti, U. Carsenty, B. W. Denevi, M. C. De Sanctis, W. B. Garry, H. U. Keller, E. Kersten, K. Krohn, J.-Y. Li, S. Marchi, K. D. Matz, T. B. McCord, H. Y. McSween, S. C. Mest, D. W. Mittlefehldt, S. Mottola, A. Nathues, G. Neukum, D. P. O'Brien, C. M. Pieters, T. H. Prettyman, C. A. Raymond, T. Roatsch, C. T. Russell, P. Schenk, B. E. Schmidt, F. Scholten, K. Stephan, M. V. Sykes, P. Tricarico, R. Wagner, M. T. Zuber, and H. Sierks (May 2012). "Vesta's Shape and Morphology". eng. In: *Science* 336.6082, pp. 687–690. ISSN: 0036-8075. DOI: 10.1126/science.1219122.

Johansen, A., E. Jacquet, J. N. Cuzzi, A. Morbidelli, and M. Gounelle (2015). "New Paradigms for Asteroid Formation". en. In: *Asteroids IV*. Ed. by Patrick Michel, Francesca E. DeMeo, and William F. Bottke. University of Arizona Press. ISBN: 978-0-8165-3213-1. DOI: 10.2458/azu_uapress_9780816532131-ch025. URL: http://muse.jhu.edu/chapter/1705181 (visited on 07/19/2021).

Keihm, S., F. Tosi, M. T. Capria, M. C. De Sanctis, A. Longobardo, E. Palomba, C. T. Russell, and C. A. Raymond (Dec. 2015). "Separation of thermal inertia and roughness effects from Dawn/VIR measurements of Vesta surface temperatures in the vicinity of Marcia Crater". In: *Icarus* 262, pp. 30–43. ISSN: 0019-1035.

Keil, K. (2002). "Geological History of Asteroid 4 Vesta: The "Smallest Terrestrial Planet"". In: *Asteroids III*, p. 573.

King, Penelope, M.S. Ramsey, Paul McMillan, and Gregg Swayze (Jan. 2004). "Laboratory Fourier Transform infrared spectroscopy methods for geologic samples". In: vol. 33, pp. 57–91.

Kirkwood, Daniel (1867). *Meteoric astronomy: a treatise on shooting-stars, fireballs, and aerolites*. Ed. by Daniel Kirkwood. Philadelphia: J. B. Lippincott & Co.

Kleer, Katherine de, Saverio Cambioni, and Michael Shepard (Aug. 2021). "The Surface of (16) Psyche from Thermal Emission and Polarization Mapping". en. In: *Planet. Sci. J.* 2.4. Publisher: IOP Publishing, p. 149. ISSN: 2632-3338. DOI: 10.3847/PSJ/ac01ec. URL: https://iopscience.iop.org/article/10.3847/PSJ/ac01ec/meta (visited on 11/15/2021).

Konopliv, A. S., S. W. Asmar, B. G. Bills, N. Mastrodemos, R. S. Park, C. A. Raymond, D. E. Smith, and M. T. Zuber (Dec. 2011). "The Dawn Gravity Investigation at Vesta and Ceres". In: *Space Science Reviews* 163, pp. 461–486. ISSN: 0038-6308. DOI: 10.1007/s11214-011-9794-8.

Krohn, K., R. Jaumann, D. Elbeshausen, T. Kneissl, N. Schmedemann, R. Wagner, J. Voigt, K. Otto, K. D. Matz, F. Preusker, T. Roatsch, K. Stephan, C. A. Raymond, and C. T. Russell (Nov. 2014a). "Asymmetric craters on Vesta: Impact on sloping surfaces". English. In: *Planetary and Space Science* 103, pp. 36–56. ISSN: 0032-0633. DOI: 10.1016/j.pss.2014.04.011.

Krohn, K., R. Jaumann, K. Otto, T. Hoogenboom, R. Wagner, D. L. Buczkowski, B. Garry, D. A. Williams, R. A. Yingst, J. Scully, M. C. De Sanctis, T. Kneissl, N. Schmedemann, E. Kersten, K. Stephan, K. D. Matz, C. M. Pieters, F. Preusker, T. Roatsch, P. Schenk, C. T. Russell, and C. A. Raymond (2014b). "Mass movement on Vesta at steep scarps and crater rims". In: *Icarus* 244, pp. 120–132. ISSN: 0019-1035. DOI: 10.1016/j.icarus.2014.03.013.

Krot, A. N., Michail I. Petaev, Sara S. Russell, Shoichi Itoh, Timothy J. Fagan, Hisayoshi Yurimoto, Lysa Chizmadia, Michael K. Weisberg, Matsumi Komatsu, Alexander A. Ulyanov, and Klaus Keil (Sept. 2004). "Amoeboid olivine aggregates and related objects in carbonaceous chondrites: records of nebular and asteroid processes". en. In: *Geochemistry* 64.3, pp. 185–239. ISSN: 0009-2819. DOI: 10.1016/j.chemer.2004.05.001. URL: https://www.sciencedirect.com/science/article/pii/S0009281904000212 (visited on 07/21/2021).

Le Corre, Lucille, Vishnu Reddy, Andreas Nathues, and Edward A. Cloutis (Dec. 2011). "How to characterize terrains on 4 Vesta using Dawn Framing Camera color bands?" In: *Icarus* 216, p. 376. ISSN: 0019-1035. DOI: 10.1016/j.icarus.2011.09.014.

Le Corre, Lucille, Vishnu Reddy, Nico Schmedemann, Kris J. Becker, David P. O'Brien, Naoyuki Yamashita, Patrick N. Peplowski, Thomas H. Prettyman, Jian-Yang Li, Edward A. Cloutis, Brett W. Denevi, Thomas Kneissl, Eric Palmer, Robert W. Gaskell, Andreas Nathues, Michael J. Gaffey, David W. Mittlefehldt, William B. Garry, Holger Sierks, Christopher T. Russell, Carol A. Raymond, Maria C. De Sanctis, and Eleonora Ammannito (2013). "Olivine or impact melt: Nature of the "Orange" material on Vesta from Dawn". In: *Icarus* 226.2, pp. 1568–1594. ISSN: 0019-1035. DOI: 10.1016/j.icarus.2013.08.013.

Lebofsky, Larry A. (Jan. 1978). "Asteroid 1 Ceres: evidence for water of hydration". In: *Monthly Notices of the Royal Astronomical Society* 182.1, 17P–21P. ISSN: 0035-8711. DOI: 10.1093/mnras/182.1.17P. URL: https://doi.org/10.1093/mnras/182.1.17P (visited on 06/15/2021).

Li, J. -Y., J. -P. Combe, A. Longobardo, F. Capaccioni, M. C. De Sanctis, E. Ammannito, M. T. Capria, E. Palomba, F. Tosi, F. Zambon, S. E. Schröder, B. W. Denevi, V. Reddy, C. T. Russell, and C. A. Raymond (2013). "The Photometric Properties of Vesta in Visible and Near-Infrared from Dawn VIR Instrument". In: *Lunar and Planetary Science Conference, #2343*.

Li, Shuai, Paul G. Lucey, Abigail A. Fraeman, Andrew R. Poppe, Vivian Z. Sun, Dana M. Hurley, and Peter H. Schultz (Sept. 2020). "Widespread hematite at high latitudes of the Moon". en. In: *Sci. Adv.* 6.36, eaba1940. ISSN: 2375-2548. DOI: 10.1126/sciadv.aba1940. URL: https://www.science.org/doi/10.1126/sciadv.aba1940 (visited on 11/05/2021).

Macke, Robert J., Daniel T. Britt, and Guy J. Consolmagno (Feb. 2011a). "Density, porosity, and magnetic susceptibility of achondritic meteorites". In: *Meteoritics & Planetary Science* 46, p. 311. ISSN: 1086-9379. DOI: 10.1111/j.1945-5100.2010.01155.x.

Macke, Robert J., Guy J. Consolmagno, and Daniel T. Britt (Dec. 2011b). "Density, porosity, and magnetic susceptibility of carbonaceous chondrites". In: *Meteoritics & Planetary Science* 46, p. 1842. ISSN: 1086-9379. DOI: 10.1111/j.1945-5100.2011.01298.x.

Marchi, S., W. F. Bottke, B. A. Cohen, K. Wünnemann, D. A. Kring, H. Y. McSween, M. C. de Sanctis, D. P. O'Brien, P. Schenk, C. A. Raymond, and C. T. Russell (Apr. 2013). "High-velocity collisions from the lunar cataclysm recorded in asteroidal meteorites". In: *Nature Geoscience* 6, pp. 303–307.

Marchi, S., C. R. Chapman, O. S. Barnouin, J. E. Richardson, and J.-B. Vincent (2015). "Cratering on Asteroids". en. In: *Asteroids IV*. Ed. by Patrick Michel, Francesca E. DeMeo, and William F. Bottke. University of Arizona Press. ISBN: 978-0-8165-3213-1. DOI: 10.2458/azu_uapress_9780816532131-ch037. URL: http://muse.jhu.edu/chapter/1705194 (visited on 07/19/2021).

Marchi, S., H. Y. McSween, D. P. O'Brien, P. Schenk, M. C. De Sanctis, R. Gaskell, R. Jaumann, S. Mottola, F. Preusker, C. A. Raymond, T. Roatsch, and C. T. Russell (May 2012). "The Violent Collisional History of Asteroid 4 Vesta". eng. In: *Science* 336.6082, pp. 690–694. ISSN: 0036-8075. DOI: 10.1126/science.1218757.

Marchi, Simone, Hal Levison, Cathy Olkin, and Keith Noll (Aug. 2020). "The NASA Lucy Mission: Surveying the Diversity of Trojan Asteroids". en. In: Conference Name: EPSC2020. Copernicus Meetings. DOI: 10.5194/epsc2020-163. URL: https://meetingorganizer.copernicus.org/EPSC2020/EPSC2020-163.html (visited on 11/15/2021).

Marov, Mikhail (May 2018). "The Formation and Evolution of the Solar System". en. In: *Oxford Research Encyclopedia of Planetary Science*. Oxford University Press. ISBN: 978-0-19-064792-6. DOI: 10.1093/acrefore/9780190647926.013.2. URL: https://oxfordre.com/planetaryscience/view/10.1093/acrefore/9780190647926.001.0001/acrefore-9780190647926-e-2 (visited on 07/29/2021).

Masiero, J. R., F. E. DeMeo, T. Kasuga, and A. H. Parker (2015). "Asteroid Family Physical Properties". en. In: *Asteroids IV*. Ed. by Patrick Michel, Francesca E. DeMeo, and William F. Bottke. University of Arizona Press. ISBN: 978-0-8165-3213-1. DOI: 10.2458/azu_uapress_9780816532131-ch017. URL: http://muse.jhu.edu/chapter/1705171 (visited on 08/03/2021).

Maturilli, A. and J. Helbert (Mar. 2016). *The Planetary Spectroscopy Laboratory (PSL): Spectral Measurements of Planetary Analogues from UV to FIR*. 47th Lunar and Planetary Science Conference, Abstract 1986.

Maturilli, A., J. Helbert, and G. Arnold (2019). "The newly improved set-up at the Planetary Spectroscopy Laboratory (PSL)". In: *Infrared Remote Sensing and Instrumentation XXVII*. Vol. 11128. International Society for Optics and Photonics, 111280T. DOI: 10.1117/12.2529266. URL: https://www.spiedigitallibrary.org/conference-proceedings-of-spie/11128/111280T/The-newly-improved-set-up-at-the-Planetary-Spectroscopy-Laboratory/10.1117/12.2529266.short (visited on 09/07/2021).

Maturilli, A., J. Helbert, I. Varatharajan, and M. D'Amore (Sept. 2017). *The Planetary Spectroscopy Laboratory (PSL)*. European Planetary Science Congress 2017, Abstract EPSC2017-568.

McCanta, Molly C. and M. Darby Dyar (Dec. 2020). "Effects of oxidation on pyroxene visible-near infrared and mid-infrared spectra". en. In: *Icarus* 352, p. 113978. ISSN: 0019-1035. DOI: 10.1016/j.icarus.2020.113978. URL: https://www.sciencedirect.com/science/article/pii/S0019103520303444 (visited on 11/10/2021).

McCord, T. B., John B. Adams, and Torrence V. Johnson (June 1970). "Asteroid Vesta: Spectral Reflectivity and Compositional Implications". In: *Science* 168, pp. 1445–1447. ISSN: 0036-8075.

McCord, T. B., J.-Y. Li, J.-P. Combe, H. Y. McSween, R. Jaumann, V. Reddy, F. Tosi, D. A. Williams, D. T. Blewett, D. Turrini, E. Palomba, C. M. Pieters, M. C. de Sanctis, E. Ammannito, M. T. Capria, L. Le Corre, A. Longobardo, A. Nathues, D. W. Mittlefehldt, S. E. Schröder, H. Hiesinger, A. W. Beck, F. Capaccioni, U. Carsenty, H. U. Keller, B. W. Denevi, J. M. Sunshine, C. A. Raymond, and C. T. Russell (Nov. 2012). "Dark material on Vesta from the infall of carbonaceous volatile-rich material". eng. In: *Nature* 491.7422, pp. 83–86. ISSN: 0028-0836. DOI: 10.1038/nature11561.

McGetchin, T. R., M. Settle, and J. W. Head (Oct. 1973). "Radial thickness variation in impact crater ejecta: implications for lunar basin deposits". en. In: *Earth and Planetary Science Letters* 20.2, pp. 226–236. ISSN: 0012-821X. DOI: 10.1016/0012-821X(73)90162-3. URL: https://www.sciencedirect.com/science/article/pii/0012821X73901623 (visited on 06/09/2021).

McSween, Harry Y., Eleonora Ammannito, Vishnu Reddy, Thomas H. Prettyman, Andrew W. Beck, M. Cristina de Sanctis, Andreas Nathues, Lucille Le Corre, David P. O'Brien, Naoyuki Yamashita, Timothy J. McCoy, David W. Mittlefehldt, Michael J. Toplis, Paul Schenk, Ernesto Palomba, Diego Turrini, Federico Tosi, Francesca Zambon, Andrea Longobardo, Fabrizio Ca-

paccioni, Carol A. Raymond, and Christopher T. Russell (Feb. 2013a). "Composition of the Rheasilvia basin, a window into Vesta's interior". English. In: *JGR Planets* 118.2, pp. 335–346. ISSN: 0148-0227. DOI: 10.1002/jgre.20057.

McSween, Harry Y., Richard P. Binzel, M. Cristina de Sanctis, Eleonora Ammannito, Thomas H. Prettyman, Andrew W. Beck, Vishnu Reddy, Lucille Corre, Michael J. Gaffey, Thomas B. McCord, Carol A. Raymond, and Christopher T. Russell (Nov. 2013b). "Dawn; the Vesta-HED connection; and the geologic context for eucrites, diogenites, and howardites". In: *Meteoritics and Planetary Science* 48, pp. 2090–2104. ISSN: 1086-9379.

McSween, Harry Y., David W. Mittlefehldt, Andrew W. Beck, Rhiannon G. Mayne, and Timothy J. McCoy (Dec. 2011). "HED Meteorites and Their Relationship to the Geology of Vesta and the Dawn Mission". In: *Space Science Reviews* 163, pp. 141–174. ISSN: 0038-6308.

Meibom, Anders and Beth E. Clark (1999). "Evidence for the insignificance of ordinary chondritic material in the asteroid belt". en. In: *Meteoritics & Planetary Science* 34.1. _eprint: https://onlinelibrary.wiley.com/doi/pdf/10.1111/j.1945-5100.1999.tb01728.x, pp. 7–24. ISSN: 1945-5100. DOI: 10.1111/j.1945-5100.1999.tb01728.x. URL: https://onlinelibrary.wiley.com/doi/abs/10.1111/j.1945-5100.1999.tb01728.x (visited on 08/24/2021).

Melosh, H. J. (1989). *Impact cratering: A geologic process*. Ed. by H. J. Melosh. Oxford Monographs on Geology and Geophysics, No. 11. New York: Oxford University Press.

Michalik, T., K. -D. Matz, S. E. Schröder, R. Jaumann, K. Stephan, K. Krohn, F. Preusker, C. A. Raymond, C. T. Russell, and K. A. Otto (Nov. 2021). "The unique spectral and geomorphological characteristics of pitted impact deposits associated with Marcia crater on Vesta". en. In: *Icarus* 369, p. 114633. ISSN: 0019-1035. DOI: 10.1016/j.icarus.2021.114633. URL: https://www.sciencedirect.com/science/article/pii/S0019103521002943 (visited on 08/18/2021).

Minitti, Michelle E., John F. Mustard, and Malcolm J. Rutherford (2002). "Effects of glass content and oxidation on the spectra of SNC-like basalts: Applications to Mars remote sensing". en. In: *Journal of Geophysical Research: Planets* 107.E5. _eprint: https://onlinelibrary.wiley.com/doi/pdf/10.1029/2001JE001518, pp. 6–1–6–14. ISSN: 2156-2202. DOI: 10.1029/2001JE001518. URL: https://onlinelibrary.wiley.com/doi/abs/10.1029/2001JE001518 (visited on 11/13/2021).

Mittlefehldt, D. W. (June 2015). "Asteroid (4) Vesta: I. The howardite-eucrite-diogenite (HED) clan of meteorites". English. In: *Chemie der Erde / Geochemistry* 75.2, pp. 155–183. ISSN: 0009-2819. DOI: 10.1016/j.chemer.2014.08.002.

Mittlefehldt, D. W., R. C. Greenwood, Z. X. Peng, D. K. Ross, E. L. Berger, and T. J. Barrett (Mar. 2016). *Petrologic and Oxygen-Isotopic Investigations of Eucritic and Anomalous Mafic Achondrites*. 47th Lunar and Planetary Science Conference, Abstract 1240.

Miyamoto, H., T. Niihara, K. Wada, K. Ogawa, N. Baresi, P. Abell, E. Asphaug, D. Britt, G. Dodbiba, T. Fujita, K. Fukui, M. Grott, K. Hashiba, R. Hemmi, P. Hong, T. Imada, H. Kikuchi, P. Mitchel, K. Mogi, and T. Nakamura (2018). *Phobos Environment Model and Regolith Simulant for MMX Mission*. 49th Lunar and Planetary Science Conference, Abstract 1882.

Miyamoto, Hideaki, Takafumi Niihara, Koji Wada, Kazunori Ogawa, Hiroki Senshu, Patrick Michel, Hiroshi Kikuchi, Ryodo Hemmi, Tomoki Nakamura, Akiko M. Nakamura, Naoyuki Hirata, Sho Sasaki, Erik Asphaug, Dan T. Britt, Paul A. Abell, Ronald-Louis Ballouz, Olivier S. Barnouin, Nicola Barsei, Maria A. Barucci, Jens Biele, Matthias Grott, Hideitsu Hino, Peng K. Hong, Takane Imada, Shingo Kameda, Makito Kobayashi, Guy Libourel, Katsuro Mogi, Naomi Murdoch, Yuki Nishio, Shogo Okamoto, Yuichiro Ota, Masatsugu Otsuki, Katharina A. Otto, Naoya Sakaani, Yuta Shimizu, Tomohiro Takemura, Naoki Terada, Masafumi Tsukamoto, Tomohiro Usui, and Konrad Willner (Sept. 2021). *Surface Environment of Phobos and Phobos Simulant UTPS*. Tech. rep. ISSN: 2693-5015 Type: article. DOI: 10.21203/rs.3.rs-150345/v1. URL: https://www.researchsquare.com/article/rs-150345/v1 (visited on 09/07/2021).

Miyamoto, M. (June 1991). "Thermal Metamorphism of CI and CM Carbonaceous Chondrites: an Internal Heating Model". In: *Meteoritics* 26, p. 111. ISSN: 0026-1114. DOI: 10.1111/j.1945-5100.1991.tb01026.x.

Miyamoto, M. and T. Mikouchi (Mar. 2001). "Diffuse Reflectance Spectra of a Eucrite: Resistance to Heating at Different Oxygen Fugacities". In: *Lunar and Planetary Science Conference*. Lunar and Planetary Science Conference, p. 1261.

Morbidelli, A., K. J. Walsh, D. P. O'Brien, D. A. Minton, and W. F. Bottke (2015). "The Dynamical Evolution of the Asteroid Belt". en. In: *Asteroids IV*. Ed. by Patrick Michel, Francesca E. DeMeo, and William F. Bottke. University of Arizona Press. ISBN: 978-0-8165-3213-1. DOI: 10.2458/azu_uapress_9780816532131-ch026. URL: http://muse.jhu.edu/chapter/1705182 (visited on 07/19/2021).

Morbidelli, Alessandro, Ramon Brasser, Rodney Gomes, Harold F. Levison, and Kleomenis Tsiganis (Oct. 2010). "Evidence from the asteroid belt for a violent past evolution of Jupiter's orbit". en. In: *AJ* 140.5. Publisher: American Astronomical Society, pp. 1391–1401. ISSN: 1538-3881. DOI: 10.1088/0004-6256/140/5/1391. URL: https://doi.org/10.1088/0004-6256/140/5/1391 (visited on 08/02/2021).

Morbidelli, Alessandro, Kleomenis Tsiganis, Aurélien Crida, Harold F. Levison, and Rodney Gomes (Sept. 2007). "Dynamics of the Giant Planets of the Solar System in the Gaseous Protoplanetary Disk and Their Relationship to the Current Orbital Architecture". en. In: *AJ* 134.5. Publisher: IOP Publishing, p. 1790. ISSN: 1538-3881. DOI: 10.1086/521705. URL: https://iopscience.iop.org/article/10.1086/521705/meta (visited on 08/02/2021).

Morris, Richard V., David G. Agresti, Howard V. Lauer Jr., Jeffery A. Newcomb, Tad D. Shelfer, and A. V. Murali (1989). "Evidence for pigmentary hematite on Mars based on optical, magnetic, and Mossbauer studies of superparamagnetic (nanocrystalline) hematite". en. In: *Journal of Geophysical Research: Solid Earth* 94.B3. _eprint: https://onlinelibrary.wiley.com/doi/pdf/10.1029/JB094iB03p02760, pp. 2760–2778. ISSN: 2156-2202. DOI: 10.1029/JB094iB03p02760. URL: https://onlinelibrary.wiley.com/doi/abs/10.1029/JB094iB03p02760 (visited on 11/13/2021).

Morris, Richard V., III Bell James F., and Jr. Lauer H. V. (Mar. 1994). "Hematite Formed from Pyroxene on Mars by Meteoritic Impact". In: *Lunar and Planetary Science Conference*. Lunar and Planetary Science Conference, p. 939.

Morris, Richard V., D. C. Golden, James F. Bell III, Tad D. Shelfer, Andreas C. Scheinost, Nancy W. Hinman, George Furniss, Stanley A. Mertzman, Janice L. Bishop, Douglas W. Ming, Carlton C. Allen, and Daniel T. Britt (2000). "Mineralogy, composition, and alteration of Mars Pathfinder rocks and soils: Evidence from multispectral, elemental, and magnetic data on terrestrial analogue, SNC meteorite, and Pathfinder samples". en. In: *Journal of Geophysical Research: Planets* 105.E1. _eprint: https://onlinelibrary.wiley.com/doi/pdf/10.1029/1999JE001059, pp. 1757–1817. ISSN: 2156-2202. DOI: 10.1029/1999JE001059. URL: https://onlinelibrary.wiley.com/doi/abs/10.1029/1999JE001059 (visited on 11/15/2021).

Morris, Richard V., Howard V. Lauer Jr., Charles A. Lawson, Everett K. Gibson Jr., Georg Ann Nace, and Cheri Stewart (1985). "Spectral and other physicochemical properties of submicron powders of hematite (α-Fe2O3), maghemite (γ-Fe2O3), magnetite (Fe3O4), goethite (α-FeOOH), and lepidocrocite (γ-FeOOH)". en. In: *Journal of Geophysical Research: Solid Earth* 90.B4. _eprint: https://onlinelibrary.wiley.com/doi/pdf/10.1029/JB090iB04p03126, pp. 3126–3144. ISSN: 2156-2202. DOI: 10.1029/JB090iB04p03126. URL: https://onlinelibrary.wiley.com/doi/abs/10.1029/JB090iB04p03126 (visited on 11/18/2021).

Morrison, David (1976). "The densities and bulk compositions of Ceres and Vesta". en. In: *Geophysical Research Letters* 3.12. _eprint: https://agupubs.onlinelibrary.wiley.com/doi/pdf/10.1029/GL003i012p00701, pp. 701–704. ISSN: 1944-8007. DOI: 10.1029/GL003i012p00701. URL: https://agupubs.onlinelibrary.wiley.com/doi/abs/10.1029/GL003i012p00701 (visited on 06/15/2021).

Nakamura, Tomoki (Jan. 2005). "Post-hydration thermal metamorphism of carbonaceous chondrites". In: *Journal of Mineralogical and Petrological Sciences* 100, pp. 260–272. DOI: 10.2465/jmps.100.260.

Nathues, A., M. Hoffmann, E. A. Cloutis, M. Schäfer, V. Reddy, U. Christensen, H. Sierks, G. S. Thangjam, L. Le Corre, K. Mengel, J.-B. Vincent, C. T. Russell, T. H. Prettyman, N. Schmedemann, T. Kneissl, C. Raymond, P. Gutierrez-Marques, I. Hall, and I. Büttner (Sept. 2014). "Detection of serpentine in exogenic carbonaceous chondrite material on Vesta from Dawn FC data". In: *Icarus* 239, pp. 222–237. ISSN: 0019-1035.

Nathues, Andreas, Martin Hoffmann, Michael Schäfer, Guneshwar Thangjam, Lucille Le Corre, Vishnu Reddy, Ulrich Christensen, Kurt Mengel, Holger Sierks, Jean-Baptist Vincent, Edward

A. Cloutis, Christopher T. Russell, Tanja Schäfer, Pablo Gutierrez-Marques, Ian Hall, Joachim Ripken, and Irene Büttner (Sept. 2015). "Exogenic olivine on Vesta from Dawn Framing Camera color data". en. In: *Icarus* 258, pp. 467–482. ISSN: 0019-1035. DOI: 10.1016/j.icarus.2014.09.045. URL: https://www.sciencedirect.com/science/article/pii/S001910351400520X (visited on 08/17/2021).

Neish, C. D., K. M. Cannon, L. L. Tornabene, R. L. Flemming, M. Zanetti, and E. Pilles (June 2021). "Spectral properties of lunar impact melt deposits from Moon Mineralogy Mapper (M¡SUP¿3¡/SUP¿) data". In: *Icarus* 361, p. 114392. ISSN: 0019-1035. DOI: 10.1016/j.icarus.2021.114392.

Nesvorný, D., M. Broz, and V. Carruba (2015). "Identification and Dynamical Properties of Asteroid Families". en. In: *Asteroids IV*. Ed. by Patrick Michel, Francesca E. DeMeo, and William F. Bottke. University of Arizona Press. ISBN: 978-0-8165-3213-1. DOI: 10.2458/azu_uapress_9780816532131-ch016. URL: http://muse.jhu.edu/chapter/1705170 (visited on 08/03/2021).

Newsom, Horton E., Günther Graup, Terry Sewards, and Klaus %J Journal of Geophysical Research Keil (Sept. 1986). "Fluidization and hydrothermal alteration of the suevite deposit at the Ries crater, West Germany, and implications for Mars". In: *JGR Solid Earth* 91, E239. ISSN: 0148-0227. DOI: 10.1029/JB091iB13p0E239.

O'Brien, David P., Simone Marchi, Alessandro Morbidelli, William F. Bottke, Paul M. Schenk, Christopher T. Russell, and Carol A. Raymond (2014). "Constraining the cratering chronology of Vesta". en. In: *Planetary and Space Science* 103, pp. 131–142. ISSN: 0032-0633. DOI: 10.1016/j.pss.2014.05.013. URL: https://www.sciencedirect.com/science/article/pii/S0032063314001585 (visited on 08/02/2021).

Okrusch, Martin and Siegfried Matthes (2010). *Mineralogie*. Springer-Verlag Berlin Heidelberg. ISBN: 978-3-540-78201-8.

Olbers, Wilhelm, Carl Friedrich Gauss, and C. Schilling (1894). *Wilhelm Olbers, sein Leben und seine Werke. Im Auftrage der Nachkommen hrsg. von C. Schilling.* ger. Berlin J. Springer. URL: http://archive.org/details/p1wilhelmolberss02olbeuoft (visited on 08/03/2021).

Osinski, Gordon R. (2003). "Impact glasses in fallout suevites from the Ries impact structure, Germany: An analytical SEM study". en. In: *Meteoritics & Planetary Science* 38.11. _eprint: https://onlinelibrary.wiley.com/doi/pdf/10.1111/j.1945-5100.2003.tb00006.x, pp. 1641–1667. ISSN: 1945-5100. DOI: https://doi.org/10.1111/j.1945-5100.2003.tb00006.x. URL: https://onlinelibrary.wiley.com/doi/abs/10.1111/j.1945-5100.2003.tb00006.x (visited on 06/04/2021).

Osinski, Gordon R., Livio L. Tornabene, and Richard A. F. Grieve (Oct. 2011). "Impact ejecta emplacement on terrestrial planets". In: *Earth and Planetary Science Letters* 310, pp. 167–181. ISSN: 0012-821X. DOI: 10.1016/j.epsl.2011.08.012.

Otto, Katharina A., Ralf Jaumann, Katrin Krohn, Klaus-Dieter Matz, Frank Preusker, Thomas Roatsch, Paul Schenk, Frank Scholten, Katrin Stephan, Carol A. Raymond, and Christopher T. Russell (Nov. 2013). "Mass-wasting features and processes in Vesta's south polar basin Rheasilvia". English. In: *JGR Planets* 118.11, pp. 2279–2294. ISSN: 0148-0227. DOI: 10.1002/2013JE004333.

Palmer, Elizabeth M., Essam Heggy, Maria T. Capria, and Federico Tosi (Dec. 2015). "Dielectric properties of Asteroid Vesta's surface as constrained by Dawn VIR observations". In: *Icarus* 262, p. 93. ISSN: 0019-1035. DOI: 10.1016/j.icarus.2015.08.031.

Palomba, E., A. Longobardo, M. C. De Sanctis, A. Zinzi, E. Ammannito, S. Marchi, F. Tosi, F. Zambon, M. T. Capria, C. T. Russell, C. A. Raymond, and E. A. Cloutis (Sept. 2015). "Detection of new olivine-rich locations on Vesta". English. In: *Icarus* 258, pp. 120–134. ISSN: 0019-1035. DOI: 10.1016/j.icarus.2015.06.011.

Palomba, Ernesto, Andrea Longobardo, Maria Cristina De Sanctis, Francesca Zambon, Federico Tosi, Eleonora Ammannito, Fabrizio Capaccioni, Alessandro Frigeri, Maria Teresa Capria, Edward A. Cloutis, Ralf Jaumann, Jean-Philippe Combe, Carol A. Raymond, and Christopher T. Russell (Sept. 2014). "Composition and mineralogy of dark material units on Vesta". In: *Icarus* 240, p. 58. ISSN: 0019-1035. DOI: 10.1016/j.icarus.2014.04.040.

Parker, Joel Wm, S. Alan Stern, Peter C. Thomas, Michel C. Festou, William J. Merline, Eliot F. Young, Richard P. Binzel, and Larry A. Lebofsky (Jan. 2002). "Analysis of the First Disk-resolved Images of Ceres from Ultraviolet Observations with the Hubble Space Telescope". en. In: *AJ* 123.1. Publisher: IOP Publishing, p. 549. ISSN: 1538-3881. DOI: 10.1086/338093. URL: https://iopscience.iop.org/article/10.1086/338093/meta (visited on 06/18/2021).

Pasckert, J. H., H. Hiesinger, O. Ruesch, D. A. Williams, A. Naß, T. Kneissl, S. C. Mest, D. L. Buczkowski, J. E. C. Scully, N. Schmedemann, R. Jaumann, T. Roatsch, F. Preusker, A. Nathues, M. Hoffmann, M. Schäfer, M. C. De Sanctis, C. A. Raymond, and C. T. Russell (2018). "Geologic mapping of the Ac-2 Coniraya quadrangle of Ceres from NASA's Dawn mission: Implications for a heterogeneously composed crust". In: *Icarus* 316, pp. 28–45. ISSN: 0019-1035. DOI: 10.1016/j.icarus.2017.06.015.

Pierazzo, E. and H. J. Melosh (2000). "Hydrocode modeling of oblique impacts: The fate of the projectile". In: *Meteoritics & Planetary Science* 35, pp. 117–130. DOI: 10.1111/j.1945-5100.2000.tb01979.x.

Pieters, C. M., E. Ammannito, D. T. Blewett, B. W. Denevi, M. C. de Sanctis, M. J. Gaffey, L. Le Corre, J.-Y. Li, S. Marchi, T. B. McCord, L. A. McFadden, D. W. Mittlefehldt, A. Nathues, E. Palmer, V. Reddy, C. A. Raymond, and C. T. Russell (Nov. 2012). "Distinctive space weathering on Vesta from regolith mixing processes". eng. In: *Nature* 491.7422, pp. 79–82. ISSN: 0028-0836. DOI: 10.1038/nature11534.

Pieters, C. M., M. I. Staid, E. M. Fischer, S. Tompkins, and G. He (Dec. 1994). "A Sharper View of Impact Craters from Clementine Data". In: *Science* 266, pp. 1844–1848.

Pieters, C. M., Larry A. Taylor, Sarah K. Noble, Lindsay P. Keller, Bruce Hapke, Richard V. Morris, Carl C. Allen, David S. McKay, and Susan Wentworth (Sept. 2000). "Space weathering on airless bodies: Resolving a mystery with lunar samples". English. In: *Meteorit Planet Sci* 35.5, pp. 1101–1107. ISSN: 1086-9379. DOI: 10.1111/j.1945-5100.2000.tb01496.x.

Poch, Olivier, Antoine Pommerol, Bernhard Jost, Nathalie Carrasco, Cyril Szopa, and Nicolas Thomas (Mar. 2016). "Sublimation of water ice mixed with silicates and tholins: Evolution of surface texture and reflectance spectra, with implications for comets". In: *Icarus* 267, p. 154. ISSN: 0019-1035.

Polanskey, Carol, Linda Elkins-Tanton, James Bell, Richard Binzel, David Lawrence, Jose Merayo, Ryan Park, Benjamin Weiss, and David Williams (Aug. 2020). "Mission to (16) Psyche". en. In: Conference Name: EPSC2020. Copernicus Meetings. DOI: 10.5194/epsc2020-988. URL: https://meetingorganizer.copernicus.org/EPSC2020/EPSC2020-988.html (visited on 11/15/2021).

Prettyman, T. H., William C. Feldman, Harry Y. McSween, Robert D. Dingler, Donald C. Enemark, Douglas E. Patrick, Steven A. Storms, John S. Hendricks, Jeffery P. Morgenthaler, Karly M. Pitman, and Robert C. Reedy (Dec. 2011). "Dawn's Gamma Ray and Neutron Detector". English. In: *Space Science Reviews* 163.1-4, pp. 371–459. ISSN: 0038-6308. DOI: 10.1007/s11214-011-9862-0.

Prettyman, T. H., D. W. Mittlefehldt, N. Yamashita, A. W. Beck, W. C. Feldman, J. S. Hendricks, D. J. Lawrence, T. J. McCoy, H. Y. McSween, P. N. Peplowski, R. C. Reedy, M. J. Toplis, L. Le Corre, H. Mizzon, V. Reddy, T. N. Titus, C. A. Raymond, and C. T. Russell (Nov. 2013). "Neutron absorption constraints on the composition of 4 Vesta". English. In: *Meteorit Planet Sci* 48.11, pp. 2211–2236. ISSN: 1086-9379. DOI: 10.1111/maps.12244.

Prettyman, T. H., D. W. Mittlefehldt, N. Yamashita, D. J. Lawrence, A. W. Beck, W. C. Feldman, T. J. McCoy, H. Y. McSween, M. J. Toplis, T. N. Titus, P. Tricarico, R. C. Reedy, J. S. Hendricks, O. Forni, L. Le Corre, J.-Y. Li, H. Mizzon, V. Reddy, C. A. Raymond, and C. T. Russell (Oct. 2012). "Elemental Mapping by Dawn Reveals Exogenic H in Vesta's Regolith". In: *Science* 338, p. 242. ISSN: 0036-8075.

Preusker, F., F. Scholten, K.-D. Matz, T. Roatsch, R. Jaumann, C. A. Raymond, and C. T. Russell (Feb. 2014). *Global Shape of (4) Vesta from Dawn FC Stereo Images*. Vesta in the Light of Dawn: First Exploration of a Protoplanet in the Asteroid Belt, Abstract 2027.

Preusker, F., F. Scholten, K.-D. Matz, T. Roatsch, R. Jaumann, C. A. Raymond, and C. T. %J NASA Planetary Data System Russell (Oct. 2016). "Dawn FC2 Derived Vesta DTM SPG V1.0". In: *NASA Planetary Data System*, DAWN–A–FC2–5–VESTADTMSPG–V1.0.

Quick, Lynnae C., Debra L. Buczkowski, Ottaviano Ruesch, Jennifer E. C. Scully, Julie Castillo-Rogez, Carol A. Raymond, Paul M. Schenk, Hanna G. Sizemore, and Mark V. Sykes (Mar. 2019). "A Possible Brine Reservoir Beneath Occator Crater: Thermal and Compositional Evolution and Formation of the Cerealia Dome and Vinalia Faculae". en. In: *Icarus*. Occator Crater on Ceres 320, pp. 119–135. ISSN: 0019-1035. DOI: 10.1016/j.icarus.2018.07.016. URL: https://www.sciencedirect.com/science/article/pii/S0019103517306371 (visited on 08/17/2021).

Raponi, Andrea, Maria Cristina De Sanctis, Filippo Giacomo Carrozzo, Mauro Ciarniello, Batiste Rousseau, Marco Ferrari, Eleonora Ammannito, Simone De Angelis, Vassilissa Vinogradoff, Julie C. Castillo-Rogez, Federico Tosi, Alessandro Frigeri, Michelangelo Formisano, Francesca Zambon, Carol A. Raymond, and Christopher T. Russell (Jan. 2021). "Organic Material on Ceres: Insights from Visible and Infrared Space Observations". en. In: *Life* 11.1. Number: 1 Publisher: Multidisciplinary Digital Publishing Institute, p. 9. DOI: 10.3390/life11010009. URL: https://www.mdpi.com/2075-1729/11/1/9 (visited on 08/31/2021).

Rayman, Marc D., Thomas C. Fraschetti, Carol A. Raymond, and Christopher T. Russell (June 2006). "Dawn: A mission in development for exploration of main belt asteroids Vesta and Ceres". English. In: *Acta Astronautica* 58.11, pp. 605–616. ISSN: 0094-5765. DOI: 10.1016/j.actaastro.2006.01.014.

Rayman, Marc D. and Robert A. Mase (2014). "Dawn's exploration of Vesta". In: *Acta Astronautica* 94.1, pp. 159–167. ISSN: 0094-5765. DOI: 10.1016/j.actaastro.2013.08.003.

Raymond, Carol, C. T. Russell, Andreas Nathues, Julie Castillo-Rogez, Maria Cristina De Sanctis, Thomas Prettyman, and Marc Rayman (July 2018). "Results of Dawn's Extended Mission at Ceres: A New Low". In: *42nd COSPAR Scientific Assembly*. Vol. 42, B1.1–18–18.

Reddy, V., Lucille Le Corre, David P. O'Brien, Andreas Nathues, Edward A. Cloutis, Daniel D. Durda, William F. Bottke, Megha U. Bhatt, David Nesvorny, Debra Buczkowski, Jennifer E. C. Scully, Elizabeth M. Palmer, Holger Sierks, Paul J. Mann, Kris J. Becker, Andrew W. Beck, David Mittlefehldt, Jian-Yang Li, Robert Gaskell, Christopher T. Russell, Michael J. Gaffey, Harry Y. McSween, Thomas B. McCord, Jean-Philippe Combe, and David Blewett (Nov. 2012a). "Delivery of dark material to Vesta via carbonaceous chondritic impacts". In: *Icarus* 221, pp. 544–559. ISSN: 0019-1035. DOI: 10.1016/j.icarus.2012.08.011.

Reddy, V., A. Nathues, L. Le Corre, H. Sierks, J.-Y. Li, R. Gaskell, T. J. McCoy, A. W. Beck, S. E. Schröder, C. M. Pieters, K. J. Becker, B. J. Buratti, B. W. Denevi, D. T. Blewett, U. Christensen, M. J. Gaffey, P. Gutierrez-Marques, M. D. Hicks, H. U. Keller, T. Maue, S. Mottola, L. A. McFadden, H. Y. McSween, D. Mittlefehldt, D. P. O'Brien, C. Raymond, and C. Russell (May 2012b). "Color and Albedo Heterogeneity of Vesta from Dawn". eng. In: *Science* 336.6082, pp. 700–704. ISSN: 0036-8075. DOI: 10.1126/science.1219088.

Roatsch, Th, E. Kersten, K.-D. Matz, F. Preusker, F. Scholten, S. Elgner, R. Jaumann, C. A. Raymond, and C. T. Russell (Sept. 2013). "High-resolution Vesta Low Altitude Mapping Orbit Atlas derived from Dawn Framing Camera images". In: *Planetary and Space Science* 85, pp. 293–298. ISSN: 0032-0633.

Roatsch, Th, E. Kersten, K.-D. Matz, F. Preusker, F. Scholten, R. Jaumann, C. A. Raymond, and C. T. Russell (Dec. 2012). "High resolution Vesta High Altitude Mapping Orbit (HAMO) Atlas derived from Dawn framing camera images". In: *Planetary and Space Science* 73, pp. 283–286. ISSN: 0032-0633.

Rousseau, B., M. C. De Sanctis, A. Raponi, M. Ciarniello, E. Ammannito, P. Scarica, S. Fonte, A. Frigeri, F. G. Carrozzo, and F. Tosi (Dec. 2020a). "Correction of the VIR-visible dataset from the Dawn mission at Vesta". In: *Review of Scientific Instruments* 91.12. Publisher: American Institute of Physics, p. 123102. ISSN: 0034-6748. DOI: 10.1063/5.0022902. URL: https://aip.scitation.org/doi/10.1063/5.0022902 (visited on 08/31/2021).

Rousseau, B., A. Raponi, M. Ciarniello, E. Ammannito, F. G. Carrozzo, M. C. De Sanctis, S. Fonte, A. Frigeri, and F. Tosi (Dec. 2019). "Correction of the VIR-visible data set from the Dawn mission". In: *Review of Scientific Instruments* 90.12. Publisher: American Institute of Physics, p. 123110. ISSN: 0034-6748. DOI: 10.1063/1.5123362. URL: https://aip.scitation.org/doi/10.1063/1.5123362 (visited on 08/31/2021).

Rousseau, B., M. C. De Sanctis, A. Raponi, M. Ciarniello, E. Ammannito, A. Frigeri, M. Ferrari, S. De Angelis, F. C. Carrozzo, F. Tosi, S. E. Schröder, C. A. Raymond, and C. T. Russell

(Oct. 2020b). "The surface of (1) Ceres in visible light as seen by Dawn/VIR". en. In: *A&A* 642. Publisher: EDP Sciences, A74. ISSN: 0004-6361, 1432-0746. DOI: 10.1051/0004-6361/202038512. URL: https://www.aanda.org/articles/aa/abs/2020/10/aa38512-20/aa38512-20.html (visited on 08/31/2021).

Royle, Samuel H., Jonathan S.W. Tan, Jonathan S. Watson, and Mark A. Sephton (June 2021). "Pyrolysis of Carboxylic Acids in the Presence of Iron Oxides: Implications for Life Detection on Missions to Mars". In: *Astrobiology* 21.6. Publisher: Mary Ann Liebert, Inc., publishers, pp. 673–691. ISSN: 1531-1074. DOI: 10.1089/ast.2020.2226. URL: https://www.liebertpub.com/doi/full/10.1089/ast.2020.2226 (visited on 11/16/2021).

Ruesch, O., H. Hiesinger, E. Cloutis, L. Le Corre, J. Kallisch, P. Mann, K. Markus, K. Metzler, A. Nathues, and V. Reddy (Sept. 2015). "Near infrared spectroscopy of HED meteorites: Effects of viewing geometry and compositional variations". In: *Icarus* 258, p. 384. ISSN: 0019-1035. DOI: 10.1016/j.icarus.2015.06.034.

Ruesch, O., H. Hiesinger, M. C. De Sanctis, E. Ammannito, E. Palomba, A. Longobardo, F. Zambon, F. Tosi, M. T. Capria, F. Capaccioni, A. Frigeri, S. Fonte, G. Magni, C. A. Raymond, and C. T. Russell (Sept. 2014). "Detections and geologic context of local enrichments in olivine on Vesta with VIR/Dawn data". In: *JGR Planets* 119, pp. 2078–2108. ISSN: 0148-0227.

Ruesch, O., L. C. Quick, M. E. Landis, M. M. Sori, O. Čadek, P. Brož, K. A. Otto, M. T. Bland, S. Byrne, J. C. Castillo-Rogez, H. Hiesinger, R. Jaumann, K. Krohn, L. A. McFadden, A. Nathues, A. Neesemann, F. Preusker, T. Roatsch, P. M. Schenk, J. E. C. Scully, M. V. Sykes, D. A. Williams, C. A. Raymond, and C. T. Russell (Mar. 2019). "Bright carbonate surfaces on Ceres as remnants of salt-rich water fountains". en. In: *Icarus*. Occator Crater on Ceres 320, pp. 39–48. ISSN: 0019-1035. DOI: 10.1016/j.icarus.2018.01.022. URL: https://www.sciencedirect.com/science/article/pii/S0019103517306218 (visited on 08/17/2021).

Russell, C. T., M. A. Barucci, R. P. Binzel, M. T. Capria, U. Christensen, A. Coradini, M. C. De Sanctis, W. C. Feldman, R. Jaumann, H. U. Keller, A. S. Konopliv, T. B. McCord, L. A. McFadden, K. D. McKeegan, H. Y. McSween, S. Mottola, A. Nathues, G. Neukum, C. M. Pieters, T. H. Prettyman, C. A. Raymond, H. Sierks, D. E. Smith, T. Spohn, M. V. Sykes, F. Vilas, and M. T. Zuber (Jan. 2007). "Exploring the asteroid belt with ion propulsion: Dawn mission history, status and plans". en. In: *Advances in Space Research* 40.2, pp. 193–201. ISSN: 0273-1177. DOI: 10.1016/j.asr.2007.05.083. URL: https://www.sciencedirect.com/science/article/pii/S0273117707005868 (visited on 08/04/2021).

Russell, C. T., A. Coradini, U. Christensen, M. C. De Sanctis, W. C. Feldman, R. Jaumann, H. U. Keller, A. S. Konopliv, T. B. McCord, L. A. McFadden, H. Y. McSween, S. Mottola, G. Neukum, C. M. Pieters, T. H. Prettyman, C. A. Raymond, D. E. Smith, M. V. Sykes, B. G. Williams, J. Wise, and M. T. Zuber (Apr. 2004). "Dawn: A journey in space and time". In: *Planetary and Space Science* 52, pp. 465–489. ISSN: 0032-0633. DOI: 10.1016/j.pss.2003.06.013.

Russell, C. T., H. Y. McSween, R. Jaumann, and C. A. Raymond (2015). "The Dawn Mission to Vesta and Ceres". In: *Asteroids IV*. Ed. by Patrick Michel, pp. 419–432.

Russell, C. T., C. A. Raymond, A. Coradini, H. Y. McSween, M. T. Zuber, A. Nathues, M. C. De Sanctis, R. Jaumann, A. S. Konopliv, F. Preusker, S. W. Asmar, R. S. Park, R. Gaskell, H. U. Keller, S. Mottola, T. Roatsch, J. E. C. Scully, D. E. Smith, P. Tricarico, M. J. Toplis, U. R. Christensen, W. C. Feldman, D. J. Lawrence, T. J. McCoy, T. H. Prettyman, R. C. Reedy, M. E. Sykes, and T. N. Titus (May 2012). "Dawn at Vesta: Testing the Protoplanetary Paradigm". English. In: *Science* 336.6082, pp. 684–686. ISSN: 0036-8075. DOI: 10.1126/science.1219381.

Schenk, P., J. Scully, D. Buczkowski, H. Sizemore, B. Schmidt, C. Pieters, A. Neesemann, D. O'Brien, S. Marchi, D. Williams, A. Nathues, M. De Sanctis, F. Tosi, C. T. Russell, J. Castillo-Rogez, and C. Raymond (Aug. 2020). "Impact heat driven volatile redistribution at Occator crater on Ceres as a comparative planetary process". In: *Nature Communications* 11, p. 3679. ISSN: 2041-1723. DOI: 10.1038/s41467-020-17184-7.

Schenk, Paul, David P. O'Brien, Simone Marchi, Robert Gaskell, Frank Preusker, Thomas Roatsch, Ralf Jaumann, Debra Buczkowski, Thomas McCord, Harry Y. McSween, David Williams, Aileen Yingst, Carol Raymond, and Chris Russell (May 2012). "The Geologically Recent Giant Impact Basins at Vesta's South Pole". English. In: *Science* 336.6082, pp. 694–697. ISSN: 0036-8075. DOI: 10.1126/science.1223272.

Schmedemann, N., T. Kneissl, B. A. Ivanov, G. G. Michael, R. J. Wagner, G. Neukum, O. Ruesch, H. Hiesinger, K. Krohn, T. Roatsch, F. Preusker, H. Sierks, R. Jaumann, V. Reddy, A. Nathues, S. H. G. Walter, A. Neesemann, C. A. Raymond, and C. T. Russell (Nov. 2014). "The cratering record, chronology and surface ages of (4) Vesta in comparison to smaller asteroids and the ages of HED meteorites". English. In: *Planetary and Space Science* 103, pp. 104–130. ISSN: 0032-0633. DOI: 10.1016/j.pss.2014.04.004.

Schröder, S. E., T. Maue, P. Gutiérrez Marqués, S. Mottola, K. M. Aye, H. Sierks, H. U. Keller, and A. Nathues (Nov. 2013). "In-flight calibration of the Dawn Framing Camera". In: *Icarus* 226, pp. 1304–1317. ISSN: 0019-1035. DOI: 10.1016/j.icarus.2013.07.036.

Schröder, S. E., S. Mottola, K.-D. Matz, and T. Roatsch (May 2014). "In-flight calibration of the Dawn Framing Camera II: Flat fields and stray light correction". In: *Icarus* 234, pp. 99–108. ISSN: 0019-1035. DOI: 10.1016/j.icarus.2014.02.018.

Scott, E. R. D., R. C. Greenwood, I. A. Franchi, and I. S. Sanders (Oct. 2009). "Oxygen isotopic constraints on the origin and parent bodies of eucrites, diogenites, and howardites". In: *Geochimica et Cosmochimica Acta* 73, p. 5835. ISSN: 0016-7037.

Scott, E. R. D. and A. N. Krot (Jan. 2014). "1.2 - Chondrites and Their Components". In: *Treatise on Geochemistry (Second Edition)*. Ed. by Heinrich D. Holland and Karl K. Turekian. Oxford: Elsevier, pp. 65–137. ISBN: 978-0-08-098300-4.

Scully, Jennifer E. C., Debra L. Buczkowski, Carol A. Raymond, Timothy Bowling, David A. Williams, Adrian Neesemann, Paul M. Schenk, Julie C. Castillo-Rogez, and Christopher T. Russell (Mar. 2019). "Ceres' Occator crater and its faculae explored through geologic mapping". en. In: *Icarus*. Occator Crater on Ceres 320, pp. 7–23. ISSN: 0019-1035. DOI: 10.1016/j.icarus.2018.04.014. URL: https://www.sciencedirect.com/science/article/pii/S0019103517307352 (visited on 08/17/2021).

Scully, Jennifer E. C., Christopher T. Russell, An Yin, Ralf Jaumann, Elizabeth Carey, Julie Castillo-Rogez, Harry Y. McSween, Carol A. Raymond, Vishnu Reddy, and Lucille Le Corre (Feb. 2015). "Geomorphological evidence for transient water flow on Vesta". English. In: *Earth and Planetary Science Letters* 411, pp. 151–163. ISSN: 0012-821X. DOI: 10.1016/j.epsl.2014.12.004.

Shkuratov, Y., V. Kaydash, V. Korokhin, Y. Velikodsky, N. Opanasenko, and G. Videen (Oct. 2011). "Optical measurements of the Moon as a tool to study its surface". en. In: *Planetary and Space Science*. Exploring Phobos 59.13, pp. 1326–1371. ISSN: 0032-0633. DOI: 10.1016/j.pss.2011.06.011. URL: https://www.sciencedirect.com/science/article/pii/S0032063311001954 (visited on 10/20/2021).

Sierks, H., H. U. Keller, R. Jaumann, H. Michalik, T. Behnke, F. Bubenhagen, I. Büttner, U. Carsenty, U. Christensen, R. Enge, B. Fiethe, P. Gutiérrez Marqués, H. Hartwig, H. Krüger, W. Kühne, T. Maue, S. Mottola, A. Nathues, K.-U. Reiche, M. L. Richards, T. Roatsch, S. E. Schröder, I. Szemerey, and M. Tschentscher (Dec. 2011). "The Dawn Framing Camera". In: *Space Science Reviews* 163, pp. 263–327. ISSN: 0038-6308. DOI: 10.1007/s11214-011-9745-4.

Sizemore, H. G., T. Platz, N. Schorghofer, T. H. Prettyman, M. C. De Sanctis, D. A. Crown, N. Schmedemann, A. Neesemann, T. Kneissl, S. Marchi, P. M. Schenk, M. T. Bland, B. E. Schmidt, K. H. G. Hughson, F. Tosi, F. Zambon, S. C. Mest, R. A. Yingst, D. A. Williams, C. T. Russell, and C. A. Raymond (July 2017). "Pitted terrains on (1) Ceres and implications for shallow subsurface volatile distribution". In: *Geophysical Research Letters* 44, pp. 6570–6578.

Stephan, K., R. Jaumann, M. C. De Sanctis, E. Ammannito, K. Krohn, K. A. Otto, F. Tosi, J.-P. Combe, T. Roatsch, K.-D. Matz, L. A. McFadden, F. Preusker, C. A. Raymond, and C. T. Russell (Oct. 2015). "The Sextilia-region on Asteroid 4Vesta - Stratigraphy and variegation". In: *Icarus* 259, pp. 162–180. ISSN: 0019-1035. DOI: 10.1016/j.icarus.2015.05.016.

Stephan, K., R. Jaumann, M. C. De Sanctis, F. Tosi, E. Ammannito, K. Krohn, F. Zambon, S. Marchi, O. Ruesch, K.-D. Matz, F. Preusker, T. Roatsch, C. A. Raymond, and C. T. Russell (Apr. 2014). "Small fresh impact craters on asteroid 4 Vesta: A compositional and geological fingerprint". In: *JGR Planets* 119, pp. 771–797.

Stephan, K., R. Jaumann, K. Krohn, N. Schmedemann, F. Zambon, F. Tosi, F. G. Carrozzo, L. A. McFadden, K. Otto, M. C. De Sanctis, E. Ammannito, K.-D. Matz, T. Roatsch, F. Preusker, C. A. Raymond, and C. T. Russell (2017). "An investigation of the bluish material

on Ceres". en. In: *Geophys. Res. Lett.* ISSN: 00948276. DOI: 10.1002/2016GL071652. URL: http://doi.wiley.com/10.1002/2016GL071652 (visited on 10/01/2021).

Straub, D'Arcy W., Roger G. Burns, and Stephen F. Pratt (1991). "Spectral signature of oxidized pyroxenes: implications to remote sensing of terrestrial planets". en. In: *Journal of Geophysical Research: Planets* 96.E3. _eprint: https://onlinelibrary.wiley.com/doi/pdf/10.1029/91JE01893, pp. 18819–18830. ISSN: 2156-2202. DOI: 10.1029/91JE01893. URL: https://onlinelibrary.wiley.com/doi/abs/10.1029/91JE01893 (visited on 11/12/2021).

Stubbs, Timothy J. and Yongli Wang (Jan. 2012). "Illumination conditions at the Asteroid 4 Vesta: Implications for the presence of water ice". In: *Icarus* 217, p. 272. ISSN: 0019-1035.

Thangjam, Guneshwar, Andreas Nathues, Kurt Mengel, Martin Hoffmann, Michael Schäfer, Vishnu Reddy, Edward A. Cloutis, Ulrich Christensen, Holger Sierks, Lucille Le Corre, Jean-Baptiste Vincent, and Christopher T. Russell (Oct. 2014). "Olivine-rich exposures at Bellicia and Arruntia craters on (4) Vesta from Dawn FC". In: *Meteoritics and Planetary Science* 49, pp. 1831–1850. ISSN: 1086-9379.

Thangjam, Guneshwar, Vishnu Reddy, Lucille Le Corre, Andreas Nathues, Holger Sierks, Harald Hiesinger, Jian-Yang Li, Juan A. Sanchez, Christopher T. Russell, Robert Gaskell, and Carol Raymond (Nov. 2013). "Lithologic mapping of HED terrains on Vesta using Dawn Framing Camera color data". English. In: *Meteorit Planet Sci* 48.11, pp. 2199–2210. ISSN: 1086-9379. DOI: 10.1111/maps.12132.

Thomas, Peter C, Richard P Binzel, Michael J Gaffey, Benjamin H Zellner, Alex D Storrs, and Eddie Wells (July 1997). "Vesta: Spin Pole, Size, and Shape from HST Images". en. In: *Icarus* 128.1, pp. 88–94. ISSN: 0019-1035. DOI: 10.1006/icar.1997.5736. URL: https://www.sciencedirect.com/science/article/pii/S0019103597957365 (visited on 08/03/2021).

Tompkins, Stefanie and Carlé M. Pieters (July 2010). "Spectral characteristics of lunar impact melts and inferred mineralogy". In: *Meteoritics and Planetary Science* 45, pp. 1152–1169. ISSN: 1086-9379. DOI: 10.1111/j.1945-5100.2010.01074.x.

Tornabene, L. L., A. S. McEwen, G. R. Osinski, P. J. Mouginis-Mark, J. M. Boyce, R. M. E. Williams, J. J. Wray, J. A. Grant, and HiRISE Team (July 2007). "Impact Melting and the Role of Sub-Surface Volatiles: Implications for the Formation of Valley Networks and Phyllosilicate-rich Lithologies on Early Mars". In: vol. 1353. Seventh International Conference on Mars, Pasadena, California, USA, p. 3288.

Tornabene, L. L., G. R. Osinski, A. S. McEwen, J. M. Boyce, V. J. Bray, C. M. Caudill, J. A. Grant, C. W. Hamilton, S. Mattson, and P. J. Mouginis-Mark (Aug. 2012). "Widespread crater-related pitted materials on Mars: Further evidence for the role of target volatiles during the impact process". In: *Icarus* 220, p. 348. ISSN: 0019-1035.

Tosi, F., M. T. Capria, M. C. De Sanctis, J.-Ph Combe, F. Zambon, A. Nathues, S. E. Schröder, J.-Y. Li, E. Palomba, A. Longobardo, D. T. Blewett, B. W. Denevi, E. Palmer, F. Capaccioni, E. Ammannito, T. M. Titus, D. W. Mittlefehldt, J. M. Sunshine, C. T. Russell, and C. A. Raymond (Sept. 2014). "Thermal measurements of dark and bright surface features on Vesta as derived from Dawn/VIR". In: *Icarus* 240, pp. 36–57. ISSN: 0019-1035.

Vilas, Faith, Kandy S. Jarvis, and Michael J. Gaffey (June 1994). "Iron Alteration Minerals in the Visible and Near-Infrared Spectra of Low-Albedo Asteroids". en. In: *Icarus* 109.2, pp. 274–283. ISSN: 0019-1035. DOI: 10.1006/icar.1994.1093. URL: https://www.sciencedirect.com/science/article/pii/S0019103584710931 (visited on 11/22/2021).

Walsh, Kevin J., A. Morbidelli, S. N. Raymond, D. P. O'brien, and A. M. Mandell (2012). "Populating the asteroid belt from two parent source regions due to the migration of giant planets—"The Grand Tack"". en. In: *Meteoritics & Planetary Science* 47.12. _eprint: https://onlinelibrary.wiley.com/doi/pdf/10.1111/j.1945-5100.2012.01418.x, pp. 1941–1947. ISSN: 1945-5100. DOI: 10.1111/j.1945-5100.2012.01418.x. URL: https://onlinelibrary.wiley.com/doi/abs/10.1111/j.1945-5100.2012.01418.x (visited on 08/02/2021).

Wasson, John T. (Nov. 2013). "Vesta and extensively melted asteroids: Why HED meteorites are probably not from Vesta". In: *Earth and Planetary Science Letters* 381, pp. 138–146. ISSN: 0012-821X.

White, William M. (2013). *Geochemistry*. en. Chichester, West Sussex : Hoboken, NJ: Wiley-Blackwell. ISBN: 978-1-118-48525-5.

Williams, D. A., Brett W. Denevi, David W. Mittlefehldt, Scott C. Mest, Paul M. Schenk, R. Aileen Yingst, Debra L. Buczkowski, Jennifer E. C. Scully, W. Brent Garry, Thomas B. McCord, Jean-Phillipe Combe, Ralf Jaumann, Carle M. Pieters, Andreas Nathues, Lucille Le Corre, Martin Hoffmann, Vishnu Reddy, Michael Schäfer, Thomas Roatsch, Frank Preusker, Simone Marchi, Thomas Kneissl, Nico Schmedemann, Gerhard Neukum, Harald Hiesinger, Maria Cristina De Sanctis, Eleonora Ammannito, Alessandro Frigeri, Thomas H. Prettyman, Christopher T. Russell, and Carol A. Raymond (2014a). "The geology of the Marcia quadrangle of asteroid Vesta: Assessing the effects of large, young craters". In: *Icarus* 244, pp. 74–88. ISSN: 0019-1035. DOI: 10.1016/j.icarus.2014.01.033.

Williams, D. A., R. Jaumann, H. Y. McSween, S. Marchi, N. Schmedemann, C. A. Raymond, and C. T. Russell (Dec. 2014b). "The chronostratigraphy of protoplanet Vesta". English. In: *Icarus* 244, pp. 158–165. ISSN: 0019-1035. DOI: 10.1016/j.icarus.2014.06.027.

Williams, D. A., David P. O'Brien, Paul M. Schenk, Brett W. Denevi, Uri Carsenty, Simone Marchi, Jennifer E. C. Scully, Ralf Jaumann, Maria Cristina De Sanctis, Ernesto Palomba, Eleonora Ammannito, Andrea Longobardo, Gianfranco Magni, Alessandro Frigeri, Christopher T. Russell, Carol A. Raymond, and Thomas M. Davison (Nov. 2014c). "Lobate and flow-like features on asteroid Vesta". In: *Planetary and Space Science* 103, p. 24. ISSN: 0032-0633. DOI: 10.1016/j.pss.2013.06.017.

Williams, Jean-Pierre, Carolyn H. van der Bogert, Asmin V. Pathare, Gregory G. Michael, Michelle R. Kirchoff, and Harald Hiesinger (2018). "Dating very young planetary surfaces from crater statistics: A review of issues and challenges". en. In: *Meteoritics & Planetary Science* 53.4. _eprint: https://onlinelibrary.wiley.com/doi/pdf/10.1111/maps.12924, pp. 554–582. ISSN: 1945-5100. DOI: 10.1111/maps.12924. URL: https://onlinelibrary.wiley.com/doi/abs/10.1111/maps.12924 (visited on 06/10/2021).

Wilson, Lionel and Klaus Keil (1996). "Volcanic eruptions and intrusions on the asteroid 4 Vesta". en. In: *Journal of Geophysical Research: Planets* 101.E8. _eprint: https://agupubs.onlinelibrary.wiley.com/doi/pdf/10.1029/96JE01390, pp. 18927–18940. ISSN: 2156-2202. DOI: 10.1029/96JE01390. URL: https://onlinelibrary.wiley.com/doi/abs/10.1029/96JE01390 (visited on 09/20/2021).

Yamashita, S., T. Nakamura, K. Jogo, M. Matsuoka, and S. Okumura (July 2015). "Progressive Changes in Mineralogy, Reflectance Spectra and Water Contents of Experimentally Heated Murchison at 400, 600, and 900℃". In: *78th Annual Meeting of the Meteoritical Society*. Vol. 78. LPI Contributions, p. 5154.

Zambon, F., Maria Cristina De Sanctis, Stefan Schröder, Federico Tosi, Andrea Longobardo, Eleonora Ammannito, David T. Blewett, David W. Mittlefehldt, Jian-Yang Li, E. Palomba, Fabrizio Capaccioni, Alessandro Frigeri, Maria Teresa Capria, Sergio Fonte, Andreas Nathues, Carle M. Pieters, Christofer T. Russell, and Carol A. Raymond (Sept. 2014). "Spectral analysis of the bright materials on the asteroid Vesta". In: *Icarus* 240, pp. 73–85. ISSN: 0019-1035.

Zambon, F., A. Frigeri, J.-Ph Combe, F. Tosi, A. Longobardo, E. Ammannito, M. C. De Sanctis, D. T. Blewett, J. Scully, E. Palomba, B. Denevi, A. Yingst, C. T. Russell, and C. A. Raymond (Oct. 2015). "Spectral analysis of the quadrangles Av-13 and Av-14 on Vesta". In: *Icarus* 259, p. 181. ISSN: 0019-1035. DOI: 10.1016/j.icarus.2015.05.015.

Zellner, Benjamin H., Rudolph Albrecht, Richard P. Binzel, Michael J. Gaffey, Peter C. Thomas, Alex D. Storrs, and Eddie N. Wells (July 1997). "Hubble Space Telescope Images of Asteroid 4 Vesta in 1994". en. In: *Icarus* 128.1, pp. 83–87. ISSN: 0019-1035. DOI: 10.1006/icar.1997.5735. URL: https://www.sciencedirect.com/science/article/pii/S0019103597957353 (visited on 06/15/2021).

Zolensky, M. E., M. E. Lipschutz, and T. Hiroi (Mar. 1994). "Minerology of Artificially Heated Carbonaceous Chondrites". In: *Lunar and Planetary Science Conference*. Lunar and Planetary Science Conference, p. 1567.

Zolensky, M. E., Michael K. Weisberg, Paul C. Buchanan, and David W. Mittlefehldt (1996). "Mineralogy of carbonaceous chondrite clasts in HED achondrites and the Moon". In: *Meteoritics and Planetary Science* 31, pp. 518–537. ISSN: 1086-9379.

# 11 Supplementary Material from Michalik et al., 2021

## 11.1 Table S1: Spectra ID's, meteorite names, spectral values, weathering remarks from Michalik et al., 2021

**Table S1: Meteorite/sample names, spectra IDs, weathering information* and values for the ratios 750/917 [nm], 965/917 [nm] and 500/600 [nm]**

| Eucrites | spec ID | meteorite name | 750/917 [nm] | 965/917 [nm] | find/fall | weathering grade | weathering comment (Meteoritical Bulletin) | 500/600 [nm] |
|---|---|---|---|---|---|---|---|---|
| LM-TXH-029 | BKR1LM029 | Y-981651 | 1.505 | 0.932 | find | A | - | 0.925 |
| MP-TXH-118 | bkr1mp118 | EET92003 | 2.186 | 1.079 | find | A/Be | Evaporate deposit is present. | 0.847 |
| MP-TXH-119 | bkr1mp119 | PCA91006 | 1.878 | 1.026 | find | A/B | Flow marks are present, some clasts are oxidized | 0.884 |
| MP-TXH-121 | bkr1mp121 | ALHA81001 | 1.488 | 1.071 | find | Ae | Many cracks penetrate the interior of this meteorite. | 0.980 |
| MP-TXH-122 | bkr1mp122 | ALHA81011 | 1.704 | 1.000 | find | A/B | Several areas of oxidation are visible | 0.906 |
| MP-TXH-123 | bkr1mp123 | EETA79006 | 1.774 | 1.062 | find | B | Several rounded spots of oxidation are obvious and several cracks appear to penetrate the sample | 0.886 |
| MP-TXH-124 | bkr1mp124 | PCA82501 | 1.412 | 1.024 | find | A | Where there is no fusion crust the specimen is coarse grained, white and dark gray in color, with some yellowish oxidation. No individual clasts are visible. There is a very small amount of oxidation present in the interior of this stone. | 0.899 |
| MT-CMP-061 | bkr1mt061 | Y-980318 | 2.122 | 1.022 | find | B/C | - | 0.720 |
| HH-CMP-003 | c1hh03 | Millbillillie | 1.433 | 1.033 | fall | | | 0.948 |
| MB-TXH-069 | c1mb69 | Millbillillie | 1.867 | 1.021 | fall | | | 0.958 |
| MB-TXH-070-1 | c1mb70 | Juvinas | 2.065 | 1.040 | fall | | | 0.942 |
| MT-HYM-028 | c1mt28 | MAC02522 | 2.001 | 0.927 | find | B | - | 0.847 |
| MT-HYM-029 | c1mt29 | EET87520 | 2.170 | 0.995 | find | B | Some metal is visible and oxidation is moderate throughout the matrix | 0.882 |
| MT-HYM-031 | c1mt31 | PCA91078 | 1.797 | 1.007 | find | A/B | The interior is coarse-grained consisting of white plagioclase grains and black grains with some yellowish oxidation. This meteorite is moderately friable. | 0.944 |
| MT-HYM-032 | c1mt32 | BTN00300 | 3.358 | 0.991 | find | A | It has no chips or cracks and looks as though it fell to earth yesterday. | 0.655 |
| MT-HYM-033 | c1mt33 | MET01081 | 2.491 | 1.043 | find | A/B | - | 0.794 |
| MT-HYM-035 | c1mt35 | Chervony Kut | 1.872 | 1.062 | fall | | | 0.935 |
| RK-CMP-116-A | c1rk116a | Millbillillie | 1.478 | 0.993 | fall | | | 1.022 |
| RK-CMP-116-F2 | c1rk116f2 | Millbillillie | 1.338 | 0.999 | fall | | | 1.024 |
| RK-CMP-116-G | c1rk116g | Millbillillie | 1.453 | 1.039 | fall | | | 1.017 |
| RK-CMP-116-L | c1rk116l | Millbillillie | 1.687 | 1.002 | fall | | | 0.990 |
| MB-TXH-070-2 | c2mb70 | Juvinas | 2.088 | 1.038 | fall | | | 0.919 |
| MB-TXH-069-A | c3mb69 | Millbillillie | 1.739 | 1.034 | fall | | | 0.940 |
| MB-TXH-070-A | camb70 | Juvinas | 1.759 | 1.057 | fall | | | 0.921 |
| MB-TXH-071-A | camb71 | Y-74450 | 1.532 | 1.049 | find | - | - | 0.898 |
| MB-TXH-072-A | camb72 | ALHA78132 | 1.625 | 1.082 | find | A | - | 0.892 |
| MP-TXH-066-A | camp66 | GRO95533 | 1.806 | 1.033 | find | A/B | The other surface is broken and shows minor oxidation. Some brown oxidation is scattered throughout. | 0.917 |
| MP-TXH-072-A | camp72 | EETA79005 | 1.722 | 1.078 | find | A | - | 0.856 |
| MP-TXH-076-A | camp76 | EET90020 | 1.959 | 1.022 | find | A | The specimen is coherent and weathering is minimal | 0.799 |
| MP-TXH-078-A | camp78 | LEW85303 | 1.559 | 1.021 | find | A/B | from LEW85300: One large interior area shows extensive oxidation | 0.881 |
| MP-TXH-079-A | camp79 | LEW87004 | 1.621 | 1.066 | find | A | minor oxidation | 0.866 |
| MP-TXH-084-A | camp84 | Cachari | 1.958 | 1.047 | find | - | - | 0.776 |
| MP-TXH-094-A | camp94 | A-87272 | 2.048 | 1.031 | find | - | - | 0.883 |
| MP-TXH-096-A | camp96 | A-881819 | 1.813 | 1.079 | find | - | - | 0.911 |
| MS-JTW-048-A | cams48 | Millbillillie | 1.636 | 1.024 | fall | | | 0.934 |
| MT-TXH-041-A | camt41 | Y-792510 | 1.867 | 1.034 | find | - | - | 0.904 |
| MT-TXH-042-A | camt42 | Y-792769 | 1.536 | 1.042 | find | - | - | 0.930 |
| MT-TXH-043-A | camt43 | Y-793591 | 1.550 | 1.042 | find | - | - | 0.914 |
| MT-TXH-044-A | camt44 | Y-82082 | 1.513 | 1.012 | find | - | - | 0.792 |
| MB-TXH-069-B | cbmb69 | Millbillillie | 2.213 | 1.049 | fall | | | 0.936 |
| MB-TXH-070-B | cbmb70 | Juvinas | 2.182 | 1.054 | fall | | | 0.895 |
| MB-TXH-071-B | cbmb71 | Y-74450 | 1.997 | 1.062 | find | - | - | 0.856 |
| MB-TXH-072-B | cbmb72 | ALHA78132 | 2.139 | 1.103 | find | A | - | 0.866 |
| MB-TXH-096-B | cbmb96 | Padvarninkai | 1.187 | 0.999 | fall | | | 0.939 |
| MB-TXH-097-B | cbmb97 | Stannern | 1.827 | 1.050 | fall | | | 0.935 |
| MB-TXH-069-C | ccmb69 | Millbillillie | 2.224 | 1.041 | fall | | | 0.932 |
| MB-TXH-070-C | ccmb70 | Juvinas | 2.253 | 1.047 | fall | | | 0.894 |
| MB-TXH-071-C | ccmb71 | Y-74450 | 2.166 | 1.055 | find | - | - | 0.871 |
| MB-TXH-072-C | ccmb72 | ALH-78132 | 2.317 | 1.098 | find | A | - | 0.856 |
| MB-TXH-096-C | ccmb96 | Padvarninkai | 1.723 | 1.048 | fall | | | 0.924 |
| MB-TXH-069-D | cdmb69 | Millbillillie | 2.143 | 1.032 | fall | | | 0.941 |
| MB-TXH-070-D | cdmb70 | Juvinas | 2.156 | 1.036 | fall | | | 0.906 |
| MB-TXH-071-D | cdmb71 | Y-74450 | 2.088 | 1.042 | find | - | - | 0.868 |
| MB-TXH-096-D | cdmb96 | Padvarninkai | 1.947 | 1.041 | fall | | | 0.914 |
| MB-TXH-099-D | cdmb99 | ALH85001 | 1.676 | 1.093 | find | A/B | Areas devoid of fusion crust have weathered to a brownish-gray color. A discontinuous weathering rind, as thick as 4 mm, was exposed when the stone was chipped. | 0.950 |
| MB-TXH-070-E | cemb70 | Juvinas | 2.015 | 1.024 | fall | | | 0.924 |
| MB-TXH-099-W | cwmb99 | ALH85001 | 1.554 | 1.091 | find | A/B | Areas devoid of fusion crust have weathered to a brownish-gray color. A discontinuous weathering rind, as thick as 4 mm, was exposed when the stone was chipped. | 0.936 |
| TB-TJM-118 | bkr1tb118 | Bouvante | 1.682 | 1.040 | find | - | - | 0.960 |
| TB-RPB-153 | bkr1tb153 | Juvinas eucrite | 2.217 | 1.040 | fall | | | 0.877 |
| TB-RPB-007 | c1tb07 | Y-792510 | 1.901 | 1.013 | find | - | - | 0.851 |
| TB-RPB-008 | c1tb08 | Y-75011 | 1.381 | 0.995 | find | - | - | 0.956 |
| TB-RPB-009 | c1tb09 | Y-791186 | 1.561 | 1.005 | find | - | - | 0.779 |

| | | | | | | | | |
|---|---|---|---|---|---|---|---|---|
| TB-RPB-012 | c1tb12 | PCA82501 | 1.353 | 1.002 | find | A | Where there is no fusion crust the specimen is coarse grained, white and dark gray in color, with some yellowish oxidation. No individual clasts are visible. There is a very small amount of oxidation present in the interior of this stone. | 0.976 |
| TB-RPB-015 | c1tb15 | ALHA85001 | 1.754 | 1.028 | find | A/B | Areas devoid of fusion crust have weathered to a brownish-gray color. A discontinuous weathering rind, as thick as 4 mm, was exposed when the stone was chipped. | 0.968 |
| TB-RPB-019 | c1tb19 | LEW87004 | 1.701 | 1.040 | find | A | minor oxidation | 0.890 |
| TB-RPB-020 | c1tb20 | EET90020 | 2.670 | 0.991 | find | A | The specimen is coherent and weathering is minimal | 0.614 |
| TB-RPB-022 | c1tb22 | EET83251 | 1.666 | 1.045 | find | B | pairing group 79004: Several spots of severe oxidation are visible | 0.893 |
| TB-RPB-025 | c1tb25 | EETA790B | 1.734 | 1.040 | - | - | probably typo error in the database | 0.913 |
| TB-RPB-026 | c1tb26 | EETA79005 | 1.806 | 1.060 | find | A | - | 0.886 |
| TB-RPB-027 | c1tb27 | Macibini | 1.705 | 1.040 | fall | | | 0.920 |
| TB-RPB-028 | c1tb28 | Bouvante | 1.605 | 1.016 | find | - | - | 0.986 |
| TB-RPB-029 | c1tb29 | Bouvante | 1.530 | 1.015 | find | - | - | 0.986 |
| TB-RPB-030 | c1tb30 | Macibini | 1.537 | 0.942 | fall | | | 0.854 |
| MR-MJG-085 | cgp023 | Bereba | 1.594 | 1.035 | fall | | | 0.912 |
| MR-MJG-086 | cgp025 | Padvarninkai | 1.935 | 1.087 | fall | | | 0.895 |
| MR-MJG-087 | cgp027 | Sioux County | 1.449 | 1.018 | fall | | | 0.946 |
| MR-MJG-088 | cgp029 | Jonzac | 2.045 | 1.071 | fall | | | 0.890 |
| MR-MJG-089 | cgp031 | Haraiya | 1.632 | 1.050 | fall | | | 0.899 |
| MR-MJG-091 | cgp035 | Juvinas | 1.905 | 1.035 | fall | | | 0.880 |
| MR-MJG-092-C | cgp039 | Stannern | 1.361 | 1.014 | fall | | | 0.939 |
| MR-MJG-092-P | cgp041 | Stannern | 1.484 | 1.027 | fall | | | 0.947 |
| MR-MJG-093 | cgp045 | Nobleborough | 1.702 | 1.060 | fall | | | 0.884 |

| **Diogenites** | **spec ID** | **meteorite name** | **750/917 [nm]** | **965/917 [nm]** | **find/fall** | **weathering grade** | **weathering comment (Meteoritical Bulletin)** | **500/600 [nm]** |
|---|---|---|---|---|---|---|---|---|
| MP-D2M-112 | bkr1mp112 | Ellemeet | 2.328 | 1.164 | fall | | | 0.906 |
| MP-D2M-113 | bkr1mp113 | Ellemeet | 2.271 | 1.207 | fall | | | 0.926 |
| MT-AWB-168-A | bkr1mt168a | MIL07001 | 2.316 | 1.165 | find | A/B | | 0.856 |
| MT-AWB-169-A | bkr1mt169a | GRA98108 | 2.456 | 1.181 | find | B | | 0.886 |
| MT-AWB-168 | c1mt168 | MIL07001 | 2.401 | 1.153 | find | A/B | | 0.782 |
| MT-AWB-169 | c1mt169 | GRA98108 | 2.751 | 1.172 | find | B | | 0.846 |
| TB-RPB-018 | c1tb18 | LAP91900 | 3.231 | 1.159 | find | A/B | | 0.826 |
| MB-TXH-067-A | camb67 | EETA79002 | 1.902 | 1.183 | find | B | | 0.935 |
| MB-TXH-073-A | camb73 | Y-74013 | 1.655 | 1.124 | find | - | | 0.842 |
| MB-TXH-074-A | camb74 | Y-75032 | 1.924 | 1.125 | find | - | | 0.896 |
| MB-TXH-095-A | camb95 | Johnstown | 1.740 | 1.151 | fall | | | 0.891 |
| MP-TXH-068-A | camp68 | GRO95555 | 2.388 | 1.188 | find | A/B | | 0.803 |
| MP-TXH-071-A | camp71 | ALHA77256 | 2.222 | 1.188 | find | A/B | | 0.717 |
| MP-TXH-077-A | camp77 | LAP91900 | 2.456 | 1.199 | find | A/B | - | 0.887 |
| MP-TXH-081-A | camp81 | Aioun el Atrouss | 2.474 | 1.168 | fall | | The surface area not covered with fusion crust is weathered and ranges from yellowish-brown to grayish-green. The various colors are limited to discrete areas. Several areas of iron oxide staining are present on the surface. | 0.902 |
| MP-TXH-088-A | camp88 | Tatahouine | 2.404 | 1.217 | fall | | Several areas have been heavily oxidized giving these parts a red-brown color. Many fractures penetrate this meteorite. Chipping this sample revealed an extensive orange-brown weathering rind as wide as 1 cm | 0.911 |
| MP-TXH-095-A | camp95 | A-881526 | 2.574 | 1.217 | find | - | Several areas have been heavily oxidized giving these parts a red-brown color. Many fractures penetrate this meteorite. Chipping this sample revealed an extensive orange-brown weathering rind as wide as 1 cm | 0.751 |
| MS-JTW-049-A | cams49 | Johnstown | 2.637 | 1.198 | fall | | Several areas have been heavily oxidized giving these parts a red-brown color. Many fractures penetrate this meteorite. Chipping this sample revealed an extensive orange-brown weathering rind as wide as 1 cm | 0.842 |
| MB-TXH-067-B | cbmb67 | EETA79002 | 2.582 | 1.232 | find | B | Several areas have been heavily oxidized giving these parts a red-brown color. Many fractures penetrate this meteorite. Chipping this sample revealed an extensive orange-brown weathering rind as wide as 1 cm | 0.921 |
| MB-TXH-073-B | cbmb73 | Y-74013 | 2.302 | 1.179 | find | - | Several areas have been heavily oxidized giving these parts a red-brown color. Many fractures penetrate this meteorite. Chipping this sample revealed an extensive orange-brown weathering rind as wide as 1 cm | 0.830 |
| MB-TXH-074-B | cbmb74 | Y-75032 | 2.666 | 1.161 | find | - | Several areas have been heavily oxidized giving these parts a red-brown color. Many fractures penetrate this meteorite. Chipping this sample revealed an extensive orange-brown weathering rind as wide as 1 cm | 0.861 |
| MB-TXH-095-B | cbmb95 | Johnstown | 2.467 | 1.196 | fall | | Several areas have been heavily oxidized giving these parts a red-brown color. Many fractures penetrate this meteorite. Chipping this sample revealed an extensive orange-brown weathering rind as wide as 1 cm | 0.856 |

| | | | | | | | | |
|---|---|---|---|---|---|---|---|---|
| MB-TXH-067-C | ccmb67 | EETA79002 | 2.540 | 1.212 | find | B | There are some areas that appear to be rust stained or have rootbeer (pyroxene?) colored minerals. There are several rusty areas where minerals are stained. Maroon colored minerals and small black specks are distributed throughout the rock. | 0.907 |
| MB-TXH-067-D | cdmb67 | EETA79002 | 2.388 | 1.179 | find | B | There are some areas that appear to be rust stained or have rootbeer (pyroxene?) colored minerals. There are several rusty areas where minerals are stained. Maroon colored minerals and small black specks are distributed throughout the rock. | 0.911 |
| MB-TXH-067-E | cemb67 | EETA79002 | 2.149 | 1.143 | find | B | There are several penetrating fractures | 0.934 |
| MB-TXH-067-F | cfmb67 | EETA79002 | 2.051 | 1.138 | find | B | - | 0.928 |
| MB-TXH-067 | cgmb67 | EETA79002 | 1.555 | 1.134 | find | B | - | 0.923 |
| MR-MJG-098-C | cgp057 | Johnstown | 2.510 | 1.135 | fall | | - | 0.791 |
| MR-MJG-098-P | cgp059 | Johnstown | 2.757 | 1.129 | fall | | - | 0.779 |
| MR-MJG-098-P | cgp061 | Johnstown | 3.100 | 1.129 | fall | | - | 0.754 |
| MR-MJG-100-C | cgp065 | Tatahouine | 2.244 | 1.094 | fall | | - | 0.745 |
| MR-MJG-100-P | cgp067 | Tatahouine | 3.184 | 1.230 | fall | | - | 0.818 |
| MR-MJG-101 | cgp069 | Shalka | 2.290 | 1.193 | fall | | - | 0.915 |

| **Howardites** | **spec ID** | **meteorite name** | **750/917 [nm]** | **965/917 [nm]** | **find/fall** | **weathering grade** | **weathering comment (Meteoritical Bulletin)** | **500/600 [nm]** |
|---|---|---|---|---|---|---|---|---|
| MP-TXH-125 | bkr1mp125 | GRO95574 | 1.826 | 1.088 | find | A | | 0.924 |
| MP-TXH-126 | bkr1mp126 | QUE97001 | 2.155 | 1.153 | find | A | | 0.884 |
| TB-TJM-127 | bkr1tb127 | Bialystok | 2.486 | 1.055 | fall | | | 0.752 |
| MP-TXH-053 | c1mp53 | Kapoeta | 2.091 | 1.076 | fall | | | 0.897 |
| SN-CMP-011 | c1sn11 | Kapoeta | 2.204 | 1.119 | fall | | | 0.890 |
| SN-CMP-012 | c1sn12 | Kapoeta | 1.929 | 1.089 | fall | | | 0.918 |
| MB-TXH-068-A | camb68 | EET87503 | 1.556 | 1.070 | find | A | | 0.939 |
| MP-TXH-053-A | camp53 | Kapoeta | 1.586 | 1.077 | fall | | | 0.928 |
| MP-TXH-067-A | camp67 | GRO95535 | 1.647 | 1.081 | find | A/B | | 0.906 |
| MP-TXH-069-A | camp69 | QUE94200 | 1.818 | 1.137 | find | A/B | | 0.904 |
| MP-TXH-070-A | camp70 | Petersburg | 1.669 | 1.059 | fall | | | 0.605 |
| MP-TXH-073-A | camp73 | EET83376 | 1.704 | 1.073 | find | A/B | | 0.871 |
| MP-TXH-074-A | camp74 | EET87513 | 1.496 | 1.060 | find | A/B | | 0.886 |
| MP-TXH-097-A | camp97 | Y-7308 | 2.200 | 1.128 | find | - | | 0.903 |
| MP-TXH-098-A | camp98 | Y-790727 | 1.794 | 1.094 | find | - | | 0.772 |
| MP-TXH-099-A | camp99 | Y-791573 | 1.773 | 1.107 | find | - | | 0.749 |
| MB-TXH-068-B | cbmb68 | EET87503 | 1.742 | 1.080 | find | A | | 0.933 |
| MB-TXH-068-C | ccmb68 | EET87503 | 1.894 | 1.070 | find | A | | 0.940 |
| MB-TXH-068-D | cdmb68 | EET87503 | 1.850 | 1.055 | find | A | | 0.951 |
| MB-TXH-068-E | cemb68 | EET87503 | 1.699 | 1.042 | find | A | | 0.960 |
| MB-TXH-068-F | cfmb68 | EET87503 | 1.632 | 1.032 | find | A | | 0.960 |
| MB-TXH-068-G | cgmb68 | EET87503 | 1.423 | 1.063 | find | A | | 0.914 |
| MR-MJG-094 | cgp047 | Pavlovka | 1.967 | 1.117 | fall | | | 0.911 |
| MR-MJG-095 | cgp049 | Frankfort | 2.534 | 1.159 | fall | | | 0.868 |
| MR-MJG-096 | cgp051 | Le Teilleul | 1.970 | 1.123 | fall | | | 0.905 |
| MR-MJG-097 | cgp053 | Petersburg | 1.753 | 1.047 | fall | | | 0.898 |
| MB-TXH-068-H | chmb68 | EET87503 | 1.642 | 1.070 | find | A | | 0.922 |

| **Carbonaceous chon** | **spec ID** | **meteorite name** | **750/917 [nm]** | **965/917 [nm]** | **find/fall** | **weathering grade** | **weathering comment (Meteoritical Bulletin)** | **500/600 [nm]** |
|---|---|---|---|---|---|---|---|---|
| MA-ATB-062 | bkr1ma062 | Mighei | 0.936 | 1.013 | fall | | | 0.901 |
| MA-ATB-063 | bkr1ma063 | Mighei | 0.932 | 1.014 | fall | | | 0.901 |
| MA-ATB-064 | bkr1ma064 | Mighei | 0.945 | 1.010 | fall | | | 0.919 |
| MA-ATB-065 | bkr1ma065 | Mighei | 0.944 | 1.012 | fall | | | 0.907 |
| MA-ATB-066 | bkr1ma066 | Mighei | 0.950 | 1.014 | fall | | | 0.929 |
| MA-ATB-072 | bkr1ma072 | Mighei | 0.947 | 1.017 | fall | | | 0.954 |
| MA-LXM-073 | bkr1ma073 | Kaidun | 0.984 | 1.008 | fall | | | 0.924 |
| MA-LXM-074 | bkr1ma074 | Kaidun | 1.007 | 0.998 | fall | | | 0.958 |
| MA-LXM-075 | bkr1ma075 | Kaidun | 1.054 | 1.000 | fall | | | 0.955 |
| MA-LXM-076 | bkr1ma076 | Kaidun | 1.041 | 0.990 | fall | | | 0.974 |
| MA-LXM-077 | BKR1MA077 | Dhofar 735 | 1.015 | 1.000 | find | W1 | - | 0.957 |
| MA-LXM-078 | BKR1MA078 | Dhofar 225 | 1.013 | 0.997 | find | - | - | 0.988 |
| MP-TXH-022-L0 | bkr1mp022l0 | MAC88100,30 | 1.012 | 1.000 | find | Be | A thin layer of evaporite deposit appears along the fusion crust-interior boundary. | 0.918 |
| MP-TXH-022-L1 | bkr1mp022l1 | MAC88100,30 | 1.033 | 0.993 | find | Be | A thin layer of evaporite deposit appears along the fusion crust-interior boundary. | 0.930 |
| MP-KHO-131 | bkr1mp131 | El-Quss Abu Said | 1.037 | 0.989 | find | W0 | - | 0.954 |
| MP-KHO-131-A | bkr1mp131a | El-Quss Abu Said | 0.999 | 0.998 | find | W1 | - | 0.921 |
| MT-MEZ-104 | BKR1MT104 | Allende | 1.011 | 0.987 | fall | | | 0.937 |
| PH-D2M-032 | bkr1ph032 | MET00639 | 0.988 | 1.001 | find | A | - | 0.993 |
| PH-D2M-033 | bkr1ph033 | WIS91600 | 0.954 | 1.014 | find | A/Be | rusty fusion crust, A minor amount of evaporite deposit is present on the exterior and interior surfaces | 0.950 |
| PH-D2M-034 | BKR1PH034 | ALH82101 | 1.033 | 0.990 | find | A | - | 0.816 |
| PH-D2M-043 | bkr1ph043 | MET01070 | 0.992 | 1.001 | find | Be | - | 1.005 |
| PH-D2M-044 | bkr1ph044 | PCA02012 | 1.005 | 1.000 | find | B | - | 0.712 |
| PH-D2M-048 | BKR1PH048 | PCA91082 | 0.999 | 1.017 | find | Be | - | 0.630 |
| PH-D2M-051 | bkr1ph051 | QUE97077 | 0.936 | 1.015 | find | A/B | - | 0.932 |
| PH-D2M-052 | bkr1ph052 | QUE99038 | 1.010 | 0.987 | find | A/B | - | 0.905 |
| PH-D2M-054 | BKR1PH054 | QUE99177 | 0.990 | 1.013 | find | BE | - | 0.619 |
| PH-D2M-057 | BKR1PH057 | FRO99040 | 1.027 | 0.989 | find | W0 | - | 0.878 |
| MB-CMP-018 | c1mb18 | B-7904,108 | 1.009 | 0.999 | find | - | - | 0.938 |
| MB-CMP-020-1 | c1mb20 | Y-86720,77 | 1.044 | 1.001 | find | - | - | 0.944 |
| MB-TXH-052 | c1mb52 | ALH84029 | 0.938 | 1.022 | find | Ae | Many fractures are present as well as some white salt deposit. | 0.918 |
| MB-TXH-053 | c1mb53 | Bells #1226B(1) | 0.976 | 1.006 | fall | | | 0.790 |
| MB-TXH-057 | C1MB57 | Orgueil | 0.936 | 1.011 | fall | | | 0.725 |
| MB-TXH-060 | C1MB60 | Ivuna | 0.958 | 1.003 | fall | | | 0.798 |
| MB-TXH-061 | c1mb61 | Cold Bokkeveld | 1.067 | 1.021 | fall | | | 0.989 |
| MB-TXH-081-1 | C1MB81 | ALH85002 | 1.083 | 0.976 | find | A | - | 0.967 |

| | | | | | | | | |
|---|---|---|---|---|---|---|---|---|
| MB-TXH-082 | C1MB82 | EET87747 | 0.997 | 1.017 | find | B/C | - | 0.607 |
| MC-RPB-001 | c1mc01 | ALH83100,196 | 0.996 | 1.010 | find | Be | Salt deposit has formed in some areas | 0.925 |
| MC-RPB-002 | c1mc02 | LEW90500,45 | 0.987 | 1.004 | find | B | weathered in some areas and frothy in others | 0.963 |
| MC-RPB-003 | C1MC03 | EET92002 | 1.120 | 0.954 | find | A/Be | - | 0.996 |
| MC-RPB-004 | C1MC04 | ALH83108 | 1.098 | 0.974 | find | A | - | 0.859 |
| MP-TXH-014 | c1mp14 | ALH84033,21 | 1.020 | 1.005 | find | Ae | Some salt deposit has formed | 0.791 |
| MP-TXH-015 | c1mp15 | ALH84044,16 | 0.955 | 1.020 | find | Ae | some salt deposit present. | 0.931 |
| MP-TXH-016 | c1mp16 | LEW87148,15 | 0.972 | 1.007 | find | Ae | Along the edges there are evaporites | 0.959 |
| MP-TXH-017 | c1mp17 | GRO85202,16 | 0.964 | 1.013 | find | A/Be | Minute evaporite deposit lines some of the interior fractures | 0.936 |
| MP-TXH-019 | c1mp19 | ALHA77306,45 | 0.966 | 1.018 | find | A | The specimen is remarkably free of limonite stain, When the specimen was cleaved into two halves, a greenish-gray weathering rind was observed to have penetrated into the meteorite to a depth of ~l mm. | 0.918 |
| MP-TXH-020 | c1mp20 | LEW87022,26 | 0.950 | 1.007 | find | B | There are spots of oxidation and small deposits of salt in the interior of most of these pebbles and a a 1 mm weathering rind (from lew87001) | 0.941 |
| MP-TXH-021 | c1mp21 | EET87522,29 | 0.966 | 1.010 | find | Be | A 1 cm thick weathering rind was exposed along one surface. A minute amount of salt deposit is present in the interior. | 0.874 |
| MP-TXH-022 | c1mp22 | MAC88100,30 | 1.013 | 1.000 | find | Be | A thin layer of evaporite deposit appears along the fusion crust-interior boundary | 0.917 |
| MP-TXH-023 | c1mp23 | ALH85013,32 | 0.973 | 1.005 | find | A | - | 0.956 |
| MP-TXH-024 | c1mp24 | LEW85311,36 | 0.937 | 1.006 | find | Be | - | 0.912 |
| MP-TXH-026 | c1mp26 | LON94101,19 | 0.973 | 1.015 | find | Be | There are also some rusted clasts and small (<1 mm) angular white flecks. | 0.938 |
| MP-TXH-038 | C1MP38 | Y-793495 | 1.025 | 1.011 | find | - | - | 0.694 |
| MB-TXH-062-A | c2mb62 | Nogoya | 0.965 | 1.010 | fall | | | 0.948 |
| MB-TXH-063-A | C2MB63 | Allende | 1.004 | 1.000 | fall | | | 0.940 |
| MB-TXH-064-A | c2mb64 | Murchison | 0.944 | 1.016 | fall | | | 0.919 |
| MB-TXH-062-B | c3mb62 | Nogoya | 0.955 | 1.010 | fall | | | 0.938 |
| MB-TXH-063-B | C3MB63 | Allende | 0.998 | 0.997 | fall | | | 0.947 |
| MB-TXH-062-C | c4mb62 | Nogoya | 1.010 | 1.004 | fall | | | 0.977 |
| MB-TXH-064-C | c4mb64 | Murchison | 0.996 | 1.005 | fall | | | 0.942 |
| MB-TXH-081-A | CAMB81 | ALH85002 | 1.074 | 0.975 | find | A | - | 0.949 |
| MH-FPF-052-A | camh52 | Murchison | 1.027 | 0.998 | fall | | | 0.952 |
| MH-FPF-057-A | CAMH57 | Allende | 1.008 | 0.995 | fall | | | 0.929 |
| MB-TXH-064-HB | cbmb64 | Murchison | 1.027 | 1.001 | fall | | | 0.892 |
| MB-TXH-081-B | CBMB81 | ALH85002 | 1.082 | 0.971 | find | A | - | 0.978 |
| MB-TXH-081-C | CCMB81 | ALH85002 | 1.143 | 0.959 | find | A | - | 1.000 |
| MB-TXH-081-D | CDMB81 | ALH85002 | 1.123 | 0.967 | find | A | - | 0.993 |
| MS-CMP-002-G | CGMS02 | Murchison Separates | 0.948 | 1.011 | fall | | | 0.892 |
| MR-MJG-119-P1 | CGP128 | Grosnaja | 1.028 | 1.004 | fall | | | 0.883 |
| MR-MJG-016 | COLM16 | Allende | 1.086 | 0.949 | fall | | | 0.848 |

**Olivine**

| | | | | |
|---|---|---|---|---|
| DD-MDD-001 | BKR1DD001 | Chassigny olivine | 2.0103 | 0.8484 |
| DD-MDD-037 | BKR1DD037 | Fo 90 | 1.1649 | 0.9759 |
| DD-MDD-038 | BKR1DD038 | Fo 80 | 1.3298 | 0.9259 |
| DD-MDD-039 | BKR1DD039 | Fo 70 | 1.4476 | 0.9005 |
| DD-MDD-040 | BKR1DD040 | Fo 60 | 1.1601 | 0.9377 |
| DD-MDD-041 | BKR1DD041 | Fo 50 | 1.4943 | 0.9036 |
| DD-MDD-042 | BKR1DD042 | Fo 40 | 1.5682 | 0.8952 |
| DD-MDD-043 | BKR1DD043 | Fo 30 | 1.0622 | 0.9432 |
| DD-MDD-044 | BKR1DD044 | Fo 20 | 1.2364 | 0.9258 |
| DD-MDD-045 | BKR1DD045 | Fo 10 | 1.1742 | 0.9334 |
| DD-MDD-047 | BKR1DD047 | San Carlos olivine | 1.3009 | 0.8994 |
| LR-CMP-225 | C1LR225 | 72415 olivine | 1.3829 | 0.8776 |
| LR-CMP-227 | C1LR227 | 76535 olivine | 1.5223 | 0.8816 |
| LS-CMP-006 | C1LS06 | 76535 | 3.3535 | 0.7749 |
| MT-TJM-027 | C1MT27 | Thiel Mountains palla | 1.2442 | 0.9069 |
| PO-CMP-014 | C1PO14 | Olivine | 2.0713 | 0.8583 |
| PO-RGB-041 | C1PO41 | Altered Peridot | 0.8342 | 0.9785 |
| PO-RGB-042 | C1PO42 | Altered Peridot | 0.9263 | 0.9615 |
| PO-RGB-043 | C1PO43 | Altered Peridot | 0.7874 | 1.0215 |

**Impact melt**

| | | | | |
|---|---|---|---|---|
| MT-AWB-238 | bkr1mt238 | PCA 02009 | 1.7925 | 1.1203 |
| MT-AWB-239 | bkr1mt239 | PCA 02013 | 1.4954 | 1.0952 |
| MP-DTB-029-A | camp29 | Walters Clast & Melt | 1.3518 | 1.0082 |
| MB-TXH-096-B | cbmb96 | Padvarninkai impact | 1.1875 | 0.9993 |
| MP-DTB-029-C | ccmp29 | Walters Clast & Melt | 1.4918 | 0.9992 |
| MP-DTB-028-M | cmmp28 | Orvinio Clast & Melt | 1.1290 | 0.9963 |
| MP-DTB-029-M | cmmp29 | Walters Clast & Melt | 1.2614 | 0.9869 |
| TB-TJM-117 | bkr1tb117 | Calci## (found in mus | 1.1313 | 0.9636 |
| TB-RPB-030 | c1tb30 | Macibini Cl.3 Melt | 1.5370 | 0.9420 |

**Figure 12**

**U Winnipeg data (provided by Dr. E. Cloutis)**

| Sample name | Grain size | 750/917 [nm] | 965/917 [nm] | fall/find | WG |
|---|---|---|---|---|---|
| JAH626 | <45 um | 1.465 | 0.901 | find | low |
| JAH626 | 45-90 um | 1.624 | 0.904 | | |
| JAH626 | 90-250 um | 1.628 | 0.916 | | |
| JAH626 | 250-500 um | 1.447 | 0.930 | | |
| Millbillillie | <45 um | 1.785 | 1.003 | fall | |
| Millbillillie | 45-90 um | 2.175 | 0.992 | | |
| Millbillillie | 90-250 um | 2.119 | 0.984 | | |
| Millbillillie | 250-500 um | 2.038 | 0.984 | | |
| NWA1836 | <45 um | 2.389 | 0.966 | find | W0 |
| NWA1836 | 45-90 um | 2.390 | 0.959 | | |
| NWA1836 | 90-250 um | 2.442 | 0.961 | | |
| NWA1836 | 250-500 um | 2.590 | 0.956 | | |
| NWA1942 | <45 um | 1.736 | 1.047 | find | - |
| NWA1942 | 45-90 um | 2.333 | 1.047 | | |
| NWA1942 | 90-250 um | 2.090 | 1.031 | | |
| NWA1942 | 250-500 um | 1.893 | 1.016 | | |
| NWA1943 | <45 um | 1.602 | 1.019 | find | - |
| NWA1943 | 45-90 um | 1.807 | 1.021 | | |
| NWA1943 | 90-250 um | 1.874 | 1.007 | | |
| NWA1943 | 250-500 um | 1.713 | 1.003 | | |
| NWA2968 | <45 um | 1.043 | 0.981 | find | - |
| NWA2968 | 45-90 um | 1.104 | 0.963 | | |
| NWA2968 | 90-250 um | 1.131 | 0.958 | | |
| NWA2968 | 250-500 um | 1.102 | 0.972 | | |
| NWA5748 | <45 um | 1.596 | 1.026 | find | - |
| NWA5748 | 45-90 um | 2.114 | 1.020 | | |
| NWA5748 | 90-250 um | 1.896 | 1.011 | | |
| NWA5748 | 250-500 um | 1.702 | 1.006 | | |
| NWA5751 | <45 um | 2.054 | 1.075 | find | W1 |
| NWA5751 | 45-90 um | 2.768 | 1.076 | | |
| NWA5751 | 90-250 um | 2.520 | 1.053 | | |
| NWA5751 | 250-500 um | 2.133 | 1.035 | | |
| NWA6013 | <45 um | 1.682 | 1.058 | find | W1 |
| NWA6013 | 45-90 um | 2.733 | 1.068 | | |
| NWA6013 | 90-250 um | 2.588 | 1.049 | | |
| NWA6013 | 250-500 um | 1.715 | 1.003 | | |
| NWA6477 | <45 um | 1.505 | 1.011 | find | low |
| NWA6477 | 45-90 um | 1.791 | 1.006 | | |
| NWA6477 | 90-250 um | 1.734 | 0.997 | | |
| NWA6477 | 250-500 um | 1.583 | 0.995 | | |
| PRA04401 | <45 um | 1.173 | 1.009 | find | CE |
| PRA04401 | 45-90 um | 1.383 | 1.005 | | |
| PRA04401 | 90-250 um | 1.271 | 0.999 | | |
| Talampaya | <45 um | 1.831 | 1.038 | fall | |
| Talampaya | 45-90 um | 2.396 | 1.032 | | |
| Talampaya | 90-250 um | 2.651 | 1.024 | | |
| Talampaya | 250-500 um | 2.454 | 1.018 | | |
| Tatahouine | <45 um | 2.490 | 1.125 | fall | |
| Tatahouine | 45-90 um | 4.423 | 1.178 | | |
| Tatahouine | 90-250 um | 4.492 | 1.123 | | |
| Tatahouine | 250-500 um | 3.673 | 1.071 | | |

**RELAB data**

| Sample name | Grain size | | | | |
|---|---|---|---|---|---|
| ALHA76005 | < 25 µm | 1.518 | 1.058 | find | A |
| ALHA76005 | 25-45 µm | 1.784 | 1.063 | | |
| ALHA76005 | 45-75 µm | 1.983 | 1.061 | | |
| ALHA76005 | 75-125 µm | 1.872 | 1.052 | | |
| ALHA76005 | 125-250 µm | 1.775 | 1.037 | | |
| ALHA76005 | 250-500 µm | 1.645 | 1.034 | | |
| EETA79002 | < 25 µm | 1.902 | 1.183 | find | B |
| EETA79002 | 25-45 µm | 2.582 | 1.232 | | |
| EETA79002 | 45-75 µm | 2.540 | 1.212 | | |
| EETA79002 | 75-125 µm | 2.388 | 1.179 | | |
| EETA79002 | 125-250 µm | 2.149 | 1.143 | | |
| EETA79002 | 250-500 µm | 2.051 | 1.138 | | |
| EET87503 | < 25 µm | 1.556 | 1.070 | find | A |
| EET87503 | 25-45 µm | 1.742 | 1.080 | | |
| EET87503 | 45-75 µm | 1.894 | 1.070 | | |
| EET87503 | 75-125 µm | 1.850 | 1.055 | | |
| EET87503 | 125-250 µm | 1.699 | 1.042 | | |
| EET87503 | 250-500 µm | 1.632 | 1.032 | | |

*At the time of writing this work, information on collected meteorites by the National Institute of Polar Research in Japan (e.g., Yamato-named meteorites and others) were not accessible (database under construction).

## 11.2 Supplementary Figures S2-S6 from Michalik et al., 2021

**S2**

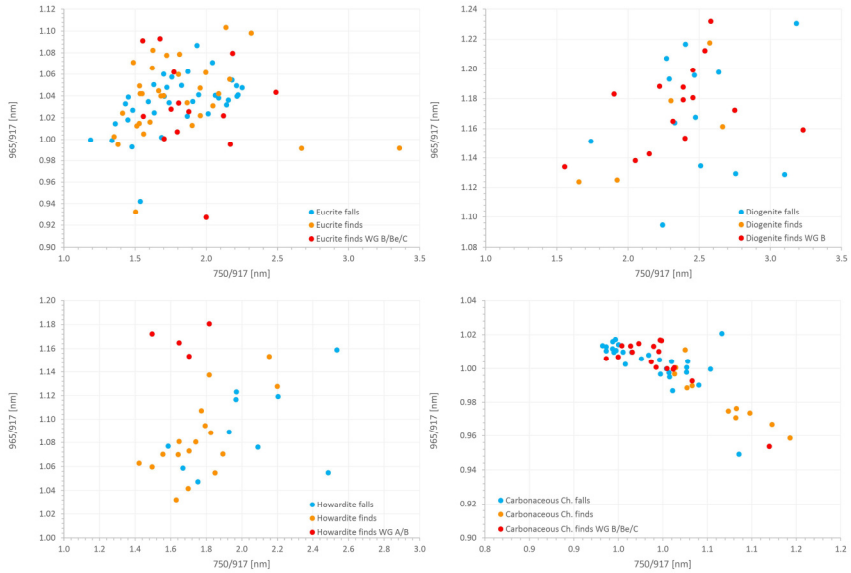


Fig. S2.1: 750/917 [nm] vs. 965/917 [nm] for each meteorite type (i.e., HED and carbonaceous chondrites) separated into falls (blue circles), finds (yellow circles), and the most altered finds identified (red circles). No meteorite group shows a definite trend that separates falls from finds.

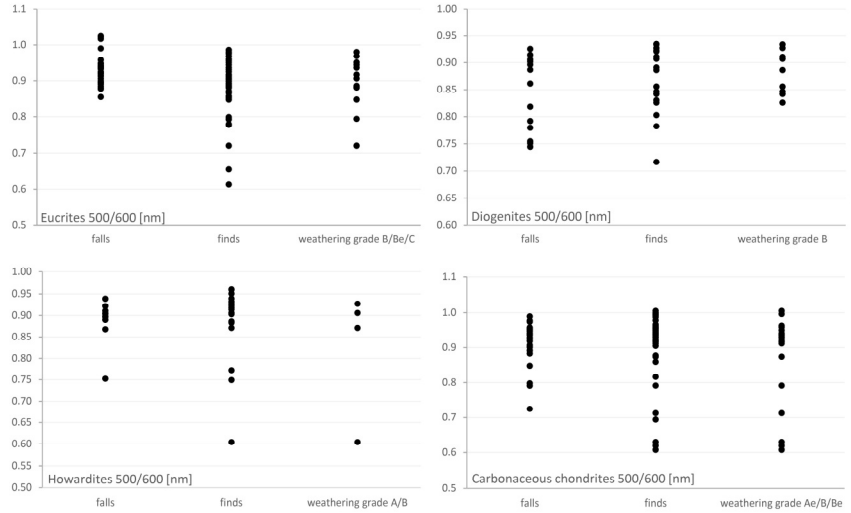


Fig. S2.2: 500/600 [nm] (after Salisbury & Hunt, 1974) for each meteorite type (i.e., HED and carbonaceous chondrites) separated into falls, finds, and the most altered finds identified. Values closer to 1 indicate less weathering. Salisbury and Hunt (1974) apply this method mostly to different chondrite groups and state that unweathered chondrites typically plot between 0.94 and 0.98. We show the HED data for completion as well but their data might scatter more due to their different compostition. The large majority of carbonaceous chondrites (lower left panel) plot well in this range and we note that Salisbury and Hunt (1974) did not observe a change for the 1 µm mafic absorption.

**S3**

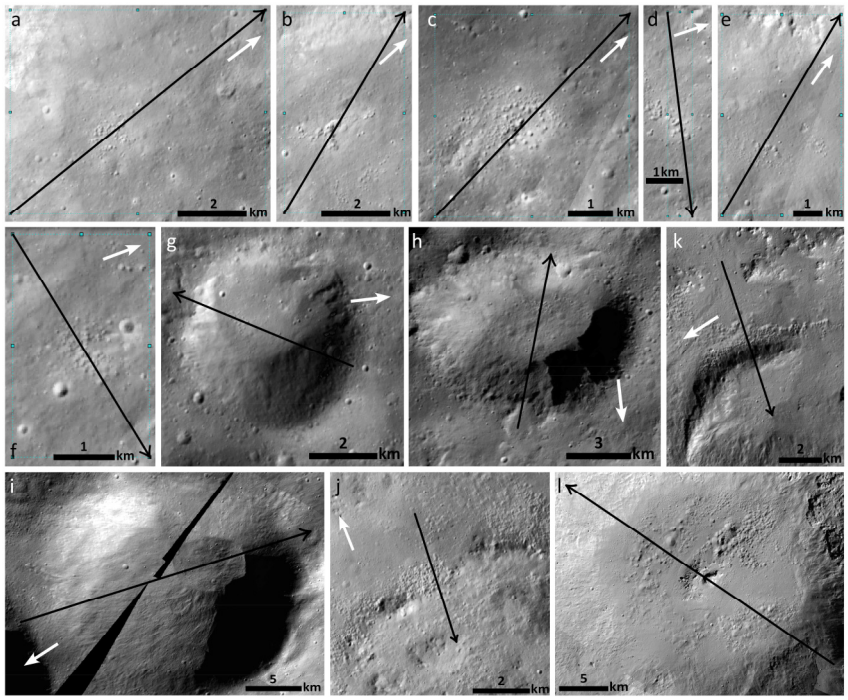


Fig. S3: Corresponding clear filter LAMO profile images with black arrows denoting the direction of the profiles from left to right in Figure 9. White arrows point toward the primary cavity of Marcia.

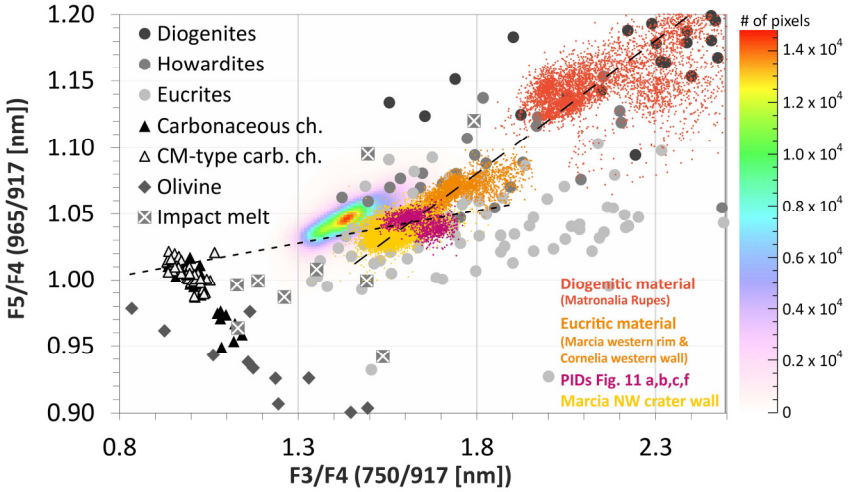


Fig. S4: Density plot of global Vestan FC data (colored data cloud) for 750/917 [nm] vs. 965/917 [nm], showing that in comparison with Figure 13, the majority of Vestan data overlap with HED data with a bulge toward carbonaceous chondrites. PIDs plot off of this trend. Figure S4 also shows that 'pure' HED lithologies identified at well-preserved outcrops (at the Matronalia Rupes scarp, Cornelia crater wall and Marcia rim) deviate from Vesta average values, yet we observe that the elongated Vesta data cloud plots roughly parallel to the HED trend (long dashes) with a small bulge towards the carbonaceous chondrites. This suggests that despite contamination by exogenous impactors, the general HED trend regarding pyroxene mineralogy on Vesta remained intact. PID pyroxene band strengths clearly deviate from the majority of Vestan pyroxene band strengths whose average values are consistent with a surficial contamination by exogenic carbonaceous chondrite material (see also Reddy et al., 2012a and 2012b) and/or space weathering processes (Pieters et al., 2012). We note that low occurrences of data points (roughly <100) are not visible in this plot of Vestan data (colored data cloud). If displayed, Vestan data points scatter throughout the whole displayed area.

**S5**

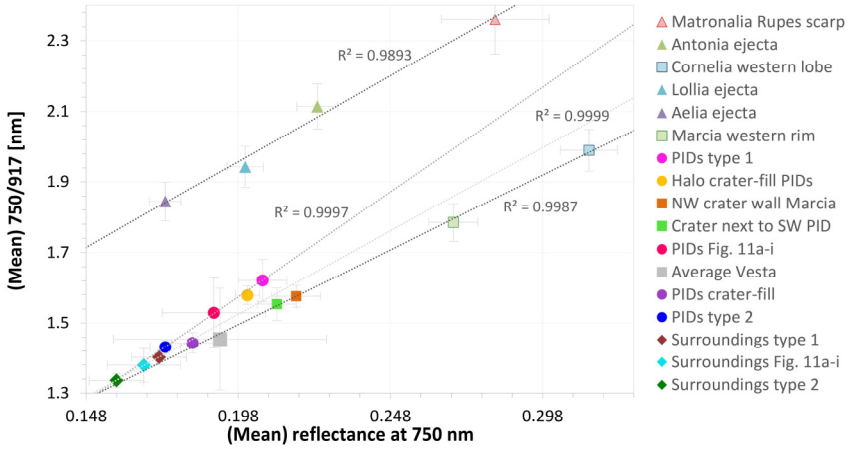


Fig. S5: Mean 750/917 [nm] vs. mean reflectance at 750 nm of regions of interest including diogenitic sites and two more eucritic sites (i.e., Marcia crater rim and Cornelia western lobe). In addition to the Matronalia Rupes scarp, craters Antonia, Lollia and Aelia show spectral characteristics consistent with a diogenitic lithology (e.g., Zambon et al., 2015; Combe et al., 2015; Stephan et al., 2015; Palomba et al., 2014; Zambon et al., 2014; respectively). Diogenitic and Marcia-related (i.e., eucritic) regions of interest plot on roughly parallel running regression lines. The regression line for eucritic regions of interest here includes only the Marcia rim (Fig. 10), Cornelia western lobe (Fig. 10), Marcia's NW crater wall and the crater next to the SW PID (Fig. 10). The diogenitic and eucritic regression lines show flatter slopes than the regression line presented in Fig. 15. Here we also included a regression line for the surroundings of PIDs (light grey) which does not plot parallel to the eucritic regions of interest. This could have several reasons: 1) The data points are too close to each other and might therefore not be representative of a 'real' trend, 2) the surroundings have also undergone some sort of devolatilization process on a lower level. Yet this effect would then be expected in other ejecta blankets as well. In summary, the spectral parameters 750/917 [nm] and reflectance at 750 nm are, in combination, indicative of PIDs, and 'typical' Vestan materials like diogenitic and eucritic lithologies show parallel trends different to the trend of PIDs.

$$\begin{aligned}\text{CM2 vol.\%} &= 31531 * \alpha^4 - 34378 * \alpha^3 + 13655 * \alpha^2 \\ &\quad - 2469.3 * \alpha + 192.48, \quad \alpha \\ &= 0.75\ \mu\text{m reflectance} \end{aligned} \tag{1}$$

$$\begin{aligned}\text{CM2 vol.\%} &= -180.88 * \beta^3 + 924.72 * \beta^2 - 1604.5 * \beta \\ &\quad + 946.35, \quad \beta \\ &= R(0.75)/R(0.92) \end{aligned} \tag{2}$$

$$\begin{aligned}\text{CM2 vol.\%} &= -178.32 * \gamma^3 + 905.99 * \gamma^2 - 1563.5 * \gamma \\ &\quad + 918.23, \quad \gamma \\ &= R(0.75)/R(0.95) \end{aligned} \tag{3}$$

Fig. S6.1: The three equations to calculate CM2 content, image taken from Reddy et al., 2012 with equation (1) and (2) were derived by Le Corre et al., 2011.

Table S6.2: Values for the given equations for the regions of interest of this study.

| | Equation (1) | | Equation (2) | | Equation (3) | |
|---|---|---|---|---|---|---|
| **Region of interest** | **750 nm** | **vol% CM2** | **750/917 [nm]** | **vol% CM2** | **750/965 [nm]** | **vol% CM2** |
| E1 | 0.185 | 22.3 | 1.443 | 13.1 | 1.391 | 16.5 |
| E2a | 0.142 | 31.6 | 1.291 | 27 | 1.251 | 31.1 |
| E2b | 0.161 | 26.6 | 1.346 | 20.9 | 1.306 | 24.4 |
| | | | | | | |
| all PIDs | 0.19 | 21.6 | 1.529 | 8.4 | 1.472 | 11.1 |
| all surroundings | 0.167 | 25.3 | 1.379 | 17.9 | 1.336 | 21.3 |
| Type 1 PIDs | 0.206 | 19.5 | 1.621 | 4.9 | 1.556 | 7.2 |
| Type 1 surroundings | 0.172 | 24.4 | 1.402 | 16 | 1.354 | 19.6 |
| Type 2 PIDs | 0.174 | 24 | 1.431 | 13.9 | 1.383 | 17.1 |
| Type 2 surroudings | 0.158 | 27.3 | 1.336 | 21.9 | 1.294 | 25.7 |
| Halo crater-fill | 0.201 | 20.1 | 1.579 | 6.3 | 1.525 | 8.5 |
| crater-fill | 0.183 | 22.6 | 1.443 | 13.1 | 1.395 | 16.1 |

## References


Combe, J.-P., McCord, T. B., McFadden, L. A., Ieva, S., Tosi, F., Longobardo, A., Frigeri, A., De Sanctis, M. C., Ammannito, E., Ruesch, O., Palomba, E., Fulchignoni, M., Raymond, C. A., & Russell, C. T. (2015). Composition of the northern regions of Vesta analyzed by the Dawn mission. *259*, 53. doi:10.1016/j.icarus.2015.04.026

Le Corre, L., Reddy, V., Nathues, A., & Cloutis, E. A. (2011). How to characterize terrains on 4 Vesta using Dawn Framing Camera color bands? *, 216*, 376. doi:10.1016/j.icarus.2011.09.014

Palomba, E., Longobardo, A., De Sanctis, M. C., Zambon, F., Tosi, F., Ammannito, E., Capaccioni, F., Frigeri, A., Capria, M. T., Cloutis, E. A., Jaumann, R., Combe, J.-P., Raymond, C. A., & Russell, C. T. (2014). Composition and mineralogy of dark material units on Vesta. *240*, 58. doi:10.1016/j.icarus.2014.04.040

Reddy, V., Le Corre, L., O'Brien, D. P., Nathues, A., Cloutis, E. A., Durda, D. D., Bottke, W. F., Bhatt, M. U., Nesvorny, D., Buczkowski, D., Scully, J. E. C., Palmer, E. M., Sierks, H., Mann, P. J., Becker, K. J., Beck, A. W., Mittlefehldt, D., Li, J.-Y., Gaskell, R., Russell, C. T., Gaffey, M. J., McSween, H. Y., McCord, T. B., Combe, J.-P., & Blewett, D. (2012). Delivery of dark material to Vesta via carbonaceous chondritic impacts. *Icarus, 221*, 544-559. doi:10.1016/j.icarus.2012.08.011

Salisbury, J. W., & Hunt, G. R. (1974). Meteorite spectra and weathering. *79*, 4439. doi:10.1029/JB079i029p04439

Stephan, K., Jaumann, R., De Sanctis, M. C., Ammannito, E., Krohn, K., Otto, K. A., Tosi, F., Combe, J.-P., Roatsch, T., Matz, K.-D., McFadden, L. A., Preusker, F., Raymond, C. A., & Russell, C. T. (2015). The Sextilia-region on Asteroid 4Vesta - Stratigraphy and variegation. *Icarus, 259*, 162-180. doi:10.1016/j.icarus.2015.05.016

Zambon, F., De Sanctis, M. C., Schröder, S., Tosi, F., Longobardo, A., Ammannito, E., Blewett, D. T., Mittlefehldt, D. W., Li, J.-Y., Palomba, E., Capaccioni, F., Frigeri, A., Capria, M. T., Fonte, S., Nathues, A., Pieters, C. M., Russell, C. T., & Raymond, C. A. (2014). Spectral analysis of the bright materials on the asteroid Vesta. *Icarus, 240*, 73-85.

Zambon, F., Frigeri, A., Combe, J.-P., Tosi, F., Longobardo, A., Ammannito, E., De Sanctis, M. C., Blewett, D. T., Scully, J., Palomba, E., Denevi, B., Yingst, A., Russell, C. T., & Raymond, C. A. (2015). Spectral analysis of the quadrangles Av-13 and Av-14 on Vesta. *259*, 181. doi:10.1016/j.icarus.2015.05.015

# 12 Appendix

## 12.1 IDL code example for PSL VIS measurement processing to Dawn FC data format

```
pro sprem_fc, lab1, labf3f4, labf5f4, labf3f8, lres3


  ;a=file_search('H:\PhD (H)\Vesta\Vesta_Exp\11-01-2018_hypersthene_vesta_tanja\Dati\*.txt')
  a=file_search('D:\D_backup\zu groß für PHD\Vesta_Exp\11-jan-2018_hypersthene_vesta_tanja\Dati\*.txt')
  ; prepare array for spectra storage
  ;lab=fltarr(16,2151)

  lab1=fltarr(17,16593) ;NOTE: Okt19 specs have one row less (16593), all other 16594

  ;loop for reading data into array
  ;wl=fltarr(1,16593)
  for i=0,size(a, /n_elements)-1 do begin data=read_ascii(a(i), data_start=0)

  ;convert from structure into array (read_ascii creates structure)
  b=data.(0)
 ; remove spike from line 9530 to 9560 (not necessary for Ed Cloutis data)
  d=b(1,9530)-b(1,9560)
  sr=fltarr(31)
  sr(0)=b(1,9530)-(d/31)
  for j=1,30 do begin sr(j)=sr(j-1)-(d/31)
;
end
srr=fltarr(1,16593)
;
srr(0,0:9529)=b(1,0:9529)
srr(0,9530:9560)=sr
srr(0,9561:16592)=b(1,9561:16592)

wl=10000000/b(0,*)

;write result into  spectra array
lab1(i+1,*)=srr*0.98
lab1(0,*)=wl ;/1000 doesn't work at lab5 generation (it takes nm)

end


;read responsivity functions (from 0.35 um to 1.1 um) from Stefan S.
resp2=read_ascii('D:/D_backup/masterarbeit/HED_Spectra_Relab/stefan_responsivity/responsivity_F2.dat',
data_start=11)
r2=resp2.(0)
resp3=read_ascii('D:/D_backup/masterarbeit/HED_Spectra_Relab/stefan_responsivity/responsivity_F3.dat',
data_start=11)
r3=resp3.(0)
resp4=read_ascii('D:/D_backup/masterarbeit/HED_Spectra_Relab/stefan_responsivity/responsivity_F4.dat',
data_start=11)
r4=resp4.(0)
resp5=read_ascii('D:/D_backup/masterarbeit/HED_Spectra_Relab/stefan_responsivity/responsivity_F5.dat',
data_start=11)
r5=resp5.(0)
resp6=read_ascii('D:/D_backup/masterarbeit/HED_Spectra_Relab/stefan_responsivity/responsivity_F6.dat',
data_start=11)
r6=resp6.(0)
resp7=read_ascii('D:/D_backup/masterarbeit/HED_Spectra_Relab/stefan_responsivity/responsivity_F7.dat',
data_start=11)
r7=resp7.(0)
resp8=read_ascii('D:/D_backup/masterarbeit/HED_Spectra_Relab/stefan_responsivity/responsivity_F8.dat',
data_start=11)
r8=resp8.(0)

;integrate over whole profile
sum7=total(r7(1,*))
sum3=total(r3(1,*))
sum4=total(r4(1,*))
sum5=total(r5(1,*))
sum6=total(r6(1,*))
sum8=total(r8(1,*))
sum2=total(r2(1,*))
sum7=total(r7(1,*))



;create vector for normal space with 5 nm (and 10 nm?)
x5nm=findgen(141, start=400, increment=5)
lab5=fltarr(size(lab1(*,0), /n_elements)-1,141)
;lab5=fltarr(size(lab1(*,0), /n_elements)-1,141)
x=fltarr(141)
```

```
;search for closest element to wavelength as in RELAB measurements
for i=0, size(x5nm, /n_elements)-1 do begin temp=nearest_element(x5nm(i), lab1(0,*),p )
x(i)=p
end
for j=0, size(lab5(*,0), /n_elements)-1 do begin lab5(j,*)=lab1(j+1,x)
end



sizec=size(lab5(*,0),/n_elements)
sizer=size(lab5(0,*),/n_elements)

l_sr2=fltarr(sizec,sizer)
l_sr3=fltarr(sizec,sizer)
l_sr4=fltarr(sizec,sizer)
l_sr5=fltarr(sizec,sizer)
l_sr6=fltarr(sizec,sizer)
l_sr7=fltarr(sizec,sizer)
l_sr8=fltarr(sizec,sizer)

;calcualte the product of spectra * responsivity function
for i=0,sizec-1 do begin l_sr3(i,*)=lab5(i,*)*r3(1,*)
l_sr4(i,*)=lab5(i,*)*r4(1,*)
l_sr5(i,*)=lab5(i,*)*r5(1,*)
l_sr6(i,*)=lab5(i,*)*r6(1,*)
l_sr8(i,*)=lab5(i,*)*r8(1,*)
l_sr7(i,*)=lab5(i,*)*r7(1,*)
l_sr2(i,*)=lab5(i,*)*r2(1,*)
end

; integrate over whole profile
lsumr3=fltarr(1,sizec)
lsumr4=fltarr(1,sizec)
lsumr5=fltarr(1,sizec)
lsumr6=fltarr(1,sizec)
lsumr8=fltarr(1,sizec)
lsumr2=fltarr(1,sizec)
lsumr7=fltarr(1,sizec)

for i=0,sizec-1 do begin lsumr3(0,i)=total(l_sr3(i,*))
lsumr4(0,i)=total(l_sr4(i,*))
lsumr5(0,i)=total(l_sr5(i,*))
lsumr6(0,i)=total(l_sr6(i,*))
lsumr8(0,i)=total(l_sr8(i,*))
lsumr2(0,i)=total(l_sr2(i,*))
lsumr7(0,i)=total(l_sr7(i,*))
end


lres3=fltarr(1,sizec)
lres4=fltarr(1,sizec)
lres5=fltarr(1,sizec)
lres6=fltarr(1,sizec)
lres8=fltarr(1,sizec)
lres2=fltarr(1,sizec)
lres7=fltarr(1,sizec)


;calculate weighted average formula
for i=0,sizec-1 do begin lres3(i)=lsumr3(i)/sum3
lres4(i)=lsumr4(i)/sum4
lres5(i)=lsumr5(i)/sum5
lres6(i)=lsumr6(i)/sum6
lres8(i)=lsumr8(i)/sum8
lres2(i)=lsumr2(i)/sum2
lres7(i)=lsumr7(i)/sum7
end

labf5f6=fltarr(1,sizec)
labf3f4=fltarr(1,sizec)
labf5f4=fltarr(1,sizec)
labf3f8=fltarr(1,sizec)
labf8f5=fltarr(1,sizec)

;calculate ratios
for i=0, sizec-1 do begin labf5f6(0,i)=lres5(0,i)/lres6(0,i)
labf3f4(0,i)=lres3(0,i)/lres4(0,i)
labf5f4(0,i)=lres5(0,i)/lres4(0,i)
labf3f8(0,i)=lres3(0,i)/lres8(0,i)
labf8f5(0,i)=lres8(0,i)/lres5(0,i)
end

end
```

## 12.2 VIR locations of PIDs, surroundings and presumable bedrock

| ROI | sample | line |
|---|---|---|
| **cube 394858895** | | |
| PID #1 | 113 | 238 |
| surrounding #1 | 100 | 237 |
| PID #2 | 171 | 247 |
| surrounding #2 | 181 | 241 |
| PID #3 | 209 | 223 |
| surrounding #3 | 196 | 214 |
| PID #4 | 104 | 104 |
| surrounding #4 | 113 | 108 |
| bedrock #1 | 174 | 230 |
| **cube 395166968** | | |
| PID #5 | 58 | 301 |
| surrounding #5 | 54 | 315 |
| PID #6 | 144 | 248 |
| surrounding #6 | 139 | 257 |
| bedrock #2 | 116 | 210 |
| bedrock #3 | 14 | 367 |
| **cube 394992761** | | |
| PID #7 | 153 | 84 |
| surrounding #7 | 155 | 73 |
| PID #8 | 150 | 26 |
| surrounding #8 | 157 | 32 |
| PID #9 | 137 | 9 |
| surrounding #9 | 136 | 21 |
| bedrock #4 | 144 | 31 |
| **cube 395301549** | | |
| crater-fill PID | 163 | 89 |
| halo | 158 | 117 |
| crater wall | 138 | 130 |

## 12.3 FC values of PIDs and other locations of interest

Data shown here are illustrated in Fig. 4.34. Regions of interest are saved as an .roi file, to open along any of the global FC filter mosaics (HAMO resolution) in ENVI, both attached in data CD.

| Region of interest | 2.8 | dev | 750/917 | dev | 750 | dev | n (px number) |
|---|---|---|---|---|---|---|---|
| PID 1 | 0.029 | 0.001 | 1.586 | 0.023 | 0.209 | 0.004 | 12 |
| PID 2 | 0.027 | 0.001 | 1.618 | 0.033 | 0.216 | 0.006 | 29 |
| PID 3 | 0.029 | 0.001 | 1.608 | 0.042 | 0.211 | 0.008 | 22 |
| PID 4 | 0.034 | 0.000 | 1.513 | 0.037 | 0.198 | 0.007 | 11 |
| PID 5 | 0.025 | 0.001 | 1.685 | 0.031 | 0.202 | 0.006 | 41 |
| PID 6 | 0.025 | 0.001 | 1.528 | 0.009 | 0.196 | 0.005 | 8 |
| PID 7 | 0.034 | 0.001 | 1.450 | 0.023 | 0.183 | 0.004 | 16 |
| PID 8 | 0.034 | 0.001 | 1.429 | 0.008 | 0.170 | 0.002 | 12 |
| PID 9 | 0.035 | 0.000 | 1.435 | 0.009 | 0.165 | 0.002 | 8 |
| PID 10 | 0.030 | 0.002 | 1.582 | 0.047 | 0.200 | 0.009 | 66 |
| PID 11 | 0.031 | 0.001 | 1.436 | 0.014 | 0.171 | 0.004 | 82 |
| PID 12 | 0.034 | 0.002 | 1.428 | 0.018 | 0.175 | 0.003 | 68 |
| | | | | | | | |
| Surrounding 1 | 0.032 | 0.001 | 1.404 | 0.020 | 0.176 | 0.005 | 151 |
| Surrounding 2 | 0.032 | 0.001 | 1.388 | 0.022 | 0.173 | 0.006 | 207 |
| Surrounding 3 | 0.035 | 0.001 | 1.387 | 0.015 | 0.168 | 0.005 | 150 |
| Surrounding 4 | 0.034 | 0.001 | 1.367 | 0.016 | 0.167 | 0.005 | 70 |
| Surrounding 5 | 0.027 | 0.002 | 1.471 | 0.024 | 0.186 | 0.007 | 275 |
| Surrounding 6 | 0.028 | 0.002 | 1.413 | 0.009 | 0.176 | 0.003 | 68 |
| Surrounding 7 | 0.035 | 0.001 | 1.352 | 0.013 | 0.162 | 0.004 | 226 |
| Surrounding 8 | 0.034 | 0.001 | 1.343 | 0.009 | 0.163 | 0.002 | 28 |
| Surrounding 9 | 0.035 | 0.000 | 1.356 | 0.011 | 0.164 | 0.002 | 37 |
| Surrounding 10 | 0.036 | 0.003 | 1.366 | 0.029 | 0.161 | 0.008 | 356 |
| Surrounding 11 | 0.034 | 0.001 | 1.342 | 0.014 | 0.165 | 0.003 | 214 |
| Surrounding 12 | 0.042 | 0.002 | 1.318 | 0.011 | 0.148 | 0.004 | 264 |
| | | | | | | | |
| crater-fill PID | 0.022 | 0.002 | 1.444 | 0.028 | 0.183 | 0.007 | 2235 |
| Halo | 0.020 | 0.002 | 1.578 | 0.032 | 0.202 | 0.004 | 481 |
| Wall above halo | 0.021 | 0.001 | 1.552 | 0.023 | 0.209 | 0.006 | 462 |
| NW crater wall (Marcia) | 0.022 | 0.001 | 1.592 | 0.019 | 0.231 | 0.007 | 266 |
| | | | | | | | |
| Aelia ejecta | 0.052 | 0.002 | 1.784 | 0.061 | 0.169 | 0.011 | 37 |
| Lollia ejecta | 0.025 | 0.001 | 1.931 | 0.044 | 0.200 | 0.005 | 180 |
| Matronalia Rupes | 0.020 | 0.001 | 2.295 | 0.161 | 0.272 | 0.018 | 243 |
| Antonia wall | 0.019 | 0.002 | 1.949 | 0.129 | 0.217 | 0.013 | 729 |
| Fonteia wall | 0.021 | 0.015 | 2.231 | 0.104 | 0.214 | 0.007 | 78 |
| Diogenitite-rich crater south of Serena crater | 0.036 | 0.002 | 1.895 | 0.066 | 0.197 | 0.011 | 43 |
| Diogenitic regolith | 0.021 | 0.002 | 1.588 | 0.033 | 0.214 | 0.008 | 11109 |
| | | | | | | | |
| Cornelia crater-fill PID | 0.035 | 0.004 | 1.305 | 0.019 | 0.167 | 0.006 | 83 |
| Cornelia western wall | 0.017 | 0.002 | 1.757 | 0.065 | 0.273 | 0.013 | 170 |
| Cornelia ejecta | 0.020 | 0.002 | 1.537 | 0.018 | 0.214 | 0.007 | 1506 |
| Fabia crater wall | 0.020 | 0.003 | 1.682 | 0.113 | 0.242 | 0.022 | 262 |
| | | | | | 0.000 | 0.000 | |
| Regolith below Teia | 0.028 | 0.001 | 1.460 | 0.011 | 0.193 | 0.005 | 1695 |
| Regolith west of Fabia | 0.027 | 0.001 | 1.462 | 0.020 | 0.199 | 0.008 | 4494 |
| Regolith east of Oppia | 0.027 | 0.001 | 1.420 | 0.019 | 0.192 | 0.006 | 1451 |

## 12.4 Spatial context of PIDs and other locations of interest

Images shown here illustrate the regions of interest generated and processed with the softwares ENVI/IDL. In the enlargement of Marcia (Fig. 12.1g), the crater-fill PID is in color purple, the halo in light green and the wall above halo in dark green (both have two separate polygons). NW crater wall is shown in red. Other ROIs in this part are PIDs and their surroundings.

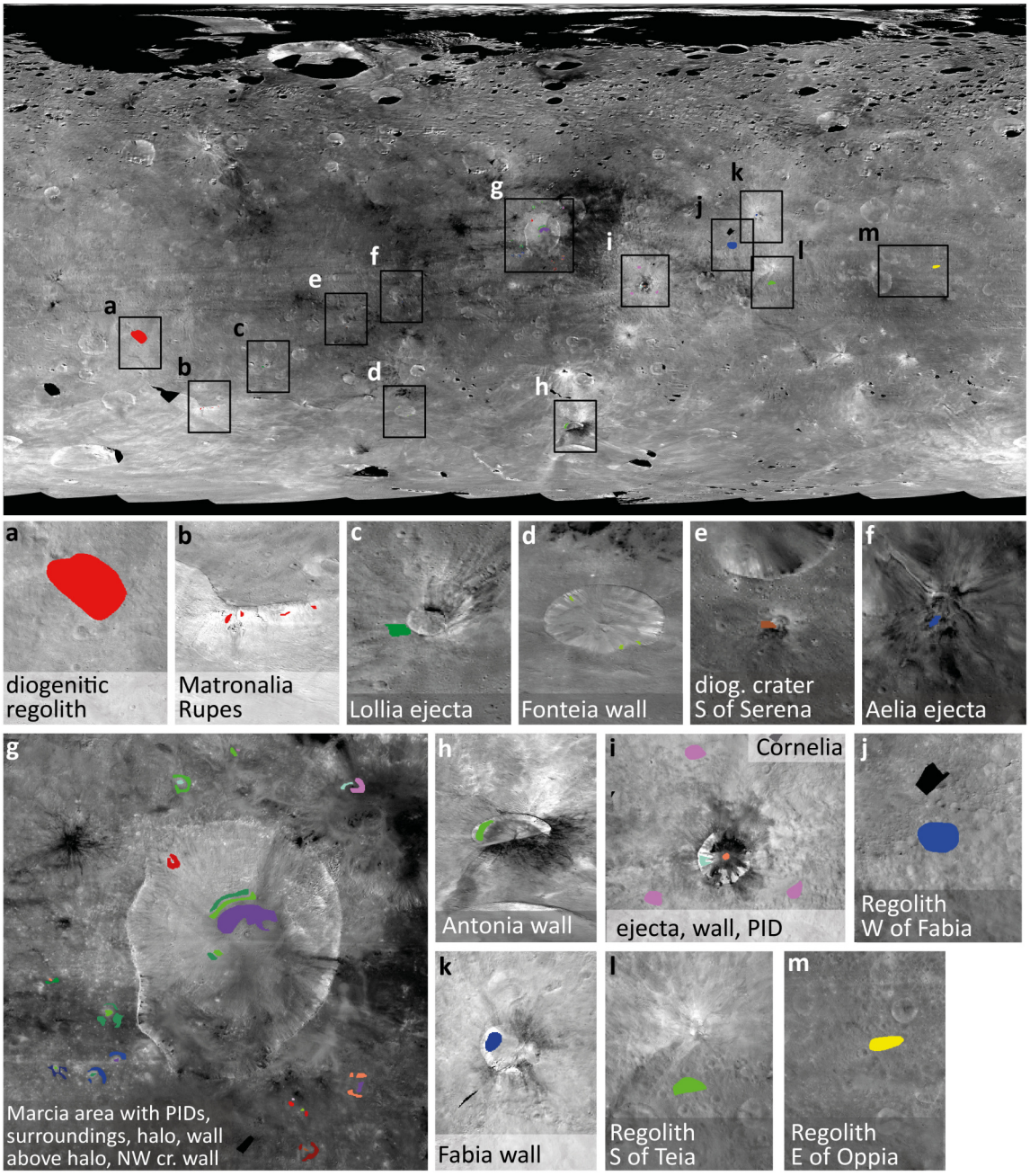


Figure 12.1

## 12.5 Complete WDS analysis

| No. | Comment | Date | SiO2 | TiO2 | Cr2O3 | FeO | MnO | Total | Fe2O3 |
|---|---|---|---|---|---|---|---|---|---|
| 1 | Murch_400_FeO-1 | 02.11.2021 13:08 | 0.05 | 0.00 | 0.04 | 89.96 | 0.00 | 90.04 | **99.967** |
| 2 | Murch_400_FeO-2 | 02.11.2021 13:10 | 0.11 | 0.00 | 0.08 | 88.99 | 0.00 | 89.19 | **98.895** |
| 3 | N5748_600_FeO | 02.11.2021 13:51 | 0.05 | 0.03 | 0.02 | 88.66 | 0.00 | 88.75 | **98.523** |
| 4 | N5748_600_FeO_2 | 02.11.2021 14:39 | 0.20 | 0.00 | 0.02 | 83.19 | 0.05 | 83.45 | **92.445** |
| 5 | N5748_600_FeO_3 | 02.11.2021 14:48 | 0.03 | 0.01 | 0.02 | 86.26 | 0.00 | 86.31 | **95.855** |

| **Standard Condition** | | | | |
|---|---|---|---|---|
| Voltage | 15 kV | | | |
| Current | 15 nA | | | |
| Probe diameter | focused | | | |
| | **Standard** | **Standard** | **counting times peak/ background** | **Crystal** |
| SiO2 | Cr-Augite | NMNH 164905 | 20/10 | TAP |
| TiO2 | Ilmenite | USNM 96189 | 20/10 | PETJ |
| Cr2O3 | Chromite | USNM 117075 | 20/10 | LIFH |
| FeO | Magnetite | USNM 114887 | 20/10 | LIFH |
| MnO | Ilmenite | USNM 96189 | 20/10 | PETJ |

## 12.6 EDS spectrum of Sulfur rich phase

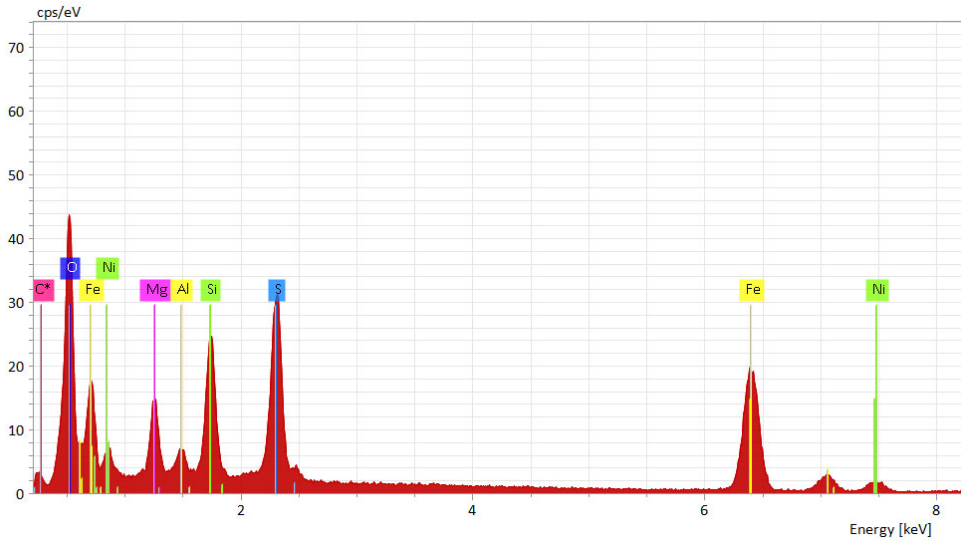


Figure 12.2